学　位　論　文

Preparation, Characterization, and Advanced Surface Functionalization of Multiple Transition Metal-Incorporated Cerium Oxides and Their Unique Catalytic Performances

（複合遷移金属が協働する酸化セリウムの調製、構造解析、
表面機能化とその触媒特性）

名古屋大学 大学院理学研究科物質理学専攻（化学系）

池　本　　悟

IKEMOTO Satoru

Abstract

In this Ph.D. thesis, I have proposed a novel design for advanced catalytic functionalization by modifying active sites with multiple metal species and organic ligands. I have focused on three topics: (1) the improvement of low-temperature redox properties of ceria-based oxides by introduction of multiple metal species and the elucidation of their structural mechanisms, (2) the enhancement of catalytic activity at low temperature on the multi-metal-incorporated ceria-based oxides, (3) the induction of catalytic activity by decoration with organic ligands. The modification with multiple metal species and organic ligands creates novel active structures and improves catalytic performances.

In chapter 1, general introduction is stated, regarding heterogeneous catalysts, in particular, ceria catalysts and catalyst designs for the modification of catalytically active sites.

In chapter 2, I report the structure and reversible low-temperature redox performances of ceria-based catalysts incorporated with Cr and a trace amount of Rh ($Cr_{0.19}Rh_{0.06}CeO_z$). The ceria-based $Cr_{0.19}Rh_{0.06}CeO_z$ catalysts were newly prepared by a hydrothermal method. Structural characterizations of ICP-OES, XRD, HAADF-STEM-EDS/EELS, XAFS, XPS revealed that the incorporation of Cr oxides dispersed Rh species on the surface of CeO_2. $Cr_{0.19}Rh_{0.06}CeO_z$ exhibited remarkable and reversible redox properties at low temperature below 373 K. The dynamic structural transformation during the redox reaction was characterized by *in situ* XAFS and *in situ* AP-XPS, and the formation of Rh nanoclusters promoted dual reduction of Cr and Ce at the oxide surface.

In chapter 3, I report the significant catalytic properties of $Cr_{0.19}Rh_{0.06}CeO_z$ for NO reduction with CO. $Cr_{0.19}Rh_{0.06}CeO_z$ was found to exhibit higher NO conversion and N_2 selectivity than those of $Rh_{0.04}CeO_z$ and $Cr_{0.17}CeO_z$. $Cr_{0.19}Rh_{0.06}CeO_z$ also exhibited remarkable durability for the NO reduction with CO. *In situ* FT-IR and *in situ* XAFS characterizations revealed that the roles of Cr and Rh in the NO reduction with CO: the Rh species adsorbed and activated both CO and NO on the catalyst surface and reduced Cr oxide species in addition to the CeO_2 surface cleaved NO adsorbed on Rh sites and transferred oxygen species from NO to CO. The co-incorporated Cr and Rh species in $Cr_{0.19}Rh_{0.06}CeO_z$ cooperatively enhanced the NO reduction performances with CO at low temperature.

In chapter 4, I report a coordination-induced trigger for catalytic activity on an organic ligand-functionalized catalyst, N-heterocyclic carbene (NHC)-decorated $Cr_{0.19}Rh_{0.06}CeO_z$. H_2-reduced $Cr_{0.19}Rh_{0.06}CeO_z$ (*r*-$Cr_{0.19}Rh_{0.06}CeO_z$) was decorated with

1,3-dicyclohexylimidazol-2-ylidene (ICy) to prepared NHC-decorated $Cr_{0.19}Rh_{0.06}CeO_z$ (ICy-*r*-$Cr_{0.19}Rh_{0.06}CeO_z$). The coordination structure of the NHC ligands on the catalyst surface was characterized by XAFS, FT-IR, XPS, and PL measurements, and it was clarified that the ICy ligand was attached as a carbene, and mainly interacted with Rh nanoclusters on *r*-$Cr_{0.19}Rh_{0.06}CeO_z$. ICy-*r*-$Cr_{0.19}Rh_{0.06}CeO_z$ exhibited catalytic activity for 1,4-arylation of cyclohexenone with phenylboronic acid, and several heterogeneity tests indicated that the catalytic reaction took place heterogeneously. *r*-$Cr_{0.19}Rh_{0.06}CeO_z$ without ICy was inactive, indicating that the coordination of the ICy carbene induced the catalytic activity. The electronic donation effect of ICy to Rh nanoclusters was negligible, and ICy offered close adsorption sites of phenyl group and cyclohexenone on the Rh cluster and facilitated the C−C bond formation of the two moieties, resulting in the changes in the cascade reaction mechanism for the C−C bond formation step, which was proposed by DFT calculations.

In chapter 5, concluding remarks are summarized for the results and discussion of this thesis.

Table of contents

Chapter 1

General introduction

1.1. Heterogenous catalysts

Catalysts are defined as substances that significantly accelerate reaction rates by lowering activation barriers and selectively synthesize desired products by controlling reaction pathways without being consumed themselves. Catalysis was first reported in the 18th century, and catalysts have developed over the past two and a half centuries. Heterogeneous catalysts are easily separable and recyclable solid catalysts and therefore play a crucial role in industry in the production of important fine chemicals such as transportation fuels, lubricants, pharmaceuticals, polymers, fibers, with over 90% of industrial chemicals being produced with the utilization of catalysts.[1] Heterogeneous catalysts are generally solid powders such as oxide nanoparticles, metal nanoparticles, or metal nanoparticles dispersed on a oxide support.[2]

Oxide catalysts such as silica (SiO_2), alumina (Al_2O_3), and zeolites generally have acid/base sites and are used as various acid-base catalysts.[2] Oxides containing reducible metal species are also used as redox catalysts, promoting reduction and oxidation processes for cleavage and formation of chemical bonds in reactants.[3]

Metal nanoparticle catalysts adsorb and activate reactants by electronically interacting with them. Metal atoms exposed on the surface exhibit specific properties depending on their sites, and lower-coordinated metal atoms (*e.g.*, corner, edge) are usually more catalytically active than full-coordinated metal atoms (*i.e.*, terrace).[4] Therefore, parameters such as size, morphology, and shape of the metal nanoparticles can greatly affect their catalytic activity.

Metal nanoparticles are generally dispersed on a support in order to enhance their catalytic properties. Dispersing metal nanoparticles on oxides increases the amount of surface metal atoms, exposing more active sites compared to bulk, and can greatly enhance their catalytic activities.[4] Porous oxide supports stabilize supported metal nanoparticles and inhibit their aggregation and deactivation.[4] With the development of nanoscience, various synthesis methods for nanocomposites with tunable morphologies and sizes have been developed over the past decades.[5] Recently, highly dispersed cluster or single atom catalysts, which are smaller than nanoparticle catalysts, have been developed, and the size effects provide new structural and electronic properties to exhibit unique catalytic performance.[6]

1.2. Cerium oxide: a unique oxide for catalysis

A cerium oxide (ceria, CeO_2) is an oxide forming a fluorite crystal structure with a face-centered cubic lattice. Ce^{4+} cations in CeO_2 coordinate to eight O^{2-} anions, which are coordinated by four Ce^{4+} cations. CeO_2 can undergo a reversible $Ce^{4+} \Leftrightarrow Ce^{3+}$ redox reaction with absorption and release of oxygen while maintaining its crystal structure (Figure 1.1).[7] The redox of Ce ions generates oxygen vacancies on the surface of ceria, which can adsorb and activate oxygen gas.[8] The reversible oxygen storage/release property assist catalytic reaction with redox process to enhance its catalytic activity. Thus, CeO_2 has been mainly used as a promoter of a gas-phase redox reaction such as three-way catalysts for purification of automobile exhaust gas, converting carbon monoxide, hydrocarbons, and nitrogen oxides into harmless carbon dioxide and nitrogen.[9] Other applications include the dry-reforming reaction of methane, water gas shift reaction, CO_2 hydrogenation, etc.[10] Recently, CeO_2 has been also applied to selective oxidation of organic compounds such as alcohols, hydrocarbons, and alkenes, in addition to the purification of pollutants and the conversion of C1 molecules (*e.g.*, CH_4, CO_2) to valuable chemicals.[11]

CeO_2 has been also used as a catalyst support of metal species. Irreducible oxides such as SiO_2 and Al_2O_3 are also widely used as supports because their large surface areas, but metal species supported on them more tend to sintering.[12] In contrast, CeO_2 provides high metal adsorption energies and retains dispersion of supported metal species, offering remarkable sintering resistance.[13] Liu *et al.* proposed to a concept of "metal affinity" to evaluate the metallophilic degree by analogizing the concept of hydrophilicity; *e.g.*, CeO_2 can be viewed as metallophilic and SiO_2 can be viewed as metallophobic (Figure 1.2).[14] The metallophilic surface of CeO_2 with high metal affinity can inhibit the diffusion and agglomeration of supported metal nanoparticles to maintain the size, the dispersion, and the catalytic activity of the metal nanoparticle catalysts. Furthermore, CeO_2 also provides a site for the formation of new active sites of metal species to enhance catalytic activity. For instance, Au nanoparticles supported on CeO_2 dynamically formed highly dispersed Au single atoms under reaction conditions of CO oxidation, suggesting that metal-support interaction is key for catalytic performances.[15]

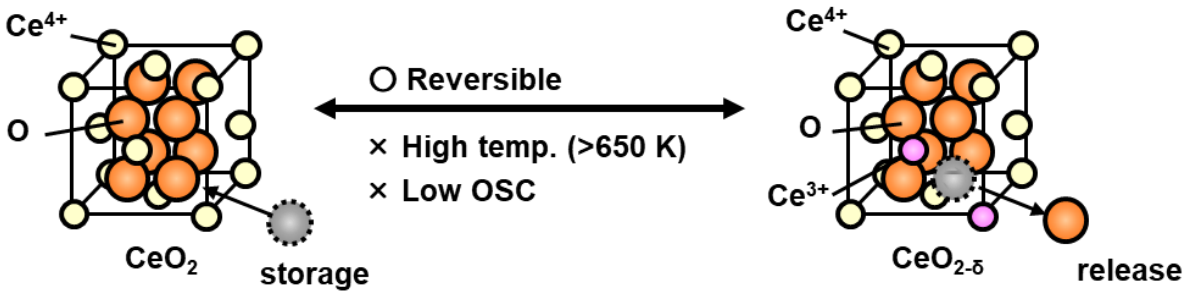

Figure 1.1. Schematic structures of CeO_2 in oxygen storage and release.

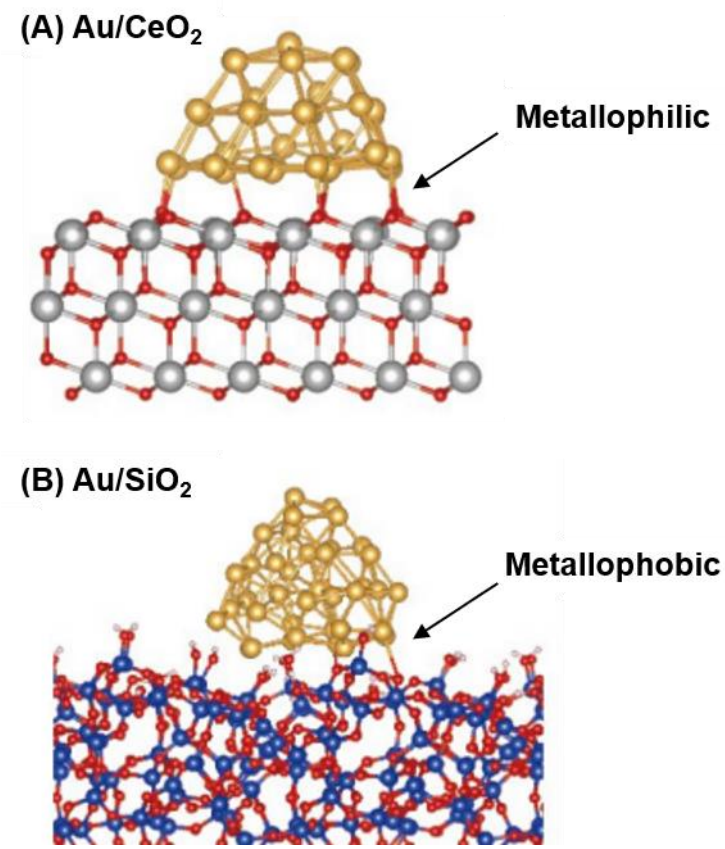

Figure 1.2. Simulated structure of Au nanoparticle on (A) CeO_2 and (B) SiO_2.[14]

1.3. Modification of catalytically active sites

1.3.1. Incorporation of additional metals

In order to improve the activity of oxide catalysts and metal-supported oxide catalysts, catalytic designs have been attempted to incorporate additives and control active structures. One such design is the addition of metals. The added metal not only forms metal nanoparticles on the oxide, but also dissolves into the oxide or alloys with the supported metal species to form new active sites.

Doping metal species into a bulk or a surface of a reducible oxide, which can be viewed as an oxide-oxide combination, distorts metal-oxygen bonds to improve the redox properties of the oxides. For instance, ceria-zirconia solid solution ($Ce_{1-x}Zr_xO_2$) has a regular atomic arrangement and higher oxygen storage/release capacity than that of CeO_2 (Figure 1.3).[16] Lower-valent cation dopants than the host oxide cation, *e.g.*, Sm^{3+} or Gd^{3+} can stabilize the formation of oxygen vacancies by doping into CeO_2 and promote oxygen diffusion in the material, and these dopants have important roles for low-temperature solid oxide fuel cells.[17] Reducible metal cation dopants into oxides can be themselves active species, and highly dispersed cations on the surface adsorb substrates and release the active oxygen, resulting in very high catalytic activity.[18]

Alloying of the added metal with the supported metal, which can be regarded as a metal-metal combination, changes the electronic state significantly and forms new active sites through the formation of hetero-metallic bonds, resulting in significant changes in catalytic activity and selectivity.[19] Recently, precise control of the active sites has been attempted by dispersing metal dopants within alloy particles in atomic level or by regulating their arrangement.[20]

Addition of metal oxides into metal-supported oxide catalysts, which can be considered as an oxide-metal combination, assists to form new active structures and provides new reaction systems. CeO_x islands on a SiO_2 support atomically disperse Pt species to enhance the catalytic activity and durability for CO oxidation with a sintering resistance, which were not observed in a Pt catalyst simply supported on CeO_2.[21] Overcoating of ZnO or Fe_2O_3 oxide layers on Pt-supported Al_2O_3 improved strong metal-oxide interaction between ZnO or Fe_2O_3 layers and Pt nanoparticles not only to suppress the sintering of metal species but also to enhance the catalytic activity in the aqueous-phase reforming (APR) of 1-propanol and the selectivity in the hydrogenation of cinnamaldehyde and 1,3-butadiene, respectively.[22] In particular, $ZnO/Pt/Al_2O_3$ catalyst with the ZnO overcoat exhibited higher catalytic activity and higher H_2 selectivity in the APR of 1-proparnol than $Pt/ZnO/Al_2O_3$, in which the Pt nanoparticles were supported on

ZnO and ZnO were dispersed on the Al_2O_3 surface, owing to both Pt-ZnO and Pt-Al_2O_3 interfaces (Figure 1.4).[22a]

However, it is still a significant challenge to elucidate detailed relationship of structure, physicochemical property, and catalytic performances.

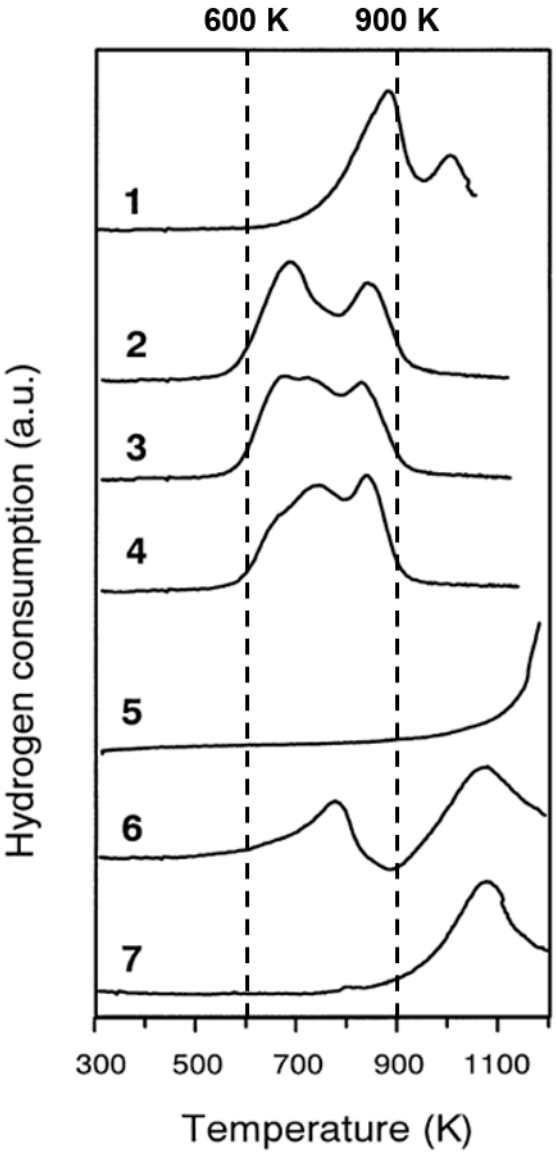

Figure 1.3. TPR profile of (1) fresh $Ce_{0.5}Zr_{0.5}O_2$ and (2-4) recycled, respectively, 1, 4, and 7 times; (5) sintered (~1 m^2 g^{-1}) $Ce_{0.5}Zr_{0.5}O_2$; (6) fresh CeO_2 and (7) recycled 2 times.[16a]

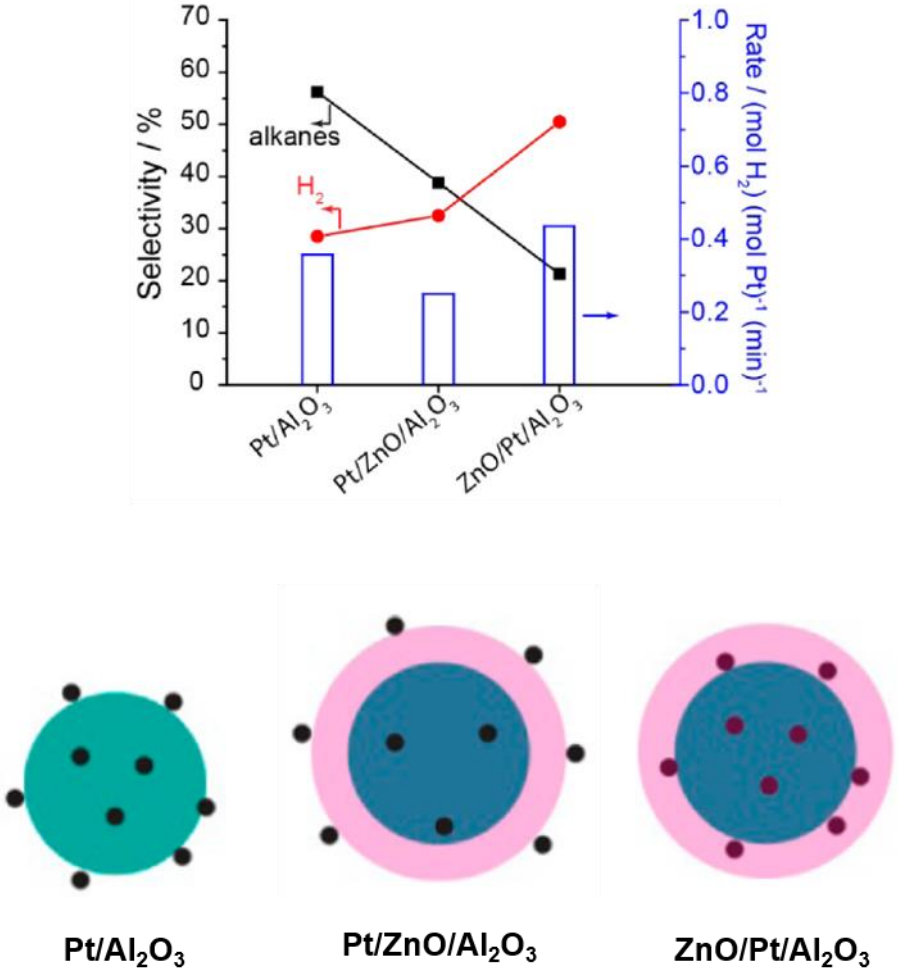

Figure 1.4. Selectivity of H_2 (red) and alkane (black) and H_2 formation rate for aqueous-phase reforming of 1-propanol on Pt/Al_2O_3, $Pt/ZnO/Al_2O_3$, and $ZnO/Pt/Al_2O_3$.[22a]

1.3.2. Decoration with organic ligands

Decoration with organic ligands have recently attracted great attention as a promising method for functionalizing metal nanoparticles and metal surfaces.[23] In the past decade, the organic ligands have been found to play an important role in controlling the shape and electronic structure of metal nanoparticles, which in turn have been crucial determinants of their catalytic properties.[24] Heterogeneous catalysis, a surface-controlled process, is closely related to the detailed surface structure of the catalyst. There are various metal coordination sites (terrace, edge, kink, or corner sites) on a metal nanoparticle, and these sites could offer very different coordination environments toward reactants, intermediates and products.[25] Since the distribution of the coordination sites depends on the size and shape of metal nanoparticles, structural changes caused by the decoration of the organic ligands have a potential to enhance catalytic performances.

In homogeneous catalysts, catalytically active metal centers are usually coordinated with organic ligands, and the ligands make a precise local reaction environment and induce significant steric and electronic effects to tailor catalytic activity and selectivity.[26] Organic ligands are also used in the synthesis of metal nanomaterials to prevent their agglomeration or control their shapes. The surface ligands have been long considered to block the active sites of metal nanoparticles to decrease their catalytic activities, and thus they are usually removed by heat treatments to develop their intrinsic catalytic activities.[27] However, in recent years, several studies have reported that surface ligands promote catalytic activity and selectivity. For example, in the industrial Lindlar's Pd catalysts, poisoning ligands (quinolone, sulfide, etc.) along with toxic metals such as Pb moderately attenuate catalytic activity and improve the selectivity toward the semihydrogenation of alkynes to alkenes.[28] Amine-capped Pt_3Co alloy nanoparticles demonstrate that a steric effect in long chain amines prevent direct contact of C=C bonds of α,β-unsaturated aldehydes with the catalyst surface to improve the selectivity for hydrogenation.[29] The best example of utilizing the steric effect of ligand decoration is the inducement of enantioselectivity by bulky chiral ligands. A cinchonidine-modified Pt catalyst on a carbon support was the first example of heterogenous asymmetric catalysis for hydrogenation of methyl pyruvate or methyl benzoylformate.[30] Recently, its detailed mechanism was investigated, and it is considered that the formation of diastereomeric complexes of chiral ligands and substrates is the key structure to induce chirality (Figure 1.5).[31] Based on this chiral nanoparticle system, other types of chiral nanoparticle catalysts have been widely investigated for asymmetric hydrogenation reactions[32] and C-C bond formation reactions.[33]

In addition to the steric effect for improvement of selectivity, electronic effect of surface ligands is also another crucial factor to tune catalytic properties. Rare literatures have been reported to propose the electronic effect of organic ligands on the surface of metal nanocatalysts.[34] In these cases, amine or phenolate ligands electronically affected to Pd nanoparticles to promote catalytic activities. To strengthen these electronic influences, NHC ligands with high electron-donating properties have also been used recently.[35] Pd-supported Al_2O_3 decorated with 1,3-bis(2,6-diisopropylphenyl)imidazol-2-ylidene (IPr) facilitated the oxidative addition of aryl halides by electron donation from IPr to Pd nanoparticles resulting in the catalytic inducement of amino-coupling reactions, which were not active without NHC ligands.[35a]

However, understanding the role of surface ligands on catalysis and precise controlling the heterogeneous catalysis are still of great challenges. In particular, it is much difficult to elucidate coordination structures of ligands on metal surfaces at the molecular level.

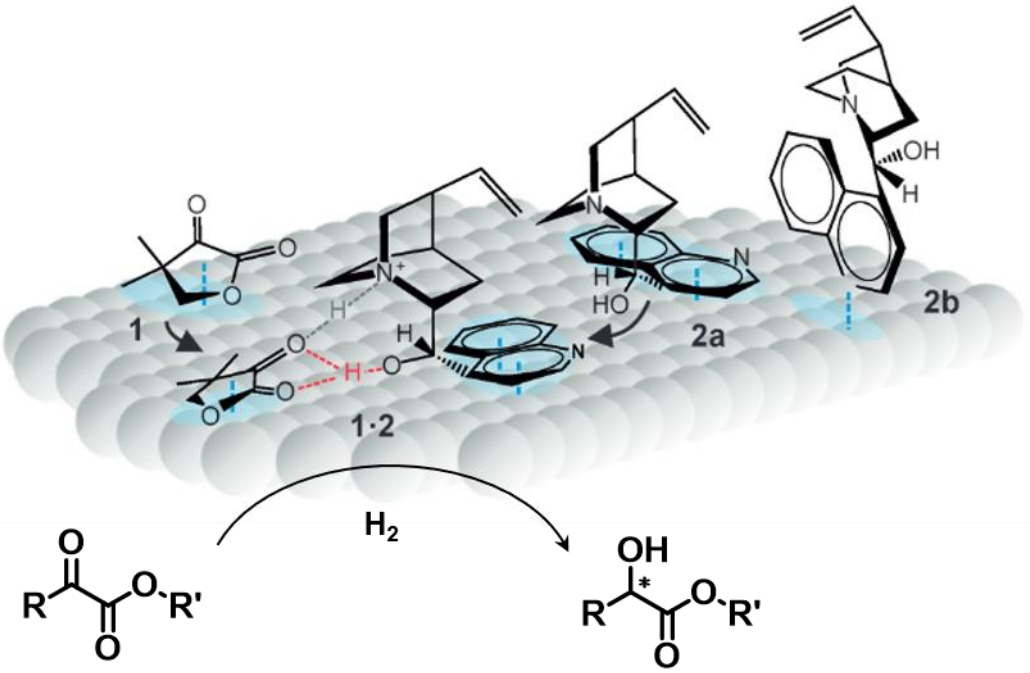

Figure 1.5. The heterogeneous asymmetric hydrogenation reaction through the formation of the surface complex of ketopantolactone (**1**) and π-bonded protonated cinchonidine (**2**) on the Pt surface.[31]

1.4. The aim of this thesis

In this thesis, I proposed novel design for advanced catalytic functionalization by modifying active sites with additional metal species and organic ligands. I have focused on three targets: (1) improvement of low-temperature redox properties of ceria-based oxides by introduction of multiple metal species and elucidation of their structural mechanisms, (2) enhancement of catalytic activity at low temperature on the multi-metal-incorporated ceria-based oxides, (3) induction of catalytic activity by decoration with organic ligands. The modification with multiple metal species and organic ligands creates novel active structures and improve catalytic performances.

In chapter 2, I report the structure and reversible low-temperature redox performances of a ceria-based catalyst incorporated with Cr and a trace amount of Rh ($Cr_{0.19}Rh_{0.06}CeO_z$). The ceria-based catalyst $Cr_{0.19}Rh_{0.06}CeO_z$ was newly prepared, and Cr oxides dispersed Rh species on the surface of CeO_2. $Cr_{0.19}Rh_{0.06}CeO_z$ exhibited the remarkable and reversible redox properties at low temperature. The dynamic structural transformation during the redox reaction was characterized by *in situ* spectroscopies.

In chapter 3, I report the remarkable catalytic properties of $Cr_{0.19}Rh_{0.06}CeO_z$ for NO reduction with CO. Modulation by Cr oxides to disperse Rh species as active sites enhanced catalytic activity, selectivity and durability for the reduction of NO with CO. *In situ* characterization clarified that Cr oxides also played an important role for the catalysis as superior oxygen mediators.

In chapter 4, I report a coordination-induced trigger for catalytic activity on an organic ligand-functionalized catalyst, N-heterocyclic carbene (NHC)-decorated $Cr_{0.19}Rh_{0.06}CeO_z$. The NHC-decorated catalyst was newly prepared, and the coordination structure of the NHC ligands on the catalyst surface was fully characterized. The prepared catalyst induced catalytic activity for 1,4-arylation reaction. DFT calculations proposed that NHC ligands tuned the active adsorption sites on Rh nanocluster of $Cr_{0.19}Rh_{0.06}CeO_z$ to promote a C−C bond formation in the 1,4-arylation reaction.

Details of the catalyst design are described in the introduction of the following chapters.

1.5. References

(1) (a) Zhang, L.; Ren, Y.; Liu, W.; Wang, A.; Zhang, T. Single-Atom Catalyst: A Rising Star for Green Synthesis of Fine Chemicals. *Natl. Sci. Rev.* **2018**, *5*, 653−672. (b) Sudarsanam, P.; Peeters, E.; Makshina, E. V.; Parvulescu, V. I.; Sels, B. F. Advances in Porous and Nanoscale Catalysts for Viable Biomass Conversion. *Chem. Soc. Rev.* **2019**, *48*, 2366−2421. (c) Murugesan, K.; Senthamarai, T.; Chandrashekhar, V. G.; Natte, K.; Kamer, P. C. J.; Beller, M.; Jagadeesh, R. V. Catalytic Reductive Aminations Using Molecular Hydrogen for Synthesis of Different Kinds of Amines. *Chem. Soc. Rev.* **2020**, *49*, 6273−6328. (d) Goh, B. H. H.; Chong, C. T.; Ge, Y.; Ong, H. C.; Ng, J.-H.; Tian, B.; Ashokkumar, V.; Lim, S.; Seljak, T.; Józsa, V. Progress in Utilisation of Waste Cooking Oil for Sustainable Biodiesel and Biojet Fuel Production. *Energy Convers. Manag.* **2020**, *223*, 113296. (e) Dai, Y.; Gao, X.; Wang, Q.; Wan, X.; Zhou, C.; Yang, Y. Recent Progress in Heterogeneous Metal and Metal Oxide Catalysts for Direct Dehydrogenation of Ethane and Propane. *Chem. Soc. Rev.* **2021**, *50*, 5590−5630. (f) Sancheti, S. V.; Yadav.; G. D. Synthesis of Environment-Friendly, Sustainable, and Nontoxic Bio-lubricants: A Critical Review of Advances and A Path Forward. *Biofuels, Bioprod. Bioref.* **2022**, *16*, 1172−1195.

(2) Xu, Y.; Cao, M.; Zhang, Q. Recent Advances and Perspective on Heterogeneous Catalysis Using Metals and Oxide Nanocrystals. *Mater. Chem. Front.* **2021**, *5*, 151−222.

(3) Védrine, J. C. Heterogeneous Catalysis on Metal Oxides. *Catalysts* **2017**, *7*, 341.

(4) Li, Z.; Ji, S.; Liu, Y.; Cao, X.; Tian, S.; Chen, Y.; Niu, Z.; Li, Y. Well-Defined Materials for Heterogeneous Catalysis: From Nanoparticles to Isolated Single-Atom Sites. *Chem. Rev.* **2020**, *120*, 623−682.

(5) Liu, L.; Corma, A. Metal Catalysts for Heterogeneous Catalysis: From Single Atoms to Nanoclusters and Nanoparticles. *Chem. Rev.* **2018**, *118*, 4981−5079.

(6) (a) Zhang, H.; Liu, G.; Ye, J. Single-Atom Catalysts: Emerging Multifunctional Materials in Heterogeneous Catalysis. *Adv. Energy Mater.* **2018**, *8*, 1701343. (b) Mitchell, S.; Vorobyeva, E.; Pérez-Ramírez, J. The Multifaceted Reactivity of Single-Atom Heterogeneous Catalysts. *Angew. Chem. Int. Ed.* **2018**, *57*, 15316−15329. (c) Dong, C.; Li, Y.; Cheng, D.; Zhang, M.; Liu, J.; Wang, Y.-G.; Xiao, D.; Ma, D. Supported Metal Clusters: Fabrication and Application in Heterogeneous Catalysis. *ACS Catal.* **2020**, *10*, 11011−11045.

(7) Li, P.; Chen, X.; Li, Y.; Schwank, J. W. A Review on Oxygen Storage Capacity of CeO_2-Based Materials: Influence Factors, Measurement Techniques, and

Applications in Reactions Related to Catalytic Automotive Emissions Control. *Catal. Today* **2019**, *327*, 90−115.

(8) Ma, Y.; Gao, W.; Zhang, Z.; Zhang, S.; Tian, Z.; Liu, Y.; Ho, J. C.; Qu, Y. Regulating the Surface of Nanoceria and Its Applications in Heterogeneous Catalysis. *Surf. Sci. Rep.* **2018**, *73*, 1−36.

(9) (a) Kaspar, J.; Fornasiero, P.; Graziani, M. Use of CeO_2-based Oxides in the Three-Way Catalysis. *Catal. Today* **1999**, *50*, 285−298. (b) Shan, Y.; Liu, Y.; Li, Y.; Yang, W. A Review on Application of Cerium-Based Oxides in Gaseous Pollutant Purification. *Sep. Purif. Technol.* **2020**, *250*, 117181.

(10) (a) Trovarelli, A. Catalytic Properties of Ceria and CeO_2-Containing Materials. *Catal. Rev.* **1996**, *38*, 439−520. (b) Laosiripojana, N.; Assabumrungrat, S. Catalytic Dry Reforming of Methane over High Surface Area Seria. *Appl. Catal. B* **2005**, *60*, 107−116. (c) Rodoriguez, J. A.; Grinter, D. C.; Liu, Z.; Palomino, R. M.; Senanayake, S. D. Ceria-Based Model Catalysts: Fundamental Studies on the Importance of the Metal-Ceria Interface in CO Oxidation, the Water-Gas Shift, CO_2 Hydrogenation, and Methane and Alcohol Reforming. *Chem. Soc. Rev.* **2017**, *46*, 1824−1841. (d) Boaro, M.; Colussi, S.; Trovarelli, A. Ceria-Based Materials in Hydrogenation and Reforming Reactions for CO_2 Valorization. *Front. Chem.* **2019**, *7*, 28.

(11) (a) Vivier, L.; Duprez, D. Ceria-Based Solid Catalysts for Organic Chemistry. *ChemSusChem* **2010**, *3*, 654−678. (b) Chang. K.; Zhang, H.; Cheng, M.; Lu, Q. Application of Ceria in CO_2 Conversion Catalysis. *ACS Catal.* **2020**, *10*, 613−631. (c) Lei, L.; Wanng, Y.; Zhang, Z.; An, J.; Wang, F. Transformations of Biomass, Its Derivatives, and Downstream Chemicals over Ceria Catalysts. *ACS Catal.* **2020**, *10*, 8788−8814. (d) Huang, X.; Zhang, K.; Peng, B.; Wang, G.; Muhler, M.; Wang, F. Ceria-Based Materials for Thermocatalytic and Photocatalytic Organic Synthesis. *ACS Catal.* **2021**, *11*, 9618−9678.

(12) (a) Olthof, B.; Khodakov, A.; Bell, A. T.; Iglesia, E. Effects of Support Composition and Pretreatment Conditions on the Structure of Vanadia Dispersed on SiO_2, Al_2O_3, TiO_2, ZrO_2, and HfO_2. *J. Phys. Chem. B* **2000**, *104*, 1516−1528. (b) Campbell, C. T. The Energetics of Supported Metal Nanoparticles: Relationships to Sintering Rates and Catalytic Activity. *Acc. Chem. Res.* **2013**, *46*, 1712−1719. (c) Delariva, A. T.; Hansen, T. W.; Challa, S. R.; Datye, A. K. In situ Transmission Electron Microscopy of Catalyst Sintering. *J. Catal.* **2013**, *308*, 291−305.

(13) (a) Farmer, J. A.; Campbell, C. T. Ceria Maintains Smaller Metal Catalyst Particles by Strong Metal-Support Bonding. *Science* **2010**, *329*, 933−936. (b) Jones, J.; Xiong,

H.; DeLaRiva, A. T.; Peterson, E. J.; Pham, H.; Challa, S. R.; Qi, G.; Oh, S.; Wiebenga, M. H.; Hernández, X. I. P. Thermally Stable Single-Atom Platinum-on-Ceria Catalysts via Atom Trapping. *Science* **2016**, *353*, 150−154. (c) Montini, T.; Melchionna, M.; Monai, M.; Fornasiero, P. Fundamentals and Catalytic Applications of CeO_2-Based Materials. *Chem. Rev.* **2016**, *116*, 5987−6041.

(14) Liu, J.-C.; Luo, L.; Xiao, H.; Zhu, J.; He, Y.; Li, J. Metal Affinity of Support Dictates Sintering of Gold Catalysts. *J. Am. Chem. Soc.* **2022**, *144*, 20601−20609.

(15) (a) Wang, Y. G.; Mei, D.; Glezakou, V. A.; Li, J.; Rousseau, R. Dynamic Formation of Single-Atom Catalytic Active Sites on Ceria-supported Gold Nanoparticles. *Nat. Commun.* **2015**, *6*, 6511. (b) Liu, J. C.; Wang, Y. G.; Li, J. Toward Rational Design of Oxide-Supported Single-Atom Catalysts: Atomic Dispersion of Gold on Ceria. *J. Am. Chem. Soc.* **2017**, *139*, 6190−6199.

(16) (a) Fornasiero, P.; Balducci, G.; Monte, R. D.; Kasper, J.; Sergo, V.; Gubitosa, G.; Ferrero, A.; Graziani, M. Modification of the Redox Behaviour of CeO_2 Induced by Structural Doping with ZrO_2. *J. Catal.* **1996**, *164*, 173–183. (b) Boaro, M.; Vicario, M.; de Leitenburg, C.; Dolcetti, G.; Trovarelli, A. The Use of Temperature-Programmed and Dynamic/Transient Methods in Catalysis: Characterization of Ceria-Based, Model Three-Way Catalysts. *Catal. Today* **2003**, *77*, 407−417. (c) Ozawa, M.; Kimura, M.; Isogai, A. The Application of Ce-Zr Oxide Solid Solution to Oxygen Storage Promoters in Automotive Catalysts. *J. Alloys Comp.* **1993**, *193*, 73−75. (d) Morikawa, A.; Kikuta, K.; Suda, A.; Shinjo, H. Enhancement of Oxygen Storage Capacity by Reductive Treatment of Al_2O_3 and CeO_2–ZrO_2 Solid Solution Nanocomposite. *App. Catal. B Environ.* **2009**, *88*, 542−549.

(17) McFarland, E. W.; Metiu, H. Catalysis by Doped Oxides. *Chem. Rev.* **2013**, *113*, 4391−4427.

(18) Kim, H. J.; Jang, M. G.; Shin, D.; Han, J. W. Design of Ceria Catalysts for Low-Temperature CO Oxidation. *ChemCatChem* **2020**, *12*, 11−26.

(19) (a) Docherty, S. R.; Copéret, C. Deciphering Metal−Oxide and Metal−Metal Interplay via Surface Organometallic Chemistry: A Case Study with CO_2 Hydrogenation to Methanol. *J. Am. Chem. Soc.* **2021**, *143*, 6767−6780. (b) Liu, K.; Qin, R.; Zheng, N. Insights into the Interfacial Effects in Heterogeneous Metal Nanocatalysts toward Selective Hydrogenation. *J. Am. Chem. Soc.* **2021**, *143*, 4483−4499.

(20) (a) Mao, J.; Yin, J.; Pei, J.; Wang, D.; Li, Y. Single Atom Alloy: An Emerging Atomic Site Material for Catalytic Applications. *Nano Today* **2020**, *34*, 100917. (b) Zhang,

T.; Walsh, A. G.; Yu, J.; Zhang, P. Single-Atom Alloy Catalysts: Structural Analysis, Electronic Properties and Catalytic Activities. *Chem. Soc. Rev.* **2021**, *50*, 569−588.

(21) Li, X.; Pereira-Hernández, X. I.; Chen, Y.; Xu, J.; Zhao, J.; Pao, C.-W.; Fang, C.-Y.; Wang, Y.; Gates, B. C.; Liu, J. Functional CeO_x Nanoglues for Robus Atomically Dispersed Catalysts. *Nature* **2022**, *611*, 284−288.

(22) (a) Lei, Y.; Lee, S.; Low, K.-B.; Marshall, C. L.; Elam, J. W. Combining Electronic and Geometric Effects of ZnO-Promoted Pt Nanocatalysts for Aqueous Phase Reforming of 1-Propanol. *ACS Catal.* **2016**, *6*, 3457−3460. (b) Yi, H.; Xia, Y.; Yan, H.; Lu, J. Coating Pd/Al_2O_3 Catalysts with FeO_x Enhances Both Activity and Selectivity in 1,3-Butadiene Hydrogenation. *Chin. J. Catal.* **2017**, *38*, 1581−1587. (c) Hu, Q.; Wang, S.; Gao, Z.; Li, Y.; Zhang, Q.; Xiang, Q.; Qin, Y. The Previse Decoration of Pt Nanoparticles with Fe Oxide by Atomic Layer Deposition for the Selective Hydrogenation of Cinnamaldehyde. *Appl. Catal. B: Environ.* **2017**, *218*, 591−599.

(23) Liu, P.; Qin, R.; Fu, G.; Zheng, N. Surface Coordination Chemistry of Metal Nanomaterials. *J. Am. Chem. Soc.* **2017**, *139*, 2122–2131.

(24) *Nanoscience: The Science of the Small in Physics, Engineering, Chemistry, Biology and Medicine*; Schaefer, H. E. Ed.; Springer, Heidelberg, 2010.

(25) *Selective Nanocatalysts and Nanoscience: Concepts for Heterogeneous and Homogeneous Catalysis*; Zecchina, A.; Bordiga, S.; Groppo, E. Eds.; Wiley-VCH, Weinheim, 2011.

(26) (a) Zhao, Y.; Fu, G.; Zheng, N. F. Shaping the Selectivity in Heterogeneous Hydrogenation by Using Molecular Modification Strategies: Experiment and Theory. *Catal. Today* **2017**, *279*, 36−44. (b) *Homogeneous Catalysis: Mechanisms and Industrial Applications*; Bhaduri, S.; Mukesh, D. Eds.; Wiley-Interscience, New York, 2000. (c) Schmid, A.; Dordick, J. S.; Hauer, B.; Kiener, A.; Wubbolts, M.; Witholt, B. Industrial Biocatalysis Today and Tomorrow. *Nature* **2001**, *409*, 258−268.

(27) Huang, W.; Hua, Q.; Cao, T. Influence and Removal of Capping Ligands on Catalytic Colloidal Nanoparticles. *Catal. Lett.* **2014**, *144*, 1355−1369.

(28) Marvell, E. N.; Li, T. Catalytic Semihydrogenation of the Triple Bond. *Synthesis* **1973**, *1973*, 457−468.

(29) Wu, B. H.; Huang, H. Q.; Yang, J.; Zheng, N. F.; Fu, G. Selective Hydrogenation of α,β-Unsaturated Aldehydes Catalyzed by Amine-Capped Platinum-Cobalt Nanocrystals. *Angew. Chem. Int. Ed.* **2012**, *51*, 3440−3443.

(30) (a) Orito, Y.; Imai, S.; Niwa, S. Asymmetric Hydrogenation of Methyl Pyruvate Using Pt-C Catalyst Modified with Cinchonidine. *J. Chem. Soc. Jpn.* **1979**, *8*, 1118–1120. (b) Orito, Y.; Imai, S.; Niwa, S.; Nguyen, G. H. Asymmetric Hydrogenation of Methyl Benzoylformate Using Platinum-Carbon Catalysts Modified with Cinchonidine. *J. Synth. Org. Chem., Jpn*. **1979**, *37*, 173–174.

(31) Meemken, F.; Maeda, N.; Hungerbühler, K.; Baiker, A. Platinum-Catalyzed Asymmetric Hydrogenation: Spectroscopic Evidence for an O-H-O Hydrogen-Bond Interaction between Substrate and Modifier *Angew. Chem. Int. Ed.* **2012**, *51*, 8212–8216.

(32) Heitbaum, M.; Glorius, F.; Escher, I. Asymmetric Heterogeneous Catalysis. *Angew. Chem. Int. Ed.* **2006**, *45*, 4732–4762.

(33) Yasukawa, T.; Miyamura, H.; Kobayashi, S. Chiral Metal Nanoparticle-Catalyzed Asymmetric C–C Bond Formation Reactions. *Chem. Soc. Rev.* **2014**, *43*, 1450–1461.

(34) (a) Luksirikul, P.; Tedsree, K.; Moloney, M. G.; Green, M. L. H.; Tsang, S. C. E. Electron Promotion by Surface Functional Groups of Single Wall Carbon Nanotubes to Overlying Metal Particles in a Fuel-Cell Catalyst. *Angew. Chem. Int. Ed.* **2012**, *51*, 6998−7001. (b) Jones, S.; Qu, J.; Tedsree, K.; Gong, X.-Q.; Tsang, S. C. E. Prominent Electronic and Geometric Modifications of Palladium Nanoparticles by Polymer Stabilizers for Hydrogen Production under Ambient Conditions. *Angew. Chem. Int. Ed.* **2012**, *51*, 11275−11278.

(35) (a) Ernst, J. B.; Schwermann, C.; Yokota, G.; Tada, M.; Muratsugu, S.; Doltsinis, N. L.; Glorius, F. Molecular Adsorbates Switch on Heterogeneous Catalysis: Induction of Reactivity by N-Heterocyclic Carbenes. *J. Am. Chem. Soc.* **2017**, *139*, 9144–9147. (b) Lewis, R. J.; Koy, M.; Macino, M.; Das, M.; Carter, J. H.; Morgan, D. J.; Davies, T. E.; Ernst, J. B.; Freakley; S. J.; Glorius, F.; Hutchings, G. J. N-Heterocyclic Carbene Modified Palladium Catalysts for the Direct Synthesis of Hydrogen Peroxide. *J. Am. Chem. Soc.* **2022**, *144*, 15431–15436.

Chapter 2

Reversible low-temperature redox activity from the concerted activation of multiple metal species on a Cr and Rh-incorporated ceria catalyst ($Cr_{0.19}Rh_{0.06}CeO_z$)

2.1. Introduction

2.1.1. Improvement of oxygen storage/release capacity of CeO_2

As mentioned in Section 1.2., ceria (CeO_2) is well known for its oxygen storage/release capacity (OSC) and its unique properties as a catalyst support for precious metals. It has been applied to extensive technologies such as three-way catalysis, solid oxide fuel cells, solar cells, capacitance, and chemical polishing.[1] The OSC of CeO_2 benefits the enhancement of catalytic reaction activities; however, the OSC of pure CeO_2 below 473 K is typically too low, and high temperatures above 673 K are usually necessary for sufficient redox activity.[1c,2]

In order to improve the OSC of CeO_2, the addition of other transition metals has been widely attempted.[1c,2] Ceria-zirconia solid solution ($Ce_{1-x}Zr_xO_2$) is one of the most widely studied ceria-based catalysts, and it has been reported to have an ordered atomic arrangement and high OSC.[1b,c,3] The addition of 3d transition metals to CeO_2 has demonstrated to decrease the reduction temperature and increase the amount of reducible Ce ions.[2,4] For instance, $Ce_{1-x}M_xO_{2-y}$ mixed oxides (M = Cr,[4d,g,o] Mn,[4b,k,o,q,s] Fe,[4f,j,o,s,u,z] Co,[4o,q,s] Ni,[4q-s] Cu[4e,t]) were reported to show lower reduction temperatures than pure CeO_2. It has been suggested that the reduction of 3d transition metal ions mainly contributed to the lowest reduction temperature region, and the contribution to Ce reduction was minor at low temperature. $Ce_{1-x}Cr_xO_{2-y}$,[4d] $Ce_{1-x}Fe_xO_{2-y}$,[4j] $Ce_{1-x}Ni_xO_{2-y}$,[4r] and CuO/CeO_2[4p] achieved the overall reduction of 20–30% of Ce ions; however, the reduction temperatures were in the range of 777 K and 1073 K, at which Ce^{4+} in the bulk of pure CeO_2 was also reduced. Several systems such as $Ce_{0.67}Cr_{0.33}O_{2-y}$[4d] and $Ce_{0.5}Mn_{0.5}O_{2-y}$[4k] were reported to show reversible redox properties (Figure 2.1). Other systems such as $Ce_{0.9}Cu_{0.1}O_{2-y}$[4e] could be reduced at low temperature of around 383 K but easily lost its redox activity after reoxidation (Figure 2.2).

The addition of noble metals[5] to CeO_2 has also been demonstrated to facilitate the reduction of the noble metal ions incorporated into ceria, effectively increasing the amount of reducible Ce ions while significantly lowering the reduction temperature, and the improvement in redox properties has a significant influence on catalytic activity. Noble metal ion supported/doped ceria systems (Ru/CeO_2,[5s] Rh/CeO_2,[5d,f,j,k,p,q,t] Pd/CeO_2,[5h,j,m] Pt/CeO_2[5h,j,u]) and $Ce_{1-x}M'_xO_{2-y}$ mixed oxides (M' = Ru,[5g] Rh,[5e,i,l,r] Pd[5l,n]) were reported to exhibit initial reduction of noble metal cations to metallic states, and this reduction promotes the reduction of Ce^{4+} at the similar temperature. For examples, it was reported that the reduction of Rh species in Rh/CeO_2 (1 wt% Rh)[5p] at 373–423 K occurred with 23% of the Ce reduction without the aggregation of the Rh particles. $Rh_xCe_{1-x}O_{2-y}$ (x

= 0.05, Rh: 5.5 wt%) solid solution[5r] exhibited that approximately 20% of the Ce reduction was possible below 423 K accompanied with the reversible redox and structural change of Rh species ($Rh^{3+}_xCe_{1-x}O_{2-y} \leftrightarrow Rh_n^{\delta+}/CeO_{2-y}$). However, several $Ce_{1-x}M'_xO_{2-y}$ mixed oxide systems were reported to show poor redox reversibility. The reduction of $Ce_{0.89}Pd_{0.11}O_{2-y}$[5l] irreversibly proceeded at 335 K (Figure 2.3(A)). $Ce_{0.89}Rh_{0.11}O_{2-y}$[5l] exhibited a reversible redox activity at 353 K (Figure 2.3(B)), but the redox was limited to only Rh species and Ce ions negligibly contributed the reduction at low temperature.

The introduction of multiple metal species into CeO_2 has also been also investigated to improve the redox property of Ce ions and catalytic activity.[6] On $Pt/Ce_{0.75}Zr_{0.25}O_2$,[6d] the ceria reduction reaction with CO proceeded at 773 K, and on Pt/ordered $Ce_2Zr_2O_7$ with remarkable OSC property,[6g] supported Pt nanoparticles significantly facilitated the reduction of $Ce_2Zr_2O_7$ with H_2 above 573 K. On $Pd/CeO_2–ZrO_2–Pr_2O_3$,[6n] the number of oxygen vacancies increased with the increasing Zr^{4+} to enhance metal-support interaction and catalytic activities for the elimination of CO and NO_2. Ni/ordered $Ce_2Zr_2O_x$ (x = 7–8) catalyzed steam reforming of methane above 673 K and showed a discontinuity at x = 7.5 depending on surface oxygen vacancy and oxygen diffusion efficiency of the $Ce_2Zr_2O_x$ surpport.[6o] CeO_2-based solid solutions with transition metal ions and noble metal ions (*e.g.*, $Ce_{0.83}Ti_{0.15}Pt_{0.02}O_{2-y}$,[6f] $Ce_{0.89}Fe_{0.1}Pd_{0.01}O_{2-y}$,[6i] and $Ce_{0.88}M_{0.1}Pd_{0.02}O_{2-y}$ (M = Mn, Co, Ni, Cu)[6k]) drastically improved their redox performances such as reduction temperatures, amounts of reducible Ce species, and reproducibility, and it was suggested that both the reduction of Ce^{4+} and transition metal ions proceeded after the reduction of noble metal ions. $Ce_{0.83}Ti_{0.15}Pt_{0.02}O_{2-y}$[6f] showed three peaks in temperature-programmed reduction (TPR) from 223 K to 923 K attributed to three redox couples of Pt^{2+}/Pt^0, Ti^{4+}/Ti^{3+}, and Ce^{4+}/Ce^{3+}. $Ce_{0.89}Fe_{0.1}Pd_{0.01}O_{2-y}$[6i] exhibited a TPR peak at 378 K (Figure 2.4(A)), which was suggested to include not only Pd^{2+}/Pd^0 redox couples but also Fe^{3+}/Fe^{2+} and Ce^{4+}/Ce^{3+} redox couples. $Ce_{0.88}Ni_{0.1}Pd_{0.02}O_{2-y}$[6k] showed a small TPR peak around 343 K (Figure 2.4(B)), but the low-temperature reduction made little contribution to the overall OSC of the mixed oxide. Thus, the above numerous examples indicate that it is still difficult to achieve reversible redox performances with the reduction of Ce^{4+} sites below 373 K in addition to the reduction of additional metal species in mixed oxides.

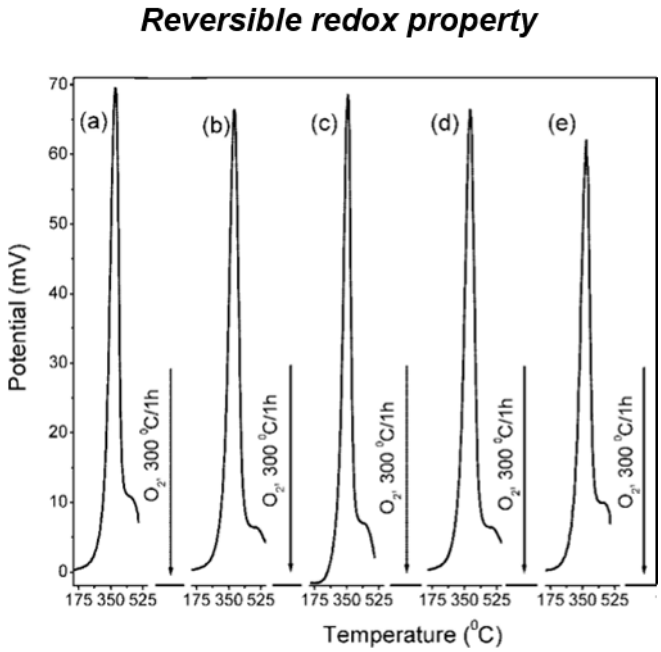

Figure 2.1. H_2-TPR profiles of $Ce_{0.67}Cr_{0.33}O_{2-y}$ in reversible reduction/oxidation for five cycles (a-e).[4d]

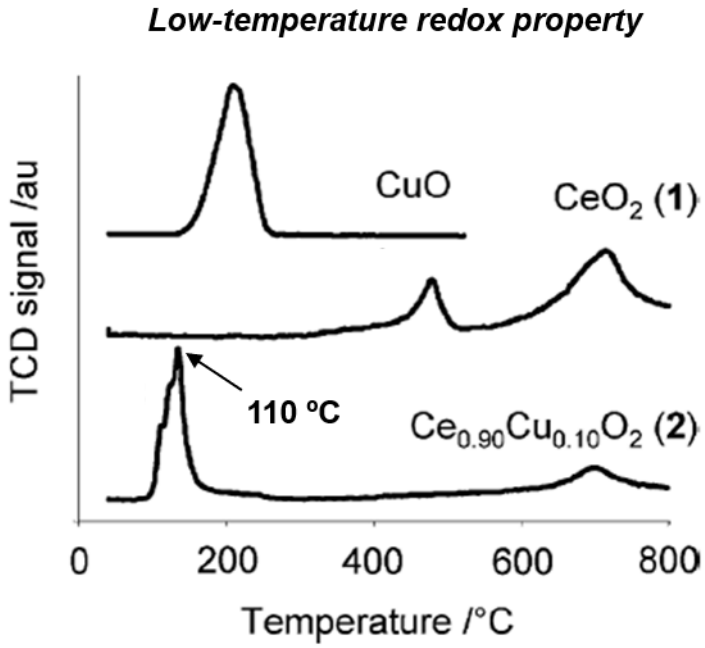

Figure 2.2. H_2-TPR profiles of CuO (profile scaled down), CeO_2 (**1**), and $Ce_{0.90}Cu_{0.10}O_2$ (**2**).[4e]

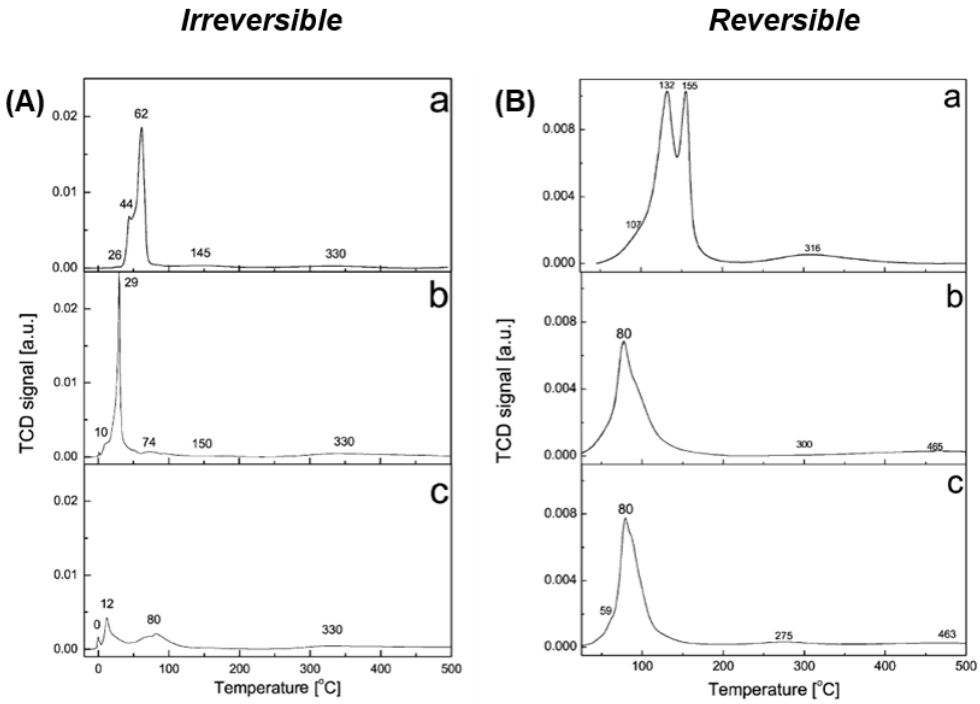

Figure 2.3. H_2-TPR profiles of (A) $Ce_{0.89}Pd_{0.11}O_{2-y}$ and (B) $Ce_{0.89}Rh_{0.11}O_{2-y}$ in reversible reduction/oxidation for five cycles (a-c).[51]

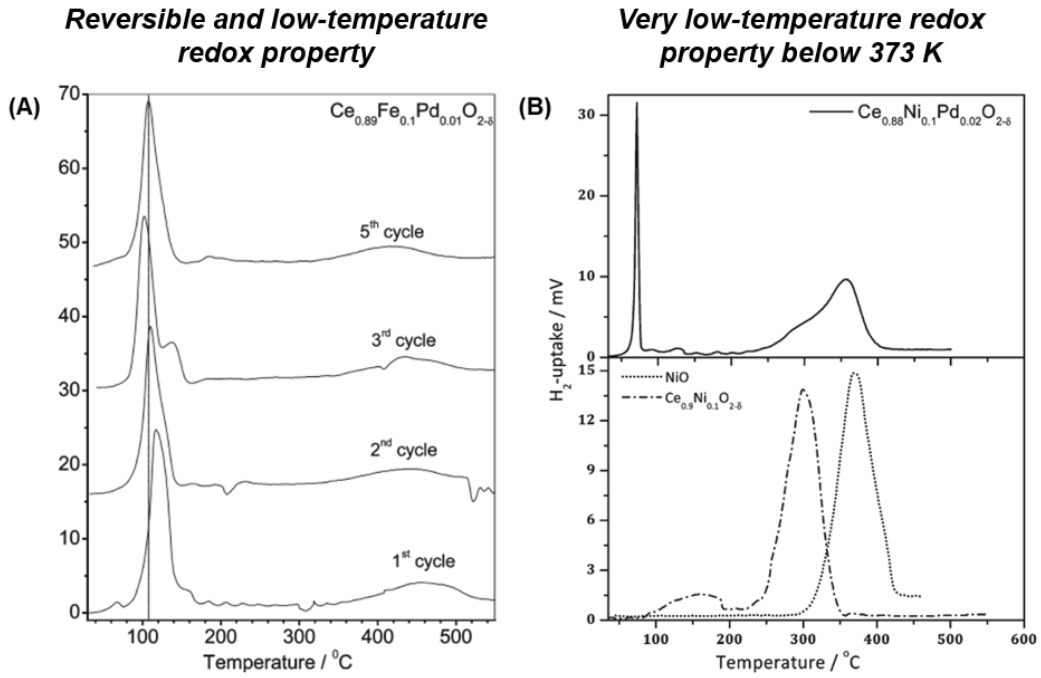

Figure 2.4. H_2-TPR profiles of (A) $Ce_{0.89}Fe_{0.1}Pd_{0.01}O_{2-y}$[6i] and (B) $Ce_{0.88}Ni_{0.1}Pd_{0.02}O_{2-y}$.[6k]

2.1.2. The aim of this research

In this chapter, I focused on the structure and the reversible low-temperature redox properties of a new ceria-based catalyst incorporated with Cr and a trace amount of Rh ($Cr_{0.19}Rh_{0.06}CeO_z$).[7,8] $Cr_{0.19}Rh_{0.06}CeO_z$ was prepared by a hydrothermal method. The bulk and surface structures of $Cr_{0.19}Rh_{0.06}CeO_z$ were fully characterized by inductively coupled plasma optical emission spectrometry (ICP-OES), X-ray diffraction (XRD), high angle annular dark-field scanning transmission electron microscopy (HAADF-STEM), X-ray absorption fine structure (XAFS), X-ray photoelectron spectroscopy (XPS), and the effect of incorporation of Cr and Rh species were investigated by comparing with other metal compositions of $Cr_xRh_yCeO_z$. The redox property of $Cr_{0.19}Rh_{0.06}CeO_z$ were evaluated by temperature-programmed reduction (TPR), and temperature-programmed oxidation (TPO), and $Cr_{0.19}Rh_{0.06}CeO_z$ exhibited the remarkable and reversible redox activity at low temperature below 373 K. The dynamic redox behaviors of Cr, Rh, and Ce were characterized by *in situ* XAFS and *in situ* ambient-pressure (AP)-XPS, and the structural transformation mechanism in the redox process was proposed.

2.2. Experimental section

2.2.1. Materials and instruments

$Cr(NO_3)_3 \cdot 9H_2O$ (99%) and $Ce(NO_3)_3 \cdot 6H_2O$ (99.99%) were purchased from Sigma-Aldrich. $RhCl_3 \cdot 3H_2O$ (40 wt% Rh) and NaOH (97.0%) were purchased form Wako. These chemicals were used without further purification. Milli-Q was obtained using an ultrapure water production system (Direct-Q UV 3, Merck). Standard solutions of Cr (1000 ppm), Rh (1000 ppm), and Ce (1000 ppm) for ICP-OES measurement were purchased from Wako. Nitrogen (N_2, G1 grade, 99.9995%) and helium (He, G1 grade, 99.99995%) gases were used for N_2 adsorption/desorption measurements. Hydrogen (H_2, G1 grade, 99.99999%) and oxygen (O_2, G1 grade, 99.99995%) gases were used for temperature-programmed reduction/oxidation measurements. H_2 (G1 grade, 99.99999%), O_2 (99.99%), and N_2 (99.9%) gases were used for *in situ* XAFS measurements.

A high-vacuum glass line with dry N_2 and a glove box with dry Ar were used for experiments under inert conditions.

2.2.2. Preparation of $Cr_xRh_yCeO_z$ and reference catalysts

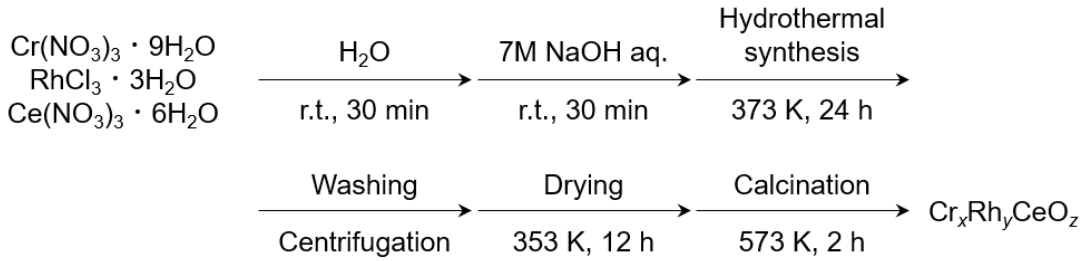

Scheme 2.1. Preparation scheme of $Cr_xRh_yCeO_z$.

A typical preparation process of $Cr_{0.19}Rh_{0.06}CeO_z$ was as follows (Scheme 2.1). $Cr(NO_3)_3 \cdot 9H_2O$ (0.67 mmol), $RhCl_3 \cdot 3H_2O$ (0.22 mmol), and $Ce(NO_3)_3 \cdot 6H_2O$ (3.5 mmol) were dissolved in ultrapure water (18 mL) under continuous stirring. A 7 M aqueous NaOH solution (53 mL) was added to the solution. After stirring for 30 min, the slurry was transferred to a Teflon-lined stainless steel vessel autoclave with a volume of 100 mL. The autoclave was sealed and heated at 373 K for 24 h. After cooling down to room temperature, precipitates were separated by centrifugation, washed with ultrapure water and ethanol several times, and dried under air atmosphere at 353 K for 12 h. The solid was ground into powder and calcined at 573 K for 2 h.

Ceria samples incorporating Cr and Rh with other metal compositions ($Cr_xRh_yCeO_z$) were prepared by this method as the preparation of $Cr_{0.19}Rh_{0.06}CeO_z$, by changing the amount of metal salt precursors as shown in Table 2.1. $Rh_{0.04}CeO_z$, $Cr_{0.17}CeO_z$, and CeO_2 were prepared by this procedure without the Cr and/or Rh precursors.

Table 2.1. Preparation Conditions of $Cr_xRh_yCeO_z$ with Different Cr and Rh Ratios

Sample	$Cr(NO_3)_3 \cdot 9H_2O$ /mg (/mmol)	$RhCl_3 \cdot 3H_2O$ /mg (/mmol)	$Ce(NO_3)_3 \cdot 6H_2O$ /g (/mmol)
$Cr_{0.19}Rh_{0.06}CeO_z$	267 (0.667)	58.2 (0.221)	1.53 (3.52)
$Rh_{0.04}CeO_z$	—	58.2 (0.221)	1.82 (4.19)
$Cr_{0.17}CeO_z$	267 (0.667)	—	1.63 (3.74)
CeO_2	—	—	1.77 (4.07)
$Cr_{0.06}Rh_{0.04}CeO_z$	88.8 (0.222)	58.2 (0.221)	1.72 (3.96)
$Cr_{0.12}Rh_{0.06}CeO_z$	178 (0.445)	58.2 (0.221)	1.62 (3.74)
$Cr_{0.24}Rh_{0.07}CeO_z$	356 (0.890)	58.2 (0.221)	1.43 (3.30)
$Cr_{0.35}Rh_{0.07}CeO_z$	445 (1.111)	58.2 (0.221)	1.34 (3.08)
$Cr_{0.18}Rh_{0.01}CeO_z$	262 (0.655)	11.3 (0.043)	1.59 (3.65)
$Cr_{0.18}Rh_{0.04}CeO_z$	264 (0.659)	34.5 (0.131)	1.56 (3.59)
$Cr_{0.19}Rh_{0.08}CeO_z$	266 (0.664)	81.2 (0.308)	1.49 (3.44)
$Cr_{0.19}Rh_{0.11}CeO_z$	268 (0.669)	105.9 (0.402)	1.47 (3.38)

2.2.3. Structural characterizations of $Cr_xRh_yCeO_z$

Inductively coupled plasma optical emission spectrometry (ICP-OES)

The metal compositions of the prepared samples were analyzed by ICP-OES (Vista-Pro-AX, Varian). The oxide samples were treated with fuming nitric acid at 353 K until complete dissolution. The solutions were diluted with ultrapure water and filtered with a syringe filter (pore size: 0.2 μmϕ) prior to ICP-OES analysis. Emission spectra were measured at 267.716 nm (Cr), 343.488 nm (Rh), and 418.659 nm (Ce), and the atomic ratios of Cr, Rh, and Ce were calculated from the calibration curves prepared from standard solutions (Figure 2.5). Measurement conditions for ICP-OES were listed in Table 2.2.

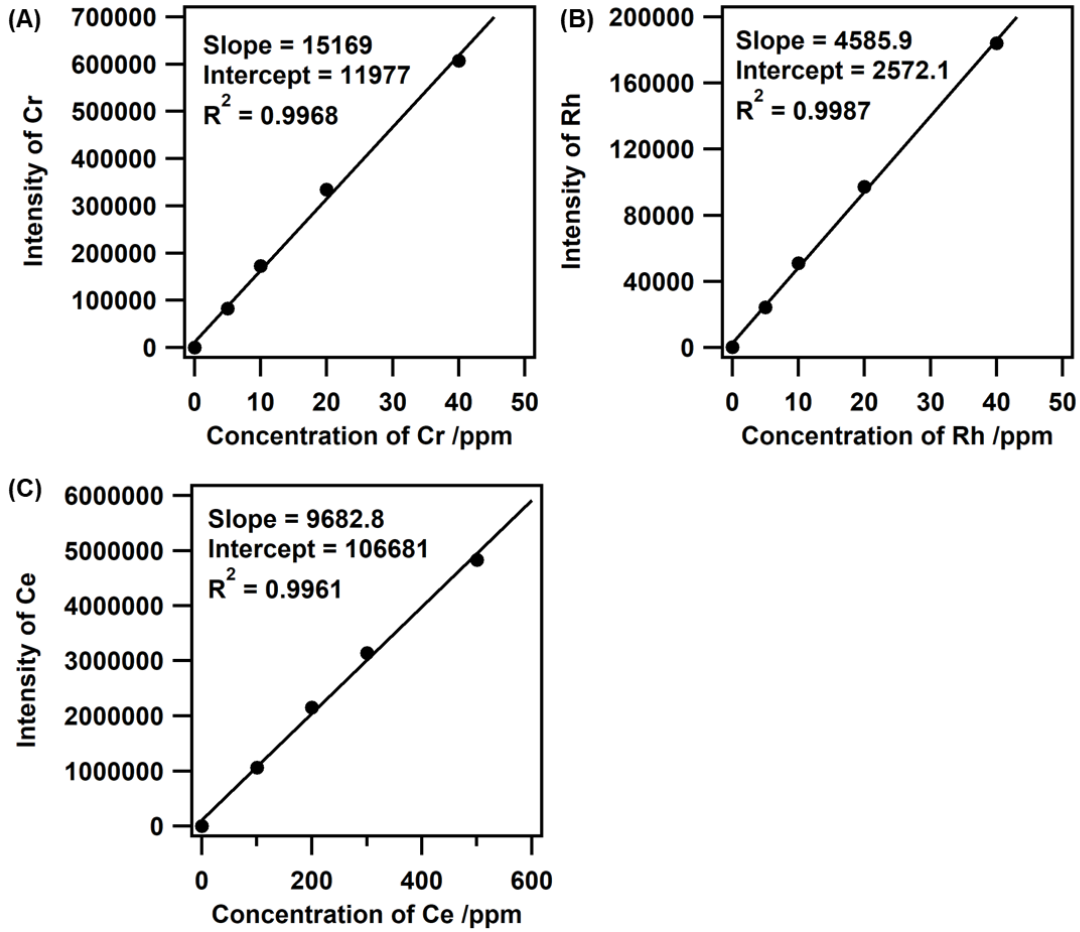

Figure 2.5. Calibration curves of (A) Cr, (B) Rh, and (C) Ce for ICP-OES.

Table 2.2. Measurement Conditions for ICP-OES

Power	1.20 kW	Sample capture time	10 s
Plasma flow	15.0 L min^{-1}	Rinse time	10 s
Auxiliary flow	1.50 L min^{-1}	Pump speed	15 rpm
Nebulizer flow	0.75 L min^{-1}	High speed pump	On
Repetition time	3.00 s	Repetitive measurement	3 times
Stabilization time	10 s		

Brunauer-Emmett-Teller (BET) analysis

Nitrogen adsorption and desorption was performed on a surface adsorption analyzer (Micromeritics ASAP-2020, Shimadzu) at 77 K. The oxide samples (100–480 mg) were degassed at 423 K for 2 h under vacuum before the sorption measurement. Dead volume was measured with helium after degassing before the adsorption measurement. Measurement conditions for nitrogen sorption were listed in Table 2.3.

An average diameter of the oxide particles was estimated from a BET surface area using Equation 2.1.

$$D = \frac{6}{dS} \qquad \text{(Equation 2.1)}$$

D: average diameter of particles, *d*: density, *S*: specific surface area.

Table 2.3. Measurement Conditions for Nitrogen Adsorption and Desorption

Evacuation phase		Heating phase	
Temperature ramp rate	10 K min^{-1}	Ramp rate	10 K min^{-1}
Target temperature	403 K	Hold temperature	403 K
Evacuation rate	2.0 mmHg s^{-1}	Hold time	120 min
Unrestricted evacuation	15.0 mmHg	Evacuation and Heating phase	
Vacuum setpoint	15 μmHg	Hold pressure	15 mmHg
Evacuation time	10 min		

Powder X-ray diffraction (XRD)

XRD patterns were measured by an X-ray diffractometer (MultiFlex, Rigaku; Cu K_α, λ = 1.5418 Å, 40 kV, 30 mA) at a scan rate of 2° min^{-1} at 293–298 K under air. Measurement conditions for XRD were listed in Table 2.4.

Table 2.4. Measurement Conditions for XRD

X-ray source	Cu K_α (8.048 keV)	Scan speed	2.0 º min^{-1}
Voltage	40 kV	Divergence slit	1 º
Current	30 mA	Scattering slit	1 º
Measurement range	3-90 º	Receiving slit	0.3 mm

Transmission electron microscopy (TEM) and high-angle annular dark field-scanning transmission electron microscopy (HAADF-STEM) with energy dispersive X-ray spectroscopy (EDS) and electron energy loss spectroscopy (EELS)

TEM and HAADF-STEM images with EDS and EELS spectra were taken using a transmission electron microscope (JEM-ARM 200F, JEOL; accelerating voltage of 200 kV) at the High Voltage Electron Microscope Laboratory, Institute of Materials and Systems for Sustainability, Nagoya University, Japan. Oxide samples were directly deposited on a copper microgrid and were blown with an air duster gun to remove excess particles. HAADF-STEM-EELS was initially measured, and then HAADF-STEM-EDS was consequently measured at the same view. As for HAADF-STEM-EDS images of Cr and Ce, Cr K fluorescence (5269 − 5555 eV, relatively very weak intensity) was deconvoluted from Ce L_α (4701−4977 eV) fluorescence. Measurement conditions for HAADF-STEM-EDS/EELS were listed in Tables 2.5, 2.6.

Table 2.5. Measurement Conditions for HAADF-STEM-EDS

Element	Characteristic X-ray	Energy range /eV
Cr	K	5269−5555
Rh	L_α	2603−2789
Ce	L_α	4701−4977
O	K	469−581

Acceleration voltage: 200 kV, magnification: 1.6×10^7, image resolution: 512×512, map resolution: 256×256.

Table 2.6. Measurement Conditions for HAADF-STEM-EELS

Element	Characteristic X-ray	Energy range /eV
Cr	L_{III}, L_{II}	574.0−604.1
Ce	M_V, M_{IV}	883.1−918.1
O	K	532.1−554.1

Acceleration voltage: 200 kV, magnification: 1.0×10^7, size in pixel: 100×100.

X-ray photoelectron spectroscopy (XPS)

XPS was performed using an X-ray photoelectron spectrometer (Scienta Omicron R4000, base pressure: 1×10^{-7} Pa) with the monochromatized Al K_α X-ray source (Scienta Omicron MX650, photon energy: 1486.7 eV, power: 180 W). Oxide samples were pressed into pellet disks (10 mmϕ, 40 mg, pressed at 18 MPa), which were attached to a cell holder using carbon tape. The binding energies were referenced to the Au $4f_{7/2}$ peak of metallic Au foil (83.96 eV).[9] The Shirley background was subtracted, and each peak was fitted by Voigt function.[10] Measurement conditions for XPS were listed in Table 2.7.

Table 2.7. Measurement Conditions for XPS

Name	Energy range /eV	Time per step /ms	Repeats
Test	0-1200	20	1
Ce 3d	870-940	40	150
O 1s	520-545	40	50
Cr 2p	565-600	40	250
Rh 3d	300-325	40	250
Rh 3p	490-540	40	200
C 1s	270-310	40	150
Survey	0-1200	20	1

Path energy: 200 eV, energy step: 0.1 eV.

X-ray absorption fine structure (XAFS)

XAFS spectra at the Cr *K*-edge and Ce L_{III}-edge were measured in transmission mode at room temperature at the BL9C and BL12C stations of the Photon Factory (PF) at KEK-IMSS (Tsukuba, Japan), the BL11S2 of the Aichi Synchrotron Radiation Center (Aichi SR, Seto, Japan), and the BL36XU of SPring-8 (Sayo, Japan). The energy and current of the electrons in the storage ring were 2.5 GeV and 450 mA in the Photon Factory, and 8 GeV and 100 mA in SPring-8, respectively. X-rays from the storage ring were monochromatized with a Si(111) double-crystal monochromator. Ni-coated mirrors (cut-off energy = 10 keV) and Au-coated mirrors (cut-off energy = 12 keV) were inserted in the BL12C beamline of the PF and the BL11S2 beamline of the Aichi SR, respectively, to remove higher order X-ray. At the BL9C and BL12C of the PF and BL36XU of the SPring-8, two ionization chambers filled with a mixture of N_2 and He gases (3/7, v/v) and a mixture of N_2 and Ar gases (8.5/1.5, v/v) were used to monitor the incident (I_0) and transmitted (I) X-rays, respectively. At the BL11S2 of the Aichi SR, two ionization chambers filled with a mixture of N_2 and He gases (3/7, v/v) and a mixture of N_2 and Ar gases (7.5/2.5, v/v) were used to monitor the incident (I_0) and transmitted (I) X-rays, respectively. Cr *K*-edge XAFS spectrum of $Cr_{0.06}Rh_{0.06}CeO_z$ was measured in fluorescence mode with a 7-element silicon drift detector (SDD) at room temperature at the BL11S2 of the Aichi SR. CeO_2, $Ce_2(CO_3)_3$, Cr_2O_3, $Cr(OH)_3$, CrO_3 (diluted with boron nitride), and Cr foil were used as references.

XAFS spectra at the Rh *K*-edge were measured in transmission mode at room temperature at the NW10A stations of the PF at KEK-IMSS and the BL11S2 of Aichi SR. The energy and current of the electrons in the storage ring were 6.5 GeV and 60 mA in the Photon Factory, and 1.2 GeV and 300 mA in Aichi Synchrotron, respectively. X-rays from the storage ring were monochromatized with a Si(311) double-crystal monochromator. At the NW10A stations of the PF, two ionization chambers filled with pure Ar and Kr gases were used to monitor the incident (I_0) and transmitted (I) X-rays, respectively. At the BL11S2 of Aichi SR, two ionization chambers filled with pure Ar and a mixture of Ar and Kr gases (8.5/1.5, v/v) gases were used to monitor the incident (I_0) and transmitted (I) X-rays, respectively. Rh foil and Rh_2O_3 (diluted with boron nitride) were used as references.

The XAFS spectra were analyzed using ATHENA and ARTEMIS with IFEFFIT (version 1.2.11).[11] The threshold energy was tentatively set at the inflection point for the Cr *K*-edge (Cr foil: 5988.8 eV)[10] and Rh *K*-edge (Rh foil: 23219.8 eV),[12] and at the first peak top of the white line for the Ce L_{III}-edge (CeO_2: 5734.4 eV). Background subtraction

was performed using the Autobk method and the spline smoothing algorithm in ATHENA.[13] The average oxidation states of Ce, Cr, and Rh were determined from the changes at 5741.3 eV (second peak top of the white line), 5991.4 eV (pre-edge), and 23238 eV (white line peak top), respectively. The k^3-weighted extended XAFS (EXAFS) oscillations were Fourier transformed into *R*-space. Curve-fitting analysis was carried out in the *R*-space. The fitting parameters for each shell were coordination number (CN), interatomic distance (*R*), Debye–Waller factor (σ^2: mean-square displacement), and correction-of-edge energy (ΔE_0). For the Rh *K*-edge, S_0^2 was fixed to be 1 based on the fitting of Rh foil, and S_0^2 for Rh_2O_3 was fitted to be 0.92, which was rounded to 1. Phase shifts and backscattering amplitudes for Rh–O and Rh–Rh were calculated with FEFF 8 code[14] using structural parameters obtained from the crystal structures of Rh[15] and Rh_2O_3[16].

Temperature-programmed reduction/oxidation (TPR/TPO) measurements

TPR and TPO were carried out in a closed glass reactor with a gas circulation unit and a pressure gauge (Figure 2.6). Typically, an oxide sample (200 mg) was evacuated in a reactor for 30 min, hydrogen gas was introduced into the reactor, and the system was heated to the target temperatures (5 K min^{-1}). Water vapor formed during the TPR was trapped by a liquid-nitrogen trap. Changes in the system pressure were recorded at appropriate intervals. TPO was performed after the TPR measurement. Oxygen gas was put into the reactor at 293 K. Then, the system was heated to 573 K (5 K min^{-1}) and kept at 573 K for 1 h. Finally, the system was cooled to 293 K and changes in the pressure of the system were measured at appropriate intervals. Desorbed H_2O was trapped by a dry-ice/acetone trap during the TPO measurement.

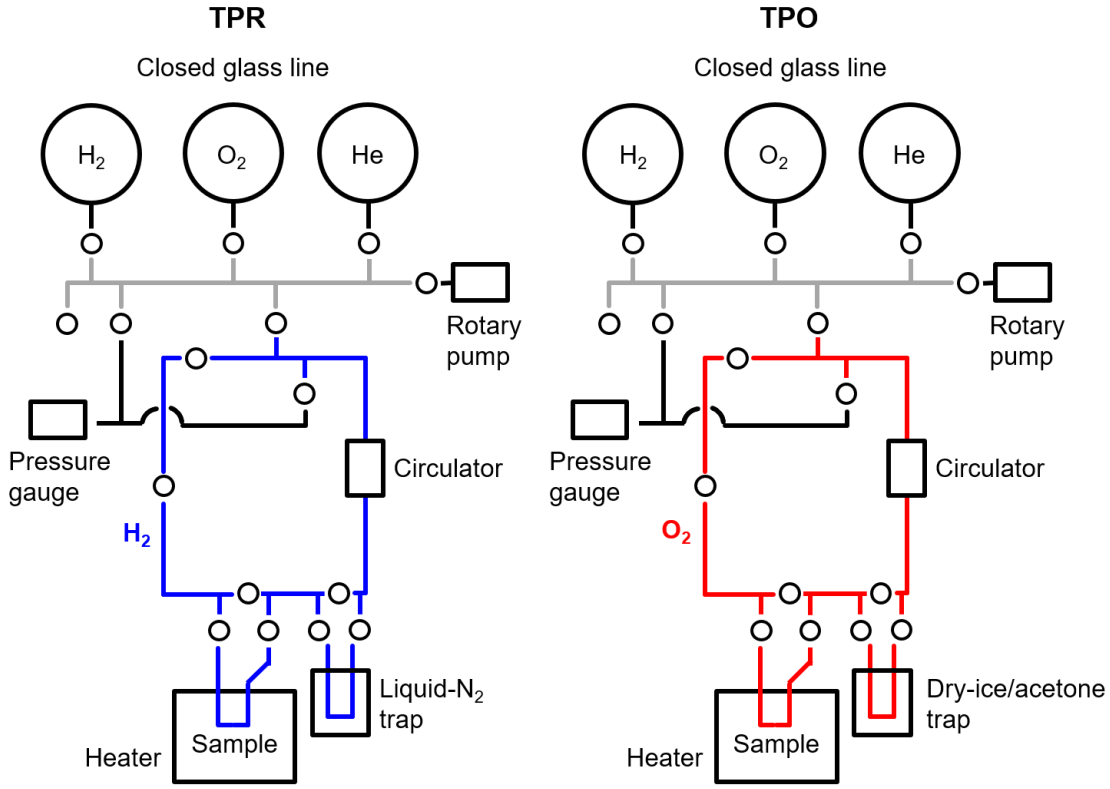

Figure 2.6. Setup for the TPR/TPO measurements.

2.2.4. *In situ* structural characterizations to reveal the redox property

In situ XAFS measurements

In situ quick XAFS (QXAFS) measurements during reduction with H_2 or oxidation with O_2 conditions were performed at the BL12C and NW10A beamlines of the Photon Factory at KEK-IMSS as follows. A sample was pelletized into a disk in a ring-shaped cell and placed in an *in situ* XAFS cell placed in an experimental setup as shown in Figure 2.7. After flushing with N_2 (100 sccm) for 10 min, the cell was heated to 303 K and kept at this temperature for 5 min. Then, the QXAFS measurement was started. The protocols are shown in Figure 2.8, and the energy range, scan time, and scan interval are listed in Table 2.8. After 5 min, the gas was changed to H_2 + N_2 (50 + 50 sccm) and the temperature was held for another 5 min. Then, the cell was heated to 423 K at a rate of 2 K min^{-1}. After keeping the temperature at 423 K for 10 min, the gas was changed to N_2 (100 sccm), and the cell was cooled to room temperature. The cell was heated again to 303 K and kept at this temperature for 5 min, and the QXAFS measurement was started. After 5 min, the gas was changed to O_2 + N_2 (50 + 50 sccm) and the temperature was held for another 5 min. Then, the cell was heated to 573 K at a rate of 5 K min^{-1}. After keeping the temperature at 573 K for 1 h, the gas was changed to N_2 (100 sccm), and the cell was cooled to room temperature.

Oxidation states were estimated from adsorption coefficients (μt) at the pre-edge peak of Cr *K*-edge (5991.4 eV), the white line of Rh *K*-edge (23238 eV), and the 2nd maximum peak of Ce L_{III}-edge (5741.3 eV) following Equations 2.1-2.3. Amounts of released and absorbed oxygen species were estimated from the changes in the oxidation states.

$$\text{Oxidation state of Cr} = 3 + 3\frac{\mu t_{\text{Cr}} - \mu t_{\text{Cr3+}}}{\mu t_{\text{Cr6+}} - \mu t_{\text{Cr3+}}} \qquad \text{(Equation 2.1)}$$

μt_{Cr}: μt of $Cr_{0.19}Rh_{0.06}CeO_z$ at 5991.4 eV

$\mu t_{\text{Cr3+}}$: μt of Cr_2O_3 at 5991.4 eV

$\mu t_{\text{Cr6+}}$: μt of CrO_3 at 5991.4 eV

$$\text{Oxidation state of Rh} = 3\frac{\mu t_{\text{Rh}} - \mu t_{\text{Rh0}}}{\mu t_{\text{Rh3+}} - \mu t_{\text{Rh0}}} \qquad \text{(Equation 2.2)}$$

μt_{Rh}: μt of $Cr_{0.19}Rh_{0.06}CeO_z$ at 23238 eV

μt_{Rh0}: μt of Rh foil at 23238 eV

$\mu t_{\text{Rh3+}}$: μt of Rh_2O_3 at 23238 eV

$$\text{Oxidation state of Ce} = 3 + \frac{\mu t_{\text{Ce}} - \mu t_{\text{Ce3+}}}{\mu t_{\text{Ce4+}} - \mu t_{\text{Ce3+}}} \qquad \text{(Equation 2.3)}$$

μt_{Ce}: μt of $Cr_{0.19}Rh_{0.06}CeO_z$ at 5741.3 eV

$\mu t_{\text{Ce3+}}$: μt of $Ce_2(CO_3)_3$ at 5741.3 eV

$\mu t_{\text{Ce4+}}$: μt of CeO_2 at 5741.3 eV

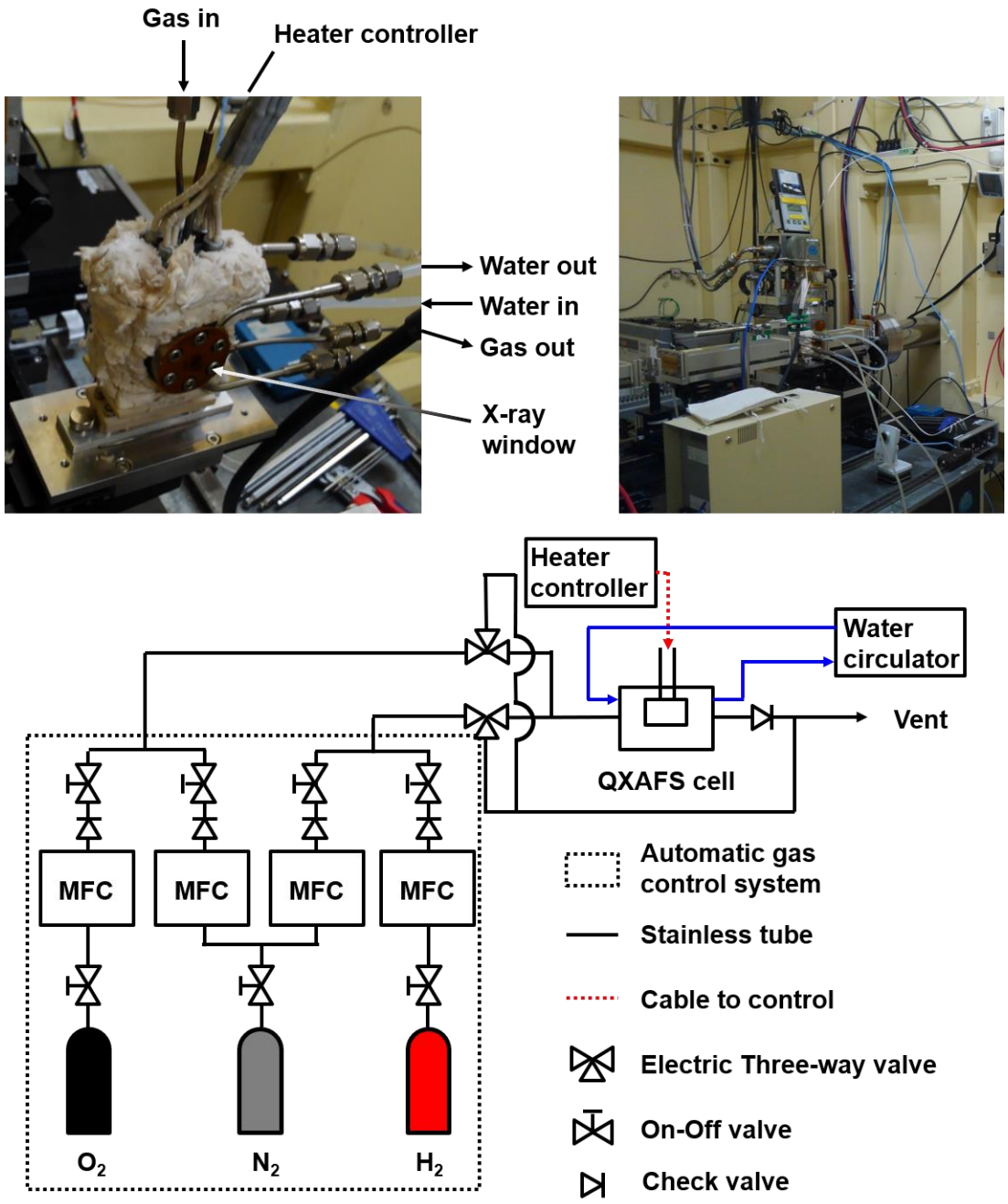

Figure 2.7. Setup for *in situ* QXAFS measurements.

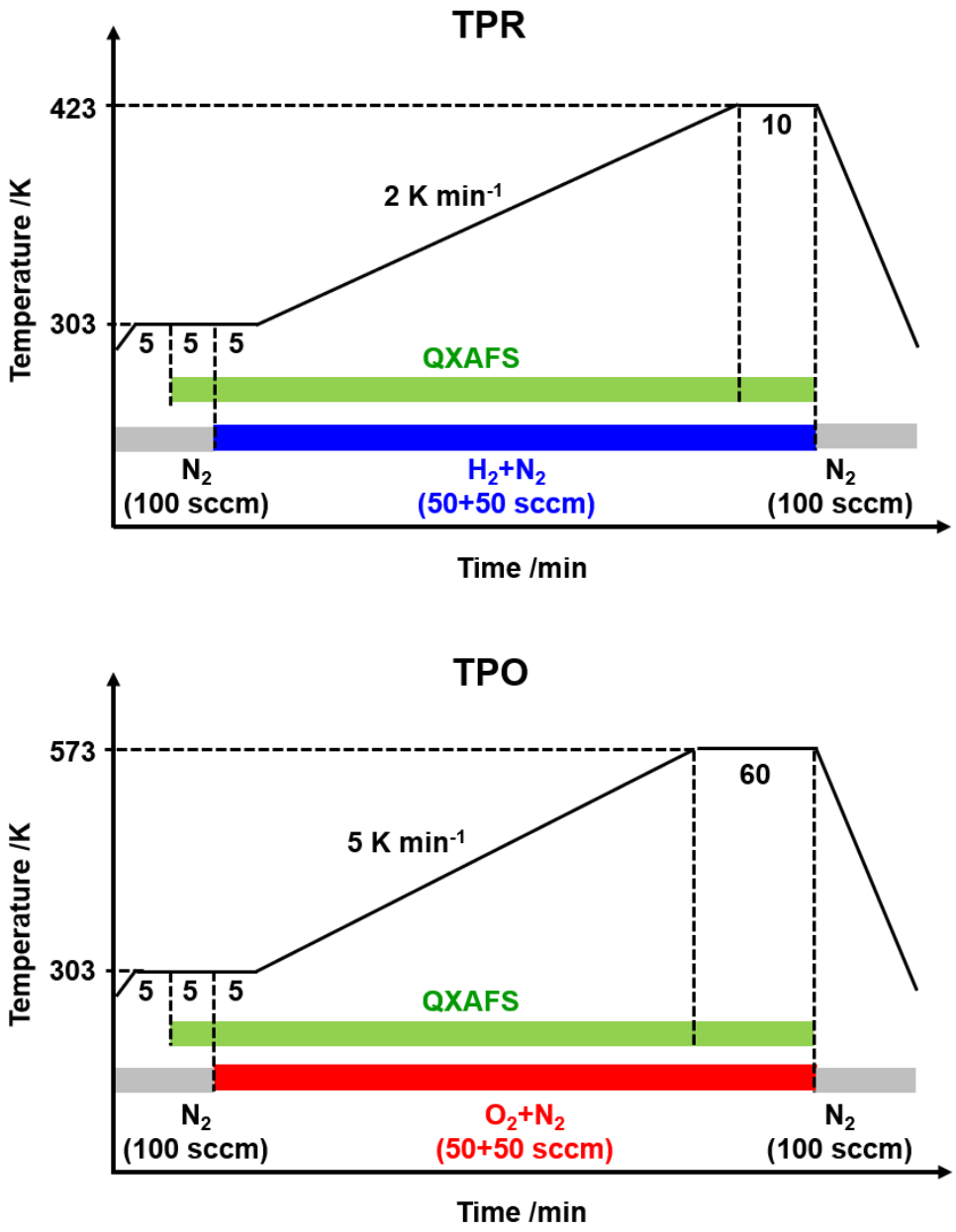

Figure 2.8. Temperature-time protocols for *in situ* QXAFS measurements.

Table 2.8. Parameters for *In Situ* QXAFS Measurements

Element, Edge	Energy range /eV	Scan time /s	Scan interval /s	Data Points
Ce L_{III}-edge	5670-5820	10	15	300
Cr *K*-edge	5950-6100	10	15	303
Rh *K*-edge	22900-24300	55	60	1422

***In situ* ambient pressure (AP)-XPS measurements**

AP-XPS measurements under H_2-reduction and O_2-oxidation conditions were performed at the soft X-ray undulator beamline BL07LSU of SPring-8 (Sayo, Japan) (Figure 2.9).[17] In the reduction (oxidation) experiments, the sample was exposed to 130 Pa of H_2 gas (200 Pa of O_2 gas) at room temperature, followed by heating to 385 K (573 K), respectively. O 1s, Cr 2p, and Rh 3d measurements under ambient conditions were conducted at a photon energy of 760 eV, whereas the Ce 3d spectra were collected at a photon energy of 1070 eV. A slight peak shift to higher binding energy was observed under the H_2 reduction conditions due to sample charging, and the binding energy was referenced to the O 1s peak of CeO_2 lattice oxygen (529.6 eV). The binding energies of the AP-XPS spectra measured under oxidation conditions at 573 K were referenced to the Fermi edge of Au foil (0 eV). The spectra were fitted by Voigt functions after Shirley background subtraction.[10]

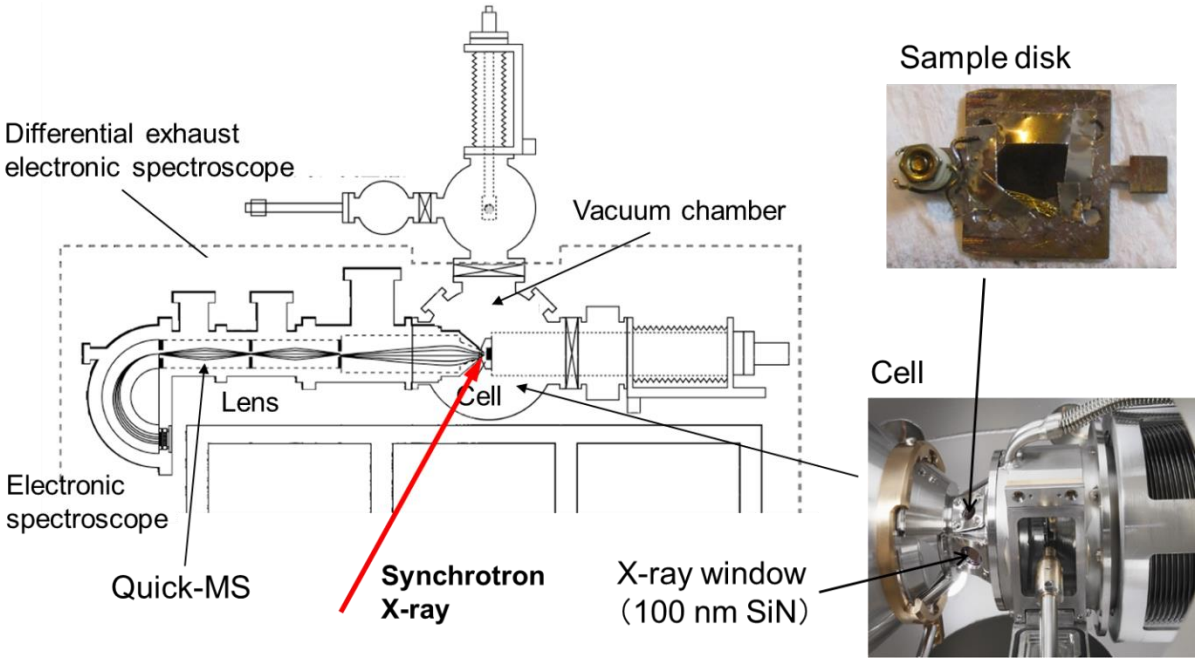

Figure 2.9. Setup for *in situ* AP-XPS (SPring-8, BL07LSU beamline).

2.3. Results and discussions

2.3.1. Structural characterizations of the prepared $Cr_xRh_yCeO_z$: Improvement of rhodium dispersion by chromium oxides

$Cr_{0.19}Rh_{0.06}CeO_z$ was prepared by a hydrothermal method using three metal salt precursors. The composition of Cr, Rh, and Ce in $Cr_{0.19}Rh_{0.06}CeO_z$ was analyzed by ICP-OES measurement (Table 2.9). The specific surface area of $Cr_{0.19}Rh_{0.06}CeO_z$ was 98 m^2 g^{-1}, which was comparable to 118 m^2 g^{-1} for CeO_2 (Table 2.9). The metal compositions in the other $Cr_xRh_yCeO_z$ were also determined, and they were comparable to the molar ratios of used metal precursors in preparation. BET surface areas of $Cr_xRh_yCeO_z$ were in the range of 66-138 m^2 g^{-1}, and their averaged particle sizes estimated from the surface areas were around 10 nm (Table 2.9).

Table 2.9. Composition, BET Surface Area, and Average Diameter of $Cr_xRh_yCeO_z$

Sample	Composition of Cr/Rh/Ce	BET surf. area /m^2 g^{-1}	Average diameter [a] /nm
$Cr_{0.19}Rh_{0.06}CeO_z$	0.1897/0.0602/1	98	8.5
$Rh_{0.04}CeO_z$	<0.0023/0.0378/1	66	12.6
$Cr_{0.17}CeO_z$	0.1716/<0.0005/1	106	7.8
CeO_2	—	118	7.0
$Cr_{0.06}Rh_{0.04}CeO_z$	0.0583/0.0357/1	105	7.9
$Cr_{0.12}Rh_{0.06}CeO_z$	0.1171/0.0599/1	110	7.6
$Cr_{0.24}Rh_{0.07}CeO_z$	0.2398/0.0663/1	129	6.4
$Cr_{0.35}Rh_{0.07}CeO_z$	0.3540/0.0673/1	138	6.0
$Cr_{0.18}Rh_{0.01}CeO_z$	0.1758/0.0123/1	100	8.3
$Cr_{0.18}Rh_{0.04}CeO_z$	0.1785/0.0363/1	99	8.4
$Cr_{0.19}Rh_{0.08}CeO_z$	0.1874/0.0836/1	100	8.3
$Cr_{0.19}Rh_{0.11}CeO_z$	0.1928/0.1117/1	95	8.7

[a] Average diameter was calculated from the BET surface area. The density of $Cr_xRh_yCeO_z$ was assumed to be 7.215 g cm^{-3} of CeO_2.[18]

XRD pattern of $Cr_{0.19}Rh_{0.06}CeO_z$ showed only the XRD pattern of a fluorite structure of CeO_2, and there was almost no peak shift from the peak pattern of CeO_2 (*e.g.*, 28.9 vs 28.8 2θ/° of CeO_2(111) plane) as shown in Figure 2.10 and Table 2.10, which suggested a negligible effect of incorporated Cr and Rh on the bulk framework of CeO_2. The TEM and STEM images of $Cr_{0.19}Rh_{0.06}CeO_z$ in Figures 2.11-12 revealed clear lattice patterns of CeO_2 (111) (d = 0.32-0.33 nm), supporting that $Cr_{0.19}Rh_{0.06}CeO_z$ had a fluorite crystal structure similar to CeO_2. No XRD patterns attributed to Cr oxides (Cr_2O_3 and CrO_3) and metallic and oxidic Rh species (Rh and Rh_2O_3) were observed, indicating no presence of large Cr or Rh particles in $Cr_{0.19}Rh_{0.06}CeO_z$. $Cr_xRh_yCeO_z$ with different metal compositions showed also negligible shift of diffraction patterns, suggesting Cr and Rh species existed near the surface of the CeO_2 particles.

HAADF-STEM-EELS/EDS images of $Cr_{0.19}Rh_{0.06}CeO_z$ displayed dispersed Cr and Rh species on the surface of CeO_2, forming nanodomains of around 1 nm as shown in Figure 2.12. The dispersed Rh species were located at similar positions to the Cr species (Figure 2.12 (D-f,g)). HAADF-STEM-EDS images of $Rh_{0.04}CeO_z$ without Cr also imaged clear lattice patterns of CeO_2 (111) (d = 0.32 nm) with dispersed Rh species on the surface of CeO_2(Figure 2.13).

HAADF-STEM-EELS/EDS images of $Cr_{0.35}Rh_{0.07}CeO_z$ and $Cr_{0.19}Rh_{0.11}CeO_z$ with larger amounts of Cr or Rh than $Cr_{0.19}Rh_{0.06}CeO_z$ are shown in Figures 2.14-15. Both HAADF-STEM images of $Cr_{0.35}Rh_{0.07}CeO_z$ and $Cr_{0.19}Rh_{0.11}CeO_z$ displayed clear lattice patterns of CeO_2 (111) (d = 0.31-0.34 nm). However, their HAADF-STEM-EELS/EDS mappings showed difference sizes and positions of Cr and Rh nanodomains compared with that of $Cr_{0.19}Rh_{0.06}CeO_z$. $Cr_{0.35}Rh_{0.07}CeO_z$ had larger Cr and Rh nanodomains of around 2 nm at similar positions than those of $Cr_{0.19}Rh_{0.06}CeO_z$ (Figure 2.14). $Cr_{0.19}Rh_{0.11}CeO_z$ had a similar-sized Cr and Rh nanodomains to that of $Cr_{0.19}Rh_{0.06}CeO_z$, but Rh species were also located at positions where Cr nanodomains were absent (Figure 2.15).

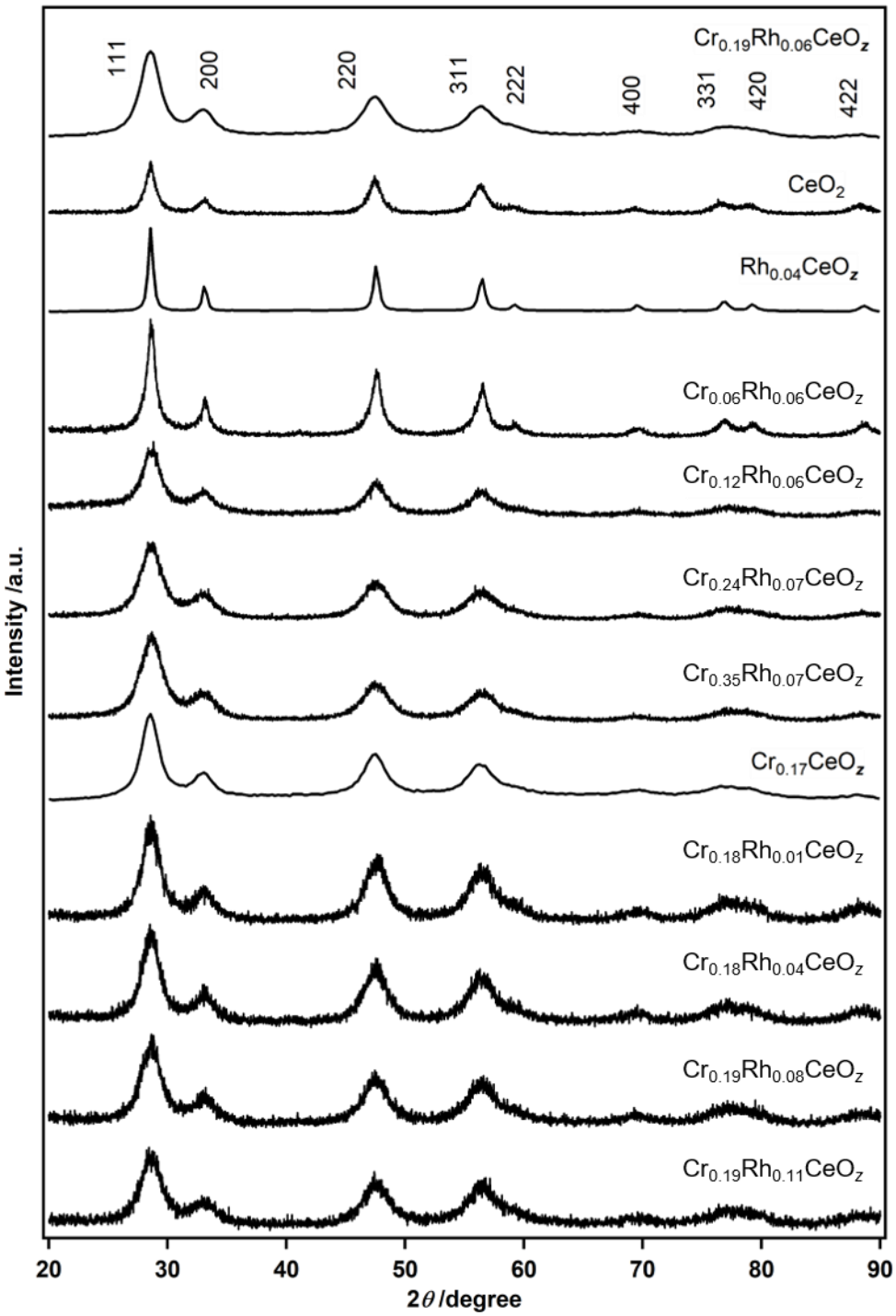

Figure 2.10. XRD patterns of $Cr_xRh_yCeO_z$ ($x = 0 – 0.35$, $y = 0 – 0.11$).

Table 2.10. XRD Peak Positions of $Cr_xRh_yCeO_z$

Sample	2θ of lattice plane /degree			
	(111)	(200)	(220)	(311)
$Cr_{0.19}Rh_{0.06}CeO_z$	28.57	33.06	47.53	56.26
CeO_2	28.60	33.16	47.42	56.34
$Rh_{0.04}CeO_z$	28.57	33.06	47.53	56.26
$Cr_{0.06}Rh_{0.04}CeO_z$	28.56	33.14	47.58	56.50
$Cr_{0.12}Rh_{0.06}CeO_z$	28.58	32.96	47.62	56.44
$Cr_{0.24}Rh_{0.07}CeO_z$	28.60	33.14	47.52	56.36
$Cr_{0.35}Rh_{0.07}CeO_z$	28.57	33.14	47.46	56.34
$Cr_{0.17}CeO_z$	28.57	33.06	47.53	56.51
$Cr_{0.18}Rh_{0.01}CeO_z$	28.58	33.02	47.62	56.50
$Cr_{0.18}Rh_{0.04}CeO_z$	28.52	33.08	47.52	56.46
$Cr_{0.19}Rh_{0.08}CeO_z$	28.64	33.22	47.46	56.38
$Cr_{0.19}Rh_{0.11}CeO_z$	28.68	33.12	47.62	56.36

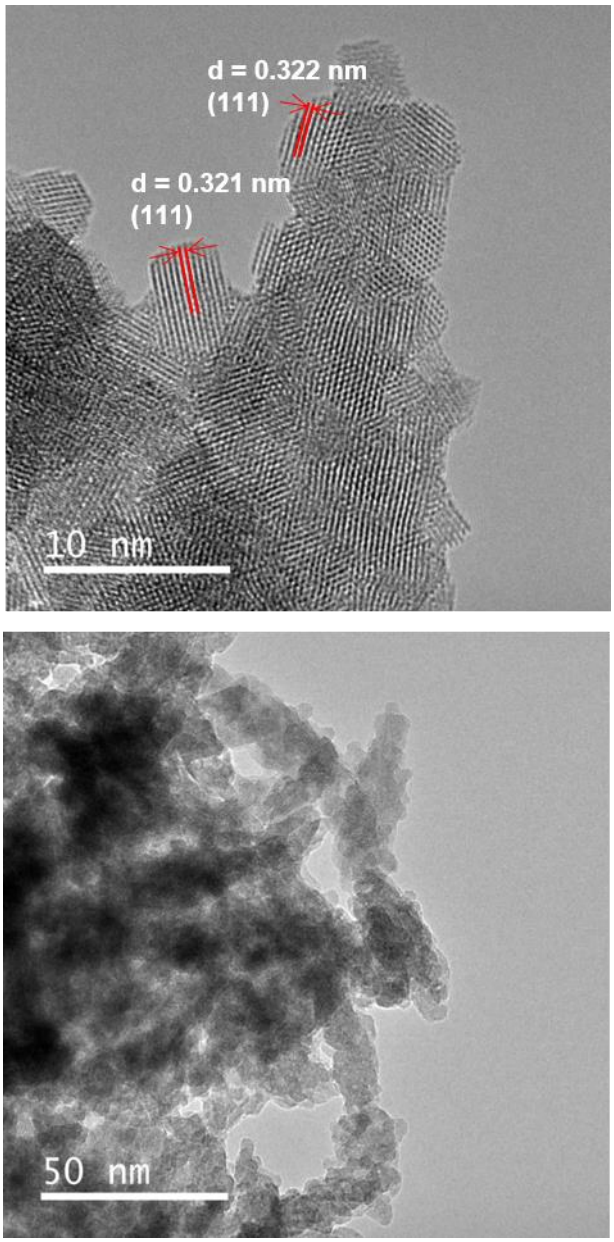

Figure 2.11. TEM images of $Cr_{0.19}Rh_{0.06}CeO_z$.[7]

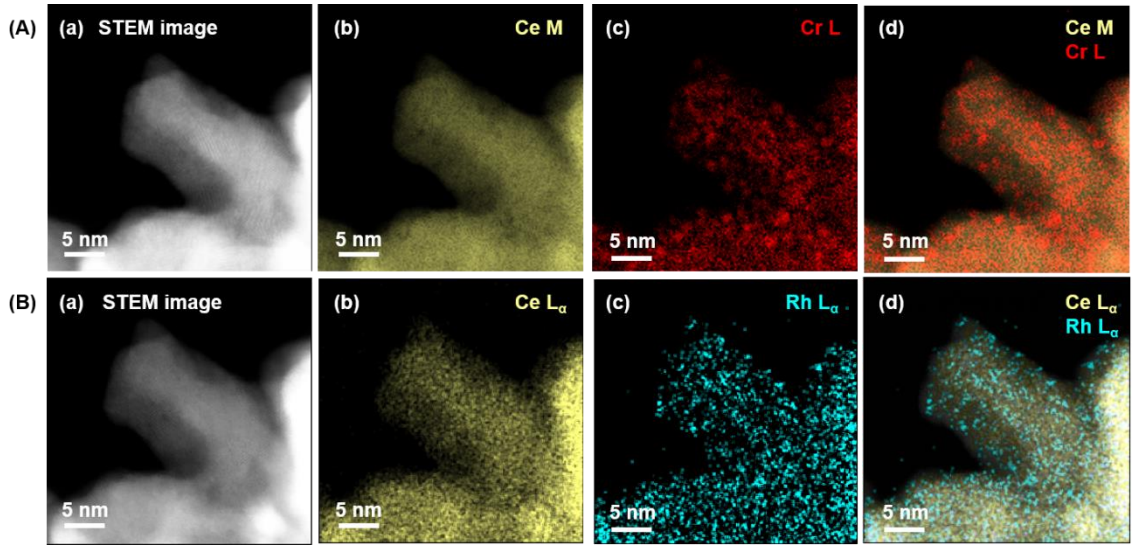

Figure 2.12. (A) HAADF-STEM-EELS images of $Cr_{0.19}Rh_{0.06}CeO_z$; (a) HAADF-STEM image, (b) EELS mapping of Ce, (c) EELS mapping of Cr, and (d) an overlaid EELS mapping of Ce and Cr.[8] (B) HAADF-STEM-EDS images of $Cr_{0.19}Rh_{0.06}CeO_z$ at the same view as HAADF-STEM-EELS; (a) HAADF-STEM image, (b) EDS mapping of Ce, (c) EDS mapping of Rh, and (d) an overlaid EDS mapping of Ce and Rh.[8] (C) HAADF-STEM-EELS images of $Cr_{0.19}Rh_{0.06}CeO_z$ at different position to Figure 1(A,B); (a) HAADF-STEM image, (b) EELS mapping of Ce, (c) EELS mapping of Cr, and (d) an overlaid EELS mapping of Ce and Cr.[8] (D) HAADF-STEM-EDS images of $Cr_{0.19}Rh_{0.06}CeO_z$ at the same position to Figure 1(C): (a) HAADF-STEM image, (b) EDS mapping of Ce, (c) EDS mapping of Rh, (d) overlaid EDS mapping of Ce and Rh, (e) EDS mapping of Cr, (f) overlaid EDS mapping of Ce, Rh, and Cr., and (g) line profiles of Rh L_α, and Cr K_α along the light green line in the overlaid EDS mapping.[8] The energy regions of interest for EDS of Ce L_α, Rh L_α, and Cr K_α were 4701–4977 eV, 2580–2812 eV, and 5269–5555 eV, respectively. These HAADF-STEM-EELS/EDS images of (A, B) and (C, D) show different positions.

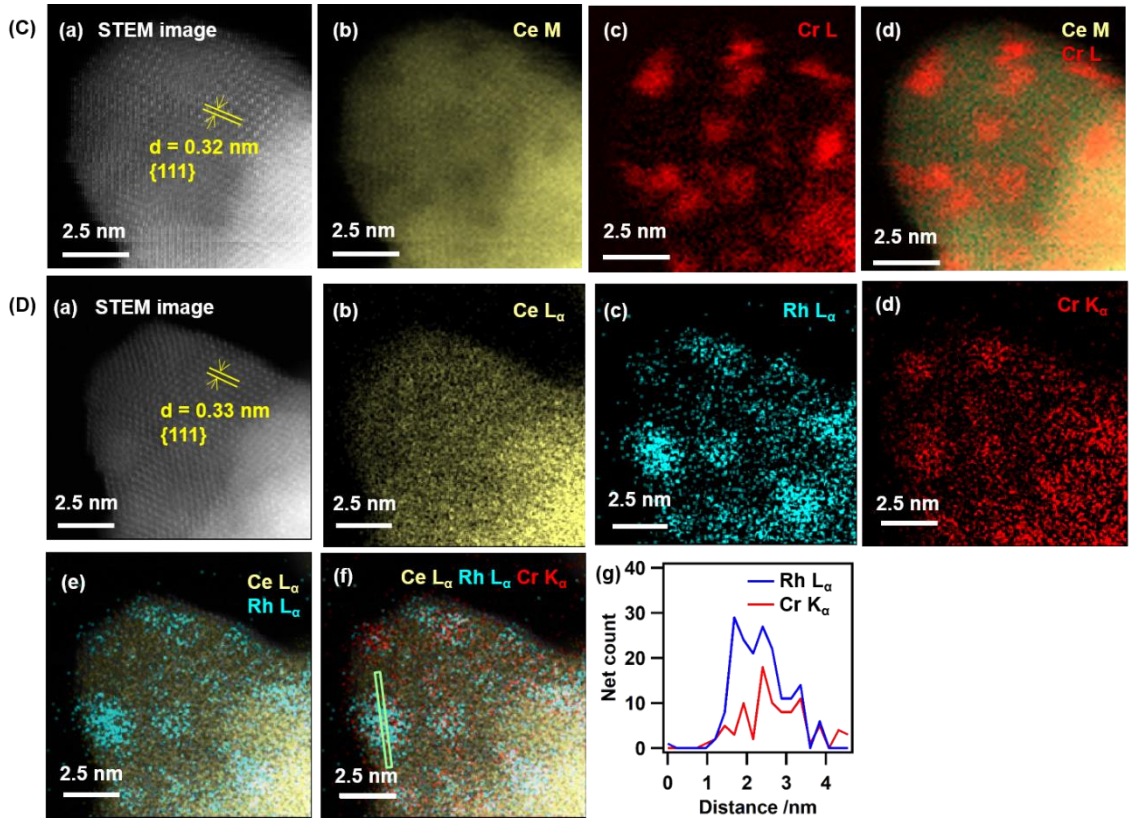

Figure 2.12. [Continued] (A) HAADF-STEM-EELS images of $Cr_{0.19}Rh_{0.06}CeO_z$; (a) HAADF-STEM image, (b) EELS mapping of Ce, (c) EELS mapping of Cr, and (d) an overlaid EELS mapping of Ce and Cr.[8] (B) HAADF-STEM-EDS images of $Cr_{0.19}Rh_{0.06}CeO_z$ at the same view as HAADF-STEM-EELS; (a) HAADF-STEM image, (b) EDS mapping of Ce, (c) EDS mapping of Rh, and (d) an overlaid EDS mapping of Ce and Rh.[8] (C) HAADF-STEM-EELS images of $Cr_{0.19}Rh_{0.06}CeO_z$ at different position to Figure 1(A,B); (a) HAADF-STEM image, (b) EELS mapping of Ce, (c) EELS mapping of Cr, and (d) an overlaid EELS mapping of Ce and Cr.[8] (D) HAADF-STEM-EDS images of $Cr_{0.19}Rh_{0.06}CeO_z$ at the same position to Figure 1(C): (a) HAADF-STEM image, (b) EDS mapping of Ce, (c) EDS mapping of Rh, (d) overlaid EDS mapping of Ce and Rh, (e) EDS mapping of Cr, (f) overlaid EDS mapping of Ce, Rh, and Cr., and (g) line profiles of Rh L_α, and Cr K_α along the light green line in the overlaid EDS mapping.[8] The energy regions of interest for EDS of Ce L_α, Rh L_α, and Cr K_α were 4701–4977 eV, 2580–2812 eV, and 5269–5555 eV, respectively. These HAADF-STEM-EELS/EDS images of (A, B) and (C, D) show different positions.

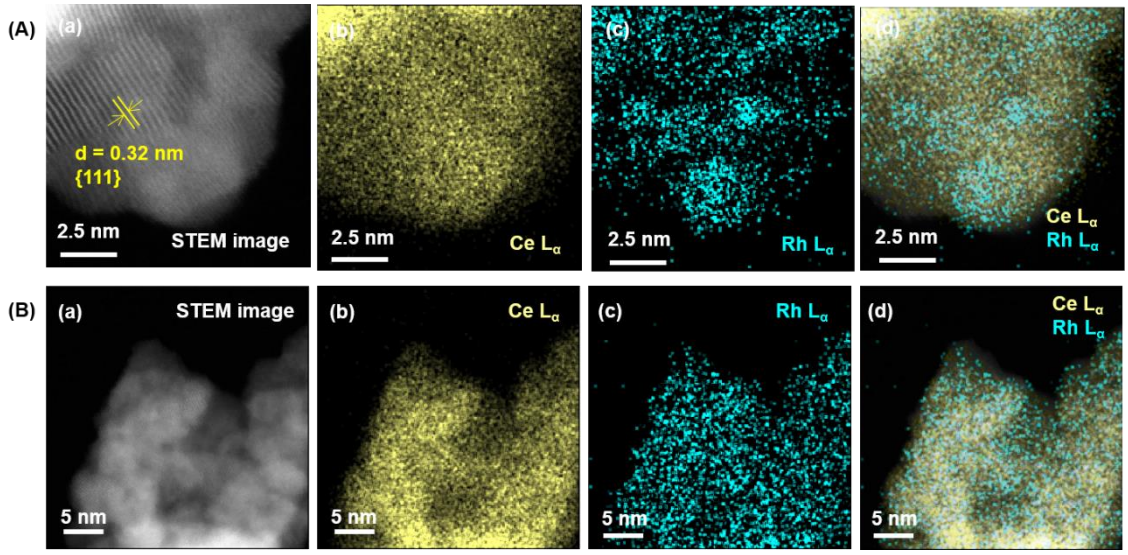

Figure 2.13. HAADF-STEM-EDS images of $Rh_{0.04}CeO_z$; (a) HAADF-STEM image, (b) EDS mapping of Ce, (c) EDS mapping of Rh, and (d) an overlaid EDS mapping of Ce and Rh.[8] These HAADF-STEM-EDS images of (A) and (B) show different positions.

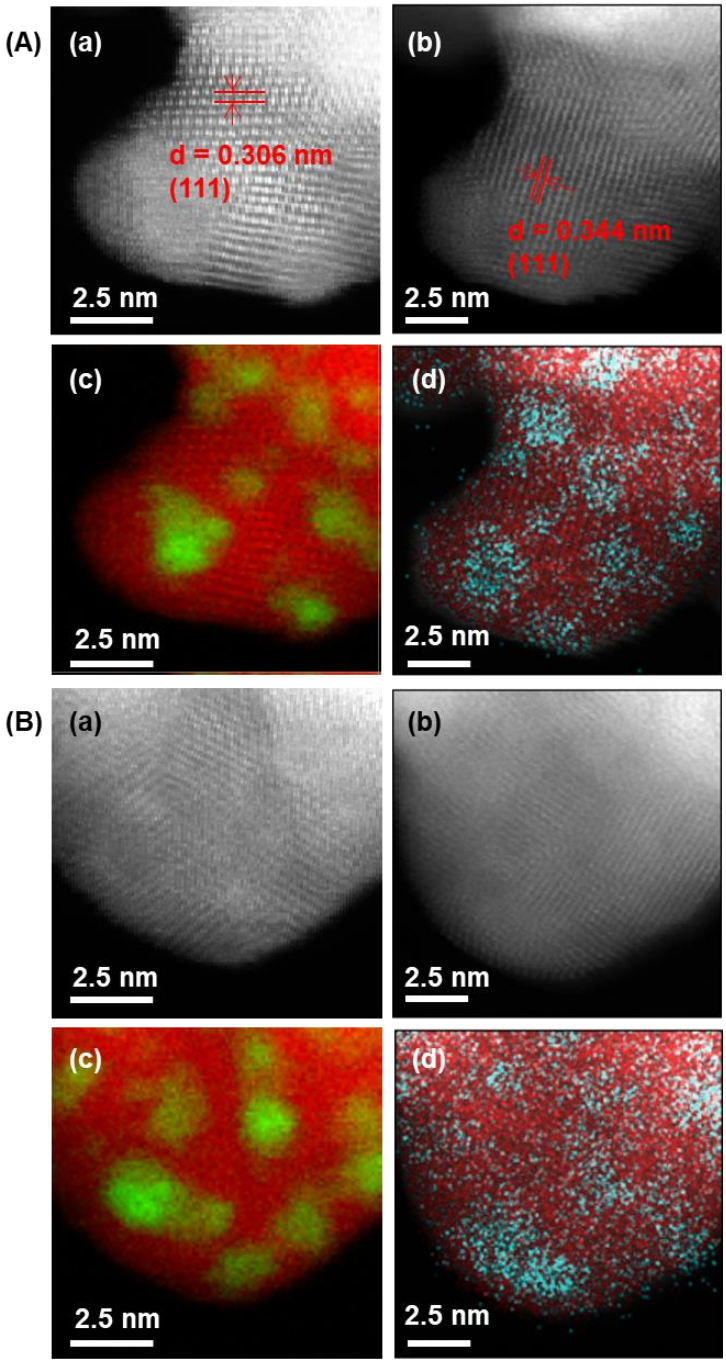

Figure 2.14. HAADF-STEM-EELS/EDS mapping at same view of $Cr_{0.35}Rh_{0.07}CeO_z$. (a) HAADF-STEM images in EELS measurement. (b) HAADF-STEM images in EDS measurement. (c) HAADF-STEM-EELS mapping of Cr (green) and Ce (red). (d) HAADF-STEM-EDS mapping of Rh (blue) and Ce (red). These HAADF-STEM-EELS/EDS images of (A) and (B) show different positions.

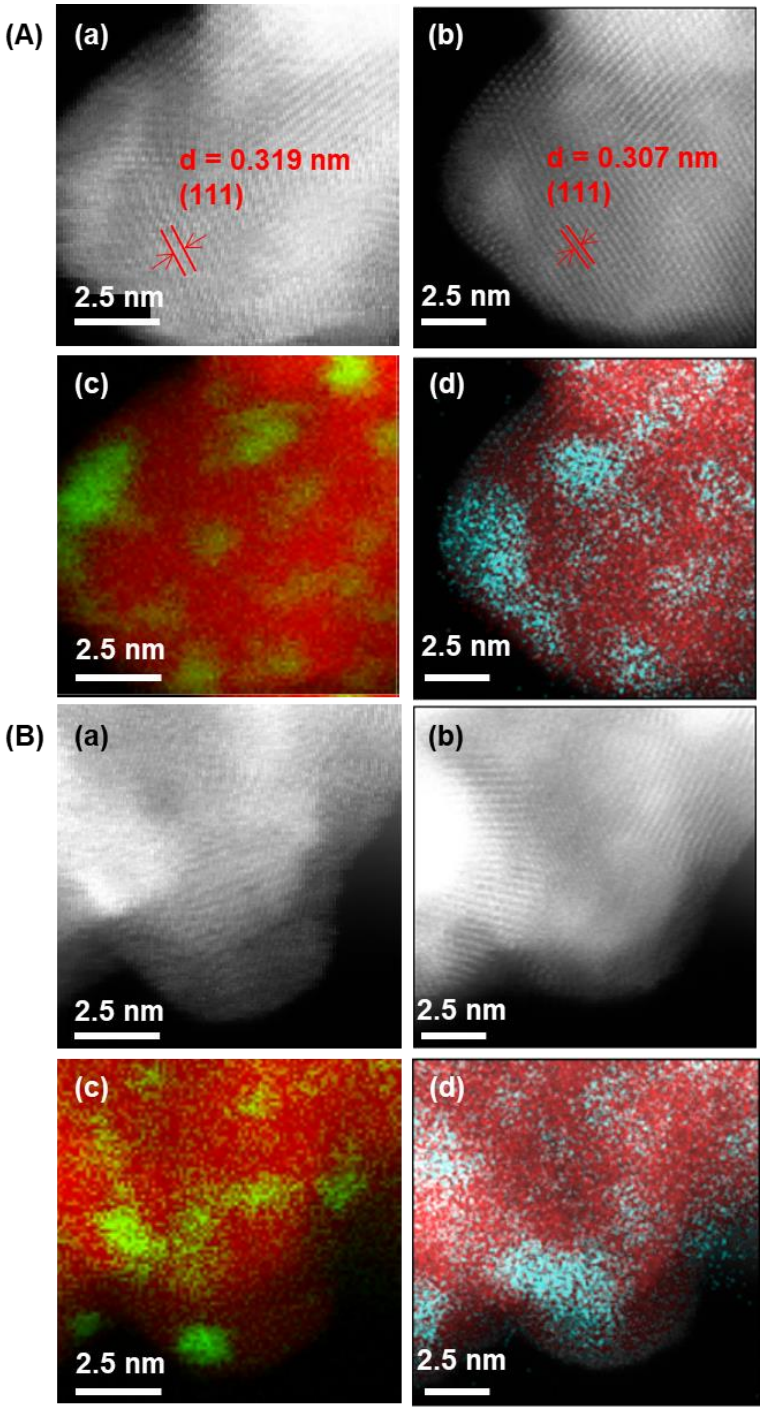

Figure 2.15. HAADF-STEM-EELS/EDS mapping at same view of $Cr_{0.19}Rh_{0.11}CeO_z$. (a) HAADF-STEM images in EELS measurement. (b) HAADF-STEM images in EDS measurement. (c) HAADF-STEM-EELS mapping of Cr (green) and Ce (red). (d) HAADF-STEM-EDS mapping of Rh (blue) and Ce (red). These HAADF-STEM-EELS/EDS images of (A) and (B) show different positions.

Cr *K*-edge, Rh *K*-edge and Ce L_{III}-edge X-ray adsorption near edge structure (XANES) (Figure 2.16) and XPS (Figure 2.17) spectra revealed the oxidation states of each metal in $Cr_{0.19}Rh_{0.06}CeO_z$. The Cr *K*-edge XANES spectrum was similar to that of CrO_3 with a pre-edge peak of a Cr^{6+} feature (Figure 2.16 (A)), suggesting the formation of Cr^{6+} oxide.[19] In the Cr 2p XPS spectrum (Figure 2.17 (A)), a major peak was observed at 579.0 eV (Cr $2p_{3/2}$) and 588.3 eV (Cr $2p_{1/2}$), also suggesting the presence of Cr^{6+}.[20] Thus, $Cr^{6-\gamma}O_{3-x}$ nanodomains with oxygen defects were most likely formed on the CeO_2 surface. The Rh *K*-edge XANES spectrum of $Cr_{0.19}Rh_{0.06}CeO_z$ had a higher white line than that of Rh_2O_3 (Figure 2.16 (B)). The Rh $3d_{5/2}$ XPS peak of $Cr_{0.19}Rh_{0.06}CeO_z$ was observed at a higher energy of 309.4 eV than that of 308.4 eV for Rh_2O_3 (Figure 2.17 (B)).[21] A similar positively charged Rh^{3+} species on CeO_2 was reported to be attributed to a high valence Rh species $Rh^{3+\delta}$ strongly interacting with CeO_2.[5j,l,p,r] Ce valence was attributed to be 4+ from Ce L_{III}-edge XANES[22] (Figure 2.16 (C)), Ce 3d XPS[23] (Figure 2.17 (C), Table 2.11), and EELS analysis. In consequence, the XANES, XPS, and HAADF-STEM-EDS/EELS analysis revealed that the major species of Cr, Rh, and Ce in $Cr_{0.19}Rh_{0.06}CeO_z$ are $Cr^{6-\gamma}$, $Rh^{3+\delta}$, and Ce^{4+}.

Rh *K*-edge XAFS and Rh 3d XPS spectra clarified differences in oxidation states and local coordination structures of the Rh species in $Cr_{0.19}Rh_{0.06}CeO_z$ and $Rh_{0.04}CeO_z$. Although Cr *K*-edge XANES spectra showed almost no change with the different metal composition of $Cr_xRh_yCeO_z$ (Figure 2.18 (A)), Rh *K*-edge XANES spectra exhibited a little difference in the white line structure by the addition of Cr (Figure 2.18 (B)). The Rh $3d_{5/2}$ XPS peaks of $Rh_{0.04}CeO_z$ showed two components at 309.2 and 307.7 eV (Figure 2.19 (B), Table 2.12), the latter of which was assigned to reduced Rh clusters.[5o,r,24] From Rh curve-fitting analysis of Rh *K*-edge EXAFS of $Cr_{0.19}Rh_{0.06}CeO_z$, Rh–O bonds at 0.203 ± 0.001 nm (coordination number (CN) = 5.7 ± 1.1) were observed, and the Rh–Rh bonds of metallic Rh and the Rh–O–Rh bonds of Rh_2O_3 were not observed (Figure 2.20, Table 2.13). In contrast, the Rh–Rh bonds at 0.268 ± 0.002 nm (CN = 3.2 ± 1.6) were clearly observed in addition to the Rh–O bonds at 0.206 ± 0.001 nm (CN = 3.3 ± 0.8) in $Rh_{0.04}CeO_z$ (Figure 2.20, Table 2.13). The Rh–Rh bond with a low CN in the Rh *K*-edge EXAFS and the 307.7 eV peak in the Rh $3d_{5/2}$ XPS indicated the formation of reduced Rh aggregations on $Rh_{0.04}CeO_z$ in addition to $Rh^{3+\delta}$ species.

In the Rh *K*-edge EXAFS of $Cr_xRh_yCeO_z$ with different loading amounts of Cr, the Rh–Rh bond was disappeared as the Cr loading was increased (Figure 2.20, Table 2.13). The white line structures of the Rh *K*-edge XANES spectra of $Cr_xRh_yCeO_z$ was slightly changed with different loading amounts of Cr (Figure 2.18 (B)), whereas the changes of

the Cr *K*-edge and Ce L_{III}-edge XANES spectra of $Cr_xRh_yCeO_z$ were negligible (Figure 2.18 (A, C)). Thus, it was suggested that the incorporation of the certain amount of Cr together with Rh precursor during the preparation step affected the dispersion of Rh species on $Cr_xRh_yCeO_z$.

Considering the negligible peak shifts in the XRD patterns between $Cr_{0.19}Rh_{0.06}CeO_z$ and CeO_2, surface sensitivity of the XPS analysis, and the observed nanodomain structures of Cr and Rh in the STEM-EELS/EDS mappings, a schematic structure of $Cr_{0.19}Rh_{0.06}CeO_z$ is proposed in Figure 2.21 (A), where $Cr^{6-\gamma}O_{3-x}$ nanodomains and $Rh^{3+\delta}$ species are dispersed on the fluorite CeO_2 support. Whereas, in $Rh_{0.04}CeO_z$ without Cr, aggregated Rh nanoclusters formed on the CeO_2 surface in addition to the $Rh^{3+\delta}$ species (Figure 2.21 (B)). It was proposed that the incorporation of Cr in the Rh-containing ceria led to the dispersion of the positively-charged Rh species, which can effectively increase the number of the active Rh sites that are responsible for the reaction performance (see Chapter 3).

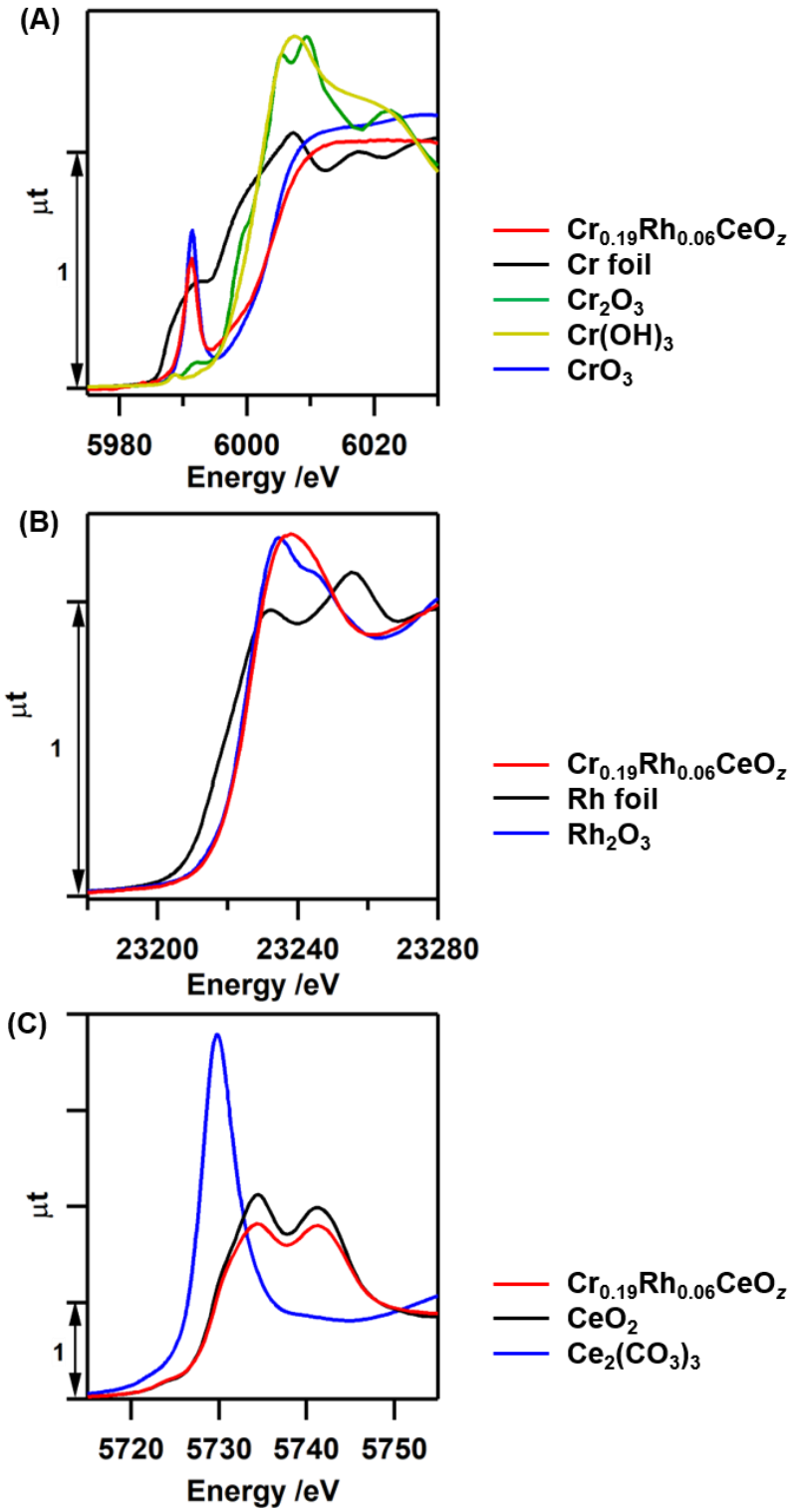

Figure 2.16. (A) Cr *K*-edge, (B) Rh *K*-edge, and (C) Ce L_{III}-edge XANES spectra of $Cr_{0.19}Rh_{0.06}CeO_z$ with standard samples.[7]

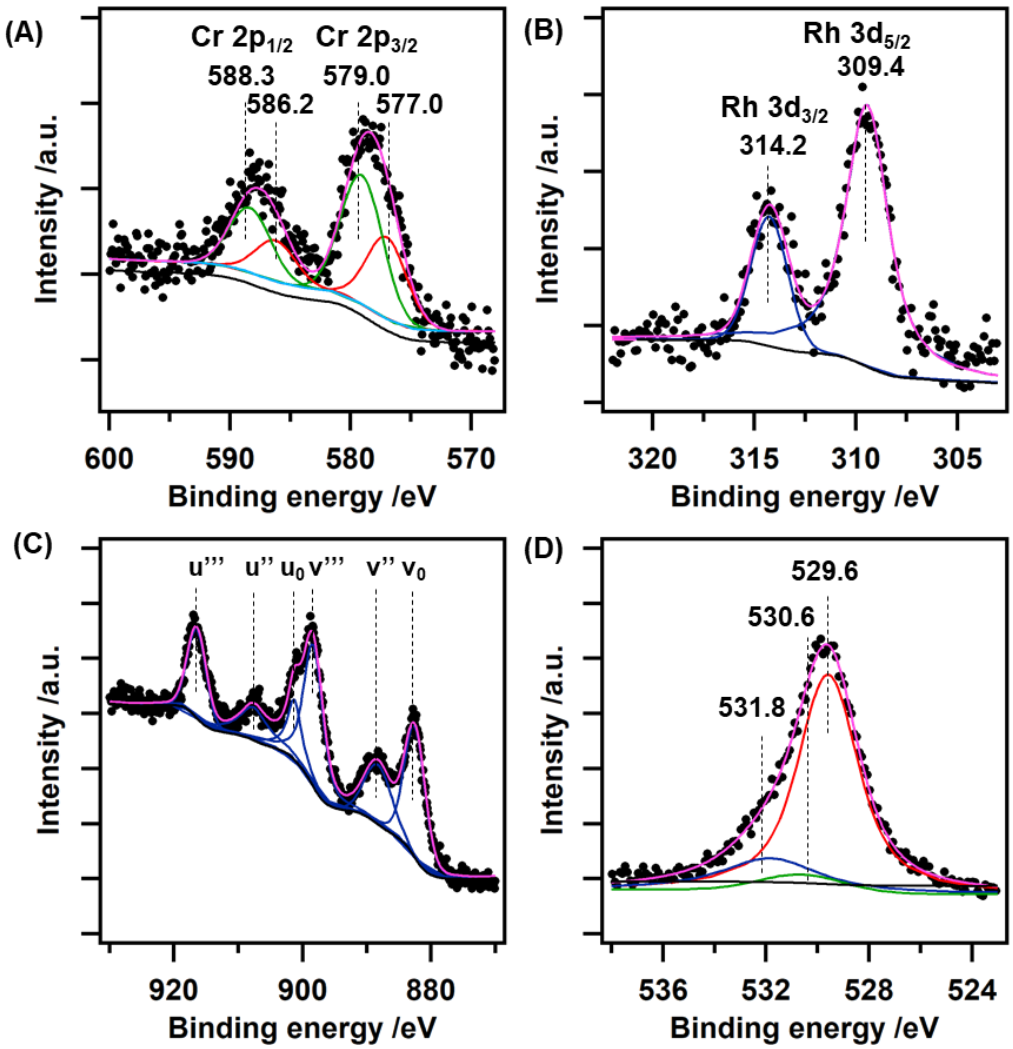

Figure 2.17. (A) Cr 2p, (B) Rh 3d, (C) Ce 3d, and (D) O 1s XPS spectra of $Cr_{0.19}Rh_{0.06}CeO_z$ and their curve-fitting analyses.[7]

Table 2.11. Binding Energies and Ratio of Chemical Species in Cr 2p, Rh 3d, and Ce 3d XPS Spectra of $Cr_{0.19}Rh_{0.06}CeO_z$

XPS peak			Binding Energy /eV	Ratio %
Cr 2p	Cr^{3+}	Cr $2p_{3/2}$	577.0	38
		Cr $2p_{1/2}$	586.2	
	Cr^{6+}	Cr $2p_{3/2}$	579.0	62
		Cr $2p_{1/2}$	588.3	
Rh 3d	$Rh^{3+\delta}$	Rh $3d_{5/2}$	309.4	100
		Rh $3d_{3/2}$	314.2	
Ce 3d	Ce^{4+}	Ce $3d_{5/2}$ (v_0)	882.7	100
		Ce $3d_{5/2}$ (v'')	888.9	
		Ce $3d_{5/2}$ (v''')	898.5	
		Ce $3d_{3/2}$ (u_0)	901.1	
		Ce $3d_{3/2}$ (u'')	907.5	
		Ce $3d_{3/2}$ (u''')	916.8	

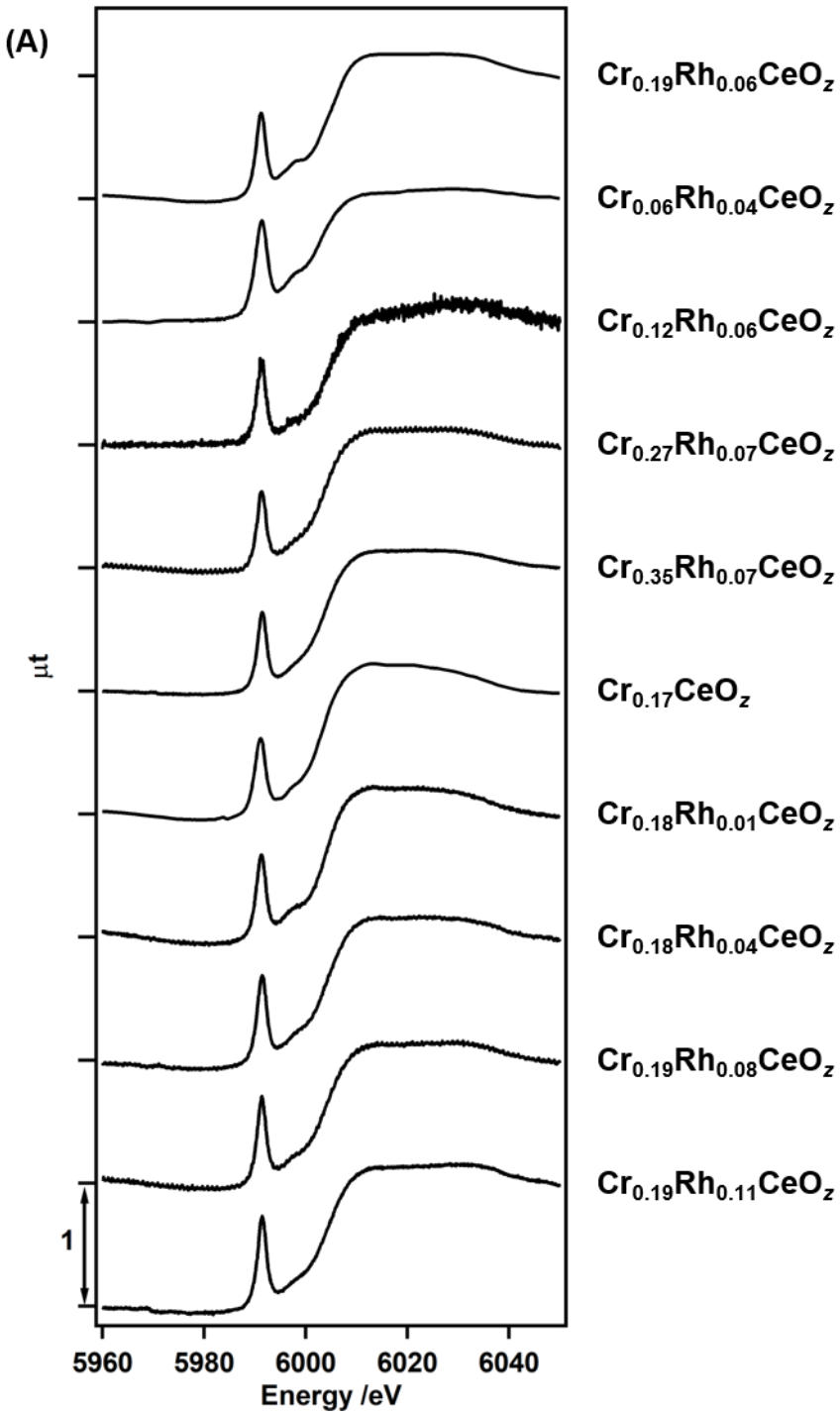

Figure 2.18. (A) Cr *K*-edge, (B) Rh *K*-edge, and (C) Ce L_{III}-edge XANES spectra of $Cr_xRh_yCeO_z$ ($x = 0 – 0.37$, $y = 0 – 0.12$).

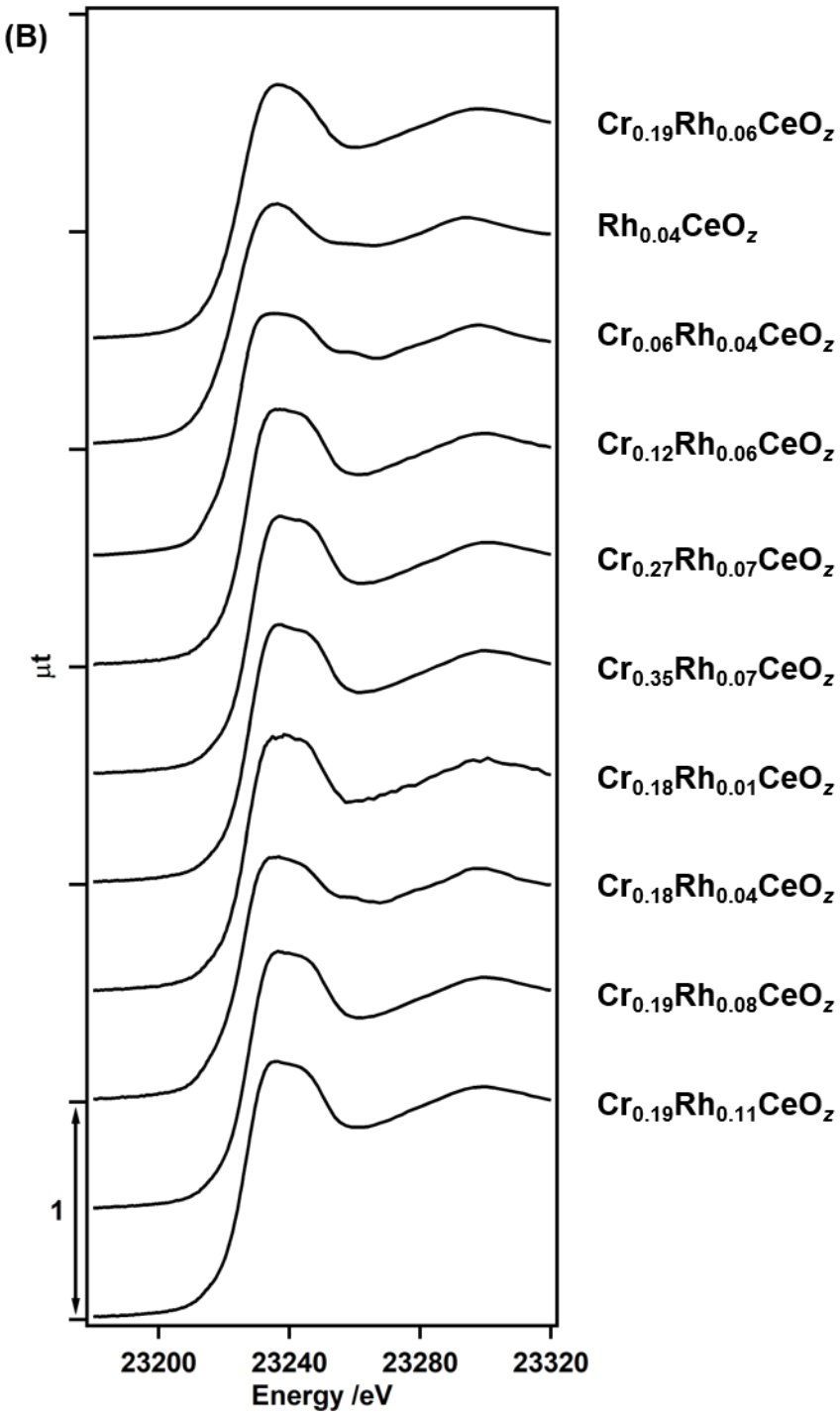

Figure 2.18. [continued] (A) Cr *K*-edge, (B) Rh *K*-edge, and (C) Ce L_{III}-edge XANES spectra of $Cr_xRh_yCeO_z$ ($x = 0 – 0.37$, $y = 0 – 0.12$).

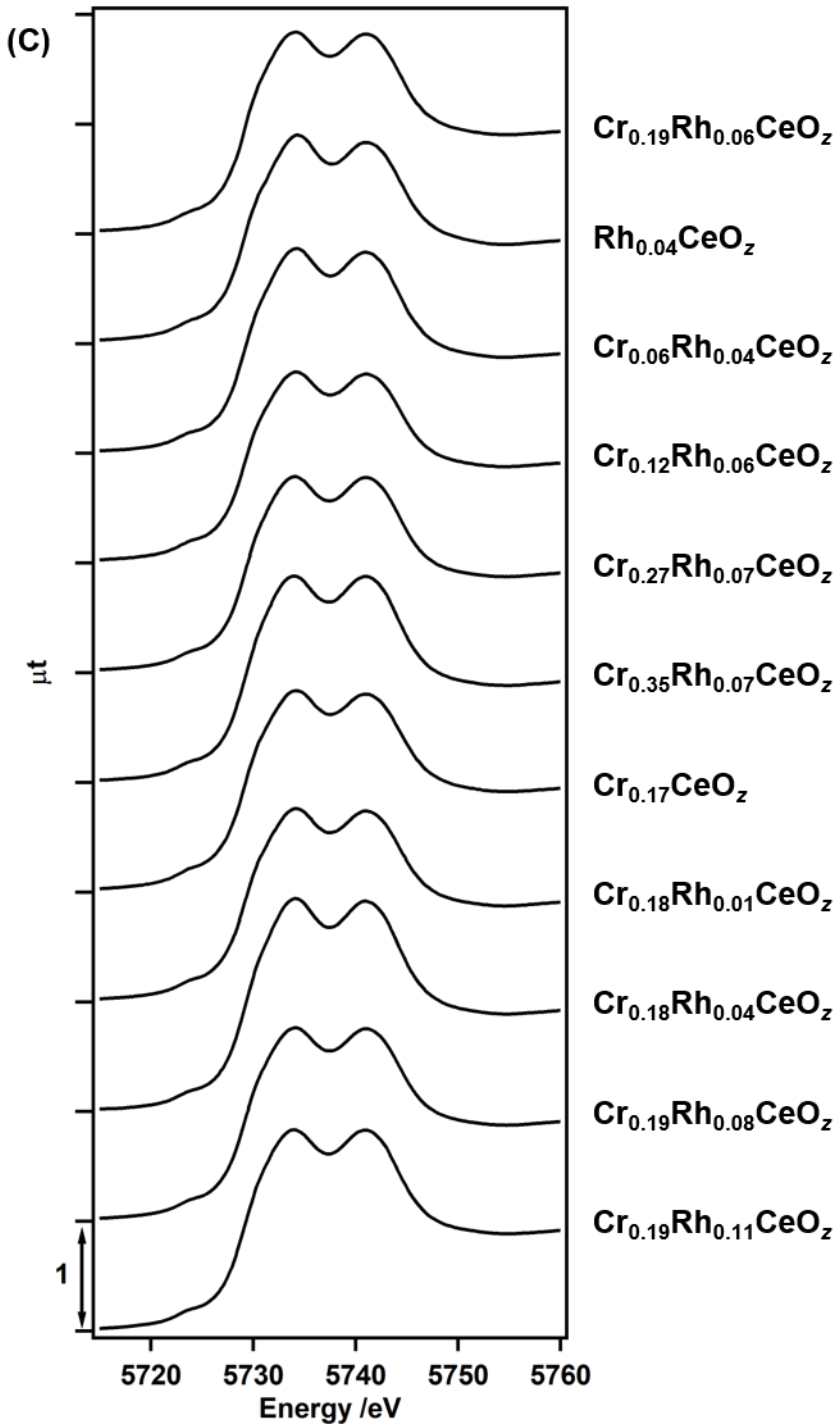

Figure 2.18. [continued] (A) Cr *K*-edge, (B) Rh *K*-edge, and (C) Ce L_{III}-edge XANES spectra of $Cr_xRh_yCeO_z$ ($x = 0 – 0.37$, $y = 0 – 0.12$).

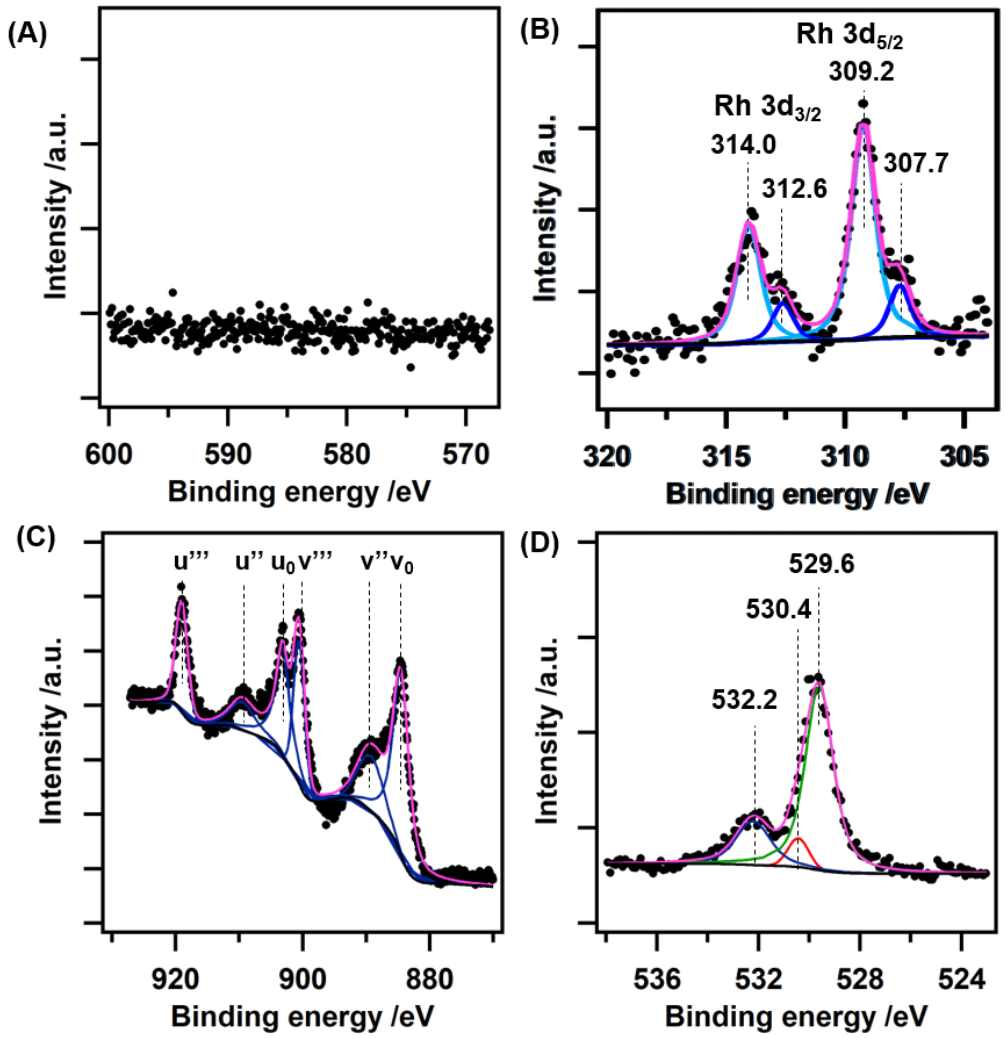

Figure 2.19. (A) Cr 2p, (B) Rh 3d, (C) Ce 3d, and (D) O 1s XPS spectra of $Rh_{0.04}CeO_z$ and their curve-fitting analyses.

Table 2.12. Binding Energies and Ratio of Chemical Species in Rh 3d and Ce 3d XPS Spectra of $Rh_{0.04}CeO_z$

XPS peak			Binding Energy /eV	Ratio %
Rh 3d	Rh^0	Rh $3d_{5/2}$	307.7	16
		Rh $3d_{3/2}$	312.6	
	$Rh^{3+\delta}$	Rh $3d_{5/2}$	309.2	84
		Rh $3d_{3/2}$	314.0	
Ce 3d	Ce^{4+}	Ce $3d_{5/2}$ (v_0)	884.7	100
		Ce $3d_{5/2}$ (v'')	889.5	
		Ce $3d_{5/2}$ (v''')	900.7	
		Ce $3d_{3/2}$ (u_0)	903.3	
		Ce $3d_{3/2}$ (u'')	909.6	
		Ce $3d_{3/2}$ (u''')	919.2	

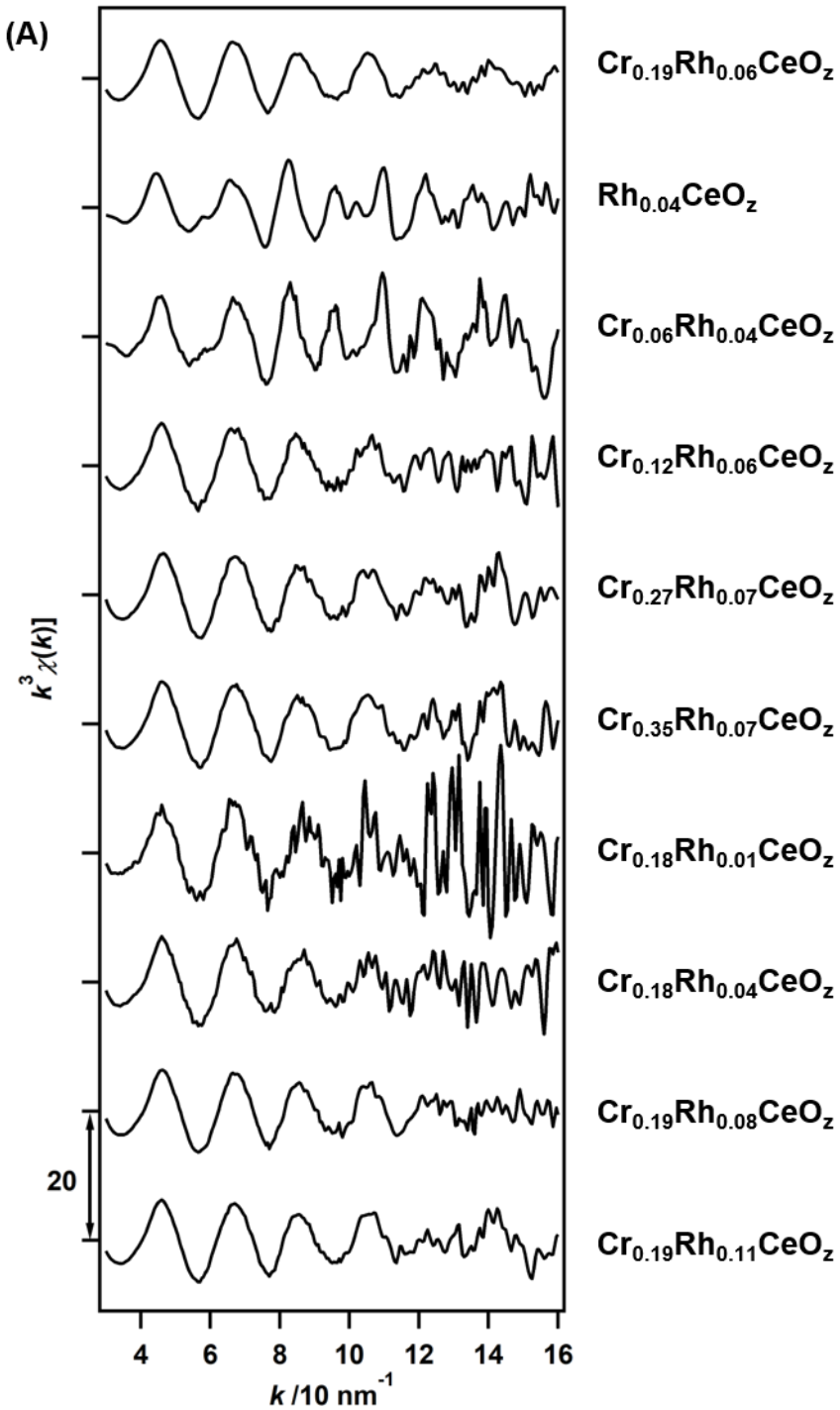

Figure 2.20. (A) k^3-Weighted Rh *K*-edge EXAFS oscillations and (B) their Fourier transforms (k = 30-140 nm^{-1}) of $Cr_xRh_yCeO_z$ (x = 0 – 0.37, y = 0 – 0.12). The curve-fitting of $Cr_{0.18}Rh_{0.01}CeO_z$ did not converged due to its low S/N ratio.

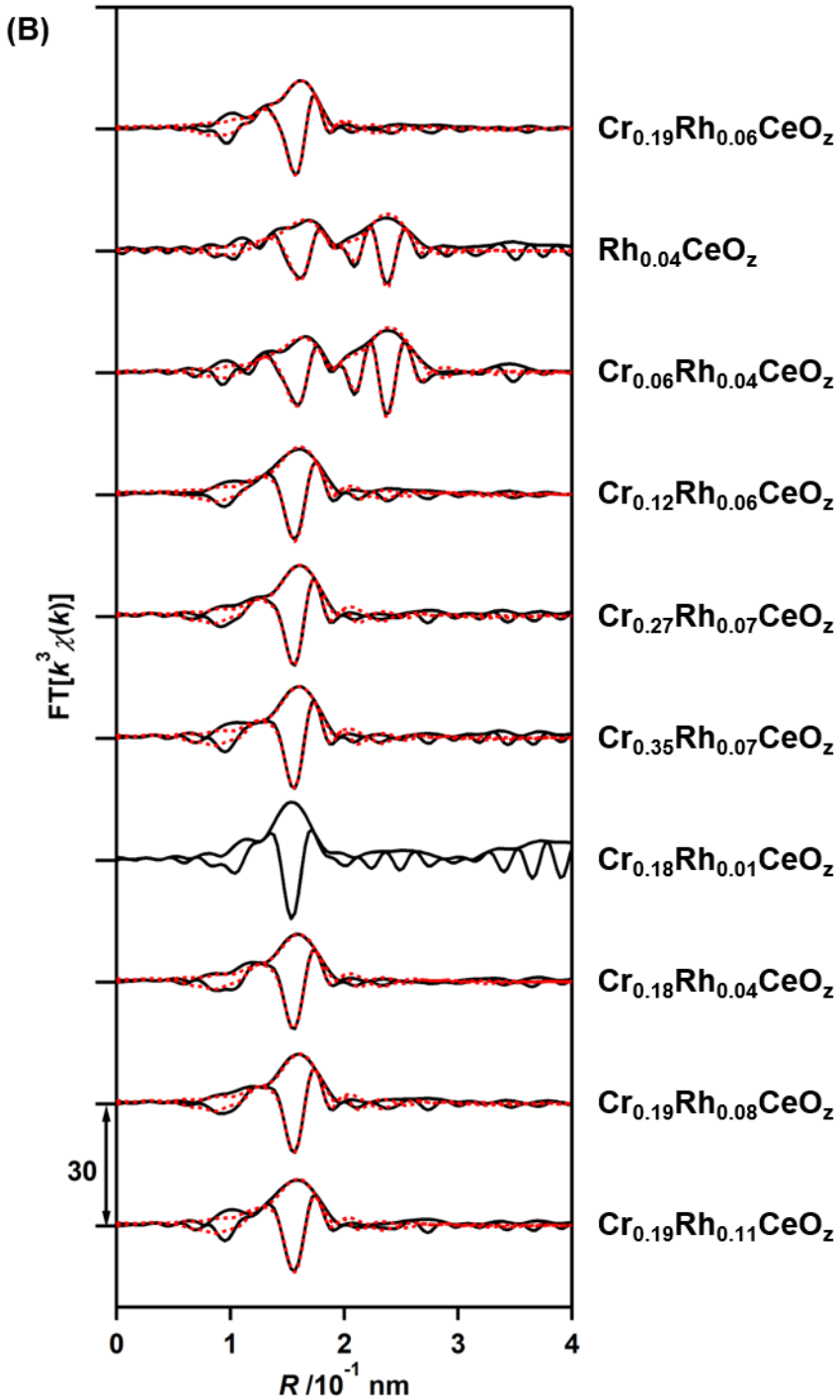

Figure 2.20. [Continued] (A) k^3-Weighted Rh *K*-edge EXAFS oscillations and (B) their Fourier transforms (k = 30-140 nm^{-1}) of $Cr_xRh_yCeO_z$ (x = 0 – 0.37, y = 0 – 0.12). The curve-fitting of $Cr_{0.18}Rh_{0.01}CeO_z$ did not converged due to its low S/N ratio.

Table 2.13. Structural Parameters Determined by Curve-fitting Analysis of Rh *K*-edge EXAFS of $Cr_xRh_yCeO_z$ (x = 0 – 0.37, y = 0 – 0.12)

Sample	Shell	CN	R /nm	ΔE /eV	σ^2 /10^{-5} nm^2	R_f %
$Cr_{0.19}Rh_{0.06}CeO_z$ [a]	Rh-O	5.7 ± 1.1	0.203 ± 0.001	10 ± 3	5 ± 2	1.6
$Rh_{0.04}CeO_z$ [b]	Rh-O	3.3 ± 0.8	0.206 ± 0.001	8 ± 4	4 ± 2	3.1
	Rh-Rh	3.2 ± 1.6	0.268 ± 0.002	2 ± 3	7 ± 2	
$Cr_{0.06}Rh_{0.04}CeO_z$ [b]	Rh-O	4.1 ± 1.0	0.203 ± 0.002	9 ± 4	5 ± 2	1.5
	Rh-Rh	2.9 ± 0.9	0.269 ± 0.001	4 ± 4	5 ± 1	
$Cr_{0.12}Rh_{0.06}CeO_z$ [a]	Rh-O	5.3 ± 1.2	0.203 ± 0.001	11 ± 2	4 ± 2	1.5
$Cr_{0.27}Rh_{0.07}CeO_z$ [a]	Rh-O	4.9 ± 0.7	0.203 ± 0.001	13 ± 2	3 ± 1	0.6
$Cr_{0.35}Rh_{0.07}CeO_z$ [a]	Rh-O	5.0 ± 0.9	0.203 ± 0.001	12 ± 2	3 ± 1	0.8
$Cr_{0.18}Rh_{0.04}CeO_z$ [a]	Rh-O	5.2 ± 1.1	0.203 ± 0.001	12 ± 2	4 ± 1	0.8
$Cr_{0.19}Rh_{0.08}CeO_z$ [a]	Rh-O	4.9 ± 0.9	0.203 ± 0.001	12 ± 2	3 ± 1	0.8
$Cr_{0.19}Rh_{0.11}CeO_z$ [a]	Rh-O	5.3 ± 1.3	0.203 ± 0.001	10 ± 3	4 ± 2	1.8

S_0^2 was fixed as 1. [a, b] k = 30-140 nm^{-1}, [a] R = 0.12-0.20 nm, [b] R = 0.12-0.27 nm.

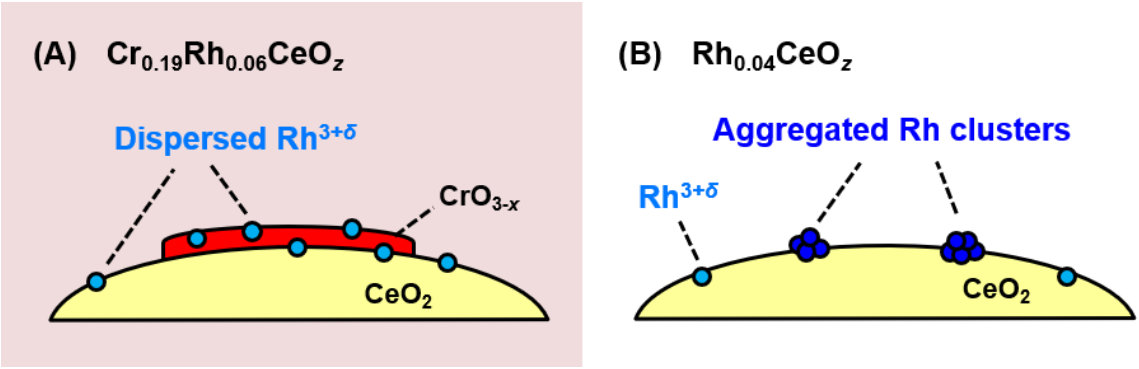

Figure 2.21. Schematic structural models of (A) $Cr_{0.19}Rh_{0.06}CeO_z$ and (B) $Rh_{0.04}CeO_z$.

2.3.2. Low-temperature redox property and structural changes of $Cr_{0.19}Rh_{0.06}CeO_z$

$Cr_{0.19}Rh_{0.06}CeO_z$ showed remarkable redox properties at lower temperatures below 373 K (Figure 2.22). TPR with H_2 was performed and the amount of consumed H_2 was quantified. The reduction of $Cr_{0.19}Rh_{0.06}CeO_z$ initiated at around 308 K and showed a TPR peak at 351 K, and $Cr_{0.19}Rh_{0.06}CeO_z$ consumed H_2 of 1.96 mmol g^{-1} in the TPR peak. On the other hand, $Cr_{0.17}CeO_z$ without Rh was reduced at a much higher temperature of 628 K (Figure 2.22 (A)). As for $Rh_{0.04}CeO_z$ without Cr, the amount of consumed H_2 (0.55 mmol g^{-1}) was much small as 28% of the case of $Cr_{0.19}Rh_{0.06}CeO_z$, although the reduction occurred at a similar temperature (353 K). Similar low-temperature reduction properties on $Ce_xRh_{1-x}O_{2-y}$ have been reported.[5l,r] CeO_2 was gradually reduced above 673 K (which can be attributed to surface region of CeO_2[4e,5e,k]), and CrO_3 and Rh_2O_3 showed TPR peaks at 628 and 438 K, respectively. These results suggest that the Cr and Rh species incorporated in $Cr_{0.19}Rh_{0.06}CeO_z$ dramatically enhanced its redox properties at the low temperatures (< 373 K).

The reoxidation of a reduced $Cr_{0.19}Rh_{0.06}CeO_z$ sample after the TPR proceeded readily with O_2 at 303 K, and the amount of consumed O_2 was 0.96 mmol g^{-1}, which was comparable to the amount of H_2 consumed (2 mol of H_2 and 1 mol of O_2 react to generate 2 mol of H_2O.). After the reoxidation, the low-temperature reduction proceeded again in a similar manner, and the redox process of $Cr_{0.19}Rh_{0.06}CeO_z$ was reversibly repeated up to four times (Figure 2.22 (B)). The reversible low-temperature redox properties of $Cr_{0.19}Rh_{0.06}CeO_z$ can efficiently contribute to catalysis with oxygen transfer at low temperatures.

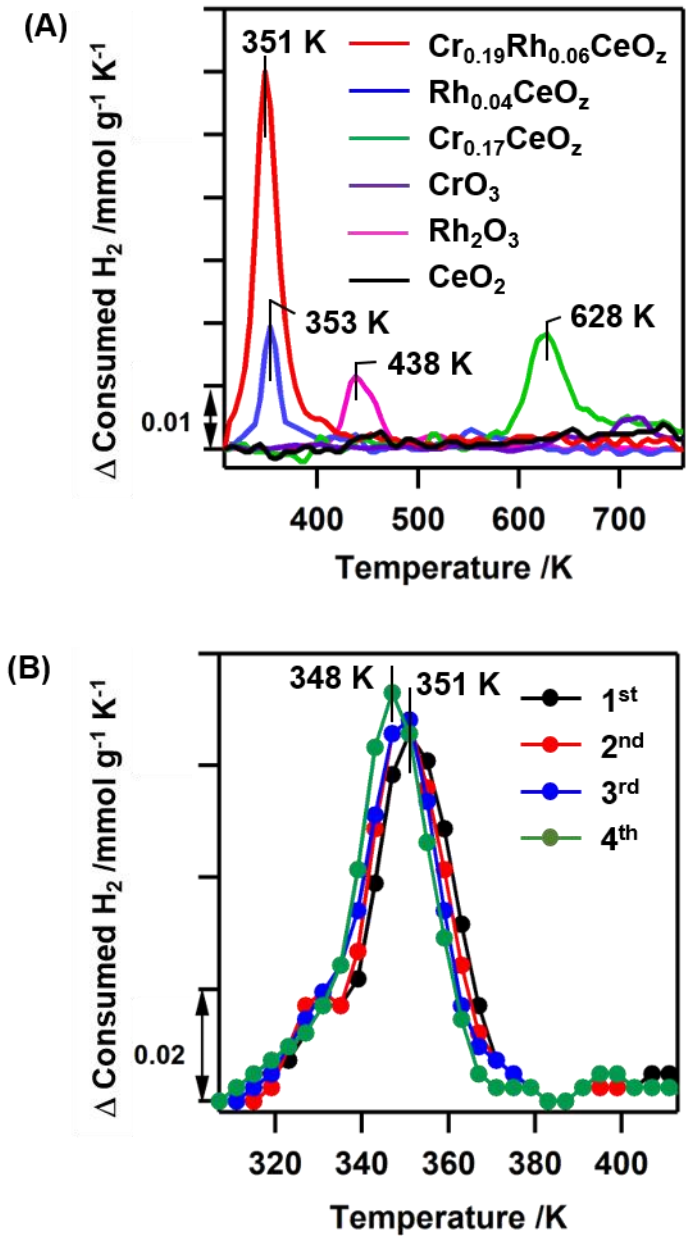

Figure 2.22. (A) TPR profiles with H_2 on $Cr_{0.19}Rh_{0.06}CeO_z$ (red), $Cr_{0.17}CeO_z$ (green), $Rh_{0.04}CeO_z$ (blue), CrO_3 (purple), Rh_2O_3 (pink), and CeO_2 (black).[7] (B) TPR profiles with H_2 on $Cr_{0.19}Rh_{0.06}CeO_z$ for four TPR/TPO cycles (black: first cycle; red: second cycle; blue: third cycle; green: fourth cycle).[7] TPO was conducted from 293 to 573 K after TPR up to 423 K.

It is reported that the incorporation of noble metal ions and 3d transition metal ions to ceria systems occurs the reduction of Ce^{4+} at lowered temperatures.[5b,c,6f,i-l,s] In order to examine the contribution of Ce^{4+} ions together with Cr and Rh ions to the reduction process, *in situ* Cr *K*-edge, Rh *K*-edge, and Ce L_{III}-edge XAFS spectra were measured in the reduction process of $Cr_{0.19}Rh_{0.06}CeO_z$ with H_2 from 293 to 423 K. The *in situ* XANES spectra demonstrated the reduction of all the three metal ions at low temperatures (Figure 2.23). The Rh *K*-edge XANES spectra firstly changed at the lowest temperature of 332 K, and the average oxidation state of Rh rapidly changed from +3.6 to +1.4 (Figure 2.23 (A)). Following the reduction of Rh, both Cr *K*-edge and Ce L_{III}-edge XANES spectra significantly changed (Figure 2.23 (B, C)), which proved the decrease in the oxidation states of both Cr and Ce ions. The analysis of XANES spectral changes revealed that the average oxidation states of Cr and Ce gradually changed from +5.4 to +3.0 (Cr) and from +3.8 to +3.5 (Ce). The reduction-temperature profiles are presented in Figure 2.24, which displays definite changes in the oxidation states of the Rh, Cr, and Ce ions. The total oxidation state changes in the three metals correspond to the consumed H_2 molecules of 2.28 mmol g^{-1} (Table 2.14), which is comparable to the net consumed H_2 within the experimental error bars in the TPR process. These results demonstrate that the low-temperature reduction of $Cr_{0.19}Rh_{0.06}CeO_z$ proceeded via the concerted reduction of the multiple metal species including Ce, not by a single metal source in CeO_2. The gap of the reduction temperature between Rh and Cr or Ce (Figure 2.24) suggests that the reduced Rh species formed in the first reduction step facilitates the subsequent reduction of Cr^{6+} and Ce^{4+} on the surface of CeO_2.

In situ AP-XPS measurements under the H_2-reduction conditions revealed the reduced state of $Cr_{0.19}Rh_{0.06}CeO_z$ at the surface region. *In situ* Rh 3d AP-XPS spectra appeared a new $3d_{5/2}$ peak at 307.5 eV attributed to reduced Rh nanoclusters (Figure 2.25 (A)).[5o,r,24] But the peaks at 309.2 eV ($Rh^{3+\delta}$)[5l,o,r,24] and 308.4 eV (Rh^{3+})[5l,o,r,24] remained, which indicated that all Rh ions were not reduced to the metallic level. *In situ* Ce 3d AP-XPS spectra (Figure 2.25 (C)) showed the formation of Ce^{3+} (u', v', u_0, and v_0 peaks),[23] and the decrease in the average oxidation state of Ce to +3.5 indicates that Ce^{4+} ions at the surface of $Cr_{0.19}Rh_{0.06}CeO_z$ was partially reduced. *In situ* Cr $2p_{3/2}$ AP-XPS peak shifted from 579.1 to 577.0 eV, indicating the complete reduction to the Cr^{3+} state (Figure 2.25 (B)),[4d,20] which corresponds to the results of Cr *K*-edge XANES (Figure 2.23 (B)). The shape of the Cr *K*-edge XANES spectrum of $Cr_{0.19}Rh_{0.06}CeO_z$ after the reduction was similar to that of $Cr(OH)_3$ (Figures 2.16, 2.23 (B)), suggesting the formation of $Cr(OH)_3$ below 373 K. *In situ* O 1s AP-XPS appeared a new peak at 531.6 eV attributed to a

hydroxyl group, which supported the formation of $Cr(OH)_3$ after the reduction (Figure 2.25 (D)).[20a]

The *in situ* XANES spectra under the oxidation with O_2 (Figure 2.26) also revealed the changes in the average oxidation states of Rh, Cr, and Ce in $Cr_{0.19}Rh_{0.06}CeO_z$ during the reoxidation process (Figure 2.27). The oxidation on Rh and Ce rapidly proceeded at 303 K by the introduction of O_2. In contrast, Cr species was gradually reoxidized from 350 to 550 K. *In situ* AP-XPS spectra also clarified reversible changes in the oxidation states of Rh, Cr, and Ce after the reoxidation process at the surface region (Figure 2.28). The disappearance of the O 1s peak at 531.6 eV attributed to hydroxyl group indicated the gradual oxidation of Cr to $Cr^{6-\gamma}O_{3-x}$ accompanied with the desorption of H_2O (Figure 2.28 (D)). The change in the oxidation state of Ce (30–40% of Ce; estimated from Ce L_{III}-edge XANES and Ce 3d AP-XPS (Table 2.16)) during the redox processes corresponded to approximately two monolayers of the most stable CeO_2 (111) surface,[25] considering the BET surface area of 98 $m^2\ g^{-1}$ and the average particle size of 10 nm from the STEM image.

The first reaction of Rh was suggested to be crucial in the low-temperature redox properties of $Cr_{0.19}Rh_{0.06}CeO_z$. Then, the local coordination structure of the Rh species was investigated by *in situ* Rh *K*-edge EXAFS analysis (Figures 2.29-30 and Tables 2.17-18). Before the reduction at 330 K, there were only Rh–O bonds at 0.204 ± 0.001 nm (coordination number (CN) = 5.8 ± 1.3), and the Rh–Rh bonds of metallic Rh and the Rh–O–Rh bonds in Rh_2O_3 were not observed (Figure 2.29 (a)). After the reduction at 334 K, Rh–Rh bonds at 0.270 ± 0.002 nm (CN = 2.6 ± 0.7) appeared in addition to the Rh–O bonds at 0.205 ± 0.002 nm (Figure 2.29 (b)). The local coordination structure of Rh recovered after the reoxidation with O_2 (Figure 2.30). Therefore, it is concluded that Rh species reversibly transform between dispersed $Rh^{3+\delta}$ species and small Rh nanoclusters during the redox processes of $Cr_{0.19}Rh_{0.06}CeO_z$.

Based on the *in situ* characterizations, the following reversible structural changes of $Cr_{0.19}Rh_{0.06}CeO_z$ during the low-temperature redox processes are proposed (Figure 2.31).
(1) As-prepared structure of $Cr_{0.19}Rh_{0.06}CeO_z$: $Rh^{3+\delta}$ ions and $Cr^{6-\gamma}O_{3-x}$ nanodomains were dispersed on the surface of CeO_2.
(2) Low-temperature reduction with H_2: the $Rh^{3+\delta}$ species were firstly reduced and clusterized at 332 K. Then, the dual reduction of Cr and Ce was facilitated at around 360 K: $Cr^{6-\gamma}O_{3-x}$ was reduced to $Cr^{3+}(OH)_3$, and Ce^{4+} species at the CeO_2 surface layers of was reduced to Ce^{3+}.
(3) The reversible reoxidation with O_2: The concerted oxidation of the Rh nanoclusters

and the surface Ce^{3+} species proceeded immediately after O_2 introduction below 303 K. Then, the $Cr^{3+}(OH)_3$ gradually reverted to $Cr^{6-\gamma}O_{3-x}$ at 303– 573 K.

The structural transformation of the dispersed Rh species can decrease the redox temperatures of both CrO_{3-x} and Ce ions at the surface layers at the similar temperature below 373 K, resulting in the overall redox properties of $Cr_{0.19}Rh_{0.06}CeO_z$.

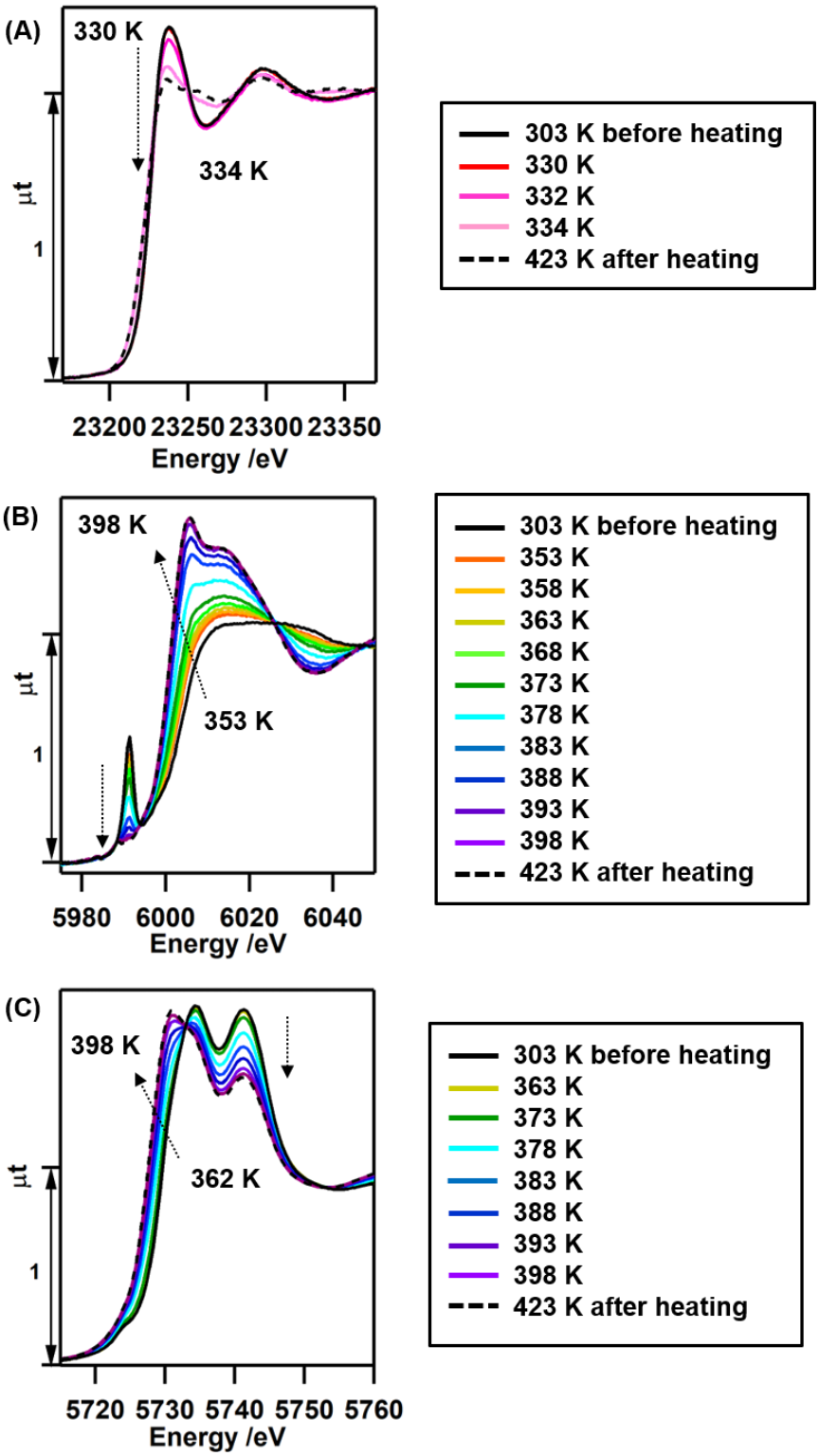

Figure 2.23. *In situ* (A) Rh *K*-edge, (B) Cr *K*-edge, (C) Ce L_{III}-edge XANES spectra of $Cr_{0.19}Rh_{0.06}CeO_z$ under H_2 reduction condition (303-423 K).[7]

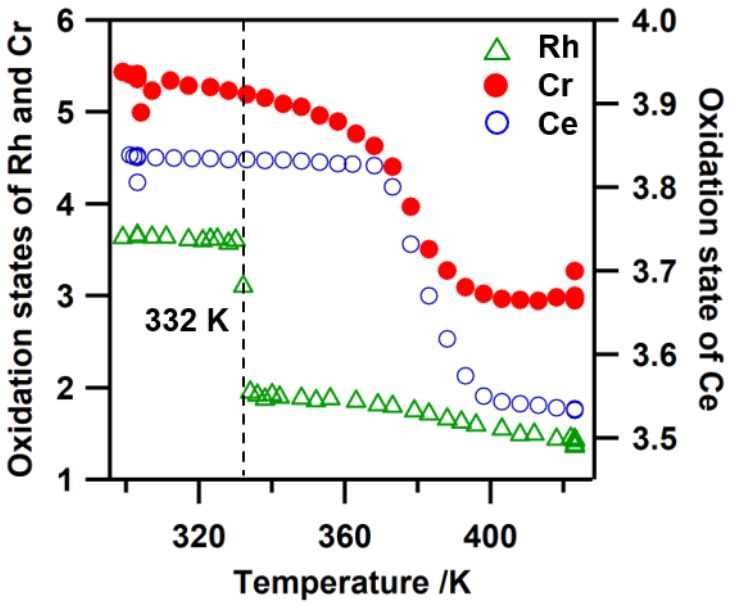

Figure 2.24. Changes in the average oxidation states of Rh, Cr, and Ce estimated from the XANES spectra for the reduction process. The average oxidation states of Rh, Cr, and Ce determined from the changes at 23238 eV (white line peak top), 5991.4 eV (pre-edge), and 5741.3 eV (second peak top of the white line), respectively.[7]

Table 2.14. Changes in the Oxidation States of Rh, Cr, and Ce upon *in situ* XAFS Spectral Change and Estimated H_2 Consumption under H_2 Reduction

Element	Oxidation state		Estimated H_2
	303 K (initial)	423 K (after reduction)	consumption /mmol g^{-1}
Rh	+3.6	+1.4	0.36
Cr	+5.4	+3.0	1.15
Ce	+3.8	+3.5	0.77
Total			2.28

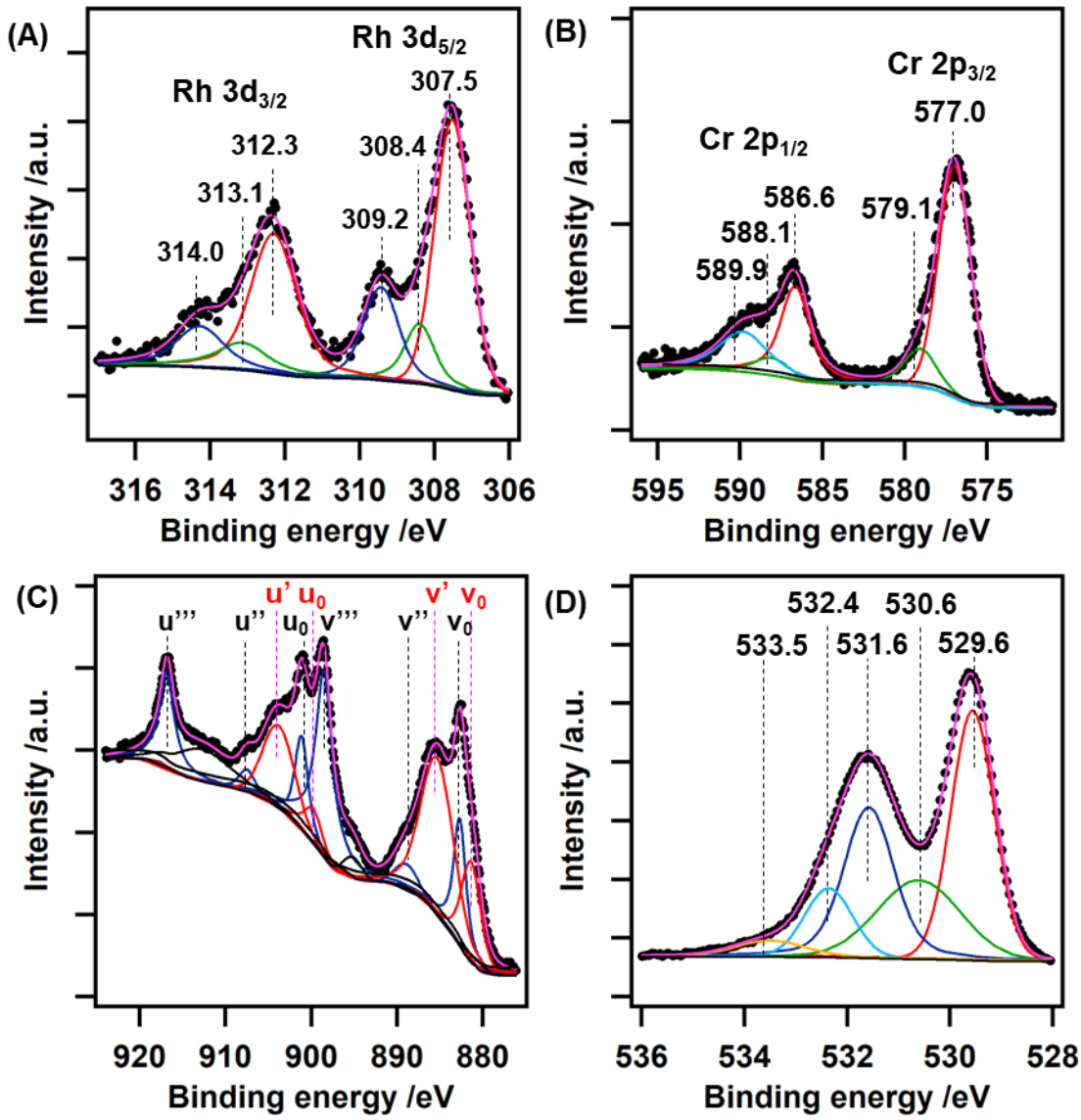

Figure 2.25. *In situ* (A) Rh 3d, (B) Cr 2p, (C) Ce 3d, and (D) O 1s AP-XPS spectra of $Cr_{0.19}Rh_{0.06}CeO_z$ measured under H_2 reduction at 385 K, and their curve-fitting analyses.[7]

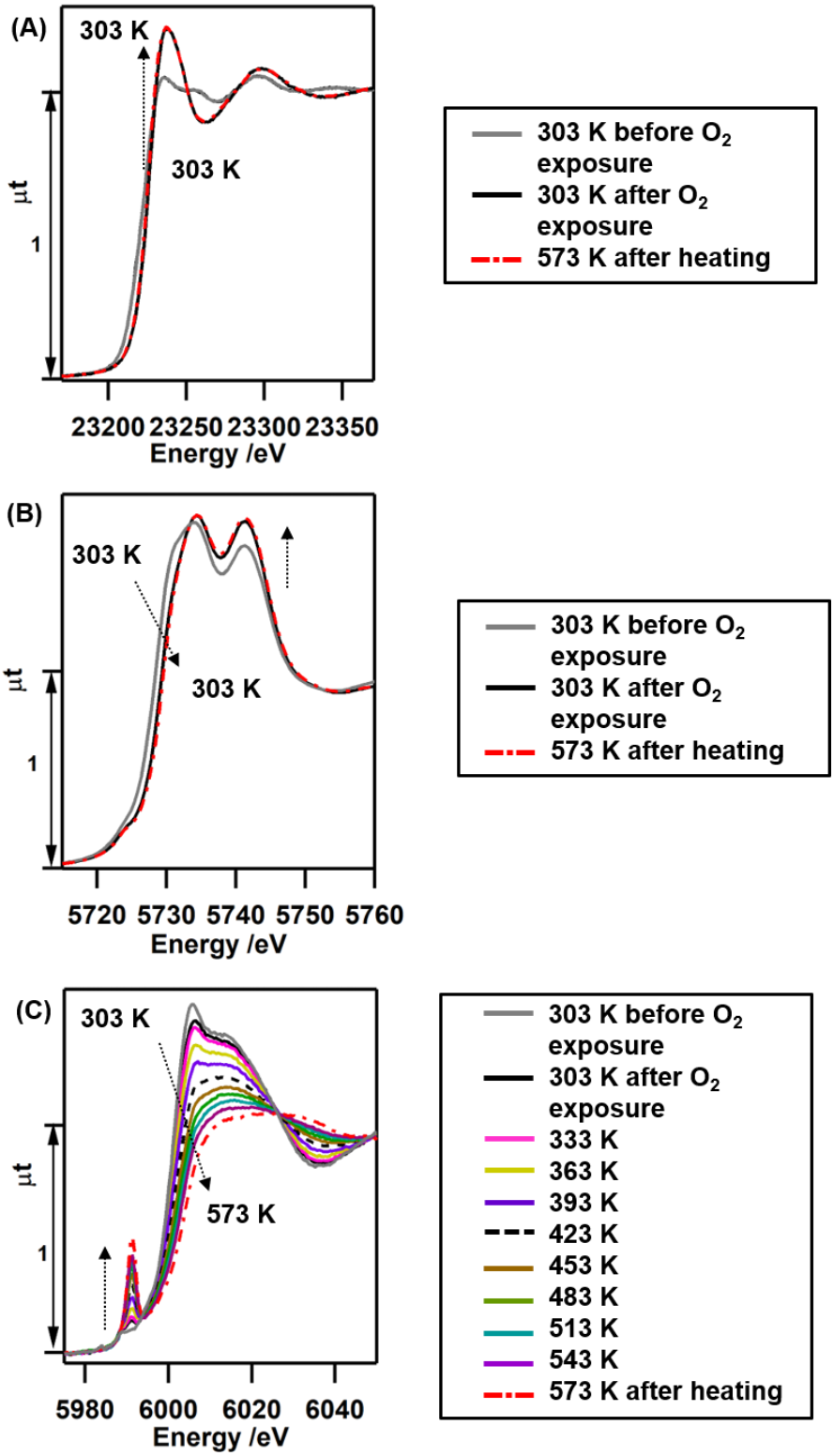

Figure 2.26. *In situ* (A) Rh *K*-edge, (B) Ce L_{III}-edge, (C) Cr *K*-edge XANES spectra of $Cr_{0.19}Rh_{0.06}CeO_z$ under O_2 oxidation condition (303-573 K).[7]

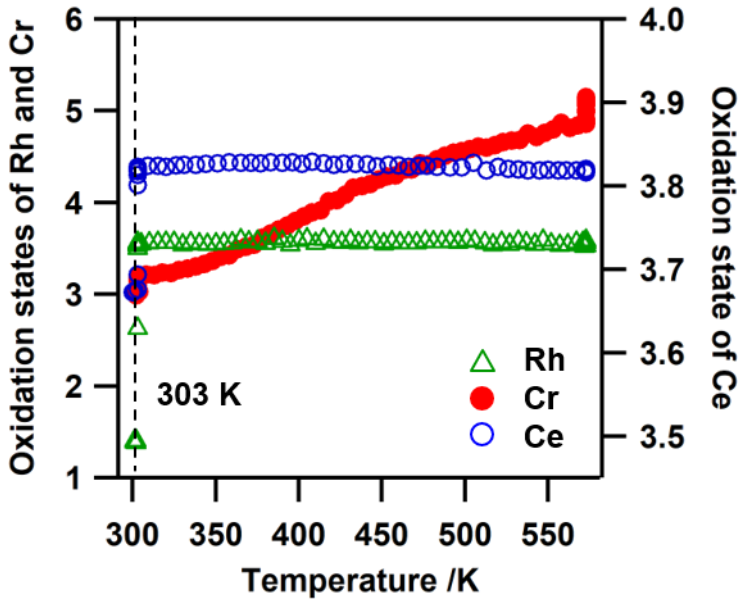

Figure 2.27. Changes in the oxidation states of Rh, Cr, and Ce estimated from the XANES spectra for the oxidation process. The average oxidation states of Rh, Cr, and Ce determined from the changes at 23238 eV (white line peak top), 5991.4 eV (pre-edge), and 5741.3 eV (second peak top of the white line), respectively.[7]

Table 2.15. Changes in the Oxidation States of Rh, Cr, and Ce upon *In situ* XAFS Spectral Change and Estimated O_2 Consumption under O_2 Oxidation

Element	Oxidation state		Estimated O_2
	303 K (initial)	573 K (after oxidation)	consumption /mmol g^{-1}
Rh	+1.4	+3.6	0.17
Cr	+3.0	+5.2	0.51
Ce	+3.7	+3.8	0.19
Total			0.87

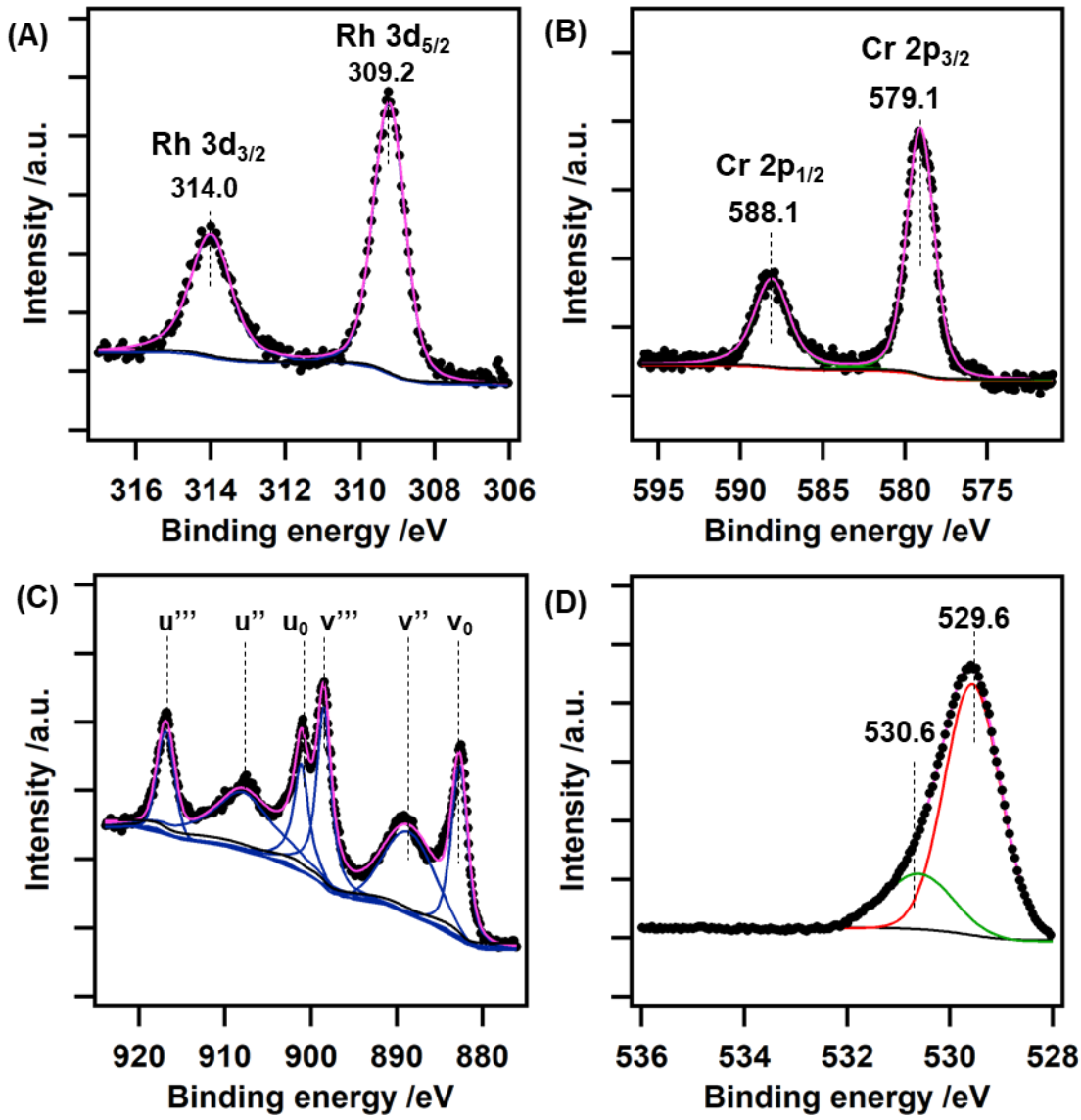

Figure 2.28. *In situ* (A) Rh 3d, (B) Cr 2p, (C) Ce 3d, and (D) O 1s AP-XPS spectra of $Cr_{0.19}Rh_{0.06}CeO_z$ measured under O_2 oxidation at 573 K, and their curve-fitting analyses.[7]

Table 2.16. Binding Energies and Ratio of Different Species in Cr 2p, Rh 3d, and Ce 3d AP-XPS Spectra of $Cr_{0.19}Rh_{0.06}CeO_z$ Measured under H_2 Reduction at 385 K and under O_2 Oxidation at 573 K

XPS peak			Binding Energy /eV	Ratio % H_2 reduction	O_2 oxidation
Cr 2p	Cr^{3+}	Cr $2p_{3/2}$	577.0	83	0
		Cr $2p_{1/2}$	586.2		
	Cr^{6+}	Cr $2p_{3/2}$	579.0	17	100
		Cr $2p_{1/2}$	588.3		
Rh 3d	Rh^0	Rh $3d_{5/2}$	307.5	62	0
		Rh $3d_{3/2}$	312.3		
	Rh^{3+}	Rh $3d_{5/2}$	308.4	15	0
		Rh $3d_{3/2}$	313.1		
	$Rh^{3+\delta}$	Rh $3d_{5/2}$	309.4	23	100
		Rh $3d_{3/2}$	314.2		
Ce 3d	Ce^{3+}	Ce $3d_{5/2}$ (v_0)	881.3	41	0
		Ce $3d_{5/2}$ (v')	885.3		
		Ce $3d_{3/2}$ (u_0)	899.8		
		Ce $3d_{3/2}$ (u')	903.8		
	Ce^{4+}	Ce $3d_{5/2}$ (v_0)	882.7	59	100
		Ce $3d_{5/2}$ (v'')	888.9		
		Ce $3d_{5/2}$ (v''')	898.5		
		Ce $3d_{3/2}$ (u_0)	901.1		
		Ce $3d_{3/2}$ (u'')	907.5		
		Ce $3d_{3/2}$ (u''')	916.8		

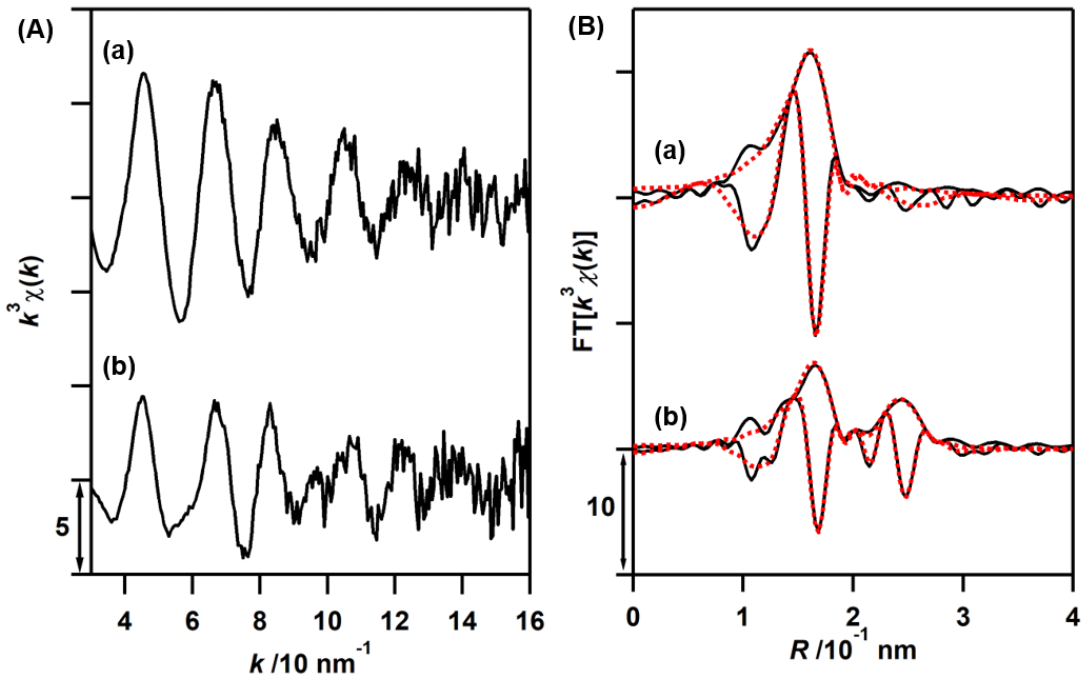

Figure 2.29. (A) *In situ* k^3-weighted Rh *K*-edge EXAFS oscillations and (B) their Fourier transforms (k = 30-140 nm^{-1}) for $Cr_{0.19}Rh_{0.06}CeO_z$ during H_2 reduction at (a) 330 K and (b) 334 K.[7] Black solid lines in (B) show observed data and red dashed lines show fitted data.

Table 2.17. Structural Parameters Obtained by Curve-Fitting Analysis of Rh *K*-edge EXAFS for $Cr_{0.19}Rh_{0.06}CeO_z$ during H_2 Reduction [a]

Shell	CN	R /nm	ΔE_0 /eV	σ^2 / 10^5 nm^2
During H_2 reduction (330 K) [b]				
Rh–O	5.8 ± 1.3	0.204 ± 0.001	11 ± 2	5 ± 2
During H_2 reduction (334 K) [c]				
Rh–O	2.8 ± 0.3	0.205 ± 0.002	9 ± 2	4 ± 1
Rh–Rh	2.6 ± 0.7	0.270 ± 0.002	4 ± 2	10 ± 2

[a] k = 30-140 nm^{-1}, S_0^2 was fixed as 1. [b] R = 0.12-0.20 nm, R_f = 0.9%. [c] R = 0.12-0.27 nm, R_f = 0.5%.

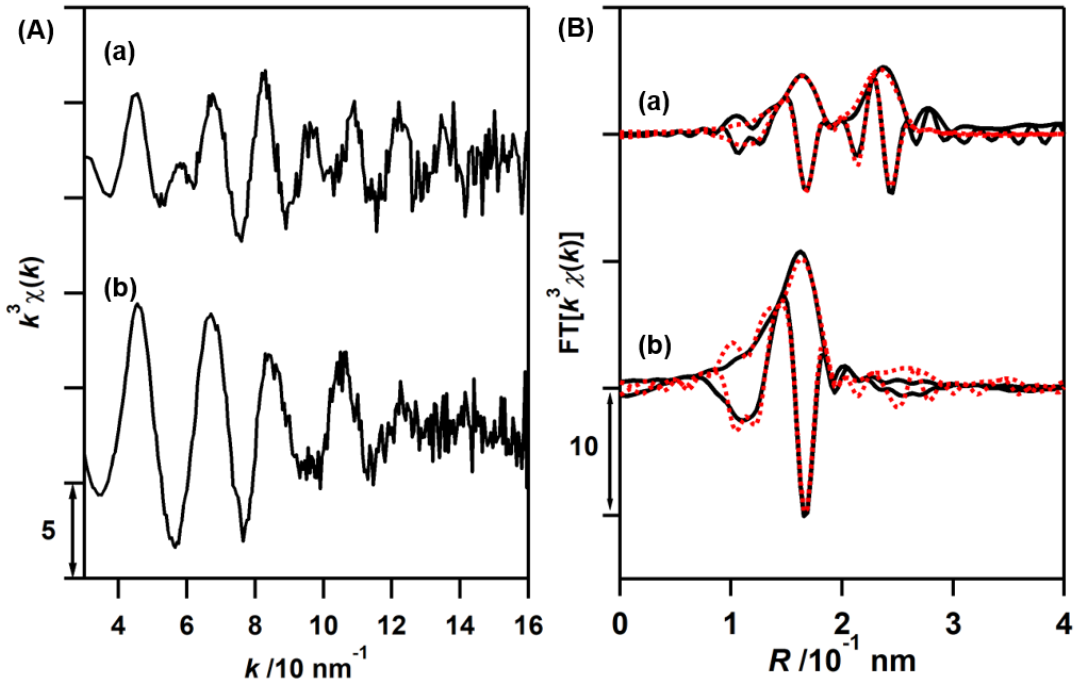

Figure 2.30. (A) k^3-Weighted Rh *K*-edge EXAFS oscillations, and (B) their Fourier transforms (k = 30-140 nm^{-1}) for $Cr_{0.19}Rh_{0.06}CeO_z$ (a) before O_2 introduction at 303 K, and (b) after O_2 introduction at 303 K.[7] Black solid lines in (B) show observed data and red dashed lines show fitted data.

Table 2.18. Structural Parameters Obtained by Curve-Fitting Analysis of Rh *K*-edge EXAFS for $Cr_{0.19}Rh_{0.06}CeO_z$ before and after O_2 Introduction [a]

Shell	CN	R /nm	ΔE_0 /eV	σ^2 / 10^5 nm^2
Before O_2 introduction (303 K) [b]				
Rh–O	1.8 ± 0.3	0.206 ± 0.003	9 ± 2	4 ± 1
Rh–Rh	3.1 ± 0.5	0.269 ± 0.001	2 ± 1	9 ± 1
After O_2 introduction (303 K) [c]				
Rh–O	5.8 ± 1.6	0.204 ± 0.001	11 ± 2	6 ± 3

[a] k = 30-140 nm^{-1}, S_0^2 was fixed as 1. [b] R = 0.12-0.27 nm, R_f = 0.4%. [c] R = 0.12-0.20 nm, R_f = 1.6%.

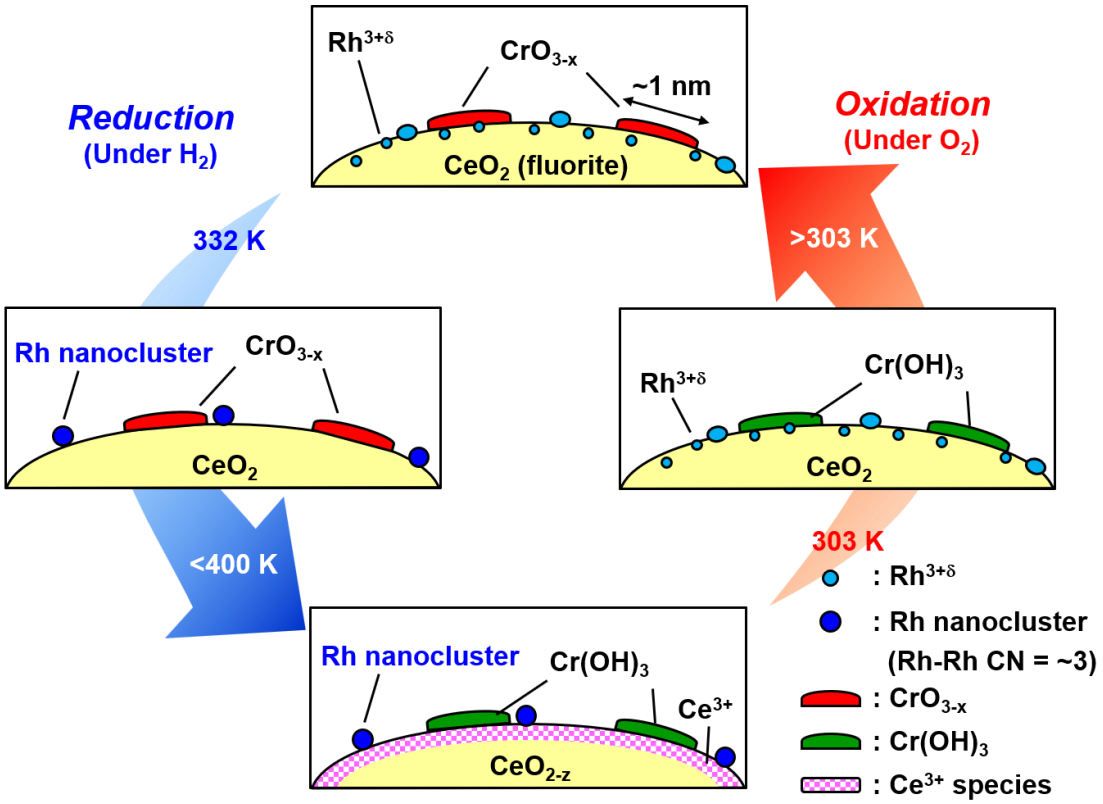

Figure 2.31. Schematic of the structural changes in the reversible low-temperature redox process of $Cr_{0.19}Rh_{0.06}CeO_z$ under H_2 reduction and O_2 oxidation based on *in situ* surface structural and electronic characterization.[7]

2.4. Conclusions

Cr and Rh-incorporated ceria ($Cr_{0.19}Rh_{0.06}CeO_z$) was newly prepared. Advanced physical characterizations also revealed $Cr_{0.19}Rh_{0.06}CeO_z$ had the structure that $Cr^{6-\gamma}O_{3-x}$ nanodomains of approximately 1 nm and $Rh^{3+\delta}$ species were dispersed on fluorite CeO_2 surface, as supported by HAADF-STEM-EDS/EELS, XAFS and XPS analysis. Whereas, $Rh_{0.04}CeO_z$ without Cr had aggregated Rh nanoclusters in addition to $Rh^{3+\delta}$ species on the surface of CeO_2. It was suggested that the incorporation of Cr in the Rh-containing ceria resulted in the Rh dispersion. $Cr_{0.19}Rh_{0.06}CeO_z$ was found to exhibit the remarkable and reversible low-temperature redox properties below 373 K. All metal species of not only Cr and Rh but also Ce cooperatively contributed to the low-temperature redox process of the $Cr_{0.19}Rh_{0.06}CeO_z$ as characterized by *in situ* XAFS and *in situ* AP-XPS. The $Rh^{3+\delta}$, $Cr^{6-\gamma}O_{3-x}$, and CeO_2 in $Cr_{0.19}Rh_{0.06}CeO_z$ were transformed to the Rh nanoclusters, the $Cr(OH)_3$ species, and CeO_{2-x} with two Ce^{3+}-oxide layers at the surface in a concerted reduction manner of all the three metal species by the H_2 reduction. The reduced species of Cr, Rh, and Ce were reversibly transformed to the initial forms during the O_2 oxidation process. The Rh dispersion assisted by Cr species and the reversible redox cycles of $Cr_{0.19}Rh_{0.06}CeO_z$ are expected to be useful for catalytic reactions.

2.5. References

(1) (a) *Catalysis by Ceria and Related Materials*; Trovarelli, A.； Fornasiero, P. Eds.; Imperial College Press, London, 2013. (b) Montini, T.； Melchionna, M.; Monai, M.; Fornasiero, P. Fundamentals and Catalytic Applications of CeO_2-Based Materials. *Chem. Rev.* **2016**, *116*, 5987−6041. (c) Li, P.; Chen, X.; Li, Y.; Schwank, J. W. A Review on Oxygen Storage Capacity of CeO_2-Based Materials: Influence Factors, Measurement Techniques, and Applications in Reactions Related to Catalytic Automotive Emissions Control. *Catal. Today* **2019**, *327*, 90−115. (d) Aneggi, E.; Boaro, M.; de Leithenburg, C.; Dolcetti, G.; Trovarelli, A. Insights into the Redox Properties of Ceria-Based Oxides and Their Implications in Catalysis. *J. Alloys Comp.* **2006**, *408-412*, 1096−1102.

(2) McFarland, E. W.; Metiu, H. Catalysis by Doped Oxides. *Chem. Rev.* **2013**, *113*, 4391−4427.

(3) (a) Boaro, M.; Vicario, M.; de Leitenburg, C.; Dolcetti, G.; Trovarelli, A. The Use of Temperature-Programmed and Dynamic/Transient Methods in Catalysis: Characterization of Ceria-Based, Model Three-Way Catalysts. *Catal. Today* **2003**, *77*, 407−417. (b) Ozawa, M.; Kimura, M.; Isogai, A. The Application of Ce-Zr Oxide Solid Solution to Oxygen Storage Promoters in Automotive Catalysts. *J. Alloys Comp.* **1993**, *193*, 73−75. (c) Morikawa, A.; Kikuta, K.; Suda, A.; Shinjo, H. Enhancement of Oxygen Storage Capacity by Reductive Treatment of Al_2O_3 and CeO_2–ZrO_2 Solid Solution Nanocomposite. *Appl. Catal. B Environ.* **2009**, *88*, 542−549.

(4) (a) Harrison, P. G.; Ball, I. K.; Azelee, W.; Daniell, W.; Goldfarb, D. Nature and Surface Redox Properties of Copper(II)-Promoted Cerium(IV) Oxide CO-Oxidation Catalysts. *Chem. Mater.* **2000**, *12*, 3715−3725. (b) Murugan, B.; Ramaswamy, A. V.; Srinivas, D.; Gopinath, C. S.; Ramaswamy, V. Nature of Manganese Species in $Ce_{1-x}Mn_xO_{2-\delta}$ Solid Solutions Synthesized by the Solution Combustion Route. *Chem. Mater.* **2005**, *17*, 3983−3993. (c) Gómez-Cortés, A.; Márquez, Y.; Arenas-Alatorre, J.; Díaz, G. Selective CO Oxidation in Excess of H_2 Over High-Surface Area CuO/CeO_2 Catalysts. *Catal. Today* **2008**, *133−135*, 743−749. (d) Singh, P.; Hegde, M. S.; Gopalakrishnan, J. $Ce_{2/3}Cr_{1/3}O_{2+y}$: A New Oxygen Storage Material Based on the Fluorite Structure. *Chem. Mater.* **2008**, *20*, 7268−7273. (e) Beckers, J.; Rothenberg, G. Redox Properties of Doped and Supported Copper–Ceria Catalysts. *Dalton Trans*, **2008**, 6573−6578. (f) Liang, C.; Ma, Z.; Lin, H.; Ding, L.; Qiu, J.; Frandsen, W.; Su, D. Template Preparation of Nanoscale $Ce_xFe_{1-x}O_2$ Solid Solutions

and Their Catalytic Properties for Ethanol Steam Reforming. *J. Mater. Chem.* **2009**, *19*, 1417−1424. (g) Singh, P.; Hegde, M. S. $Ce_{0.67}Cr_{0.33}O_{2.11}$: A New Low-Temperature O_2 Evolution Material and H_2 Generation Catalyst by Thermochemical Splitting of Water. *Chem. Mater.* **2010**, *22*, 762−768. (h) Yao, X.; Tang, C.; Ji, Z.; Dai, Y.; Cao, Y.; Gao, F.; Dong, L.; Chen, Y. Investigation of the Physicochemical Properties and Catalytic Activities of $Ce_{0.67}M_{0.33}O_2$ (M = Zr^{4+}, Ti^{4+}, Sn^{4+}) Solid Solutions for NO Removal by CO. *Catal. Sci. Tech.* **2013**, *3*, 688−698. (i) Li, Y.; Wei, Z.; Sun, J.; Gao, F.; Peden, C. H. F.; Wang, Y. Effect of Sodium on the Catalytic Properties of VO_x/CeO_2 Catalysts for Oxidative Dehydrogenation of Methanol. *J. Phys. Chem. C.* **2013**, *117*, 5722−5729. (j) Moog, I.; Prestipino, C.; Figueroa, S.; Majimel, J.; Demourgues, A. Dual Ce^{4+}/Fe^{3+} Redox Phenomena into Nanocrystalline $Ce_{1-x}Fe_xO_{2-x/2}$ Solid Solution. *J. Phys. Chem. C* **2014**, *118*, 22746−22753. (k) Zhang, P.; Lu, H.; Zhou, Y.; Zhang, L.; Wu, Z.; Yang, S.; Shi, H.; Zhu, Q.; Chen, Y.; Dai, S. Mesoporous $MnCeO_x$ Solid Solutions for Low Temperature and Selective Oxidation of Hydrocarbons. *Nat. Commun.* **2015**, *6*, 8446. (l) Konsolakis, M.; Sgourakis, M.; Carabinerio, S. A. C. Surface and Redox Properties of Cobalt–Ceria Binary Oxides: On the Effect of Co Content and Pretreatment Conditions. *Appl. Surf. Sci.* **2015**, *341*, 48−54. (m) Jampaiah, D.; Ippolito, S. J.; Sabri, Y. M.; Reddy, B. M.; Bhargava, S. K. *Catal. Sci. Tech.* **2015**, *5*, 2913−2924. (n) Konsolakis, M.; Carabinerio, S. A. C.; Papista, E.; Marnellos, G. E.; Tavares, P. B.; Agostinho Moreira, J.; Romaguera-Barcelay, Y.; Figueiredo, J. L. Effect of Preparation Method on the Solid State Properties and the deN_2O Performance of $CuO–CeO_2$ Oxides. *Catal. Sci. Tech.* **2015**, *5*, 3714−3727. (o) Deng, C.; Li, M.; Qian, J.; Hu, Q.; Huang, M.; Lin, Q.; Ruan, Y.; Dong, L.; Li, B.; Fan, M. A Study of Different Doped Metal Cations on the Physicochemical Properties and Catalytic Activities of $Ce_{20}M_1O_x$ (M=Zr, Cr, Mn, Fe, Co, Sn) Composite Oxides for Nitric Oxide Reduction by Carbon Monoxide. *Chem. Asian J.* **2016**, *11*, 2144−2156. (p) Davó-Quiñonero, A.; Navlani-García, M.; Lozano-Castelló, D.; Bueno-López, A.; Anderson, J. A. Role of Hydroxyl Groups in the Preferential Oxidation of CO over Copper Oxide−Cerium Oxide Catalysts. *ACS Catal.* **2016**, *6*, 1723−1731. (q) Jampaiah, D.; Venkataswamy, P.; Coyle, V. E.; Reddy, B. M.; Bhargava, S. K. *RSC Adv.* **2016**, *6*, 80541−80548. (r) Fuentes, R. O.; Acuña, L. M.; Albornoz, C. A.; Leyva, A. G.; Sousa, N.; Figueiredo, F. M. Structural, Physical and Chemical Properties of Nanostructured Nickel-Substituted Ceria Oxides under Reducing and Oxidizing Conditions. *RSC Adv.* **2016**, *6*, 64861−64870. (s) Lee, K. J.; Kim, Y.; Lee, J. H.; Cho, S. J.; Kwak, J. H.; Moon, H. R. Facile

Synthesis and Characterization of Nanostructured Transition Metal/Ceria Solid Solutions ($TM_xCe_{1-x}O_{2-\delta}$, TM = Mn, Ni, Co, or Fe) for CO Oxidation. *Chem. Mater.* **2017**, *29*, 2874−2882. (t) Xiong, Y.; Li, L.; Zhang, L.; Cao, Y.; Yu, S.; Tang, C.; L. Dong, L. Migration of Copper Species in $Ce_xCu_{1-x}O_2$ Catalyst Driven by Thermal Treatment and the Effect on CO Oxidation. *Phys. Chem. Chem. Phys.* **2017**, *19*, 21840−21847. (u) Li, D.; Li, K.; Xu, R.; Wang, H.; Tian, D.; Wei, Y.; Zhu, X.; Zeng, C.; Zeng, L. $Ce_{1-x}Fe_xO_{2-\delta}$ Catalysts for Catalytic Methane Combustion: Role of Oxygen Vacancy and Structural Dependence. *Catal. Today* **2018**, *318*, 73−85. (v) Li, Z.; Guo, X.; Tao, F.; Zhou, R. New Insights into the Effect of Morphology on Catalytic Properties of MnO_x–CeO_2 Mixed Oxides for Chlorobenzene Degradation. *RSC Adv.* **2018**, *8*, 25283−25291. (w) Sudarsanam, P.; Hillary, B.; Amin, M. H.; Rockstroh, N.; Bentrup, U.; Brückner, A.; Bhargava, S. K. Heterostructured Copper−Ceria and Iron−Ceria Nanorods: Role of Morphology, Redox, and Acid Properties in Catalytic Diesel Soot Combustion. *Langmuir* **2018**, *34*, 2663−2673. (x) Lu, J.; Wang, J.; Zou, Q.; He, D.; Zhang, L.; Xu, Z.; He, S.; Luo, Y. Unravelling the Nature of the Active Species as well as the Doping Effect over Cu/Ce-Based Catalyst for Carbon Monoxide Preferential Oxidation. *ACS Catal.* **2019**, *9*, 2177−2195. (y) Liu, Z.; Li, J.; Buettner, M.; Ranganathan, R. V.; Uddi, M.; Wang, R. Metal−Support Interactions in CeO_2- and SiO_2-Supported Cobalt Catalysts: Effect of Support Morphology, Reducibility, and Interfacial Configuration. *ACS Appl. Mater. Interfaces* **2019**, *11*, 17035−17049. (z) Li, D.; Li, K.; Xu, R.; Zhu, X.; Wei, Y.; Tian, D.; Cheng, X.; Wang, H. Enhanced CH_4 and CO Oxidation over $Ce_{1-x}Fe_xO_{2-\delta}$ Hybrid Catalysts by Tuning the Lattice Distortion and the State of Surface Iron Species. *ACS Appl. Mater. Interfaces* **2019**, *11*, 19227−19241.

(5) (a) Hegde, M. S.; Madras, G.; Patil, K. C. Noble Metal Ionic Catalysts. *Acc. Chem. Res.* **2009**, *42*, 704−712. (b) Bera, P.; Hegde, M. S. Noble Metal Ions in CeO_2 and TiO_2: Synthesis, Structure and Catalytic Properties. *RSC Adv.* **2015**, *5*, 94949−94979. (c) Hegde, M. S.; Bera, P. Noble Metal Ion Substituted CeO_2 Catalysts: Electronic Interaction Between Noble Metal Ions and CeO_2 Lattice. *Catal. Today* **2015**, *253*, 40−50. (d) El Fallah, J.; Boujana, S.; Dexpert, H.; Kiennemann, A.; Majerus, J.; Touret, O.; Villain, F.; Le Normand, F. Redox Processes on Pure Ceria and on Rh/CeO_2 Catalyst Monitored by X-ray Absorption (Fast Acquisition Mode). *J. Phys. Chem.* **1994**, *98*, 5522−5533. (e) Gayen, A.; Priolkar, K. R.; Sarode, P. R.; Jayaram, V.; Hegde, M. S.; Subbanna, G. N.; Emura S. $Ce_{1-x}Rh_xO_{2-\delta}$ Solid Solution Formation in Combustion-Synthesized Rh/CeO_2 Catalyst Studied by XRD, TEM, XPS, and

EXAFS. *Chem. Mater.* **2004**, *16*, 2317−2328. (f) Miyazawa, T.; Okumura, K.; Kunimori, K.; Tomishige, K. Promotion of Oxidation and Reduction of Rh Species by Interaction of Rh and CeO_2 over $Rh/CeO_2/SiO_2$. *J. Phys. Chem. B* **2008**, *112*, 2574−2583. (g) Singh, P.; Hegde, M. S. $Ce_{1-x}Ru_xO_{2-\delta}$ (x = 0.05, 0.10): A New High Oxygen Storage Material and Pt, Pd-Free Three-Way Catalyst. *Chem. Mater.* **2009**, *21*, 3337−3345. (h) Parres-Esclapez, S.; Illán-Gómez, M. J.; Salinas-Martínez de Lecea, C.; Bueno-López, A. On the Importance of the Catalyst Redox Properties in the N_2O Decomposition over Alumina and Ceria Supported Rh, Pd and Pt. *Appl. Catal. B Environ.* **2010**, *96*, 370−378. (i) Kurnatowska, M.; Kepinski, L. Structure and Thermal Stability of Nanocrystalline $Ce_{1-x}Rh_xO_{2-y}$ in Reducing and Oxidizing Atmosphere. *Mater. Res. Bull.* **2013**, *48*, 852−862. (j) Zhu, Y.; Zhang, S.; Shan, J.; Nguyen, L.; Zhan, S.; Gu, X.; Tao, F. In Situ Surface Chemistries and Catalytic Performances of Ceria Doped with Palladium, Platinum, and Rhodium in Methane Partial Oxidation for the Production of Syngas. *ACS Catal.* **2013**, *3*, 2627−2639. (k) Sato, K.; Adachi, K.; Takita, Y.; Nagaoka, K. Effect of the Nature of the CeO_2 Support of the Rh Catalyst on Triggering the Oxidative Reforming of *n*-Butane for H_2 Production from Ambient Temperature. *ChemCatChem* **2014**, *6*, 784−789. (l) Kurnatowaska, M.; Schuster, M. E.; Mista, W.; Kepinski, L. Self-Regenerative Property of Nanocrystalline $Ce_{0.89}M_{0.11}O_{2-y}$ (M = Pd, Rh) Mixed Oxides. *ChemCatChem* **2014**, *6*, 3125−3134. (m) Nelson, N. C.; Manzano, J. S.; Sadow, A. D.; Overbury, S. H.; Slowing, I. I. Selective Hydrogenation of Phenol Catalyzed by Palladium on High-Surface-Area Ceria at Room Temperature and Ambient Pressure. *ACS Catal.* **2015**, *5*, 2051−2061. (n) Hiley, C. I.; Fisher, J. M.; Thompsett, D.; Kashtiban, R. J.; Sloan, J.; Walton, R. I. Incorporation of Square-Planar Pd^{2+} in Fluorite CeO_2: Hydrothermal Preparation, Local Structure, Redox Properties and Stability. *J. Mater. Chem. A* **2015**, *3*, 13072−13079. (o) Ševčíková, K.; Nehasil, V.; Vorokhta, M.; Haviar, S.; Matolín, V.; Matolínová, I.; Mašek, K.; Píš, I.; Kobayashi, K.; Kobata, M.; Nagata, T.; Matsushita, Y.; Yoshikawa, H. Altering Properties of Cerium Oxide Thin Films by Rh Doping. *Mater. Res. Bull.* **2015**, *67*, 5−13. (p) Varga, E.; Pusztai, P.; Oszkó, A.; Baán, K.; Erdőhelyi, A.; Kónya, Z.; Kiss, J. Stability and Temperature-Induced Agglomeration of Rh Nanoparticles Supported by CeO_2. *Langmuir* **2016**, *32*, 2761−2770. (q) Ševčíková, K.; Szabová, L.; Kettner, M.; Homola, P.; Tsud, N.; Fabris, S.; Matolín, V.; Nehasil, V. Experimental and Theoretical Study on the Electronic Interaction between Rh Adatoms and CeO_x Substrate in Dependence on a Degree of Cerium Oxide Reduction. *J. Phys. Chem. C*

2016, *120*, 5468−5476. (r) Kibis, L. S.; Kardash, T. Y.; Derevyannikova, E. A.; Stonkus, O. A.; Slavinskaya, E. M.; Svetlichnyi, V. A.; Boronin, A. I. Redox and Catalytic Properties of $Rh_xCe_{1-x}O_{2-\delta}$ Solid Solution. *J. Phys. Chem. C* **2017**, *121*, 26925−26938. (s) Guo, Y.; Mei, S.; Yuan, K.; Wang, D.-J.; Liu, H.-C.; Yan, C.-H.; Zhang, Y.-W. Low-Temperature CO_2 Methanation over CeO_2-Supported Ru Single Atoms, Nanoclusters, and Nanoparticles Competitively Tuned by Strong Metal−Support Interactions and H-Spillover Effect. *ACS Catal.* **2018**, *8*, 6203−6215. (t) Jeong, H.; Lee, G.; Kim, B.-S.; Bae, J.; Han, J. W.; Lee, H. Fully Dispersed Rh Ensemble Catalyst to Enhance Low-Temperature Activity. *J. Am. Chem. Soc.* **2018**, *140*, 9558−9565. (u) Derevyannikova, E. A.; Kardash, T. Y.; Stadnichenko, A. I.; Stonkus, O. A.; Slavinskaya, E. M.; Svetlichnyi, V. A.; Boronin, A. I. Structural Insight into Strong Pt−CeO_2 Interaction: From Single Pt Atoms to PtO_x Clusters. *J. Phys. Chem. C* **2019**, *123*, 1320−1334.

(6) (a) Fornasiero, P.; Di Monte, R.; Rao, G. R.; Kašper, J.; Meriani, S.; Trovarelli, A. Graziani, M. Rh-Loaded CeO_2-ZrO_2 Solid Solutions as Highly Efficient Oxygen Exchangers: Dependence of the Reduction Behavior and the Oxygen Storage Capacity on the Structural Properties. *J. Catal.* **1995**, *151*, 168−177. (b) Fajardie, F.; Tempère, J.-F.; Manoli, J.-M.; Touret, O.; Blanchard, G.; Djéga-Mariadassou, G. Activity of Rh^{x+} Species in CO Oxidation and NO Reduction in a CO/NO/O_2 Stoichiometric Mixture over a Rh/CeO_2-ZrO_2 Catalyst. *J. Catal.* **1998**, *179*, 469−476. (c) Fornasiero, P.; Kašpar, J.; Sergo, V.; Graziani, M. Redox Behavior of High-Surface-Area Rh-, Pt-, and Pd-Loaded $Ce_{0.5}Zr_{0.5}O_2$ Mixed Oxide. *J. Catal.* **1999**, *182*, 56−69. (d) Holi, C. E.; Brenner, A.; Ng, K. Y. S.; Rahmoeller, K. M.; Belton, D. Studies of the Oxygen Release Reaction in the Platinum-Ceria-Zirconia System. *Catal. Today* **1999**, *50*, 299−308. (e) Vlaic, G.; Di Monte, R.; Fornasiero, P.; Fonda, E.; Kašpar, J.; Graziani, M. Redox Property–Local Structure Relationships in the Rh-Loaded CeO_2–ZrO_2 Mixed Oxides. *J. Catal.* **1999**, *182*, 378−389. (f) Baidya, T.; Gayen, A.; Hegde, M. S.; Ravishankar, N.; Dupont, L. Enhanced Reducibility of $Ce_{1-x}Ti_xO_2$ Compared to That of CeO_2 and Higher Redox Catalytic Activity of $Ce_{1-x-y}Ti_xPt_yO_{2-\delta}$ Compared to That of $Ce_{1-x}Pt_xO_{2-\delta}$. *J. Phys. Chem. B* **2006**, *110*, 5262−5272. (g) Yamamoto, T.; Suzuki, A.; Nagai, Y.; Tanabe, T.; Dong, F.; Inada, Y.; Nomura, M.; Tada, M.; Iwasawa, Y. Origin and Dynamics of Oxygen Storage/Release in a Pt/Ordered CeO_2–ZrO_2 Catalyst Studied by Time-Resolved XAFS Analysis. *Angew. Chem. Int. Ed.* **2007**, *46*, 9253−9256. (h) Haneda, M.; Shinoda, K.; Nagane, A.; Houshito, O.; Takagi, H.; Nakahara, Y.; Hiroe, K.; Fujitani,

T.; Hamada, H. Catalytic Performance of Rhodium Supported on Ceria–Zirconia Mixed Oxides for Reduction of NO by Propene. *J. Catal.* **2008**, *259*, 223−231. (i) Gupta, A.; Kumar, A.; Waghmare, U. V.; Hegde, M. S. Origin of Activation of Lattice Oxygen and Synergistic Interaction in Bimetal-Ionic $Ce_{0.89}Fe_{0.1}Pd_{0.01}O_{2-\delta}$ Catalyst. *Chem. Mater.* **2009**, *21*, 4880−4891. (j) Gupta, A.; Hegde, M. S.; Priolkar, K. R.; Waghmare, U. V.; Sarode, P. R.; Emura, S. Structural Investigation of Activated Lattice Oxygen in $Ce_{1-x}Sn_xO_2$ and $Ce_{1-x-y}Sn_xPd_yO_{2-\delta}$ by EXAFS and DFT Calculation. *Chem. Mater.* **2009**, *21*, 5836−5847. (k) Gupta, A.; Waghmare, U. V.; Hegde, M. S. Correlation of Oxygen Storage Capacity and Structural Distortion in Transition-Metal-, Noble-Metal-, and Rare-Earth-Ion-Substituted CeO_2 from First Principles Calculation. *Chem. Mater.* **2010**, *22*, 5184−5198. (l) Singh, P.; Hegde, M. S. Sonochemical Synthesis of $Ce_{1-x}Fe_xO_{2-\delta}$ ($0 < x < 0.45$) and $Ce_{0.65}Fe_{0.33}Pd_{0.02}O_{2-\delta}$ Nanocrystallites: Oxygen Storage Material, CO Oxidation and Water Gas Shift Catalyst. *Dalton Trans.* **2010**, *39*, 10768−10780. (m) Wang, Q.; Li, G.; Zhao, B.; Shen, M.; Zhou, R. The Effect of La Doping on the Structure of $Ce_{0.2}Zr_{0.8}O_2$ and the Catalytic Performance of its Supported Pd-Only Three-Way Catalyst. *Appl. Catal. B Environ.* **2010**, *101*, 150−159. (n) Q. Wang, G. Li, B. Zhao, R. Zhou, *J. Mol. Catal. A: Chem.* **2011**, *339*, 52−60. (o) Tada, M.; Zhang, S.; Malwadkar, S.; Ishiguro, N.; Soga, J.; Nagai, Y.; Tezuka, K.; Imoto, H.; Otsuka-Yao-Matsuo, S.; Ohkoshi, S.; Iwasawa, Y. The Active Phase of Nickel/Ordered $Ce_2Zr_2O_x$ Catalysts with a Discontinuity (x = 7–8) in Methane Steam Reforming. *Angew. Chem. Int. Ed.* **2012**, *51*, 9361−9365. (p) Mandal, S.; Santra, C.; Bando, K. K.; James, O. O.; Maity, S.; Mehta, D.; Chowdhury, B. Aerobic Oxidation of Benzyl Alcohol over Mesoporous Mn-Doped Ceria Supported Au Nanoparticle Catalyst. *J. Mol. Catal. A Chem.* **2013**, *378*, 47−56. (q) Shinde, V. M.; Madras, G. Synthesis of Nanosized $Ce_{0.85}M_{0.1}Ru_{0.05}O_{2-\delta}$ (M = Si, Fe) Solid Solution Exhibiting High CO Oxidation and Water Gas Shift Activity. *Appl. Catal. B Environ.* **2013**, *138−139*, 51−61. (r) Topka, P.; Delaigle, R.; Kaluža, L.; Gaigneaux, E. M. Performance of Platinum and Gold Catalysts Supported on Ceria–Zirconia Mixed Oxide in the Oxidation of Chlorobenzene. *Catal. Today* **2015**, *253*, 172−177. (s) Cwele, T.; Mahadevaiah, N.; Singh, S.; Friedrich, H. B.; Yadav, A. K.; Jha, S. N.; Bhattacharyya, D.; Sahoo, N. K. CO Oxidation Activity Enhancement of $Ce_{0.95}Cu_{0.05}O_{2-\delta}$ Induced by Pd Co-Substitution. *Catal. Sci. Technol.* **2016**, *6*, 8104−8116. (t) Cao, Y.; Ran, R.; Wu, X.; Wu, X.; Wan, J.; Weng, D. Ageing Resistance of Rhodium Supported on CeO_2–ZrO_2 and ZrO_2: Rhodium Nanoparticle Structure and Rh–Support Interaction under

Diverse Ageing Atmosphere. *Catal. Today* **2017**, *281*, 490−499. (u) Yang, L.; You, X.; Sheng, Z.; Ma, D.; Yu, D.; Xiao, X.; Wang, S. The Promoting Effect of Noble Metal (Rh, Ru, Pt, Pd) Doping on the Performances of MnO_x–CeO_2/graphene Catalysts for the Selective Catalytic Reduction of NO with NH_3 at Low Temperatures. *New, J. Chem.* **2018**, *42*, 11673−11681. (v) Li, S.; Yan, S.; Xia, Y.; Cui, B.; Pu, Y.; Ye, Y.; Wang, D.; Liu, Y.-Q.; Chen, B. Oxidative Reactivity Enhancement for Soot Combustion Catalysts by Co-Doping Silver and Manganese in Ceria. *Appl. Catal. A General* **2019**, *570*, 299−307.

(7) Ikemoto, S.; Huang, X.; Muratsugu, S.; Nagase, S.; Koitaya, T.; Matsui, H.; Yokota, G.; Sudoh, T.; Hashimoto, A.; Tan, Y.; Yamamoto, S.; Tang, J.; Matsuda, I.; Yoshinobu, J.; Yokoyama, T.; Kusaka, S.; Matsuda, R.; Tada, M. Reversible Low-Temperature Redox Activity and Selective Oxidation Catalysis Derived from the Concerted Activation of Multiple Metal Species on Cr and Rh-Incorporated Ceria Catalysts. *Phys. Chem. Chem. Phys.* **2019**, *21*, 20868–20877.

(8) Ikemoto, S.; Muratsugu, S.; Koitaya, T.; Tada, M. Chromium Oxides as Structural Modulators of Rhodium Dispersion on Ceria to Generate Active Sites for NO Reduction. *ACS Catal.* **2022**, *12*, 431–441.

(9) Seah, M. P.; Glimore, I. S.; Beamson, G. XPS: Binding Energy Calibration of Electron Spectrometers 5–Re-evaluation of the Reference Energies. *Surf. Interface Anal.* **1998**, *26*, 642–649.

(10) Repoux, M. Comparison of Background Removal Methods for XPS *Surf. Interface Anal.* **1992**, *18*, 567–570.

(11) (a) Ravel, B.; Newville, M. ATHENA, ARTEMIS, HEPHAESTUS: Data Analysis for X-ray Absorption Spectroscopy Using IFEFFIT. *J. Synchrotron Radiat.* **2005**, *12*, 573–541. (b) Newville, M.; Ravel, B.; Haskel, D.; Rehr, J. J.; Stern, E. A.; Yacoby, Y. Analysis of Multiple-Scattering XAFS Data Using Theoretical Standards. *Physica B* **1995**, *208–209*, 154–156.

(12) Bearden, J. A.; Burr, A. F. Reevaluation of X-Ray Atomic Energy Levels. *Rev. Mod. Phys.* **1967**, *39*, 125–142.

(13) (a) Newville, M. IFEFFIT: Interactive XAFS Analysis and FEFF Fitting. *J. Synchrotron Rad.* **2001**, *8*, 322–324. (b) Newville, M.; Livins, P.; Yacoby, Y.; Rehr, J. J.; Stern, E. A. Near-Edge X-Ray-Absorption Fine Structure of Pb: A Comparison of Theory and Experiment. *Phys. Rev. B: Condens. Matter Mater. Phys.* **1993**, *47*, 14126–14131.

(14) Ankudinov, A. L.; Ravel, B.; Rehr, J. J.; Conradson, S. D. Real-Space Multiple-Scattering Calculation and Interpretation of X-Ray-Absorption Near-Edge Structure. *Phys. Rev. B: Condens. Matter Mater. Phys.* **1998**, *58*, 7565–7576.

(15) Swanson, H. E.; Gilfrich, N. T.; Ugrinic, G. M. Standard X-ray Diffraction Powder Pattern. *National Bureau of Standards Circular (U. S.)* **1954**, *539*, 1–75.

(16) Coey, J. M. D. The Crystal Structure of Rh_2O_3. *Acta Crystallogr. B* **1970**, *26*, 1876–1877.

(17) (a) Yamamoto, S.; Senba, Y.; Tanaka, T.; Ohashi, H.; Hirono, T.; Kimura, H.; Fujisawa, M.; Miyawaki, J.; Harasawa, A.; Seike, T.; Takahashi, S.; Nariyama, N.; Matsushita, T.; Takeuchi, M.; Ohata, T.; Furukawa, Y.; Takeshita, K.; Goto, S.; Harada, Y.; Shin, S.; Kitamura, H.; Kakizaki, A.; Oshima M.; Matsuda, I. New Soft X-ray Beamline BL07LSU at SPring-8. *J. Synchrotron Radiat.* **2014**, *21*, 352−365. (b) Koitaya, T.; Yamamoto, S.; Shiozawa, Y.; Takeuchi, K.; Liu, R.-Y.; Mukai, K.; Yoshimoto, S.; Akikubo, K.; Matsuda, I.; Yoshinobu, J. Real-Time Observation of Reaction Processes of CO_2 on Cu(997) by Ambient-Pressure X-ray Photoelectron Spectroscopy. *Top. Catal.* **2016**, *59*, 526−531.

(18) Coduri, M.; Scavini, M.; Allieta, M.; Brunelli, M.; Ferrero, C. Local Disorder in Yttrium Doped Ceria ($Ce_{1-x}Y_xO_{2-x/2}$) Probed by Joint X-ray and Neutron Powder Diffraction. *J. Phys.: Conf. Ser.* **2012**, *340*, 012056.

(19) (a) Hwang, S.-J.; Choy, J.-H. Local Atomic Arrangement and Electronic Structure of Nanocrystalline Transition Metal Oxides Determined by X-ray Absorption Spectroscopy. *J. Phys. Chem. B* **2003**, *107*, 5791−5796. (b) Pantelouris, A.; Modrow, H.; Pantelouris, M.; Hormes, J.; Reinen, D. The Influence of Coordination Geometry and Valency on the K-edge Absorption Near Edge Spectra of Selected Chromium Compounds. *Chem. Phys.* **2004**, *300*, 13−22.

(20) (a) Biesinger, M. C.; Brown, C.; Mycroft, J. R.; Davidson, R. D.; McIntyre, N. S. X-ray Photoelectron Spectroscopy Studies of Chromium Compounds. *Surf. Int. Anal.* **2004**, *36*, 1550−1563. (b) Aronniemi, M.; Sainio, J.; Lahtinen, J. Chemical State Quantification of Iron and Chromium Oxides Using XPS: The Effect of the Background Subtraction Method. *Surf. Sci.* **2005**, *578*, 108−123.

(21) Abe, Y.; Kato, K.; Kawamura, M.; Sasaki, K. Rhodium and Rhodium Oxide Thin Films Characterized by XPS. *Surf. Sci. Spec.* **2001**, *8*, 117−125.

(22) Bianconi, A.; Marcelli, A.; Dexpert, H.; Karnatak, R.; Kotani, A.; Jo, T.; Petiau, J. Specific Intermediate-Valence State of Insulating 4f Compounds Detected by L_3 X-ray Absorption. *Phys. Rev. B: Condens. Matter Mater. Phys.* **1987**, *35*, 806−812.

(23) Mullins, D. R. The Surface Chemistry of Cerium Oxide. *Surf. Sci. Rep.* **2015**, *70*, 42−85.

(24) Kibis, L. S.; Svintsitskiy, D. A.; Derevyannikova, E. A.; Kardash, T. Y.; Slavinskaya, E. M.; Stonkus, O. A.; Svetlichnyi, V. A.; Boronin, A. I. From Highly Dispersed Rh^{3+} to Nanoclusters and Nanoparticles: Probing the Low-Temperature NO+CO Activity of Rh-Doped CeO_2 Catalysts. *Appl. Surf. Sci.* **2019**, *493*, 1055–1066.

(25) (a) Zhang, F.; Jin, Q.; Chan, S.-W. Ceria Nanoparticles: Size, Size Distribution, and Shape. *J. Appl. Phys.* **2004**, *95*, 4319−4326. (b) Zhou, K.; Wang, X.; Sun, X.; Peng, Q.; Li, Y. Enhanced Catalytic Activity of Ceria Nanorods from Well-Defined Reactive Crystal Planes. *J. Catal.* **2005**, *229*, 206−212.

Chapter 3

Catalytic property for NO reduction with CO of $Cr_{0.19}Rh_{0.06}CeO_z$ and elucidation of cooperative active sites of Cr and Rh

3.1. Introduction

3.1.1. NO reduction with CO

Exhaust gases from automobiles and industrial plants contain nitrogen oxides (NO_x), which are harmful to the environment and human health, and NO_x needs to detoxified at the emission stage.[1] The reduction reaction of NO, which converts NO to non-toxic N_2, is one of the fundamental reactions in exhaust gas purification and has been widely studied as a model reaction for exhaust gas catalysts.[2] For the NO reduction reaction, CO, hydrocarbons (HC), H_2, and NH_3 are used as reductants along with NO.[1] In particular, the reduction of NO with CO has been extensively studied as one of the most promising methods of the exhaust gas purification, because this reaction simultaneously converts two pollutants (NO and CO) into harmless gases (N_2 and CO_2) (Equation 3.1).[3] The NO reduction reaction with CO is mostly a stepwise reaction via N_2O greenhouse gas (Equations 3.2, 3.3), and unwanted N_2O byproducts are usually produced at low temperature. High N_2 selectivity at low temperatures (below 523 K), corresponding to the cold-start conditions of automobiles, is a key obstacle in the development of catalytic NO reduction, and it is thus necessary to develop a catalyst that can selectively reduce NO to N_2 without N_2O generation.[4]

$$NO + CO \rightarrow 1/2N_2 + CO_2 \qquad \Delta H_{298\ K} = -373\ kJ\ mol^{-1} \qquad \text{(Equation 3.1)}$$

$$2NO + CO \rightarrow N_2O + CO_2 \qquad \Delta H_{298\ K} = -381\ kJ\ mol^{-1} \qquad \text{(Equation 3.2)}$$

$$N_2O + CO \rightarrow N_2 + CO_2 \qquad \Delta H_{298\ K} = -365\ kJ\ mol^{-1} \qquad \text{(Equation 3.3)}$$

3.1.2. Ceria catalysts for NO reduction with CO

CeO_2 is an attractive oxide support with high oxygen mobility, and defects in CeO_2 have been reported to play an important role in selective NO reduction.[5] Recently reported ceria-based catalysts for NO reduction with CO were listed in Table 3.1. The addition of noble metals can also improve the NO reduction performance with CO. Among recently reported examples, CeO_2-supported catalysts incorporating Rh, Ru, or Pd exhibited good NO reduction performance at low temperatures.[3b,6] For example, small Rh_n^0 nanoparticles supported on CeO_2 mediated complete NO conversion without N_2O formation at approximately 423 K in a temperature-programmed reaction of NO and CO analyzed by FT-IR spectroscopy.[6b] Furthermore, $Ce_{0.95}Ru_{0.05}O_{2-\delta}$ solid solutions displayed complete NO conversion with 100% N_2 selectivity at 473 K,[6a] while Pd/CeO_2 catalysts pretreated with the reaction gas completely converted NO at 385 K and CO at 435 K.[3b] In addition, non-noble-metal species incorporated into CeO_2 as catalytically active sites improved the NO reduction performance with CO.[3a,7] For instance, $Ce_{20}M_1O_x$ composite oxides (M = Zr, Cr, Mn, Fe, Co, or Sn) improved NO reduction activity with CO due to increased specific surface area and surface oxygen defects of CeO_2, and Cr was reported to be a promising element for improving the activity of NO reduction on CeO_2： the Cr-doped ceria catalyst showed the best performance among the $Ce_{20}M_1O_x$ catalysts.[7] NiO/CeO_2 was reported to be capable of reducing NO at low temperatures below 473 K.[3a] From the above examples, Cr and Rh species and CeO_2 supports are good candidates for the NO reduction catalysts.

Table 3.1. Recently Reported Ceria-based Catalysts for NO Reduction with CO

Catalyst	Reaction conditions	Catalytic activity		Ref.
		Conversion	N_2 selectivity	
NiO/CeO_2 rod	NO = 1200 ppm, CO = 1200 ppm, 60000 mL h^{-1} g^{-1}	T_{100}(NO) = 427 K T_{100}(CO) = 528 K	——	(3a)
PdO/CeO_2 rod	NO = 1200 ppm, CO = 1200 ppm, 60000 mL h^{-1} g^{-1}	T_{100}(NO) = 408 K T_{100}(CO) = 451 K	——	(3b)
$Ce_{0.98}M_{0.02}O_2$ (M = Pd, Rh, Pt)	NO = 1% CO = 1%, 100 mL min^{-1}	T_{100}(NO) = 623 K (Rh), 633 K (Pd)	Rh: 100% (623 K) Pd: 100% (673 K)	(4)
$Ce_{20}M_1O_x$ (M = Zr, Cr, Mn, Fe, Co, Sn)	NO = 5% CO = 10%, 24000 mL h^{-1} g^{-1}	T_{100}(NO) = 573 K (Cr)	Cr: 80% (573 K), 100% (648 K)	(7)
$CuO/Ce_{20}M_1O_x$ (M = Zr, Cr, Mn, Fe, Co, Sn)	NO = 5% CO = 10%, 24000 mL h^{-1} g^{-1}	T_{100}(NO) = 548 K (Cr), 598 K (Sn)	Cr: 85% (548 K) Sn: 100% (598 K)	(10k)
Cr-Cu/CeO_2 (Cr/Cu = 3)	NO = 1500 ppm, CO = 1500 ppm, 120000 mL h^{-1} g^{-1}	NO conv. = 50% (523 K)	100% (523 K)	(10h)
$Cu_3Ce_{0.2}Al_{0.8}O_x$	NO = 5% CO = 10%, 50 mg, 12000 h^{-1}	T_{100}(NO) = 483 K	100% (493 K)	(10l)

3.1.3. Synergistic effects in the development of the NO reduction catalyst

Numerous heterogeneous catalysts for the reduction of NO with CO have been extensively developed from the viewpoint of synergistic effect/cooperative effect introduction, such as metal alloying,[8] single-atomic dispersion,[9] the addition of multiple oxide species,[10] and combination of metal and metal oxide species,[11] etc. In addition to the ceria-based oxides listed in Table 3.1, non-ceria-based catalysts with this effect were listed in Table 3.2.

Alloying multiple metal species is one of the direct strategies modulating the electronic and coordination structure of single metal species.[12] Tuning electronic structure and increasing a number of surface active sites benefits to enhancing catalytic activity and selectivity, and this effect is also possible to achieved with metal alloy species on the support surface.[12] For instances, $Pd(In_{0.33}Cu_{0.67})/Al_2O_3$,[8a] a CsCl-type pseudobinary alloy catalyst with the partial replacement of Cu by In in PdCu alloy, improved the catalytic activity and N_2 selectivity for NO reduction with CO (100% yield) at low temperature of 473 K by the combined effects of In and Cu: the incorporated In species facilitate CO oxidation to provide more active sites for N_2O decomposition, and Cu species promotes adsorption and subsequent dissociation of NO.[8a] Single-atom alloys (*e.g.*, Cu_5Pd_1/Al_2O_3[9a] and Rh_1Co_3/CoO[9b]) are unique catalysts that atomically isolate active metal species within metal nanoclusters/nanoparticles, and exhibited significant NO conversion and N_2 selectivity even compared to their alloyed nanoparticle counterparts. In Cu_5Pd_1/Al_2O_3, it is reported that isolated Pd promoted N–O bond cleavage of the $(NO)_2$ dimer, resulting in excellent N_2 selectivity.[9a] Rh_1Co_3/CoO had isolated Rh_1Co_3 clusters and the bimetallic sites strongly adsorbed N_2O intermediate and easily dissociate N_2O to N_2.[9b] In these cases, metal alloying or single-atomic dispersion lowers activation barriers and/or strongly adsorbs NO and intermediate N_2O, improving NO conversion and N_2 selectivity.

Mixed metal oxides doped with two or more different metal ion species in the base oxides are also effective for catalysis.[1d,e] Although there are no direct interaction between metal ion species, the doped metal ions can also establish multiple adsorption metal sites on the surface,[1d,e] and in this sense, the concept of the mixed metal oxides are similar to metal alloy catalysts. Furthermore, redox-active metal ion dopants can also increase labile oxygen species and oxygen vacant sites on the surface of mixed metal oxides, and these active oxygen species/oxygen vacant sites play an important role in enhancing catalytic performances,[13] even in NO reduction[6a-f] (*e.g.*, $Ce_{0.78}Sn_{0.2}Pd_{0.2}O_{2-\delta}$[6c], CuO-$Mn_2O_3/Al_2O_3$[6e]). Cr-$Cu/CeO_2$[6g–i] is a catalyst with Cu^+ and Cr^{3+} sites co-embedded on CeO_2 surface, and it was reported that the larger amount of Cr than Cu increased the

surface concentration of active Cu^{+} as CO adsorption sites and Ce^{3+} as NO adsorption sites on the surface of CeO_2, resulting in superior catalytic activity to Cu/CeO_2 catalysts without Cr species.[6e,g] $Cu_{0.05}Ni_{0.95}Al_{1.8}Cr_{0.2}O_4$ is a single-phase ternary spinel solid solution, and partial substitution of Cr^{3+} with Al^{3+} improves a specific surface area of the catalyst and increases the ratio of Cu^{+} to total Cu on the surface as CO adsorption sites, enhancing NO reduction activities without phase separation under dry and wet simulated exhaust gas streams.[6h] PdO–CeO_2/OMS-2 (cryptomelane-type manganese oxide) exhibited excellent catalytic NO reduction performance (>95% conversion and 100% N_2 selectivity at ca. 523 K) with significant resistance toward poisoning by SO_2.[6r] I also mentioned several examples of ceria-based catalysts in Chapter 2.

The addition of 2nd metal species to oxide-supported metal catalysts can create unique active species through the synergistic interaction between interfaces of metal species and metal oxide species.[14] An Au-FeO_x/TiO_2 catalyst[11a] prepared by the subsequent impregnation of FeO_x species on Au nanoparticles supported on TiO_2 exhibited high NO conversion of 84.4% and N_2 selectivity of 90.6% at 523 K. Although the addition of FeO_x to Au/TiO_2 did not cause the structural change of Au species itself, it was reported that interfaces of Au surface with FeO_x and a TiO_2 support created new adsorption sites for NO and CO and a new surface complex between NO and CO.[11a] Rh@NbO_x[11b] and Ni@NbO_x[11c] catalysts generated from Rh_3Nb and Ni_3Nb intermetallic precursors are unique materials enhancing catalytic performances through cooperation of metal species and metal oxide species. They efficiently catalyzed the selective reduction of NO to N_2 without N_2O generation above 573 K and 698 K, respectively, and the NbO_x matrix could cleave adsorbed NO by forming of N–Nb bonds at the metal-NbO_x interface.[11b,c]

Table 3.2. Recently Reported Non-Ceria-Based Catalysts for NO Reduction with CO

Catalyst	Reaction conditions	Catalytic activity		Ref.
		Conversion	N_2 selectivity	
$Pd(In_{0.33}Cu_{0.67})/Al_2O_3$	NO = 5000 ppm, CO = 5000 ppm, 48000 mL h^{-1} g^{-1}	T_{100}(NO) = 473 K	100 % (>448 K)	(8a)
$Cu\text{-}Ru/Al_2O_3$	NO = 0.09% CO = 0.1%, 180000 mL h^{-1} g^{-1}	T_{100}(NO) = 573 K		(8j)
Cu_5Pd/Al_2O_3	NO = 0.5% CO = 0.5%, 108000 mL h^{-1} g^{-1}	T_{100}(NO) = 473 K	100% (473 K)	(9a)
Rh_1Co_3/Co_3O_4	NO = 5% CO = 5%, 360000 mL h^{-1} g^{-1}	T_{100}(NO) = 523 K	100% (>383 K)	(9b)
$CuO\text{-}Mn_2O_3/Al_2O_3$	NO = 5% CO = 10%, 25 mg, 24000 h^{-1}	68% (573 K)	82% (573 K)	(10e)
$CuO\text{-}V_2O_5/Al_2O_3$	NO = 5% CO = 10%, 24000 mL h^{-1} g^{-1}	36% (623 K)	80% (623 K)	(10f)
$Au\text{-}FeO_x/TiO_2$	NO = 0.2% CO = 0.2%, 30000 mL h^{-1} g^{-1}	91.0% (523 K)	74.2% (523 K)	(11a)
Ni_3Nb/NbO_x	NO = 1% CO = 1%, 6000 mL h^{-1} g^{-1}	T_{100}(NO) = 698 K	100% (698 K)	(11c)

3.1.4. The aim of this research

In this chapter, I focused on catalytic activity of a Cr and Rh-incorporated ceria catalysts ($Cr_{0.19}Rh_{0.06}CeO_z$) for the NO reduction with CO.[15] In terms of synergistic effect strategies, $Cr_{0.19}Rh_{0.06}CeO_z$ with dispersed CrO_{3-x} nanodomains and $Rh^{3+\delta}$ species on the surface of CeO_2 has a potential to exhibit high NO reduction activity. The incorporation of Cr oxide not only had a great influence on the remarkable redox property of $Cr_{0.19}Rh_{0.06}CeO_z$, but also played a key role in accelerating NO reduction catalysis with CO. $Cr_{0.19}Rh_{0.06}CeO_z$ exhibited the complete reduction of NO to N_2 with CO at low temperature of 473 K. *In situ* FT-IR spectroscopy clarified that the dispersion of the catalytically active Rh species as $Rh^{3+\delta}$ on the oxide catalyst surface assisted by the added Cr oxide increased the number of adsorption sites for NO and CO. *In situ* XAFS characterization revealed the formed Cr oxide positively contributed to oxygen transfer as an oxygen mediator from the adsorbed NO to the adsorbed CO on Rh, resulting in decreasing an activation energy for the NO reduction. The incorporation of the Cr oxide not only modulated the structure of Rh species in $Cr_{0.19}Rh_{0.06}CeO_z$ to generate co-active sites effectively, but also positively involved in the enhancement of the NO reduction performance with CO at low temperature.

3.2. Experimental section

3.2.1. Materials and instruments

Chemicals for the preparation of $Cr_{0.19}Rh_{0.06}CeO_z$, $Rh_{0.04}CeO_z$, $Cr_{0.17}CeO_z$, and CeO_2 were purchased from Sigma-Aldrich and Wako Chemicals. The preparation procedure of $Cr_{0.19}Rh_{0.06}CeO_z$, $Rh_{0.04}CeO_z$, $Cr_{0.17}CeO_z$, and CeO_2 was indicated in Section 2.2.2. NO (99%), CO (G1 grade, 99.95%), N_2O (99.9%), N_2 (G1 grade, 99.9995%), CO_2 (G1 grade, 99.995%), He (G1 grade, 99.99995%), and Ar (G3 grade, 99.999%) gases were used for the experiments of NO reduction with CO. O_2 (O_2, G1 grade, 99.99995%), NO (99%), ^{12}CO (G1 grade, 99.95%), ^{13}CO (99 atom% ^{13}C, 99.93 atom% ^{16}O, ISOTEC) gases were used for *in situ* FT-IR measurement. NO (99%), CO (G1 grade, 99.95%), and N_2 (99.9%) gases were used for *in situ* XAFS measurements.

A high-vacuum glass line with dry N_2 and a glove box with dry Ar were used for experiments under inert conditions.

3.2.2. NO reduction reaction with CO

NO reduction with CO was performed in a home-made fixed-bed flow reactor (I.D.: 7 mm) (Figure 3.1). The catalyst (500 mg) was first exposed to a He flow (100 mL min^{-1}) at 573 K for 1 h. The reaction was then performed under the flow of NO (0.5%), CO (1.0%), Ar (5.0%, internal standard), and He (balance) with a total flow rate of 100 mL min^{-1} (GHSV = 6500 h^{-1}). The gases were analyzed using an online gas chromatograph equipped with a thermal conductivity detector (TCD; GC-8, Shimadzu) and a ShinCarbon ST column (Shimadzu, 3 mm (I.D.) × 8 m) located downstream. TCD-GC conditions were listed in Table 3.3. Compositions of the outlet gases were estimated form standard curves as shown in Figure 3.2. The durability test was conducted under similar conditions at 473 K for 216 h. The NO reduction with CO over catalysts (50 mg) on high GHSV was also performed under the flow of NO (0.5%), CO (1.0%), Ar (5.0%), and He (balance), total flow rate 100 mL min^{-1} (GHSV = 65,000 h^{-1})).

NO/CO partial pressure dependencies on the initial reaction rates were measured by varying the NO concentration between 0.3% and 1.0% with the CO concentration fixed at 1.0% or varying the CO concentration between 0.3% and 1.0% with the NO concentration fixed at 0.5%. The reaction temperature was maintained for the kinetic study at 413 K, such that the NO conversion did not exceed 30%, or at 453 K, such that NO conversion to N_2 did not exceed 20 %. The activation energies for the NO reduction with CO were estimated under the conditions that the NO conversion did not exceed 30%: catalyst 10 mg, NO (0.5%), CO (1.0%), Ar (5.0%), and He (balance), total flow rate 100 mL min^{-1} (GHSV = 325,000 h^{-1}).

N_2O reduction with CO was also conducted in the fixed-bed flow reactor. The catalyst (50 mg) was first exposed to He flow (100 mL min^{-1}) at 573 K for 1 h. The reaction was then performed under a flow of N_2O (0.5%), CO (1.0%), Ar (5.0%, internal standard), and He (balance) with a total flow rate of 100 mL min^{-1} (GHSV = 65,000 h^{-1}).

In these reactions, nitrogen balance and carbon balance were kept above 0.9. NO conversion, N_2 selectivity, N_2O selectivity, and N_2O conversion were calculated using Equations 3.4-3.7:

$$\text{NO conversion (\%)} = \frac{[\text{NO}]_{\text{inlet}} - [\text{NO}]_{\text{outlet}}}{[\text{NO}]_{\text{inlet}}} \times 100\% \quad \text{(Equation 3.4)}$$

$$\text{N}_2\text{ selectivity \%} = \frac{[\text{N}_2]_{\text{outlet}}}{[\text{N}_2]_{\text{outlet}} + [\text{N}_2\text{O}]_{\text{outlet}}} \times 100 \quad \text{(Equation 3.5)}$$

$$\text{N}_2\text{O selectivity \%} = \frac{[\text{N}_2\text{O}]_{\text{outlet}}}{[\text{N}_2]_{\text{outlet}} + [\text{N}_2\text{O}]_{\text{outlet}}} \times 100 \quad \text{(Equation 3.6)}$$

$$\text{N}_2\text{O conversion (\%)} = \frac{[\text{N}_2\text{O}]_{\text{inlet}} - [\text{N}_2\text{O}]_{\text{outlet}}}{[\text{N}_2\text{O}]_{\text{inlet}}} \times 100\% \quad \text{(Equation 3.7)}$$

$[X]_{inlet}$: the molar flow rate of X at the gas inlet

$[X]_{outlet}$: the molar flow rate of X at the gas outlet

The reaction rates for NO conversion (r_{NO}) and N_2 formation (r_{N2}) were calculated using Equations 3.8 and 3.9:

$$r_{NO} = ([NO]_{inlet} - [NO]_{outlet})/w_{cat} \quad \text{(Equation 3.8)}$$

$$r_{N2} = [N_2]_{outlet}/w_{cat} \quad \text{(Equation 3.9)}$$

w_{cat}: the weight of a catalyst

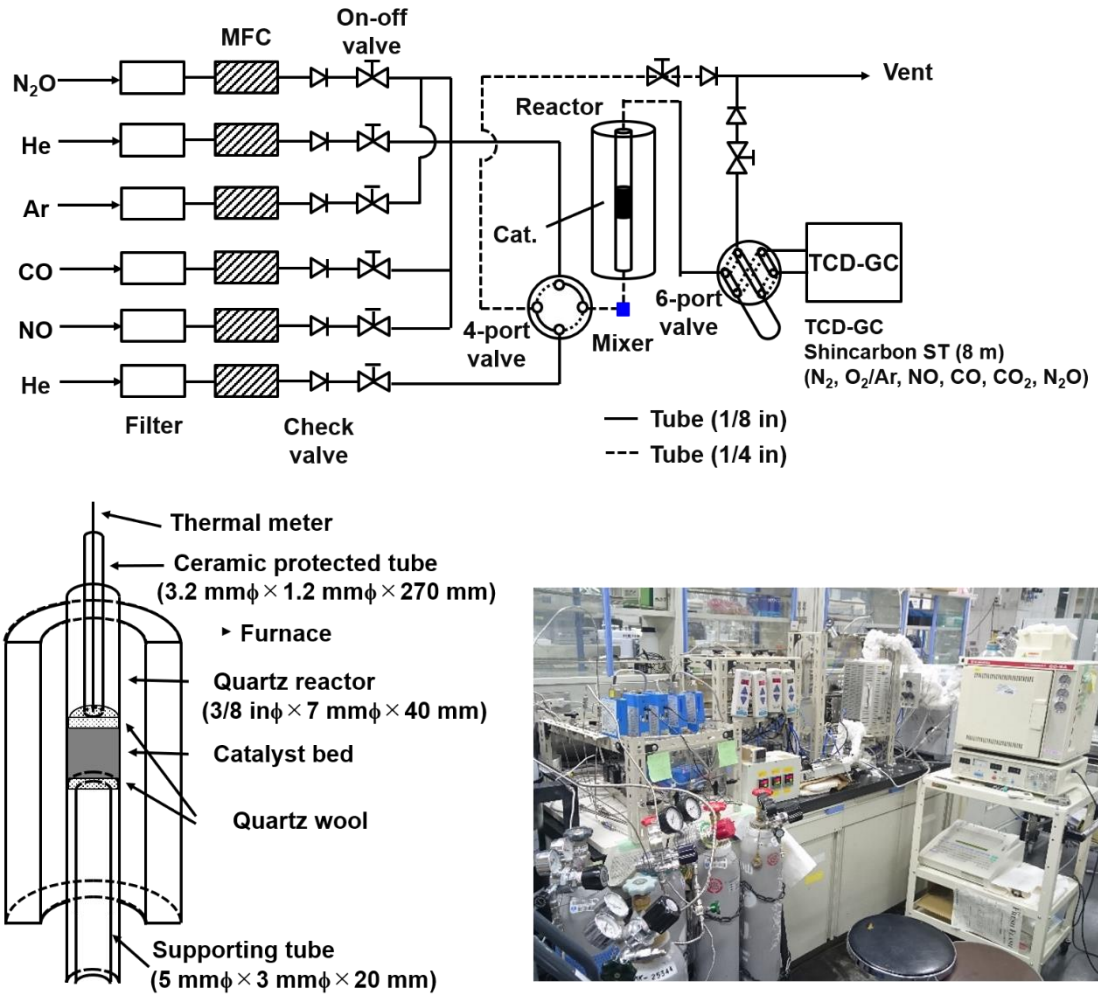

Figure 3.1. Schematic illustrations of a flow-line system and a reactor for NO reduction with CO.

Table 3.3. TCD-GC Conditions with the Flow Reactor (Shimadzu GC-8A)

Column1	SHINCARBON ST	Inj. Temp.	473 K
	(4 mmϕ×3 mmϕ×8 m)	Det. Temp.	473 K
Column2	Blank column	Column Temp.	333 K (17 min)
	(4 mmϕ×3 mmϕ×3 m)		→473 K
Carrier gas (Column1)	He (350 kPa)	Program rate	20 K min^{-1}
Carrier gas (Column2)	He (140 kPa)	Current	160 mA
		Attenuation	1

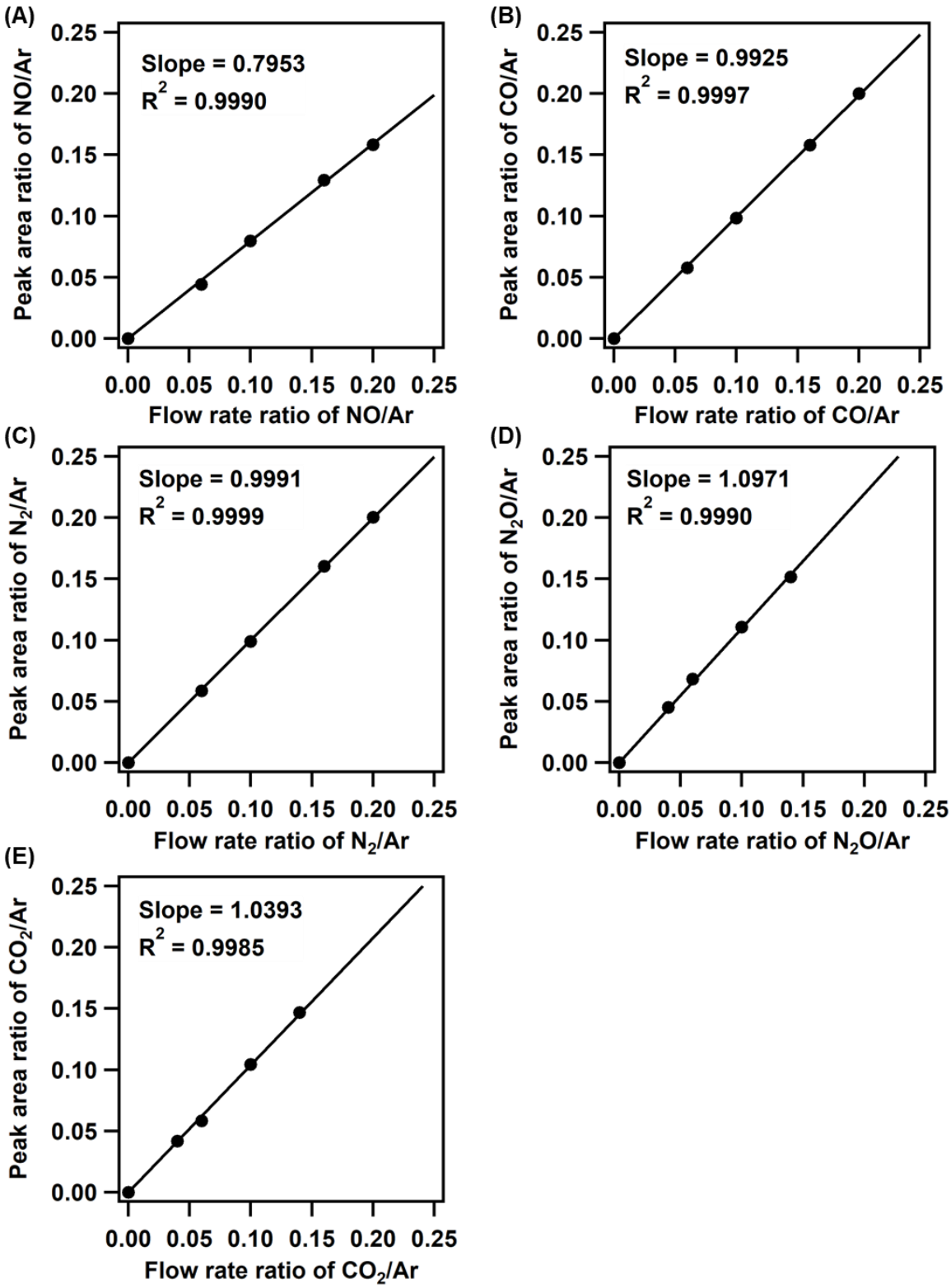

Figure 3.2. Standard curves of (A) NO, (B) CO, (C) N_2, (D) N_2O, and (E) CO_2.

3.2.3. *In situ* spectroscopic characterizations for the NO reduction with CO

***In situ* FT-IR**

In situ FT-IR spectra after the adsorption of CO and/or NO were measured on an FT/IR-6100FV spectrometer (JASCO) equipped with a double-beam unit (DB-6000) and a mercury cadmium telluride (MCT) detector in the transmission mode at a resolution of 4 cm^{-1} with 32 scans. The samples (40 mg) were mixed with silica (Aerosil 300, Nippon Aerosil Co. Ltd., 160 mg) and a sample/silica ratio was 1/4 (w/w). The mixture was pressed into a disk (5 mg cm^{-2}) and set in a quartz batch cell with CaF_2 windows. A silica disk (Aerosil 300, 4 mg cm^{-2}) was used as a reference for the double-beam IR measurement.

The sample and reference were pretreated at 573 K for 1 h under O_2 (26.7 kPa). The temperature was then decreased to 473 K and CO (5.3 kPa) was introduced into the cells and the cell was evacuated after 30 min, and the first FT-IR spectra were measured. After 10 min later, NO (5.3 kPa) was introduced to the evacuated cell. After 30 min in the presence of NO, the cell was again evacuated and the second FT-IR spectra were measured. After the evacuation of NO for 10 min, CO (5.3 kPa) was re-introduced. After 30 min on the exposure of CO, the cell was again evacuated and the third FT-IR spectrum was recorded. Temperature-time protocol for this experiment is shown in Figure 3.3.

In situ FT-IR spectra after the adsorption of ^{13}CO and the exchange of ^{12}CO were measured as follows. After the similar pretreatment, the cell temperature was decreased to room temperature, and ^{13}CO (5.3 kPa) was firstly introduced into the cells. After 30 min, the cell was evacuated and the first FT-IR spectrum was measured. After the evacuation of CO for 10 min, ^{12}CO (5.3 kPa) was reintroduced. After 30 min in the presence of ^{12}CO, the cell was again evacuated and the second FT-IR spectrum was measured.

For the reaction with CO and NO, the cell temperature was decreased to room temperature after the pretreatment, and CO (5.3 kPa) and NO (2.7 kPa) were co-introduced into the cells. The cell temperature was then increased to 473 K, and FT-IR spectra were collected in the cell atmosphere at the target temperature.

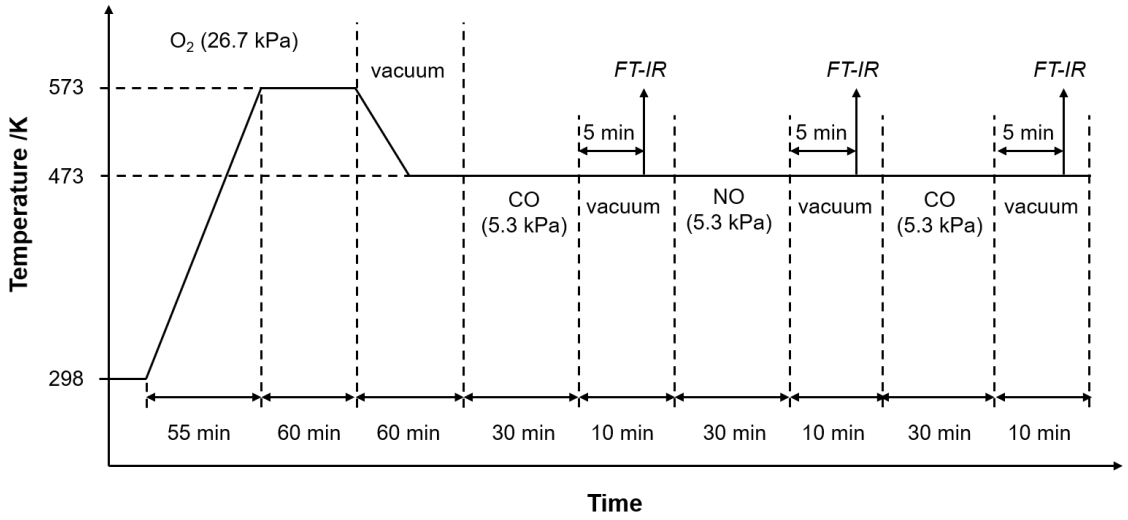

Figure 3.3. Temperature-time protocol for *in situ* FT-IR measurement after the adsorption of CO or NO.

***In situ* XAFS**

In situ quick XAFS (QXAFS) measurements during reaction with CO and/or NO were performed at the Photon Factory at KEK-IMSS as follows. A sample was pelletized into a disk in a ring-shaped cell and placed in an *in situ* XAFS cell placed in an experimental setup as shown in Figure 3.4. After pretreatment with N_2 (100 mL min^{-1}) at 573 K for 1 h (heating rate: 5 K min^{-1}), the cell temperature was decreased to 473 K under N_2 flow (100 mL min^{-1}) for 60 min. After 10 min, the QXAFS measurement was started. After 5 min, the gas was changed to CO + N_2 (5 + 95 mL min^{-1}) and the gas flow was held for 30 min. After 10 min, the cell was flushed with N_2 (100 mL min^{-1}) for 20 min. Next, the gas was changed to NO + N_2 (5 + 95 mL min^{-1}) and the gas flow was held for 30 min. The gas was then changed to N_2 (100 mL min^{-1}) and the cell was cooled to room temperature. Temperature-time protocol for this experiment under the flow of CO or NO is shown in Figure 3.5.

In the treatment with both CO and NO, CO + NO + N_2 (5 + 5 + 90 mL min^{-1}) was used after the pretreatment with the same QXAFS protocol. Temperature-time protocol for this experiment under the reaction with mixed gases of CO and NO is shown in Figure 3.6. Analysis methods of the obtained spectra are described in Section 2.2.1.

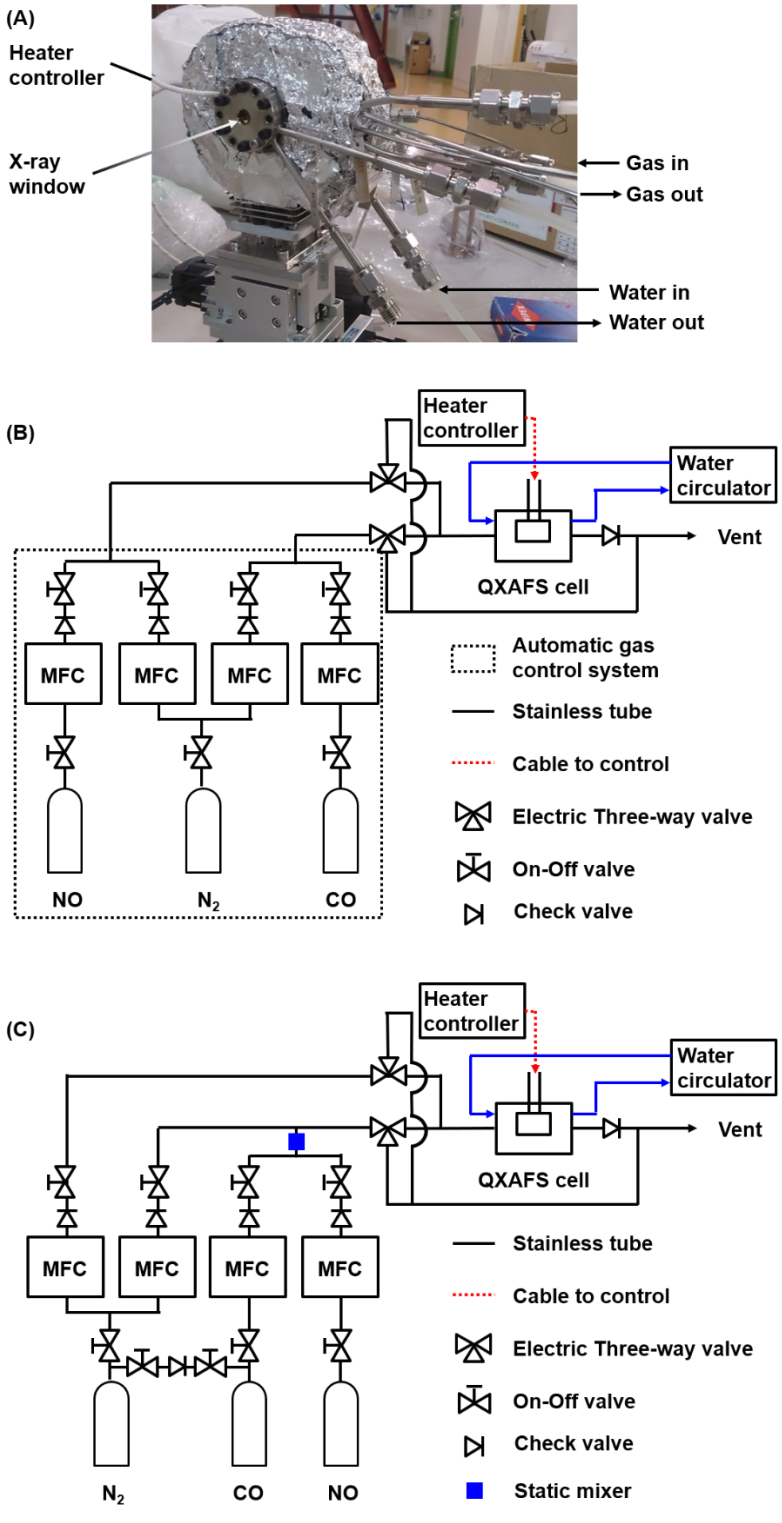

Figure 3.4. (A) An *in situ* QXAFS cell (KEK-PF). *In situ* XAFS setups (B) under CO flow/NO flow and (C) under the reaction with mixed gases of CO and NO.

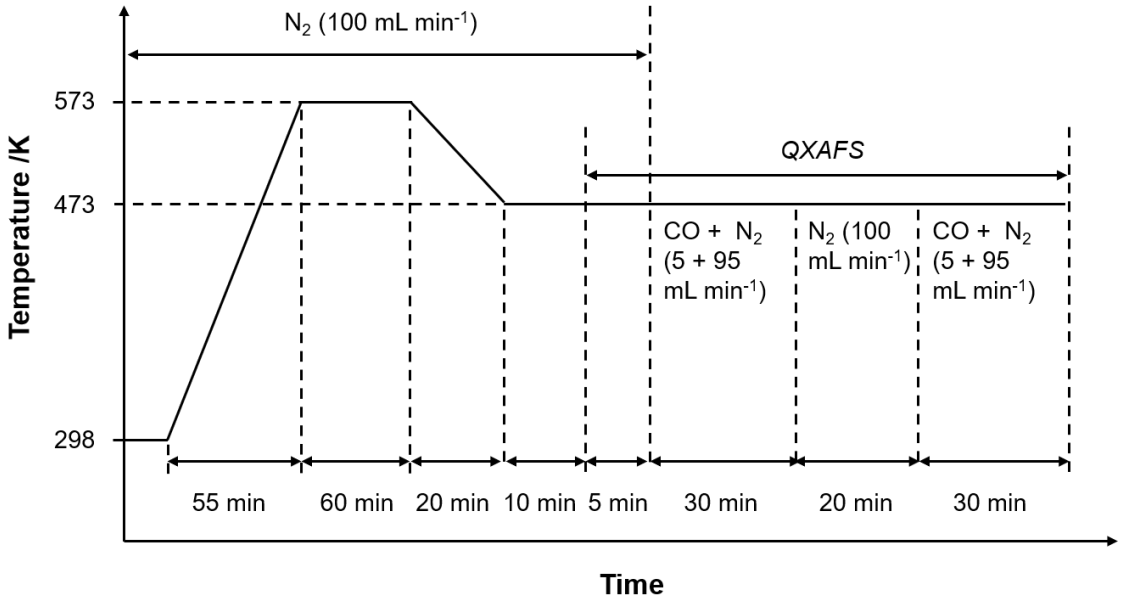

Figure 3.5. Temperature-time protocol for *in situ* XAFS measurement under the successive flow of CO and NO.

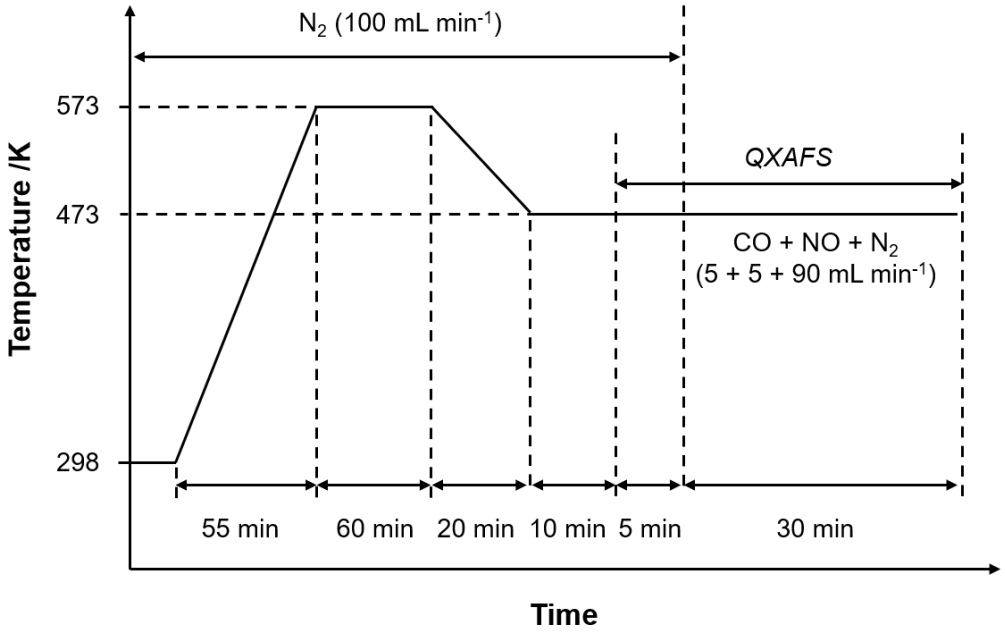

Figure 3.6. Temperature-time protocol for *in situ* XAFS measurement under the reaction with the mixed gases of CO and NO.

3.2.4. Product detection experiments with successive CO and NO treatment

Product detection experiments with successive CO and NO treatment were performed in a closed glass reactor equipped with a gas circulation unit, pressure gauge, and gas chromatograph fitted with a TCD (GC-8, Shimadzu) and a ShinCarbon ST column (Shimadzu, 3 mm (I.D.) × 2 m) as shown in Figure 3.7. After loading $Cr_{0.19}Rh_{0.06}CeO_z$ (500 mg) into the reactor, the system was kept under vacuum for 30 min. The sample was then pretreated with O_2 (26.7 kPa) at 573 K for 1 h. Next, the reactor was evacuated and the temperature was decreased to 473 K. After 30 min, CO (16 kPa, 1.0 mmol, molar ratio of CO:Cr:Rh = 6:3:1) was introduced into the reactor (defined as 0 min) and the gases were analyzed using the TCD at appropriate intervals. After an additional 30 min, the reactor was evacuated, NO (16 kPa, 1.0 mmol, molar ratio of NO:Cr:Rh = 6:3:1) was introduced (defined as 0 min), and the gases were again analyzed using the TCD at appropriate intervals. This reaction cycle using CO was repeated one more time. Temperature-time protocol for this experiment is shown in Figure 3.8. TCD-GC conditions are listed in Table 3.4.

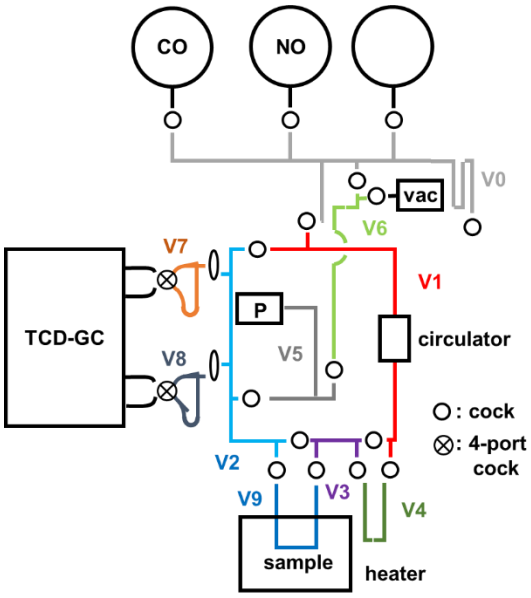

Figure 3.7. A schematic diagram for quantitative NO reduction with CO.

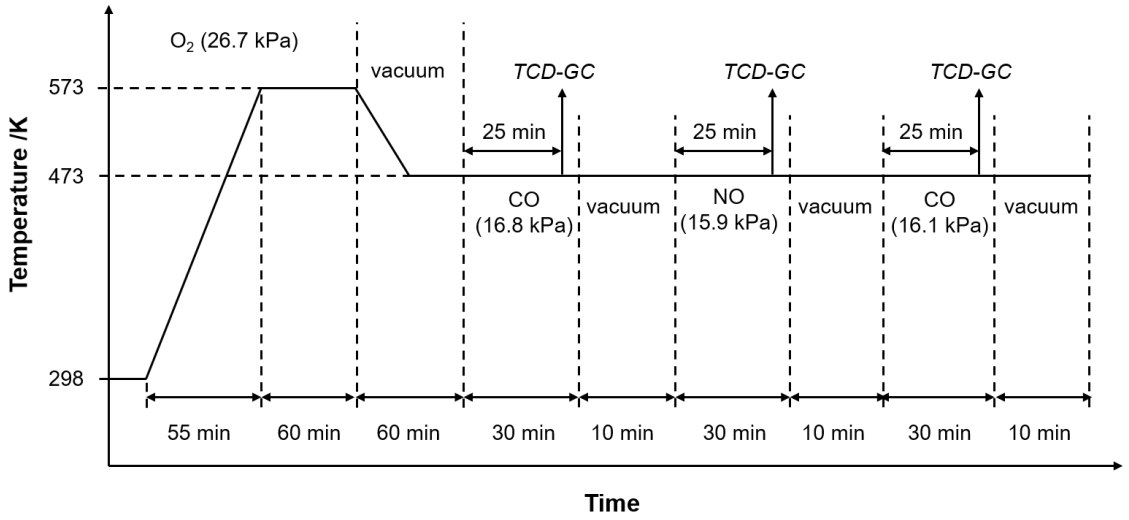

Figure 3.8. Temperature-time protocol for product detection experiments with successive CO and NO treatment on $Cr_{0.19}Rh_{0.06}CeO_z$.

Table 3.4. TCD-GC Conditions (GC-8A, Shimadzu)

Column1	SHINCARBON-ST	Inj. Temp.	383 K
	(4mmϕ×3mmϕ×2m)	Det. Temp.	383 K
Column2	PorapakT 80-100	Column Temp.	333 K
	(4mmϕ×3mmϕ×2m)	Current	100 mA
Carrier gas	He (180 kPa, 50 mL min^{-1})	Attenuation	1

3.2.5. Structural characterization after the reaction

After the durability test for NO reduction with CO of $Cr_{0.19}Rh_{0.06}CeO_z$ as described in Section 3.2.2, the used catalyst was collected in the air. The collected catalyst was characterized by XRD and HAADF-STEM-EDS/EELS. The measurement conditions of XRD and HAADF-STEM-EDS/EELS are the same as described in Section 2.2.3.

3.3. Results and discussions

3.3.1. The reduction of NO with CO on the highly dispersed rhodium species in $Cr_{0.19}Rh_{0.06}CeO_z$

The catalytic performances over $Cr_{0.19}Rh_{0.06}CeO_z$ with the dispersed Rh species were investigated for NO reduction with CO. The NO reduction reactions were conducted in a flow reactor system and the catalytic performances were evaluated compared to $Rh_{0.04}CeO_z$, $Cr_{0.17}CeO_z$, and CeO_2 as shown in Figure 3.9 (Conditions: NO (0.5%), CO (1.0%), Ar (5.0%), and He (balance), total flow rate 100 mL min^{-1} (GHSV = 6,500 h^{-1})). $Cr_{0.19}Rh_{0.06}CeO_z$ exhibited the remarkable catalytic activity for NO reduction even at 373 K, where the other catalysts were inactive. Among the catalysts, $Cr_{0.19}Rh_{0.06}CeO_z$ afforded > 99% of NO conversion at the lowest temperature (393 K), compared with $Rh_{0.04}CeO_z$ (413 K), $Cr_{0.17}CeO_z$ (513 K), and CeO_2 (> 573 K) (Figure 3.9 (A)). The N_2 selectivity of $Cr_{0.19}Rh_{0.06}CeO_z$ increased with increasing the reaction temperature, reaching > 99% at 473 K, while N_2 selectivities of $Cr_{0.17}CeO_z$, $Rh_{0.04}CeO_z$, and CeO_2 were only 51%, 56%, and *ca.* 0%, respectively (Figure 3.9 (B)). The only nitrogen by-product was N_2O, and the selectivity profiles in the temperature range of 298–573 K was shown in Figure 3.10. The NO conversions and N_2 selectivities on other reported ceria-based catalysts are summarized in Table 3.6.

NO reduction performances on high GHSV (65,000 h^{-1}) were also evaluated, and the results were presented in Figure 3.11 (Conditions: NO (0.5%), CO (1.0%), Ar (5.0%), and He (balance), total flow rate 100 mL min^{-1} (GHSV = 65,000 h^{-1})). $Cr_{0.19}Rh_{0.06}CeO_z$ also exhibited the significant NO reduction performances among the prepared catalysts under the high GHSV conditions; *e.g.,* the N_2 selectivity at 573 K on $Cr_{0.19}Rh_{0.06}CeO_z$ was > 99%, while those on $Cr_{0.17}CeO_z$, $Rh_{0.04}CeO_z$, and CeO_2 were 51%, 61%, and 34%, respectively. N_2O is proposed to be one of the typical intermediates as by-products of NO reduction[4,10b,e] and the reduction of N_2O with CO were also evaluated over $Cr_{0.19}Rh_{0.06}CeO_z$ (Conditions: N_2O (0.5%), CO (1.0%), Ar (5.0%), and He (balance), total flow rate 100 mL min^{-1} (GHSV = 65,000 h^{-1})). N_2O was efficiently converted to N_2 over $Cr_{0.19}Rh_{0.06}CeO_z$: the N_2O conversion at 473 K on $Cr_{0.19}Rh_{0.06}CeO_z$, $Cr_{0.17}CeO_z$, $Rh_{0.04}CeO_z$, and CeO_2 was 27%, 7%, 10%, and 0%, respectively (Figure 3.12). Reaction rates of N_2 formation from NO and N_2O were 2.0 and 2.1 μmol g^{-1} s^{-1}, and their comparable values indicated that the NO conversion to N_2 proceeded via the production of N_2O over $Cr_{0.19}Rh_{0.06}CeO_z$. The efficient conversion from N_2O to N_2 was suggested to be one of the factors contributing to the N_2 production efficiency on $Cr_{0.19}Rh_{0.06}CeO_z$.

The $Cr_{0.19}Rh_{0.06}CeO_z$ catalyst significantly decreased the activation energy of the NO

reduction with CO to 31.7 kJ mol^{-1}, which was lower than the activation energies on $Rh_{0.04}CeO_z$ (53.4 kJ mol^{-1}) and $Cr_{0.17}CeO_z$ (66.4 kJ mol^{-1}) (Figure 3.13). Reported activation energies on other ceria-based catalysts are summarized in Table 3.7. A similar activation energy to $Rh_{0.04}CeO_z$ was reported (*ca.* 54 kJ mol^{-1}) on the oxygen vacant sites of CeO_2 in Rh_n^0/CeO_2, suggesting that the rate-determining step was the dissociation step of NO on the adsorption sites of the oxygen vacancies.[6b,8e] The lower activation energy on $Cr_{0.19}Rh_{0.06}CeO_z$ (31.7 kJ mol^{-1}) indicates changes in the rate-determining step on the catalyst caused by the dispersed Rh species and the incorporated Cr. The reaction orders of NO and CO on $Cr_{0.19}Rh_{0.06}CeO_z$ were 1 and 0, respectively (Figure 3.14), suggesting that reaction of NO was involved in the rate-determining step of the reduction of NO to N_2.

Durability test for the NO reduction on $Cr_{0.19}Rh_{0.06}CeO_z$ at 473 K was performed as presented in Figure 3.15. The remarkable durability for the NO reduction was observed, and quantitative NO conversion (> 99%) and high N_2 selectivity (> 99%) were kept for the next 216 h, although NO was converted to N_2 incompletely (65%) in the first 10 min of the time-on-stream. The XRD patterns and HAADF-STEM-EELS/EDS images of $Cr_{0.19}Rh_{0.06}CeO_z$ after the NO reduction at 473 K for 216 h indicated negligible structural changes in the catalyst as displayed in Figures 3.16-17. Similar XRD patterns of the CeO_2 fluorite structure were observed before and after the catalytic reaction (Figure 3.16). The HAADF-STEM-EELS/EDS mappings clarified that the Cr and Rh species dispersed as the nanodomains of approximately 1 nm without large agglomeration after the reaction (Figure 3.17), indicating the structural stability for the catalytic durability of the $Cr_{0.19}Rh_{0.06}CeO_z$ catalyst under the NO reduction conditions.

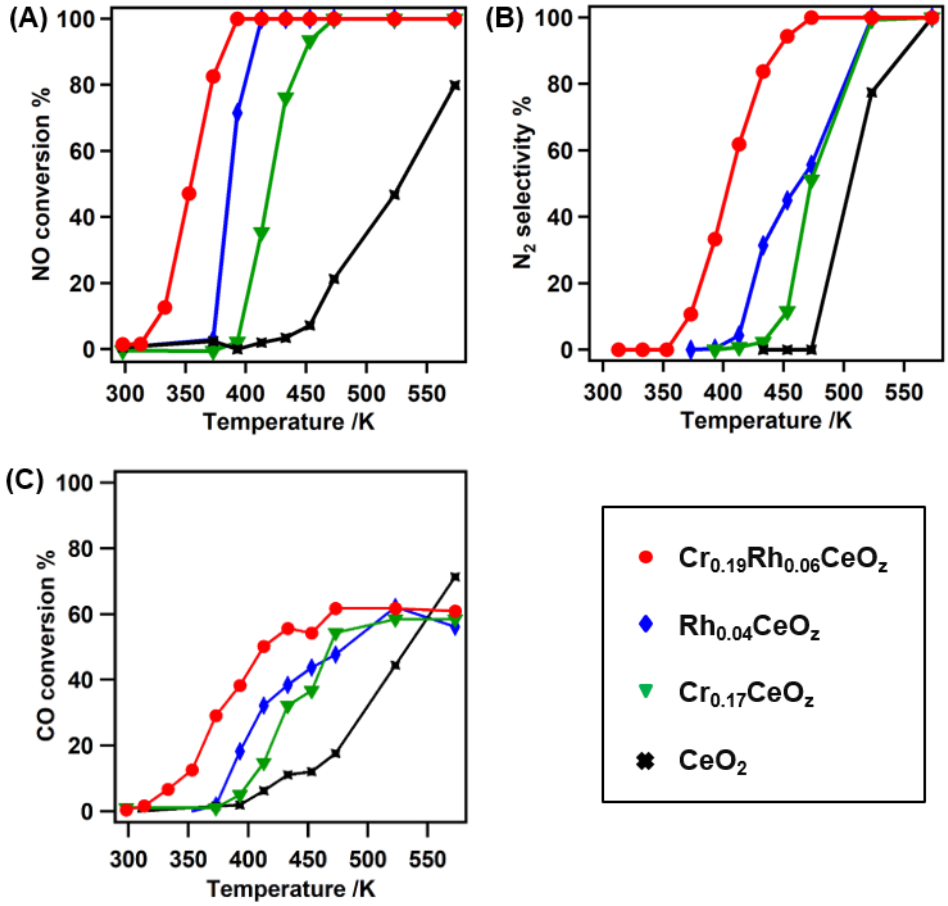

Figure 3.9. (A) NO conversion, (B) N_2 selectivity, and (C) CO conversion for NO reduction with CO over $Cr_{0.19}Rh_{0.06}CeO_z$, $Rh_{0.04}CeO_z$, $Cr_{0.17}CeO_z$, and CeO_2.[15] Conditions: catalyst 500 mg, NO (0.5%), CO (1.0%), Ar (5.0%), and He (balance), total flow rate 100 mL min^{-1} (GHSV = 6,500 h^{-1}).

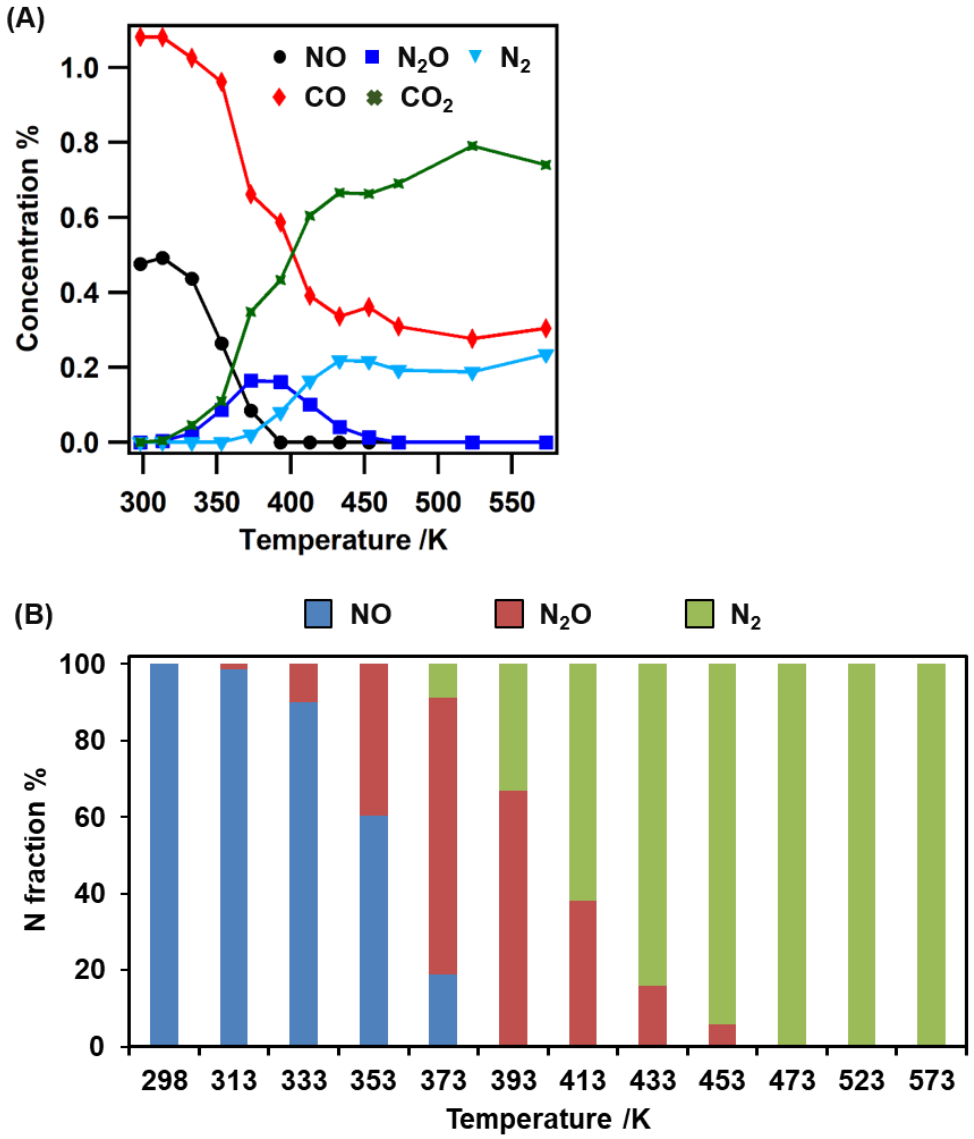

Figure 3.10. (A) The concentrations of the reaction products and (B) the N_2 selectivity profiles for NO reduction with CO over $Cr_{0.19}Rh_{0.06}CeO_z$ in the temperature range of 298-573 K.[15] Conditions: catalyst 500 mg, NO (0.5%), CO (1.0%), Ar (5.0%), and He (balance), total flow rate 100 mL min^{-1} (GHSV = 6,500 h^{-1}).

Table 3.5. NO Conversion, N_2 Selectivity, N_2O Selectivity, and Mass Balance of N for the NO Reduction with CO over $Cr_{0.19}Rh_{0.06}CeO_z$, $Rh_{0.04}CeO_z$, $Cr_{0.17}CeO_z$, and CeO_2 at 473 K

Catalyst	NO conversion %	N_2 selectivity %	N_2O selectivity %	Mass balance of N
$Cr_{0.19}Rh_{0.06}CeO_z$	>99	100	0	0.93
$Cr_{0.17}CeO_z$	>99	51	49	1.01
$Rh_{0.04}CeO_z$	>99	56	44	0.93
CeO_2	19	0	100	1.01

Reaction conditions: catalyst 500 mg, NO (0.5%), CO (1.0%), Ar (5.0%), and He (balance), total flow rate 100 mL min^{-1} (GHSV = 6,500 h^{-1}).

Table 3.6. NO Conversion and N_2 Selectivity for the NO Reduction with CO Over $Cr_{0.19}Rh_{0.06}CeO_z$, $Rh_{0.04}CeO_z$, and $Cr_{0.17}CeO_z$ and Reported Catalysts

Catalyst	Reaction conditions	Conversion %	N_2 Selectivity %	Ref.
$Cr_{0.19}Rh_{0.06}CeO_z$	NO = 0.5% CO = 1.0%, 12,000 mL h^{-1} g^{-1}	>99 (473 K)	100 (473 K)	This work
$Ce_{0.95}Ru_{0.05}O_{2-\delta}$	NO = 0.5% CO = 0.5%, 100 mL min^{-1}, 43,000 h^{-1}	100 (473 K)	100 (473 K)	(6a)
$Ce_{0.98}Rh_{0.02}O_{2-\delta}$	NO = 4.74% CO = 5.14%, 43,000 h^{-1}	64 (473 K) 100 (623 K)	23 (473 K) 100 (623 K)	(4)
$Ce_{0.98}Pd_{0.02}O_{2-\delta}$	NO = 4.74% CO = 5.14%, 43,000 h^{-1}	28 (473 K) 100 (673 K)	80 (473 K) 100 (673 K)	(4)
$Ce_{0.98}Pt_{0.02}O_{2-\delta}$	NO = 4.74% CO = 5.14%, 43,000 h^{-1}	12 (473 K) 100 (723 K)	46 (473 K) 100 (723 K)	(4)
$Ce_{0.73}Ti_{0.25}Pd_{0.02}O_{2-\delta}$	NO = 0.5% CO = 0.5%, 100 mL min^{-1}, 43,000 h^{-1}	89 (473 K) 100 (513 K)	50 (473 K) 100 (513 K)	(10b)
$Ce_{0.99}Pt_{0.01}O_{2-\delta}$	NO = 0.25%, CO = 0.25%, 16,000 mL h^{-1} g^{-1}	100 (463 K)	——	(10a)
$Ce_{0.84}Ti_{0.15}Pt_{0.01}O_{2-\delta}$	NO = 0.25%, CO = 0.25%, 16,000 mL h^{-1} g^{-1}	100 (458 K)	——	(10a)
$Ce_{0.78}Sn_{0.2}Pd_{0.02}O_{2-\delta}$	NO = 5% CO = 10%, 60,000 mL h^{-1} g^{-1}, 43,000 h^{-1}	98 (473 K) 100 (493 K)	70 (473 K) 100 (518 K)	(10c)
$Ce_{0.89}Fe_{0.1}Pd_{0.01}O_{2-\delta}$	NO = 1% CO = 1%, 60,000 mL h^{-1} g^{-1}	64 (473 K) 100 (673 K)	25 (473 K) 100 (673 K)	(10d)

Table 3.6. [Continued] NO Conversion and N_2 Selectivity for the NO Reduction with CO Over $Cr_{0.19}Rh_{0.06}CeO_z$, $Rh_{0.04}CeO_z$, and $Cr_{0.17}CeO_z$ and Reported Catalysts

Catalyst	Reaction conditions	Conversion %	N_2 Selectivity %	Ref.
$Ce_{20}Cr_1O_x$	NO = 5% CO = 10%, 24,000 mL h^{-1} g^{-1}	96 (473 K) 100 (548 K)	70 (473 K) 100 (623 K)	(7)
$CuO/Ce_{20}Cr_1O_x$	NO = 5% CO = 10%, 24,000 mL h^{-1} g^{-1}	96 (473 K) 100 (548 K)	70 (473 K) 85 (548 K)	(10k)
Cr-Cu/CeO_2 (Cr/Cu = 3)	NO = 0.15%, CO = 0.15%, 120,000 mL h^{-1} g^{-1}	50 (523 K)	100 (523 K)	(10h)
NiO/CeO_2 rod	NO = 0.12%, CO = 0.12%, 60,000 mL h^{-1} g^{-1}	100 (427 K)	——	(3a)
PdO/CeO_2 rod	NO = 0.12%, CO = 0.12%, 60,000 mL h^{-1} g^{-1}	100 (408 K)	——	(3b)
PdO-CeO_2/OMS-2	NO = 1% CO = 1%, 100 mg, 30,000 h^{-1}	90 (473 K) 100 (573 K)	23 (473 K) 100 (573 K)	(10r)
Rh_n^0/CeO_2	NO = 0.1% CO = 0.1%, 63,830 mL h^{-1} g^{-1}	100 (473 K)	100 (473 K)	(6b)
$Cu_3Ce_{0.2}Al_{0.8}O_x$	NO = 5% CO = 10%, 50 mg, 12,000 h^{-1}	98 (473 K) 100 (498 K)	23 (473 K) 100% (493 K)	(10l)
CuO-Mn_2O_3/Al_2O_3	NO = 5% CO = 10%, 25 mg, 24000 h^{-1}	68 (573 K)	82 (573 K)	(10e)
CuO-V_2O_5/Al_2O_3	NO = 5% CO = 10%, 24000 mL h^{-1} g^{-1}	36 (623 K)	80 (623 K)	(10f)

Table 3.6. [Continued] NO Conversion and N_2 Selectivity for the NO Reduction with CO Over $Cr_{0.19}Rh_{0.06}CeO_z$, $Rh_{0.04}CeO_z$, and $Cr_{0.17}CeO_z$ and Reported Catalysts

Catalyst	Reaction conditions	Conversion %	N_2 Selectivity %	Reference
Cu-Ru/Al_2O_3	NO = 0.09% CO = 0.1%, 180,000 mL h^{-1} g^{-1}	8 (473 K) 100 (573 K)	——	(8j)
Cu_5Pd_1/Al_2O_3	NO = 0.5% CO = 0.5%, 115,200 mL h^{-1} g^{-1}	100 (473 K)	100 (473 K)	(9a)
$Pd(In_{0.33}Cu_{0.67})/Al_2O_3$	NO = 0.5%, CO = 0.5%, 48,000 mL h^{-1} g^{-1}	100 (473 K)	100 (473 K)	(8a)
Rh_1Co_3/Co_3O_4	NO = 5% CO = 5%, 360,000 mL h^{-1} g^{-1}	88 (463 K) 100 (523 K)	100 (>383 K)	(9b)
Au-FeO_x/TiO_2	NO = 0.2%, CO = 0.2%, 30,000 mL h^{-1} g^{-1}	84.4 (523 K)	90.6 (523 K)	(11a)
Rh@NbO_x	NO = 1% CO = 1%, 30,000 h^{-1}	100 (573 K)	100 (573 K)	(11b)
Ni@NbO_x	NO = 1% CO = 1%, 6000 mL h^{-1} g^{-1}	25 (473 K) 100 (698 K)	100 (698 K)	(11c)

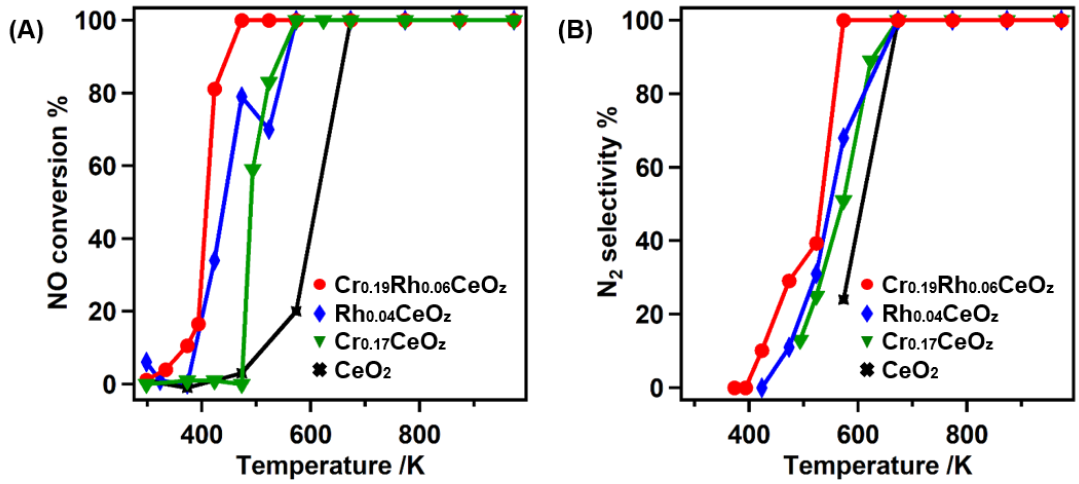

Figure 3.11. (A) NO conversion and (B) N_2 selectivity for NO reduction with CO over $Cr_{0.19}Rh_{0.06}CeO_z$, $Rh_{0.04}CeO_z$, $Cr_{0.17}CeO_z$, and CeO_2. Conditions: catalyst 50 mg, NO (0.5%), CO (1.0%), Ar (5.0%), and He (balance), total flow rate 100 mL min^{-1} (GHSV = 65,000 h^{-1}).

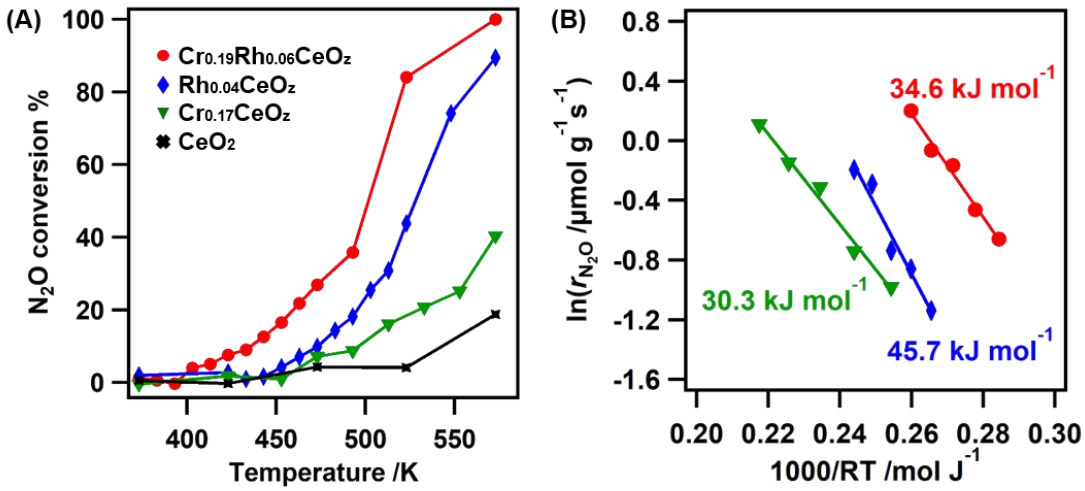

Figure 3.12. (A) N_2O conversion for N_2O reduction with CO over $Cr_{0.19}Rh_{0.06}CeO_z$, $Rh_{0.04}CeO_z$, $Cr_{0.17}CeO_z$, and CeO_2.[15] (B) Arrhenius plots for N_2O reduction with CO over $Cr_{0.19}Rh_{0.06}CeO_z$, $Rh_{0.04}CeO_z$, and $Cr_{0.17}CeO_z$.[15] Conditions: catalyst 50 mg, N_2O (0.5%), CO (1.0%), Ar (5.0%), and He (balance), total flow rate 100 mL min^{-1} (GHSV = 65,000 h^{-1}).

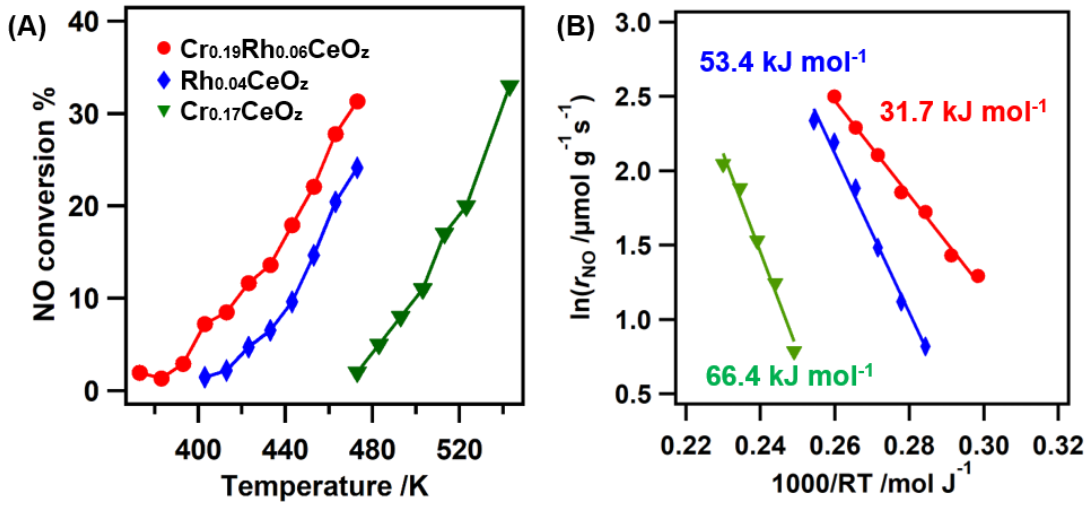

Figure 3.13. (A) NO conversion for NO reduction with CO over $Cr_{0.19}Rh_{0.06}CeO_z$, $Rh_{0.04}CeO_z$, and $Cr_{0.17}CeO_z$.[15] (B) Arrhenius plots for NO reduction with CO over $Cr_{0.19}Rh_{0.06}CeO_z$, $Rh_{0.04}CeO_z$, and $Cr_{0.17}CeO_z$.[15] r_{NO}: reaction rate of NO reduction. Conditions: catalyst 10 mg, NO (0.5%), CO (1.0%), Ar (5.0%), and He (balance), total flow rate 100 mL min^{-1} (GHSV = 325,000 h^{-1}).

Table 3.7. The Activation Energies for NO Reduction with CO Over $Cr_{0.19}Rh_{0.06}CeO_z$, $Rh_{0.04}CeO_z$, and $Cr_{0.17}CeO_z$ and Reported Catalysts

Catalyst	Activation energy (kJ mol^{-1})	Reference
$Cr_{0.19}Rh_{0.06}CeO_z$	31.7[a]	This work
$Rh_{0.04}CeO_z$	53.4[a]	This work
$Cr_{0.17}CeO_z$	66.4[a]	This work
CuO/CeO_2-rods	34.0	(21a)
CuO/CeO_2-polyhedra	34.0	(21a)
CuO/CeO_2-cubes	34.0	(21a)
CeO_2-rods	36.1	(21a)
CeO_2-polyhedra	42.2	(21a)
CeO_2-cubes	71.3	(21a)
$Ce_{0.95}Ru_{0.05}O_{2-\delta}$	41.0	(6a)
$Ce_{0.9}Ru_{0.1}O_{2-\delta}$	53.2	(6a)
$Ce_{0.98}Pd_{0.02}O_{2-\delta}$	70.2	(21b)
$Ce_{0.73}Ti_{0.25}Pd_{0.02}O_{2-\delta}$	52.9	(10b)
$Ce_{0.99}Pt_{0.01}O_{2-\delta}$	100.8	(10a)
$Ce_{0.84}Ti_{0.15}Pt_{0.01}O_{2-\delta}$	96.6	(10a)
$Ce_{0.78}Sn_{0.2}Pd_{0.02}O_{2-\delta}$	105.4	(10c)
$Ti_{0.99}Pd_{0.01}O_{2-\delta}$	64.1	(21c)
α-MnO_2	40	(21d)
Rh_n^0/CeO_2	54.2	(6b)
Cu_5Pd_1/Al_2O_3	42.7	(9a)
Cu/Al_2O_3	60.8	(9a)
Pd/Al_2O_3	99.5	(9a)
$Pd(In_{0.33}Cu_{0.67})/Al_2O_3$	30.8	(8a)
$PdIn/Al_2O_3$	23.1	(8a)

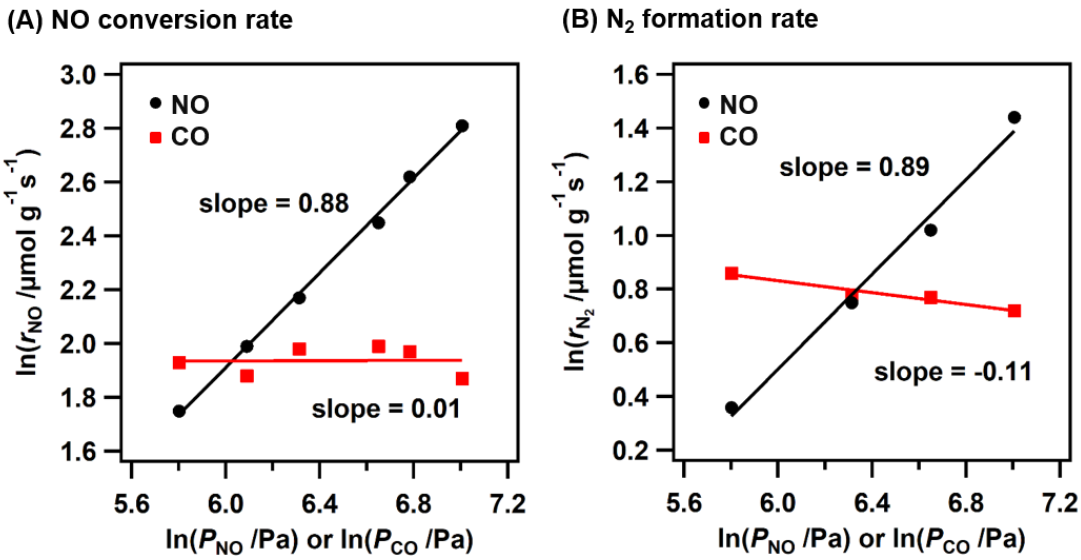

Figure 3.14. (A) Dependency of the reaction rates for NO conversion to N_2O (r_{NO}) on NO partial pressures (P_{NO}) or CO partial pressures (P_{CO}) in NO reduction with CO on $Cr_{0.19}Rh_{0.06}CeO_z$. (Catalyst 50 mg, NO (0.3−1.0%) and CO (1.0%, fixed) for NO partial pressure dependence, or NO (0.5%, fixed) and CO (0.3−1.0%) for CO partial pressure dependence, Ar (5.0%), and He (balance), total flow rate 100 mL min^{-1} (GHSV = 65,000 h^{-1}), 413 K). (B) Dependency of the reaction rates for N_2 formation (r_{N2}) on NO partial pressures (P_{NO}) or CO partial pressures (P_{CO}) in NO reduction with CO on $Cr_{0.19}Rh_{0.06}CeO_z$. (Catalyst 50 mg, NO (0.3−1.0%) and CO (1.0%, fixed) for NO partial pressure dependence, or NO (0.5%, fixed) and CO (0.3−1.0%) for CO partial pressure dependence, Ar (5.0%), and He (balance), total flow rate 100 mL min^{-1} (GHSV = 65,000 h^{-1}), 453 K).

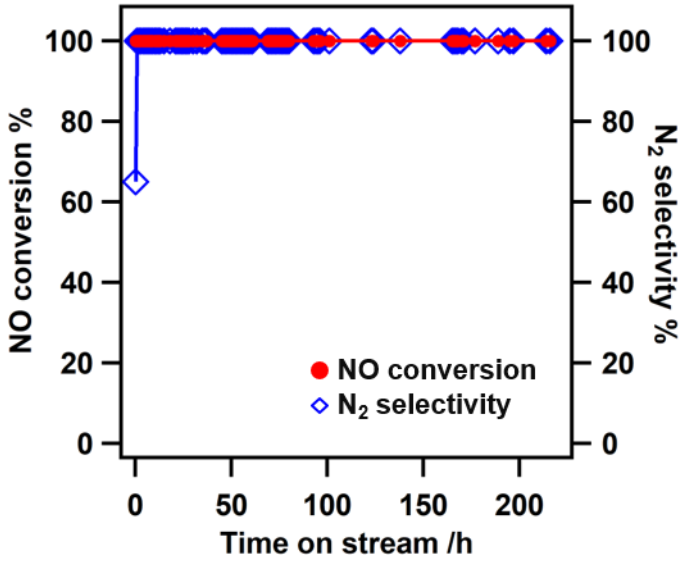

Figure 3.15. Durability test for NO reduction with CO over $Cr_{0.19}Rh_{0.06}CeO_z$ at 473 K. Conditions: catalyst 500 mg, NO (0.5%), CO (1.0%), Ar (5.0%), and He (balance), total flow rate 100 mL min^{-1} (GHSV = 6,500 h^{-1}), 473 K.

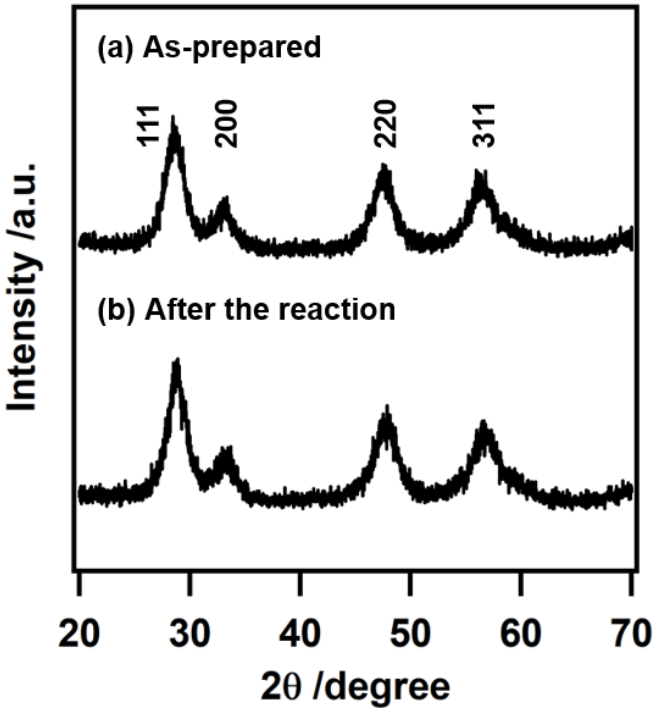

Figure 3.16. XRD patterns of $Cr_{0.19}Rh_{0.06}CeO_z$ (a) as prepared and (b) after the NO reduction with CO at 473 K for 216 h.

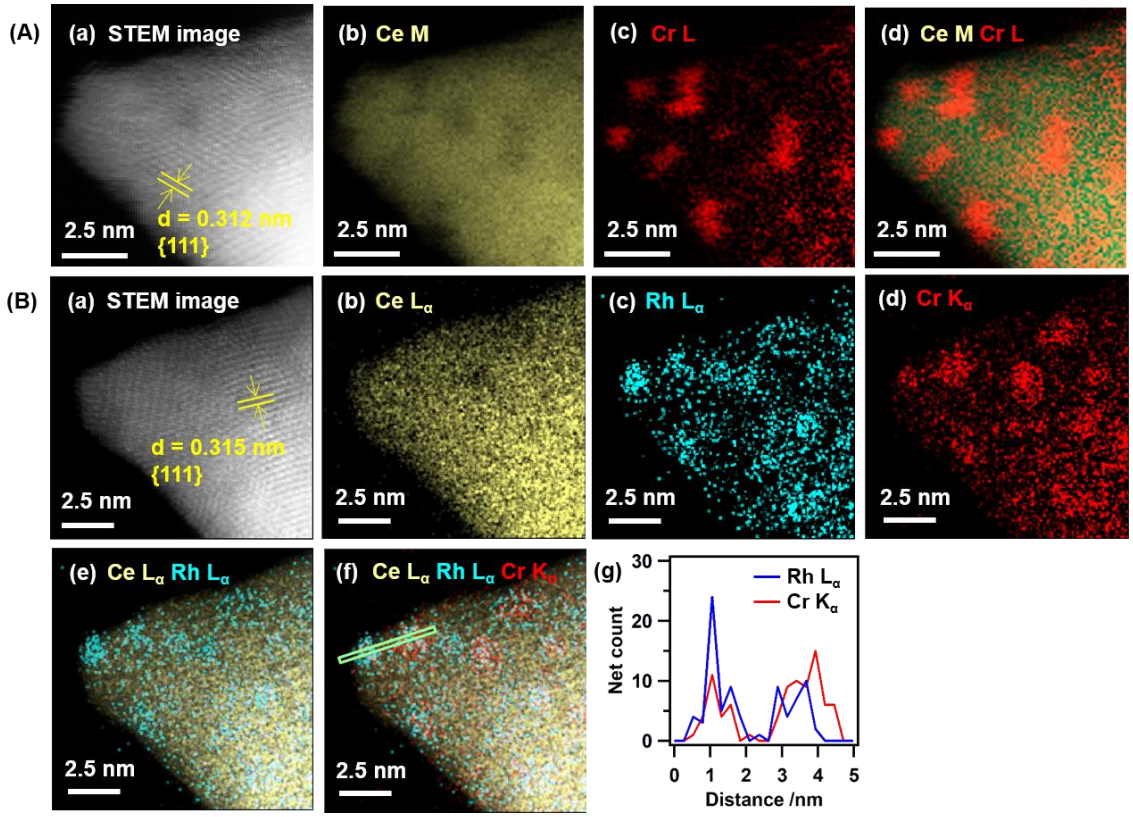

Figure 3.17. (A) HAADF-STEM-EELS images of $Cr_{0.19}Rh_{0.06}CeO_z$ after NO reduction with CO at 473 K for 216 h.; (a) a HAADF-STEM image, (b) EELS mapping of Ce, (c) EELS mapping of Cr, and (d) an overlaid EELS mapping of Ce and Cr.[15] (B) HAADF-STEM-EDS images of $Cr_{0.19}Rh_{0.06}CeO_z$ after NO reduction with CO at 473 K for 216 h at the same view as HAADF-STEM-EELS; (a) HAADF-STEM image, (b) EDS mapping of Ce, (c) EDS mapping of Rh, (d) EDS mapping of Cr, (e) the overlaid EDS mapping of Ce and Rh, (f) the overlaid EDS mapping of Ce, Rh, and Cr, and (g) the line profiles of Rh L_α, and Cr K_α along the light green line in the overlaid EDS mapping.[15] The regions of interest for EDS of Ce L_α, Rh L_α, and Cr K_α were 4701–4977 eV, 2580–2812 eV, and 5269–5555 eV, respectively.

2.3.2. Adsorption structure of CO and NO and structural change of metal species of $Cr_{0.19}Rh_{0.06}CeO_z$ clarified by *in situ* FT-IR and *in situ* XAFS

In situ FT-IR spectra were measured on $Cr_{0.19}Rh_{0.06}CeO_z$ after the successive exposure of CO and NO at 473 K as shown in Figure 3.18 (A). The catalyst was treated with CO (5.3 kPa) for 30 min, evacuated, and then a FT-IR spectrum was recorded. The *in situ* FT-IR spectrum of $Cr_{0.19}Rh_{0.06}CeO_z$ showed two sharp and distinct peaks at 2077 and 2000 cm^{-1} corresponding to the symmetric and asymmetric stretching vibration modes of $Rh^+(CO)_2$ (Figure 3.18 (A-a)).[16,17] After the subsequent exposure to NO (5.3 kPa) for 30 min and the evacuation of NO, the two peaks of $Rh^+(CO)_2$ disappeared and a new peak appeared at 1891 cm^{-1} attributed to the stretching vibration mode of $Rh^+(NO)$ (Figure 3.18 (A-b)).[16,17] The formations of N_2O, N_2, and CO_2 were detected in the process, showing that $Rh^+(CO)_2$ reacted with NO as a reaction site to generate not only N_2O and N_2 but also CO_2. Peaks assigned to CO or NO species adsorbed on the Cr oxides[18–20] were not observed in these processes. After the re-exposure to CO (5.3 kPa) in the similar manner on the NO-treated sample, the observed peak of $Rh^+(NO)$ disappeared, and the two $Rh^+(CO)_2$ peaks at 2076 and 2001 cm^{-1} reversibly appeared (Figure 3.18 (A-c)). The formation of N_2 was detected after the exposure to CO by GC, indicating that $Rh^+(NO)$ reacted with CO to form N_2 as a reaction site. A new peak also appeared at 2172 cm^{-1} in the process, which was attributed to $Ce^{3+}(NCO)$.[17] This reversible adsorption behavior was also observed on additional NO/CO treatments.

The similar experiment using ^{13}CO was performed, and two peaks attributed to the vibration modes of $Rh^+(^{13}CO)_2$ were observed at 2034 and 1961 cm^{-1} (Figure 3.19). After the introduction of ^{12}CO, the two peaks completely shifted to 2083 and 2009 cm^{-1}, indicating that adsorbed ^{13}CO on the Rh sites was completely exchanged to ^{12}CO. The results suggested that the adsorption of CO on Rh was not much strong, and the dispersed Rh species provides the efficient reaction sites for NO reduction on the catalyst surface.

Similar *in situ* FT-IR experiments with CO and NO were performed on $Rh_{0.04}CeO_z$ and $Cr_{0.17}CeO_z$ (Figure 3.18 (B, C)). Two broad peaks assigned to $Rh^+(CO)_2$ were initially observed at 2072 and 1993 cm^{-1} on $Rh_{0.04}CeO_z$ after the treatment with CO, the absorbances of which were smaller than those on $Cr_{0.19}Rh_{0.06}CeO_z$ (Figure 3.18 (B-a)).[16,17] The subsequent treatment of NO appeared a new peak at 1880 cm^{-1} attributed to $Rh^+(NO)$;[16,17] however, the broad peaks of $Rh^+(CO)_2$ still remained observed (Figure 3.18 (B-b)). It is noted that the $Rh^+(NO)$ peak also still remained in addition to distinct reappearance of the $Rh^+(CO)_2$ peaks after the subsequent re-treatment with CO (Figure 3.18 (B-c)). As for $Cr_{0.17}CeO_z$, no clear peak corresponding to adsorbed CO or NO species

was observed (Figure 3.18 (C)). These results of the control experiments demonstrate that the reversible adsorption/desorption behaviors of CO and NO were characteristic features on $Cr_{0.19}Rh_{0.06}CeO_z$ and they were not observed on $Rh_{0.04}CeO_z$ and $Cr_{0.17}CeO_z$ prepared with the introduction of the single metal source to CeO_2.

The co-adsorption of both CO and NO on $Cr_{0.19}Rh_{0.06}CeO_z$ was also observed by *in situ* FT-IR under the practical reaction conditions with CO (5.3 kPa) and NO (2.7 kPa) at 473 K as shown in Figure 3.18 (D). Similar two peaks of $Rh^+(CO)_2$ were observed at 2081 and 2010 cm^{-1}, while peaks attributed to NO adsorbed on Rh were red-shifted compared to that formed under NO alone, suggesting the partial reduction of Rh by CO under the reaction conditions.[16,17]

In situ Cr *K*-edge, Rh *K*-edge, and Ce L_{III}-edge XANES spectra of $Cr_{0.19}Rh_{0.06}CeO_z$ under the successive flow of CO and NO at 473 K were measured to investigate changes in the oxidation state of each metal species as shown in Figures 3.20-21. The *in situ* XANES spectra revealed the involvement of all the metal species in the NO reduction with CO. Under the flow of CO (5% CO/N_2, 100 mL min^{-1}), the Cr *K*-edge and Rh *K*-edge XANES spectra quickly changed within 5 min, and the average oxidation states of Cr and Rh decreased from +4.5 and +3.0 (Cr) to +3.0 and +2.0 (Rh) (Figure 3.20 (A, B, D)). These results suggest that the oxygen species of $Cr^{6-\gamma}O_{3-x}$ and around Rh species was consumed by the reaction with CO. On the other hand, the Ce L_{III}-edge XANES spectra changed gradually, with decrease in the average oxidation state of Ce to +3.63 over 30 min (Figure 3.20 (C, D)).

The subsequent flow of NO (5% NO/N_2, 100 mL min^{-1}) at 473 K showed the inverse oxidation of all the metal species on $Cr_{0.19}Rh_{0.06}CeO_z$. The Cr *K*-edge, Rh *K*-edge, and Ce L_{III}-edge XANES spectra shifted toward the direction in oxidation (Figure 3.21), which suggested that both the reduced Cr species and CeO_2 surface were re-oxidized by NO. The reduced Rh species was also partially re-oxidized by NO, which was consistent with the fact that the amount of $Rh^+(NO)$ species was smaller than that of $Rh^+(CO)_2$ species judging from the FT-IR peak intensities.

In situ Rh *K*-edge EXAFS spectra were analyzed under the flow of CO to investigate changes in the local coordination structure of the Rh species (Figure 3.22 and Table 3.8). Prior to the reaction with CO, only the Rh–O bond at 0.203 ± 0.001 nm (CN = 4.8 ± 0.9) was observed and the Rh–Rh bonds of metallic Rh and the Rh–O–Rh bonds of Rh_2O_3 were not observed (Figure 3.22). After the flow of CO for 30 min, the CN of the Rh–O bond decreased to 3.7 ± 1.9, indicating that the oxygen species around Rh atoms was consumed by the reaction with CO to form CO_2. No Rh–Rh bond was observed, although

a new scattering by O atoms in $Rh^{+}(CO)_2$ emerged. The CN of the Rh–CO bond was fitted as 1.1 ± 0.9, suggesting that the half of the Rh species formed the $Rh^{+}(CO)_2$ species on an average. The lack of Rh–Rh bond formation indicated that agglomeration of the Rh species into metallic Rh nanoparticles was sufficiently inhibited under the reaction conditions. This seems to be one of the key factors in the significant activity and durability for the NO reduction on $Cr_{0.19}Rh_{0.06}CeO_z$.

In situ Cr *K*-edge, Rh *K*-edge, and Ce L_{III}-edge XANES spectra were also investigated upon the flow of CO and NO-mixed gases (5% CO/5% NO/N_2, 100 mL min^{-1}) at 473 K (Figure 3.23). The smooth changes in the Cr and Rh *K*-edge XANES spectra were completed within 10 min, and Cr and Rh species were reduced to the average oxidation states of +3.2 and +2.2, respectively, under the steady-state reaction conditions (Figure 3.23 (A, B, D)). In contrast, the Ce L_{III}-edge XANES spectra remained almost unchanged (Figure 3.23 (C, D)). These results suggest that the oxygen vacant sites in $Cr_{0.19}Rh_{0.06}CeO_z$ to cleave NO were abundantly generated in the steady state not on the surface of the CeO_2 structure, but at Cr oxides.; *i.e.*, it was strongly suggested that reduced Cr oxide species served the main oxygen transfer pathways from NO to CO. The increase in the oxygen transfer pathways upon the addition of Cr species could facilitate the dissociation and reduction of NO with CO over $Cr_{0.19}Rh_{0.06}CeO_z$ with lowering the activation energy.

Based on the results of the *in situ* characterization for $Cr_{0.19}Rh_{0.06}CeO_z$, the roles of the Rh and Cr species for the NO reduction with CO on $Cr_{0.19}Rh_{0.06}CeO_z$ are proposed as follows (Figure 3.24). The incorporation of Cr into $Cr_{0.19}Rh_{0.06}CeO_z$ dispersed the Rh species that served the dual adsorption sites of CO and NO. Adsorbed CO and NO on the Rh sites were efficiently converted to CO_2 and N_2, respectively, and they were also detectable under the steady-state reaction conditions. The CrO_{3-x} species oxidized CO adsorbed on Rh, and thereby reduced Cr species cleaved and reduced NO. The enhancement of NO reduction with CO is considered to originate from the concerted effects of Cr oxides not only as structural modulators to disperse the Rh species as activation sites of CO and NO but also as excellent mediators of the oxygen transfer from NO and the N_2O intermediate to CO.

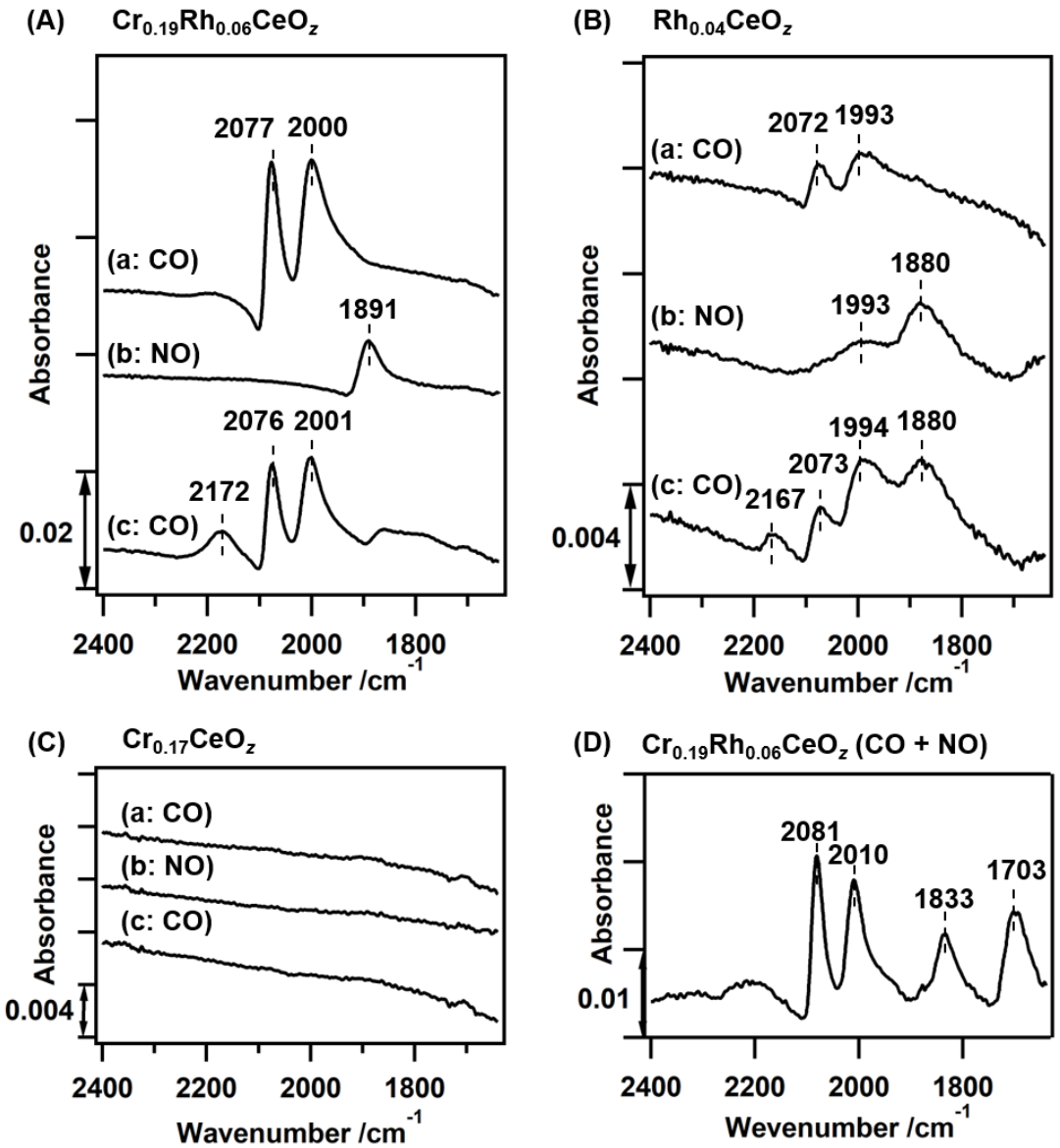

Figure 3.18. *In situ* FT-IR spectra on (A) $Cr_{0.19}Rh_{0.06}CeO_z$, (B) $Rh_{0.04}CeO_z$, and (C) $Cr_{0.17}CeO_z$ (a) after CO exposure (5.3 kPa) for 30 min and subsequent evacuation at 473 K, (b) after NO exposure (5.3 kPa) for 30 min and subsequent evacuation at 473 K, and (c) after CO re-exposure (5.3 kPa) for 30 min and subsequent evacuation at 473 K.[15] (D) *In situ* FT-IR spectrum of $Cr_{0.19}Rh_{0.06}CeO_z$ in the presence of CO (5.3 kPa) and NO (2.7 kPa) for 10 min.[15]

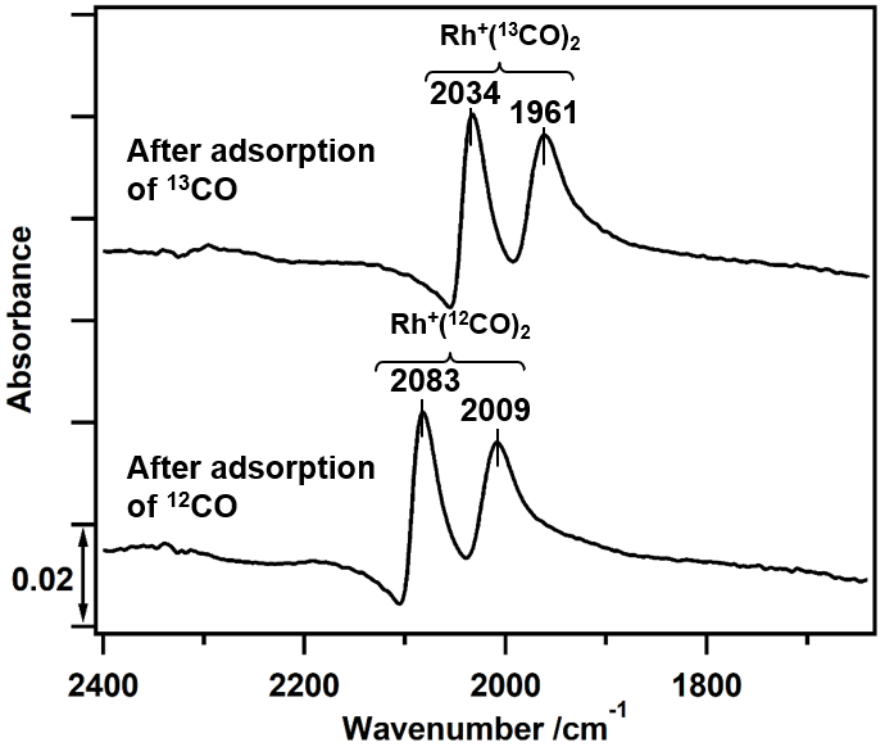

Figure 3.19. *In situ* FT-IR spectra on $Cr_{0.19}Rh_{0.06}CeO_z$ after ^{13}CO exposure (5.3 kPa) for 30 min and subsequent evacuation at 473 K, and after the successive ^{12}CO exposure (5.3 kPa) for 30 min and subsequent evacuation at 473 K.[15]

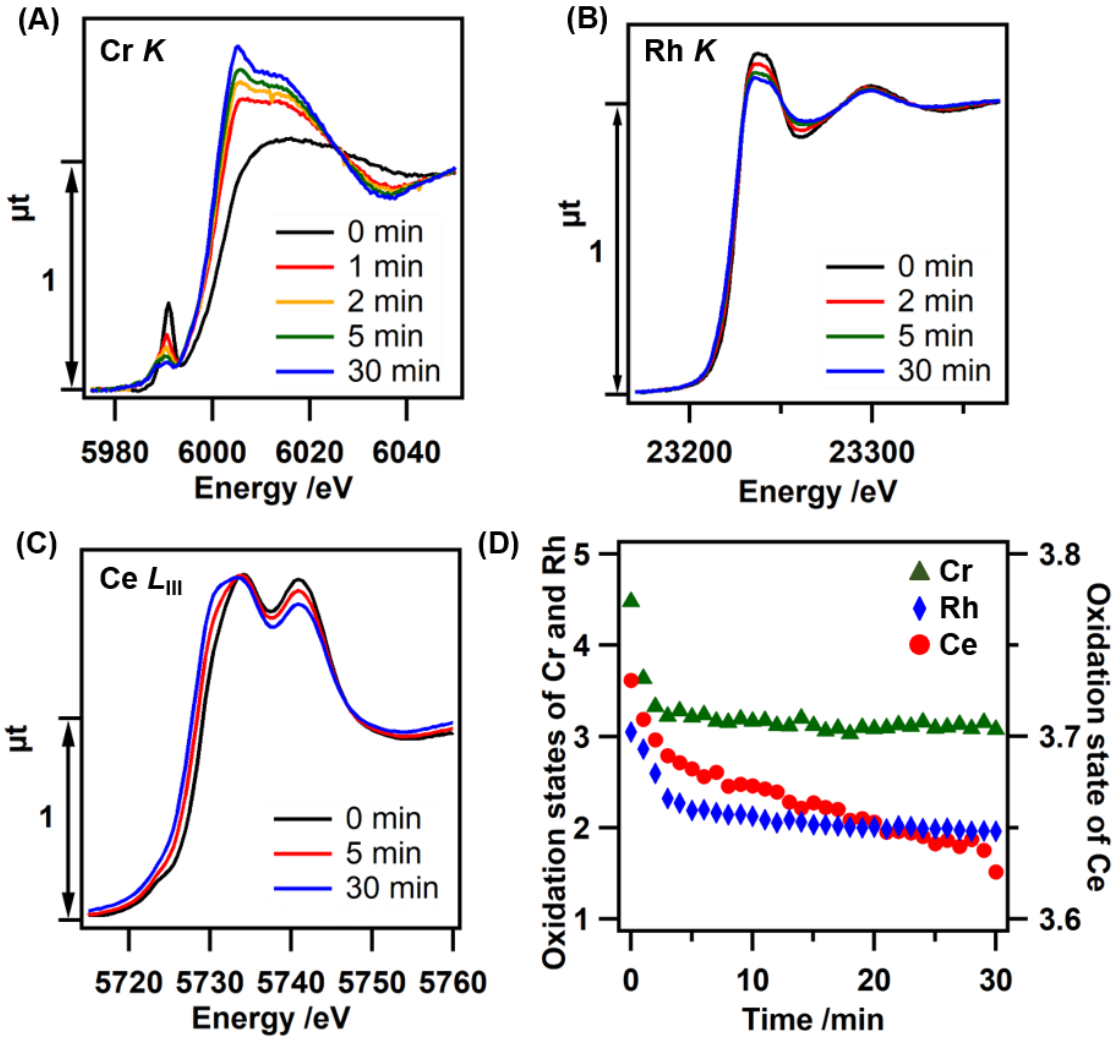

Figure 3.20. *In situ* (A) Cr *K*-edge, (B) Rh *K*-edge, and (C) Ce L_{III}-edge XANES spectra of $Cr_{0.19}Rh_{0.06}CeO_z$ under CO flow (5% CO/N_2, 100 mL min^{-1}) at 473 K.[15] (D) Changes in the oxidation states of Cr, Rh, and Ce under CO flow (5% CO/N_2, 100 mL min^{-1}) at 473 K.[15]

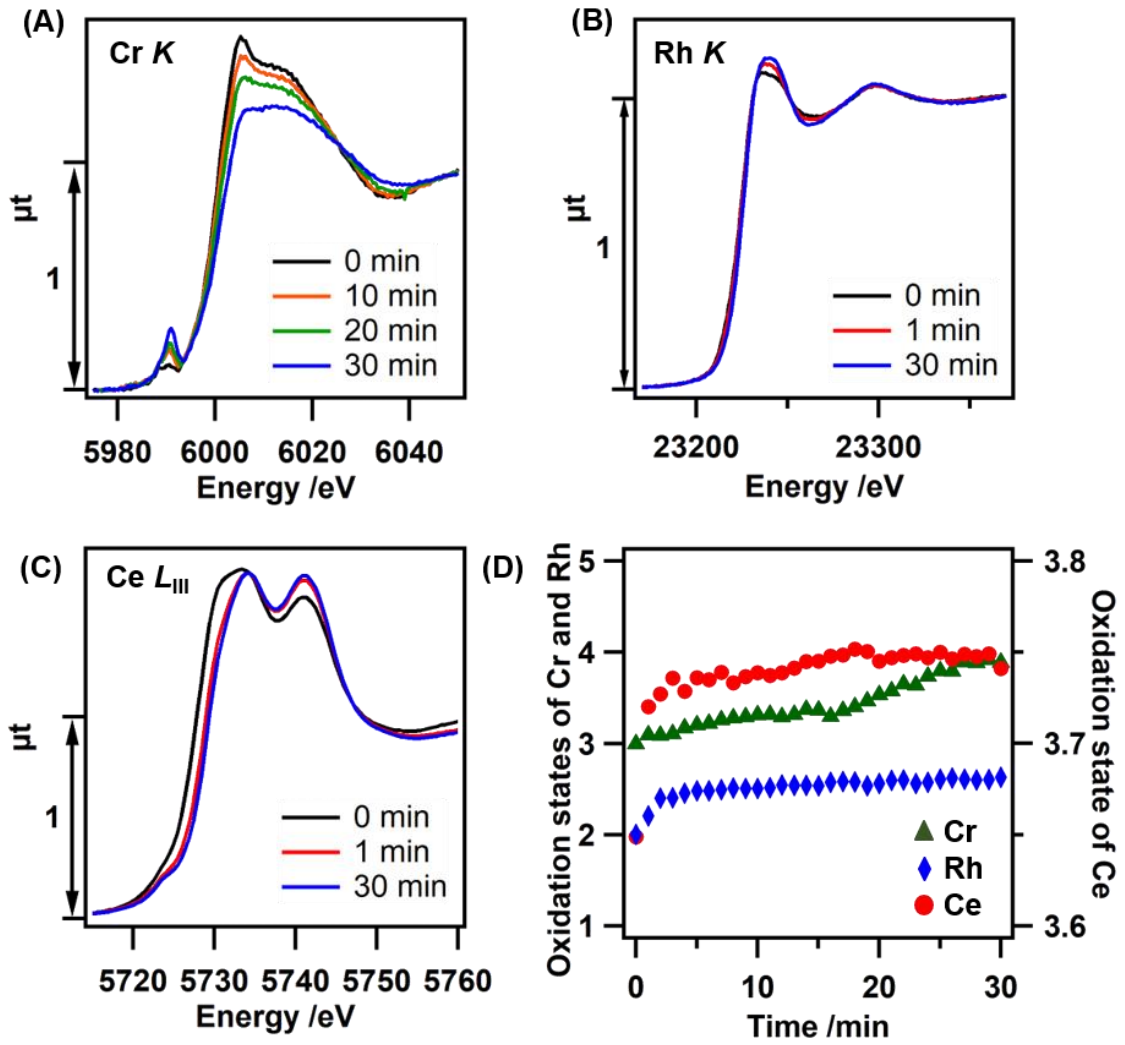

Figure 3.21. *In situ* (A) Cr *K*-edge, (B) Rh *K*-edge, and (C) Ce L_{III}-edge XANES spectra of $Cr_{0.19}Rh_{0.06}CeO_z$ under NO flow (5% NO/N_2, 100 mL min^{-1}) at 473 K.[15] (D) Changes in the oxidation states of Cr, Rh, and Ce under NO flow (5% NO/N_2, 100 mL min^{-1}) at 473 K.[15]

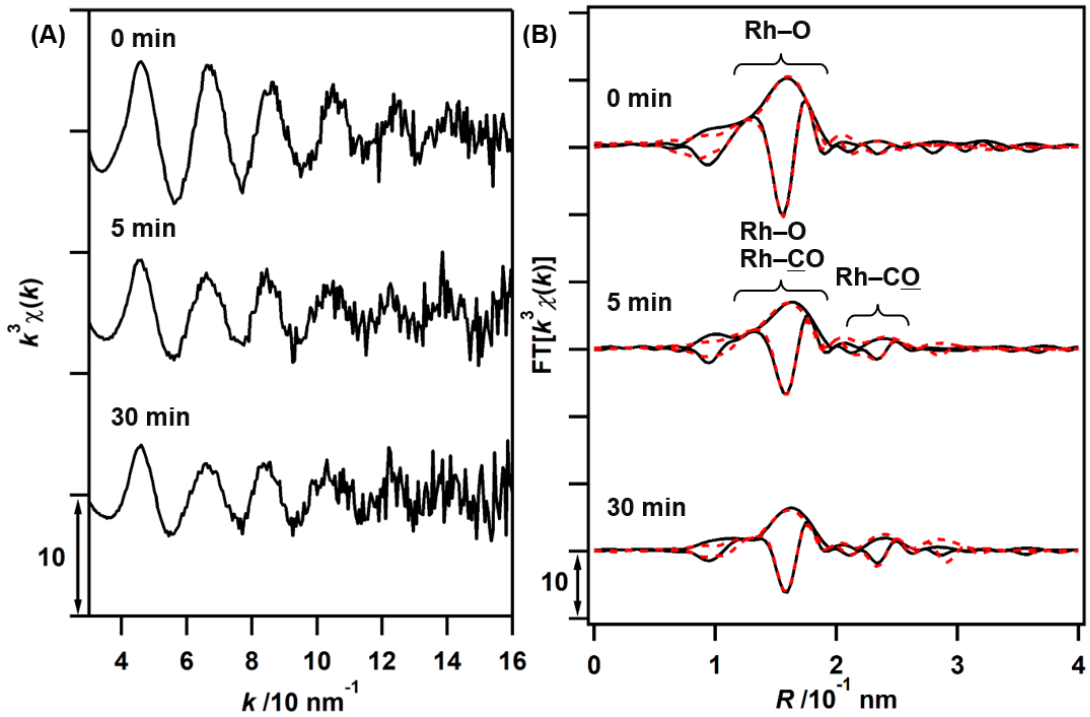

Figure 3.22. (A) *In situ* k^3-weighted Rh *K*-edge EXAFS oscillations and (B) their Fourier transforms (k = 30-140 nm^{-1}) of $Cr_{0.19}Rh_{0.06}CeO_z$ under the CO flow (5% CO/N_2, 100 mL min^{-1}) at 473 K.[15] Black solid lines show observed data and red dashed lines show fitted data.

Table 3.8. Structural Parameters Obtained by the Curve-Fitting Analysis of *in Situ* Rh *K*-edge EXAFS of $Cr_{0.19}Rh_{0.06}CeO_z$ under CO Flow (5% CO/N_2, 100 mL min^{-1}) at 473 K[a]

Shell	CN	R /nm	ΔE_0 /eV	σ^2 / 10^5 nm^2
		0 min [b]		
Rh–O (oxide)	4.8 ± 0.9	0.203 ± 0.001	11 ± 2	4 ± 1
		10 min [c]		
Rh–CO	0.7 ± 1.1	0.192 ± 0.008	5 ± 4	4 ± 9
Rh–CO	0.7 ± 1.1	0.306 ± 0.009	5 ± 4	4 ± 9
Rh–CO	0.7 ± 1.1	0.297 ± 0.001	5 ± 4	4 ± 9
Rh–CO	1.5 ± 2.2	0.322 ± 0.025	5 ± 4	4 ± 9
Rh–O (oxide)	3.9 ± 4.3	0.203 ± 0.001	5 ± 4	4 ± 9
		30 min [d]		
Rh–CO	1.1 ± 0.9	0.1.89 ± 0.005	1 ± 2	4 ± 4
Rh–CO	1.1 ± 0.9	0.251 ± 0.045	1 ± 2	4 ± 4
Rh–CO	1.1 ± 0.9	0.296 ± 0.001	1 ± 2	4 ± 4
Rh–CO	2.2 ± 1.8	0.327 ± 0.030	1 ± 2	4 ± 4
Rh–O (oxide)	3.7 ± 1.9	0.202 ± 0.001	1 ± 2	4 ± 4

[a] k = 30-140 nm^{-1}, S_0^2 was fixed as 1. [b] R = 0.12-0.20 nm, R_f = 1.0%. [c] R = 0.12-0.27 nm, R_f = 4.4%. [d] R = 0.12-0.27 nm, R_f = 2.7%

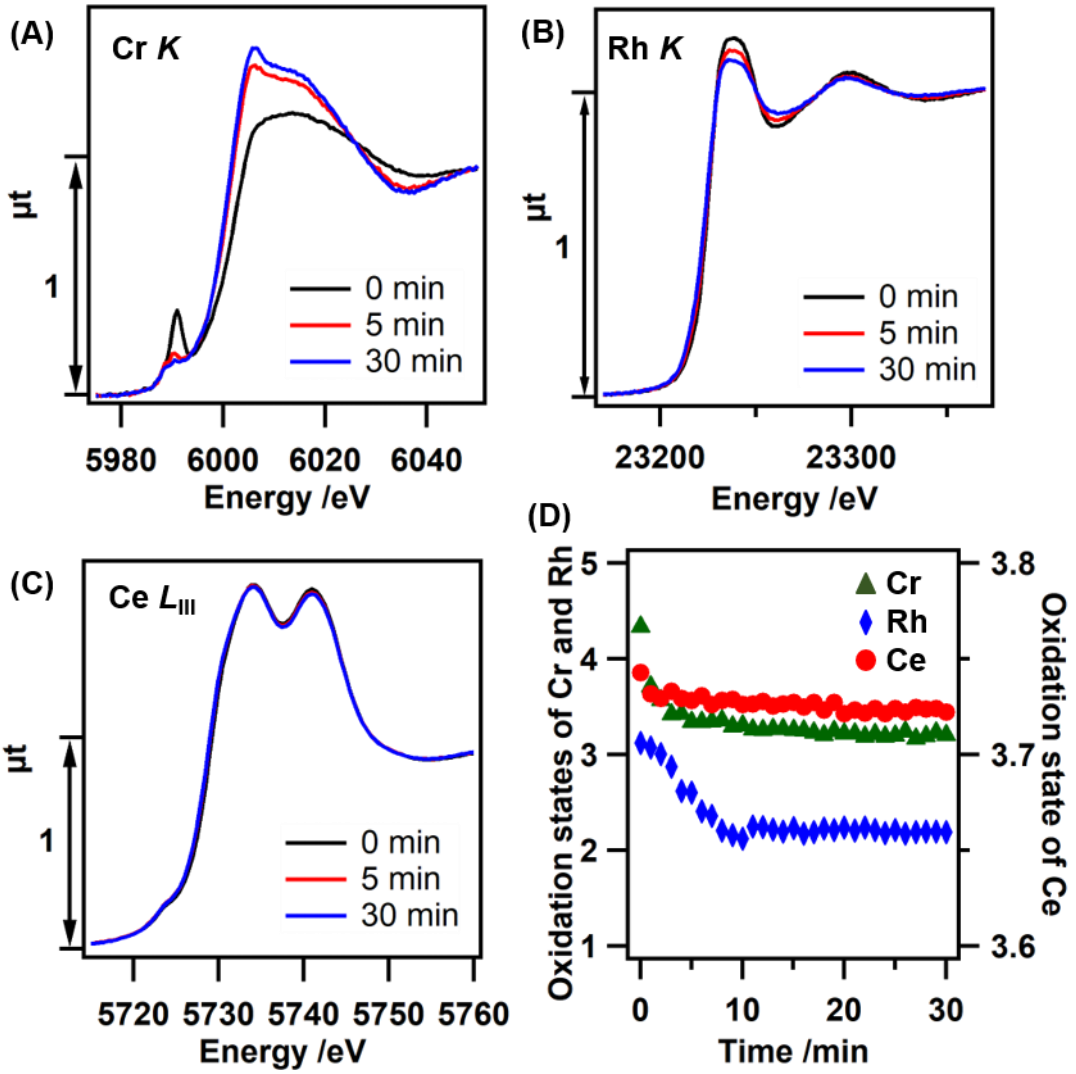

Figure 3.23. *In situ* (A) Cr *K*-edge, (B) Rh *K*-edge, and (C) Ce L_{III}-edge XANES spectra of $Cr_{0.19}Rh_{0.06}CeO_z$ under reaction with mixed gases of CO and NO (5% CO/5% NO/N_2, 100 mL min^{-1}) at 473 K.[15] (D) Changes in the oxidation states of Cr, Rh, and Ce under reaction with mixed gases of CO and NO (5% CO/5% NO/N_2, 100 mL min^{-1}) at 473 K.[15]

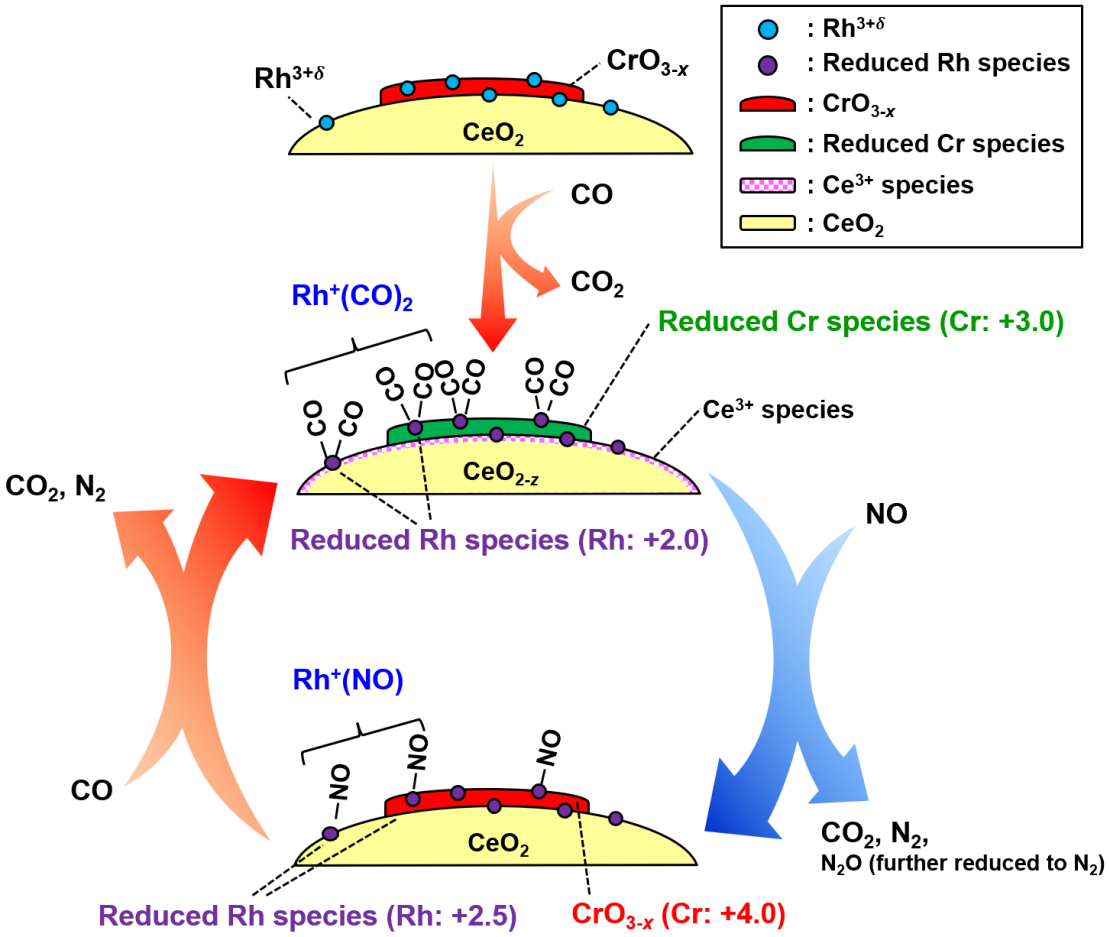

Figure 3.24. Possible mechanism of NO reduction with CO on $Cr_{0.19}Rh_{0.06}CeO_z$.[15]

3.4. Conclusions

The low-temperature redox properties of $Cr_{0.19}Rh_{0.06}CeO_z$ were found to bring about the efficient catalysis for the selective reduction of NO with high N_2 selectivity at 473 K. The roles of Rh and Cr in $Cr_{0.19}Rh_{0.06}CeO_z$ for the catalytic reaction were investigated by the comparison among $Cr_{0.19}Rh_{0.06}CeO_z$, $Rh_{0.04}CeO_z$ and $Cr_{0.17}CeO_z$. *In situ* FT-IR and XAFS characterization revealed that the roles of Cr and Rh were as follows: (1) the inclusion of Cr dispersed the Rh species, which adsorbed and activated both CO and NO on the catalyst surface, not only to increase the number of adsorption sites for CO and NO but also to suppress the agglomeration of the Rh species, and (2) reduced Cr oxide species in addition to the CeO_2 surface cleaved NO adsorbed on Rh sites and transferred oxygen species from NO to CO to lower the activation energy for NO reduction and enhance the NO reduction performances. Therefore, the incorporation of both Cr and Rh in $Cr_{0.19}Rh_{0.06}CeO_z$ enhanced the NO reduction performances with CO at low temperature, which has not previously reported in the simple metal oxide addition to mixed-metal oxides/metal-supported oxide catalysts.[5,6] The effect of dispersing the active metal species by the incorporation of the additional metal oxides in $Cr_{0.19}Rh_{0.06}CeO_z$ is similar to that of the metal alloy catalyst systems.[1g,4a,b] Such a catalyst design, in which the added second metal oxides also play a positive role in the reaction process, is promising in mixed metal oxide catalysis.

3.5. References

(1) (a) Granger, P.; Paul, D. J.-F.; Leclercq, G. An Overview of Kinetic and Spectroscopic Investigations on Three-way Catalysts: Mechanistic Aspects of the CO + NO and CO + N_2O Reactions. *J. Mol. Catal. A: Chem.* **2005**, *228*, 214–253. (b) Roy, S.; Hegde, M. S.; Madras, G. Catalysis for NO_x Abatement. *Appl. Energy* **2009**, *86*, 2283−2297. (c) Roy, S.; Baiker, A. NO_x Storage−Reduction Catalysis: From Mechanism and Materials Properties to Storage−Reduction Performance. *Chem. Rev.* **2009**, *109*, 4054–4091. (d) Bera P.; Hegde, M. S. NO Reduction Over Noble Metal Ionic Catalysts. *Catal. Surv. Asia* **2011**, *15*, 181–199. (e) Bera, P.; Hegde, M. S. Noble Metal Ions in CeO_2 and TiO_2: Synthesis, Structure and Catalytic Reaction. *RSC Adv.* **2015**, *5*, 94949–94979. (f) Mao, J.; Yin, J.; Pei, J.; Wang, D.; Li, Y. Single Atom Alloy: An Emerging Atomic Site Material for Catalytic Applications. *Nano Today* **2020**, *34*, 100917.

(2) (a) Pârvulescu, V. I.; Grange, P.; Delmon, B. Catalytic Removal of NO. *Catal. Today* **1998**, *46*, 233−316. (b) Farrauto, R. J.; Heck, R. M. Catalytic Converters: State of the Art and Perspectives. *Catal. Today* **1999**, *51*, 351–360. (c) Farrauto, R. J.; Heck, R. M. Environmental Catalysis into the 21st Century. *Catal. Today* **2000**, *55*, 179−187. (d) Shelef, M.; McCabe, R. W. Twenty-Five Years after Introduction of Automotive Catalysts: What Next? *Catal. Today* **2000**, *62*, 35–50. (e) Heck, R. M.; Farrauto, R. J. Automobile Exhaust Catalysts. *Appl. Catal., A: General* **2001**, *221*, 443−457. (f) Burch, R.; Breen, J. P.; Meunier, F. C. A Review of the Selective Reduction of NO_x with Hydrocarbons under Lean-Burn Conditions with Non-zeolitic Oxide and Platinum Group Metal Catalysts. *Appl. Catal. B: Environmental* **2002**, *39*, 283–303. (g) Kašpar, J.; Fornasiero, P. Nanostructured Materials for Advanced Automotive De-Pollution Catalysts. *J. Solid State Chem.* **2003**, *171*, 19–29. (h) Granger, P.; Dhainaut, F.; Pietrzik, S.; Malfoy, P.; Mamede, A. S.; Leclercq, L.; Leclercq, G. An Overview: Comparative Kinetic Behaviour of Pt, Rh and Pd in the NO+CO and NO+H_2 Reactions. *Top. Catal.* **2006**, *39*, 65−76. (i) Bowker, M. Automotive Catalysis Studied by Surface Science. *Chem. Soc. Rev*. **2008**, *37*, 2204−2211. (j) Hamada, H.; Haneda, M. A Review of Selective Catalytic Reduction of Nitrogen Oxides with Hydrogen and Carbon Monoxide. *Appl. Catal., A* **2012**, *421–422*, 1−13.

(3) (a) Tang, K.; Liu, W.; Li, J.; Guo, J.; Zhang, J.; Wang, S.; Niu, S.; Yang, Y. The Effect of Exposed Facets of Ceria to the Nickel Species in Nickel-Ceria Catalysts and Their Performance in a NO + CO Reaction. *ACS Appl. Meter. Interfaces* **2015**, *7*, 26839–26849. (b) Tang, K.; Ren, Y.; Liu, W.; Wei, J.; Guo, J.; Wang, S.; Yang, Y. Insight

Investigation of Active Palladium Surface Sites in Palladium-Ceria Catalysts for NO + CO Reaction. *ACS Appl. Mater. Interfaces* **2018**, *10*, 13614–13624.

(4) Roy, S.; Hegde, M. S. Pd Ion Substituted CeO_2: A Superior De-NO_x Catalyst to Pt or Rh Metal Ion Doped Ceria. *Catal. Commun.* **2008**, *9*, 811–815.

(5) Paidi, V. K.; Savereide, L.; Childers, D. J.; Notestein, J. M.; Roberts, C. A.; Lierop, J. Predicting NO_x Catalysis by Quantifying Ce^{3+} from Surface and Lattice Oxygen. *ACS Appl. Mater. Interfaces* **2017**, *9*, 30670–30678.

(6) (a) Singh, P.; Hegde M. S. $Ce_{1-x}Ru_xO_{2-\delta}$ (x = 0.05, 0.10): A New High Oxygen Storage Material and Pt, Pd-Free Threee-Way Catalysts. *Chem. Mater.* **2009**, *21*, 3337–3345. (b) Kibis, L. S.; Svintsitskiy, D. A.; Derevyannikova, E. A.; Kardash, T. Y.; Slavinskaya, E. M.; Stonkus, O. A.; Svetlichnyi, V. A.; Boronin, A. I. From Highly Dispersed Rh^{3+} to Nanoclusters and Nanoparticles: Probing the Low-Temperature NO+CO Activity of Rh-Doped CeO_2 Catalysts. *Appl. Surf. Sci.* **2019**, *493*, 1055–1066.

(7) Deng, C.; Li, M.; Qian, J.; Hu, Q.; Huang, M.; Lin, Q.; Ruan, Y.; Dong, L.; Li, B.; Fan, M. A Study of Different Doped Metal Cations on the Physicochemical Properties and Catalytic Activities of $Ce_{20}M_1O_x$ (M = Zr, Cr, Mn, Fe, Co, Sn) Composite Oxides for Nitric Oxide Reduction by Carbon Monoxide. *Chem. Asian J.* **2016**, *11*, 2144–2156.

(8) (a) Jeon, J.; Kon, K.; Toyao, T.; Shimizu, K.; Furukawa, S. Design of Pd-based Pseudo-binary Alloy Catalysts for Highly Active and Selective NO Reduction. *Chem. Sci.* **2019**, *10*, 4148–4162. (b) Holles, J. H.; Switzer, M. A.; Davis, R. J. Influence of Ceria and Lanthana Promoters on the Kinetics of NO and N_2O Reduction by CO over Alumina-Supported Palladium and Rhodium. *J. Catal.* **2000**, *190*, 247–260. (c) Granger, P.; Lecomte, J. J.; Leclercq, L.; Leclercq, G. Modelling Study of the Temperature-Programmed Conversion Curves of NO Reduction by CO over Supported Pt- and Rh-based Catalysts. *Top. Catal.* **2001**, *16–17*, 349–354. (d) Granger, P.; Lecomte, J. J.; Leclercq, L.; Leclercq, G. An Attempt at Modelling the Activity of Pt-Rh/Al_2O_3 Three-way Catalysts in the CO + NO Reaction. *Appl. Catal., A: General* **2001**, *208*, 369−379. (e) Granger, P.; Delannoy, L.; Lecomte, J. J.; Dathy, C.; Praliaud, H.; Leclercq, L.; Leclercq, G. Kinetics of the CO + NO Reaction over Bimetallic Platinum–Rhodium on Alumina: Effect of Ceria Incorporation into Noble Metals. *J. Catal.* **2002**, *207*, 202–212. (f) Sarkar, A. D.; Khanra, B. C. CO Oxidation and NO Reduction over Supported Pt-Rh and Pd-Rh Nanocatalysts: a Comparative Study. *J. Mol. Catal. A: Chem.* **2005**, *229*, 25−29. (g) Ozawa, M.; Takahashi-Morita,

M.; Kobayashi, K.; Haneda, M. Core-Shell Type Ceria Zirconia Support for Platinum and Rhodium Three Way Catalysts. *Catal. Today* **2017**, *281*, 482−489. (h) Komatsu, T.; Kobayashi, H.; Kusada, K.; Kubota, Y.; Takata, M.; Yamamoto, T.; Matsumura, S.; Sato, K.; Nagaoka, K.; Kitagawa, H. First-Principles Calculation, Synthesis, and Catalytic Properties of Rh-Cu Alloy Nanoparticles. *Chem, Eur. J.* **2017**, *23*, 57–60. (i) Wang, X.; Wang, H.; Maeda, N.; Baiker, A. Structure and Catalytic Behavior of Alumina Supported Bimetallic Au-Rh Nanoparticles in the Reduction of NO by CO. *Catalysts* **2019**, *9*, 937. (j) Ohyama, J.; Shibano, J.; Satsuma, A.; Fukuda, R.; Yamamoto, Y.; Arai, S.; Shishido, T.; Asakura, H.; Hosokawa, S.; Tanaka, T. Quantum Chemical Computation-Driven Development of Cu-Shell–Ru-Core Nanoparticle Catalyst for NO Reduction Reaction. *J. Phys. Chem. C* **2019**, *123*, 20251–20256. (k) Sato, K.; Ito, A.; Tomonaga, H.; Kanematsu, H.; Wada, Y.; Asakura, H.; Hosokawa, S.; Tanaka, T.; Toriyama, T.; Yamamoto, T.; Matsumura, S.; Nagaoka, K. Pt–Co Alloy Nanoparticles on a γ-Al_2O_3 Support: Synergistic Effect between Isolated Electron-Rich Pt and Co for Automotive Exhaust Purification. *ChemPlusChem* **2019**, *84*, 447–456. (l) Jeon, J.; Ham, H.; Xing, F.; Nakaya, Y.; Shimizu, K.; Furukawa, S. PdIn-Based Pseudo-Binary Alloy as a Catalyst for NO_x Removal under Lean Conditions. *ACS Catal.* **2020**, *10*, 11380–11384. (m) Asakura, H.; Kirihara, M.; Fujita, K.; Hosokawa, S.; Kikkawa, S.; Teramura, K.; Tanaka, T. Fe-Modified CuNi Alloy Catalyst as a Nonprecious Metal Catalyst for Three-Way Catalysis. *Ind. Eng. Chem. Res.* **2020**, *59*, 19907–19917.

(9) (a) Xing, F.; Jeon, J.; Toyao, T.; Shimizu, K.; Furukawa, S. A Cu–Pd Single-Atom Alloy Catalyst for Highly Efficient NO Reduction. *Chem. Sci.* **2019**, *10*, 8292−8298. (b) Zhang, S.; Nguyen, L.; Liang, J.-X.; Shan, J.; Liu, J.; Frenkel, A. I.; Patlolla, A.; Huang, W.; Li, J. J.; Tao, F. F. Catalysis on Singly Dispersed Bimetallic Sites. *Nat. Commun.* **2015**, *6*, 7938. (c) Roberts, C. A.; Prieto-Centurion, D.; Nagai, Y.; Nishimura, Y. F.; Desautels, R. D.; Van Lierop, J., Fanson, P. T.; Notestein, J. M. *In Situ* Characterization of Highly Dispersed, Ceria-Supported Fe Sites for NO Reduction by CO. *J. Phys. Chem. C* **2015**, *119*, 4224–4234. (d) Zhang, S; Tang, Y.; Nguyen, L.; Zhao, Y.-F.; Wu, Z.; Goh, T.-W.; Liu, J. J. Li, Y.; Zhu, T.; Huang, W.; Frenkel, A. I.; Li, J.; Tao, F. F. Catalysis on Singly Dispersed Rh Atoms Anchored on an Inert Support. *ACS Catal.* **2018**, *8*, 110–121.

(10) (a) Baidya, T.; Gayen, A;. Hegde, M. S.; Ravishankar, N.; Dupont, L. Enhanced Reducibility of $Ce_{1-x}Ti_xO_2$ Compared to That of CeO_2 and Higher Redox Catalytic Activity of $Ce_{1-x-y}Ti_xPt_yO_{2-\delta}$ Compared to That of $Ce_{1-x}Pt_xO_{2-\delta}$. *J. Phys. Chem. B* **2006**,

110, 5262–5272. (b) Baidya, T.; Marimuthu, A.; Hegde, M. S.; Ravishankar, N.; Madras, G. Higher Catalytic Activity of Nano-$Ce_{1-x-y}Ti_xPd_yO_{2-\delta}$ Compared to Nano-$Ce_{1-x}Pd_xO_{2-\delta}$ for CO Oxidation and N_2O and NO Reduction by CO: Role of Oxide Ion Vacancy. *J. Phys. Chem. C* **2007**, *111*, 830–839. (c) Baidya, T.; Gupta, A.; Deshpandey, P. A.; Madras, G.; Hegde, M. S. High Oxygen Storage Capacity and High Rates of CO Oxidation and NO Reduction Catalytic Properties of $Ce_{1-x}Sn_xO_2$ and $Ce_{0.78}Sn_{0.2}Pd_{0.02}O_{2-\delta}$. *J. Phys. Chem. C* **2009**, *113*, 4059–4068. (d) Gupta, A.; Kumar, A.; Waghmare, U. V.; Hegde, M. S. Origin of Activation of Lattice Oxygen and Synergistic Interaction in Bimetal-Ionic $Ce_{0.89}Fe_{0.1}Pd_{0.01}O_{2-\delta}$ Catalyst. *Chem. Mater.* **2009**, *21*, 4880–4891. (e) Li, D.; Yu, Q.; Li, S.-S.; Wan. H.-Q.; Liu, L.-J.; Qi, L.; Liu, B.; Gao, F.; Dong, L.; Chen, Y. The Remarkable Enhancement of CO-Pretreated CuO–Mn_2O_3/γ-Al_2O_3 Supported Catalyst for the Reduction of NO with CO: The Formation of Surface Synergetic Oxygen Vacancy. *Chem. Eur. J.* **2011**, *17*, 5668–5679. (f) Xiong,Y.; Yao, X.; Tang, C.; Zhang, L.; Cao, Y.; Deng, Y.; Gao, F.; Dong, L. Effect of CO-Pretreatment on the CuO–V_2O_5/γ-Al_2O_3 Catalyst for NO Reduction by CO. *Catal. Sci. Technol.* **2014**, *4*, 4416–4425. (g) Yoshida, H.; Yamashita, N.; Ijichi, S.; Okabe, Y.; Misumi, S.; Hinokuma, S.; Machida, M. A Thermally Stable Cr–Cu Nanostructure Embedded in the CeO_2 Surface as a Substitute for Platinum-Group Metal Catalysts. *ACS Catal.* **2015**, *5*, 6738–6747. (h) Yoshida, H.; Okabe, Y.; Misumi, S.; Oyama, H.; Tokusada, K.; Hinokuma, S.; Machida, M. Structures and Catalytic Properties of Cr–Cu Embedded CeO_2 Surfaces with Different Cr/Cu Ratios. *J. Phys. Chem. C* **2016**, *120*, 26852–26863. (i) Koizumi, K.; Yoshida, H.; Boero, M.; Tamai, K.; Hosokawa, S.; Tanaka, T.; Nobusaka, K.; Machida, M. A Detailed Insight into the Catalytic Reduction of NO Operated by Cr–Cu Nanostructures Embedded in a CeO_2 Surface. *Phys. Chem. Chem. Phys.* **2018**, *20*, 25592–25601. (j) Hirakawa, T.; Shimokawa, Y.; Tokuzumi, W.; Sato, T.; Tsushida, M.; Yoshida, H.; Hinokuma, S.; Ohyama, J.; Machida, M. Multicomponent Spinel Oxide Solid Solutions: A Possible Alternative to Platinum Group Metal Three-Way Catalysts. *ACS Catal.* **2019**, *9*, 11763–11773. (k) Deng, C.; Qian, J.; Yu, C.; Yi, Y.; Zhang, P.; Li, W.; Dong, L.; Li, B.; Fan, M. Influences of Doping and Thermal Stability on the Catalytic Performance of CuO/$Ce_{20}M_1O_x$ (M = Zr, Cr, Mn, Fe, Co, Sn) Catalysts for NO Reduction by CO. *RSC Adv.* **2016**, *6*, 113630–113647. (l) Qian, J.; Hou, X.; Wang, F.; Hu, Q.; Yuan, H.; Teng, L.; Li, R.; Tong, Z.; Dong, L.; Li, B. Catalytic Reduction of NO by CO over Promoted $Cu_3Ce_{0.2}Al_{0.8}$ Composite Oxides Derived from Hydrotalcite-Like Compounds. *J. Phys. Chem. C* **2018**, *122*, 2097–

2106. (m) Cheng, X.; Zhang, X.; Su, D.; Wang, Z.; Chang, J.; Ma, C. NO Reduction by CO over Copper Catalyst Supported on Mixed CeO_2 and Fe_2O_3: Catalysts Design and Activity Test. *Appl. Catal. B: Environ.* **2018**, *239*, 485–501. (n) Glisenti, A.; Pacella, M.; Guiotto, M.; Natile, M. M.; Canu, P. Largely Cu-Doped $LaCo_{1-x}Cu_xO_3$ Perovskites for TWC: Toward New PGM-Free Catalysts. *Appl. Catal. B: Environ.* **2016**, *180*, 94–105. (o) Pacella, M.; Garbujo, A.; Fabro, J.; Guiotto, M.; Xin, Q.; Natile, M. M.; Canu, P.; Glisenti, A.PGM-Free CuO/$LaCuO_3$ Nanocomposites: New Opportunities for TWC Application. *Appl. Catal. B: Environ.* **2018**, *227*, 446–458. (p) Shi, X.; Chu, B.; Wang, F.; Wei, X.; Teng, L.; Fan, M.; Li, B.; Dong, L.; Dong, L. Mn-Modified CuO, $CuFe_2O_4$, and γ-Fe_2O_3 Three-Phase Strong Synergistic Coexistence Catalyst System for NO Reduction by CO with a Wider Active Window. *ACS Appl. Mater. Interfaces* **2018**, *10*, 40509–40522. (q) Ueda, K.; Tsuji, M.; Ohyama, J.; Satsuma, A. Tandem Base-Metal Oxide Catalyst Superior NO Reduction Performance to the Rh Catalyst in NO–C_3H_6–CO–O_2. *ACS Catal.* **2019**, *9*, 2866–2869. (r) Guo, S.; Zhang, G.; Han, Z.-K.; Zhang, S.; Sarker, D.; Zu, W. W.; Pan, X.; Li, G.; Baiker, A. Synergistic Effects of Ternary PdO–CeO_2–OMS-2 Catalyst Afford High Catalytic Performance and Stability in the Reduction of NO with CO. *ACS Appl. Mater. Interfaces* **2021**, *13*, 622–630.

(11) (a) Wang, X.; Maeda, N.; Baiker, A. Synergistic Effects of Au and FeO_x Nanocomposites in Catalytic NO Reduction with CO. *ACS Catal.* **2016**, *6*, 7898–7906. (b) Imai, T.; Ueda, S.; Nagao, S.; Hirata, H.; Deepthi, K. R.; Abe, H. N_2O-Emission-Free Exhaust Remediation by Rh-NbO_x Nanocomposites Developed from Rh_3Nb Alloy Precursor. *RSC Adv.* **2017**, *7*, 9628–9631. (c) Tanabe, T.; Imai, T.; Tokunaga, T.; Arai, S.; Yamamoto, Y.; Ueda, S.; Ramesh, G. V.; Nagao, S.; Hirata, H.; Matsumoto, S.; Fujita T.; Abe, H. Nanophase-Separated Ni_3Nb as an Automobile Exhaust Catalyst. *Chem. Sci.* **2017**, *8*, 3374–3378.

(12) (a) Wu, Z.-P.; Shan, S.; Zang, S.-Q.; Zhong, C.-J. Dynamic Core−Shell and Alloy Structures of Multimetallic Nanomaterials and Their Catalytic Synergies. *Acc. Chem. Res.* **2020**, *53*, 2913−2924. (b) Zhang, L.; Zhou, M.; Wang, A.; Zhang, T. Selective Hydrogenation over Supported Metal Catalysts: From Nanoparticles to Single Atoms. *Chem. Rev.* **2020**, *120*, 683−733. (c) Liu, K.; Qin, R.; Zheng, N. Insights into the Interfacial Effects in Heterogeneous Metal Nanocatalysts toward Selective Hydrogenation. *J. Am. Chem. Soc.* **2021**, *143*, 4483−4499. (d) Docherty, S. R.; Copéret, C. Deciphering Metal−Oxide and Metal−Metal Interplay via Surface

Organometallic Chemistry: A Case Study with CO_2 Hydrogenation to Methanol. *J. Am. Chem. Soc.* **2021**, *143*, 6767−6780.

(13) (a) Ruiz Puigdollers, A.; Schlexer, P.; Tosoni, S.; Pacchioni, G. Increasing Oxide Reducibility: The Role of Metal/Oxide Interfaces in the Formation of Oxygen Vacancies. *ACS Catal.* **2017**, *7*, 6493−6513. (b) Yu, K.; Lou, L.-L.; Liu, S.; Zhou, W. Asymmetric Oxygen Vacancies: The Intrinsic Redox Active Sites in Metal Oxide Catalysts. *Adv. Sci.* **2020**, *7*, 1901970.

(14) (a) Gao, Z.; Qin, Y. Design and Properties of Confined Nanocatalysts by Atomic Layer Deposition. *Acc. Chem. Res.* **2017**, *50*, 2309−2316. (b) Zhang, B.; Qin, Y. Interface Tailoring of Heterogeneous Catalysts by Atomic Layer Deposition. *ACS Catal.* **2018**, *8*, 10064−10081. (c) Zhang, J.; Medlin, W. Catalyst Design Using an Inverse Strategy: From Mechanistic Studies on Inverted Model Catalysts to Applications of Oxide-Coated Metal Nanoparticles. *Surf. Sci. Rep.* **2018**, *73*, 117−152. (d) Otor, H. O.; Steiner, J. B.; Garcia-Sancho, C.; Alba-Rubio, A. C. Encapsulation Methods for Control of Catalyst Deactivation: A Review. *ACS Catal.* **2020**, *10*, 7630−7656.

(15) Ikemoto, S.; Muratsugu, S.; Koitaya, T.; Tada, M. Chromium Oxides as Structural Modulators of Rhodium Dispersion on Ceria to Generate Active Sites for NO Reduction. *ACS Catal.* **2022**, *12*, 431–441.

(16) Almusaiteer, K. A.; Chuang, S. S. C. Infrared Characterization of Rh Surface States and Their Adsorbates during the NO–CO Reaction. *J. Phys. Chem. B* **2000**, *104*, 2265–2272.

(17) Bánsági, T.; Zakar, T. S.; Solymosi, F. An FTIR Study on the Formation of NCO Surface Complexes over Rh/CeO_2. *Appl. Catal. B: Environ.* **2006**, *66*, 147–150.

(18) Little, L. H.; Amberg, C. H. Infrared Spectra of Carbon Monoxide and Carbon Dioxide Adsorbed on Chromia–Alumina and on Alumina. *Can. J. Chem.* **1962**, *40*, 1997−2006.

(19) Zecchína, A.; Coluccia, S.; Guglielminotti, E.; Ghiotti, G. An Infrared Study of Surface Properties of α-Chromia. I. Preparation and Adsorption of Water, Heavy Water, and Carbon Monoxide. *J. Phys. Chem.* **1971**, *75*, 2774−2783.

(20) Peri, J. B. Infrared Study of Nitric Oxide and Carbon Monoxide Adsorbed on Chromia/Alumina. *J. Phys. Chem.* **1974**, *6*, 588−594.

(21) (a) Liu, L.; Yao, Z.; Deng, Y.; Gao, F.; Liu, B.; Dong, L. Morphology and Crystal-Plane Effects of Nanoscale Ceria on the Activity of CuO/CeO_2 for NO Reduction by CO. *ChemCatChem* **2011**, *3*, 978–989. (b) Roy, S.; Marimuthu, A.; Hegde, M. S.;

Madras, G. High Rates of NO and N_2O Reduction by CO, CO and Hydrocarbon Oxidation by O_2 over Nano Crystalline $Ce_{0.98}Pd_{0.02}O_{2-\delta}$: Catalytic and kinetic studies. *Appl. Catal. B* **2007**, *71*, 23–31. (c) Roy, S.; Marimuthu, A.; Hegde, M. S.; Madras, G. High Rates of CO and Hydrocarbon Oxidation and NO Reduction by CO over $Ti_{0.99}Pd_{0.01}O_{1.99}$. *Appl. Catal. B* **2007**, *73*, 300–310. (d) Shan, J.; Zhu, Y.; Zhang, S.; Zhu, T.; Rouvimov, S.; Tao, F. Catalytic Performance and in situ Surface Chemistry of Pure α-MnO_2 Nanorods in Selective Reduction of NO and N_2O with CO. *J. Phys. Chem. C* **2013**, *117*, 8329–8335.

Chapter 4

Catalytic activity induction by coordination-induced trigger with N-heterocyclic carbene (NHC) decoration on the reduced $Cr_{0.19}Rh_{0.06}CeO_z$ for 1,4-arylation of α,β-unsaturated ketones

4.1. Introduction

4.1.1. Decoration of heterogeneous catalysts with NHCs

An N-heterocyclic carbene (NHC) is one of the most studied organic ligands in the field of transition metal complexes in the past decade.[1] NHCs are defined as heterocyclic species containing a carbene center and at least one nitrogen atom in the ring structure, and in this thesis, NHC denotes a 1,3-substituted imidazolylidene with a heteroaromatic ring as shown in Figure 4.1 unless noted. The ground-state electronic structure of NHCs is singlet carbenes with a large singlet−triplet gap, and the lone pair located on the plane of the NHC heterocyclic ring makes these compounds nucleophilic. Consequently, NHCs possess high electron donating ability, strong coordination affinity to metals, and a wide diversity of structures,[2] and these characteristics have led to their utilization in heterogeneous catalysis beyond coordination chemistry and homogeneous catalysis.[3] NHCs have been used for protecting metal nanomaterials (nanoclusters,[4a-f] nanoparticles,[4g-k] nanorods[4l]) and metal surfaces,[4m,n] and these materials have been applicated for various heterogeneous catalysts,[5] biosensors,[6] molecular probes for surface reactivity,[7] and microelectronics.[8]

Decoration of supported heterogeneous catalysts with NHCs has been reported.[9-12] For example, Ru/K-Al_2O_3 decorated with 1,3-dicyclohexylimidazol-2-ylidene (ICy) tuned the chemoselectivity of hydrogenation reduction by adjusting the loading amount of NHC ligands (Figure 4.2).[9b] Pd/Al_2O_3 decorated with 1,3-bis(2,6-diisopropylphenyl)-imidazol-2-ylidene (IPr) facilitated the oxidative addition of aryl halides by electron donation from IPr to Pd nanoparticles (Figure 4.3), resulting in the catalytic inducement of amino-coupling reactions, which were inactive without NHC ligands.[9c] Decoration of Cu/SiO_2 with 1,3-bis(2,4,6-trimethylphenyl)imidazol-2-ylidene (IMes) promoted selective alkyne semi-hydrogenation due to the different affinity of IMes and the reactants to the metal surface (Figure 4.4).[10] Decoration of Ru nanoparticles supported on carbon with 1,3-diadamantylimidazol-2-ylidene (IAd) switched the activity of reductive deuteration and hydrogen isotope exchange.[11] These results indicate that decorating supported metal nanoparticles with NHC ligands can drastically change the catalytic performance and can lead to remarkable catalytic activity. However, direct modification with NHCs in more complicated systems, such as supported heterogeneous catalysts with multiple metal species, has not been reported, and it is still a significant challenge to elucidate the relationship between surface structures and the catalytic performance in these systems.

ICy	(R = Cy)
IMe	(R = Me)
I*t*Bu	(R = *t*Bu)
IBn	(R = Bn)
IMes	(R = Mes)
IPr	(R = Dipp)

Figure 4.1. Molecular structures of N-heterocyclic carbenes (imidazolylidene).

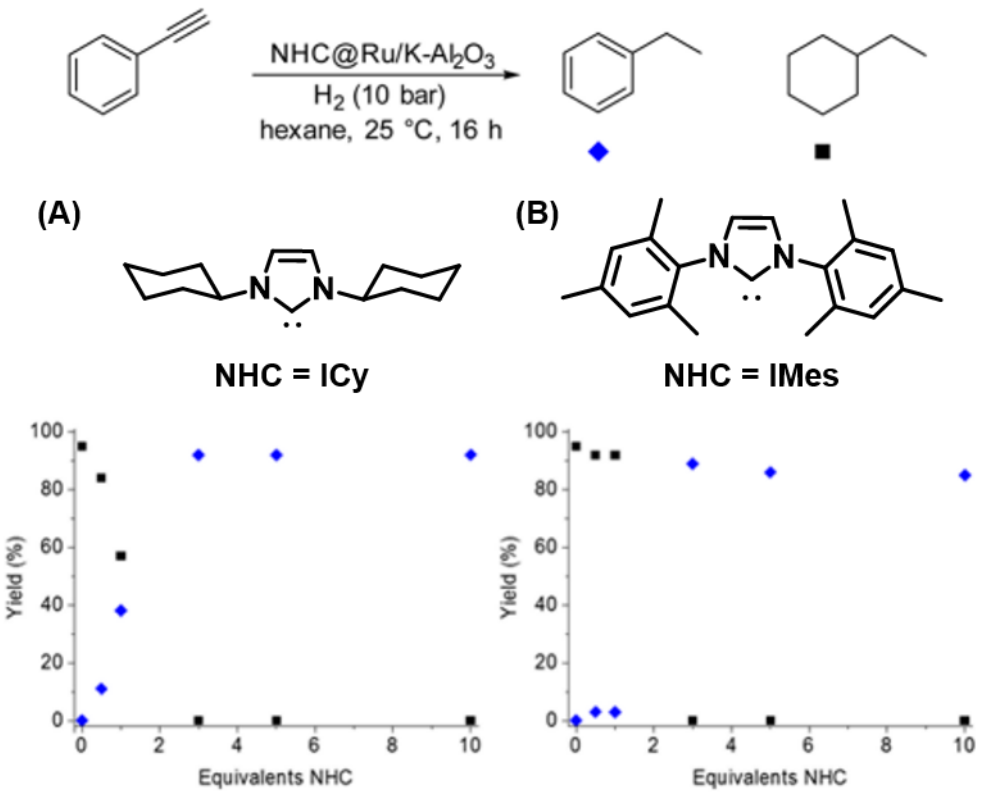

Figure 4.2. Effect of NHC-loading on the chemoselectivity in the hydrogenation of phenyl acetylene on (A) ICy@Ru/K-Al_2O_3 and (B) IMes@Ru/K-Al_2O_3.[9b]

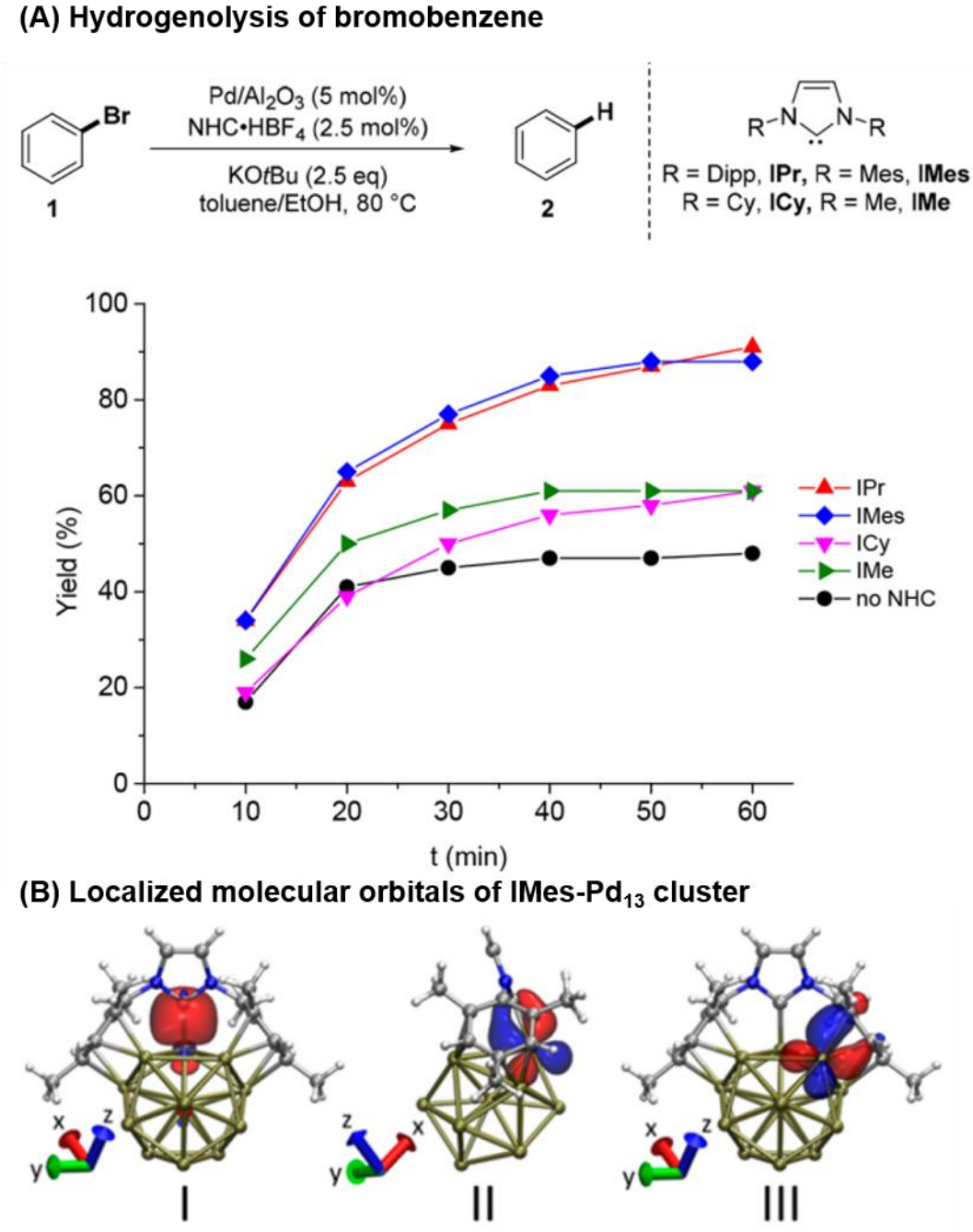

Figure 4.3. (A) Effect of the NHC-modification on Pd/Al_2O_3 for hydrogenolysis of bromobenzene and (B) Localized molecular orbitals of IMes-stabilized Pd_{13} cluster calculated by DFT.[9c]

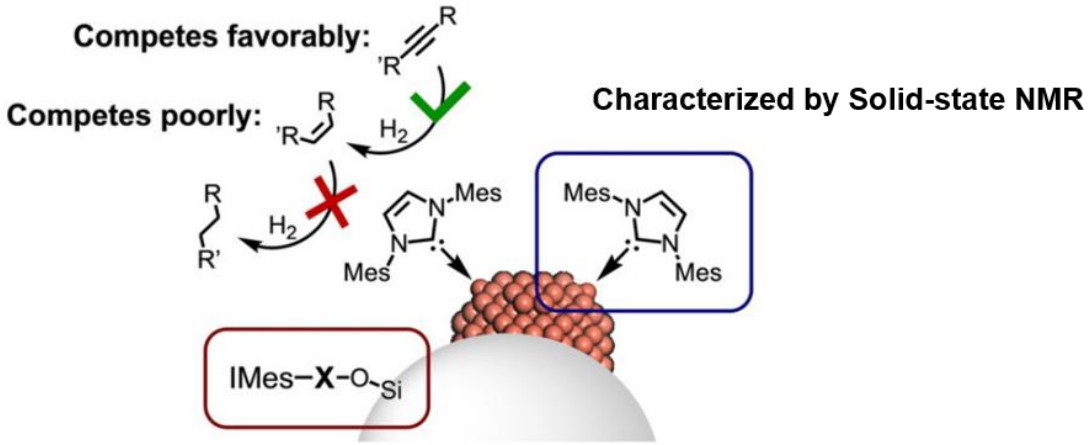

Figure 4.4. IMes/substrate binding competition during alkyne semihydrogenation at Cu/SiO_2.[10]

4.1.2. The 1,4-arylation of α,β-unsaturated ketones

Conjugate addition of organometallics to activated alkenes catalyzed by transition metal catalysts is considered as the fundamental reactions of C−C bond formation in organic synthesis.[13] The 1,4-arylation of α,β-unsaturated ketones with arylboronic acids as shown in Scheme 4.1 is one of the important conjugate addition reactions.[14] The rhodium-catalyzed 1,4-arylation of methyl vinyl ketones with aryl and boronic acids was first reported by Miyaura and co-workers in 1997.[15] Conditions of solvents, temperatures, and ligands were optimized, and a number of electron donating and withdrawing aryl boronic acids can be used in the reaction with high product yields.[15] Hayashi and co-workers first reported the enantioselective 1,4-arylation of 2-cyclohexenone with arylboronic acids catalyzed by Rh catalysts with a (*S*)-2,2'-bis(diphenylphosphino)-1,1'-binaphtyl (BINAP) ligand.[16] This reaction is tole regarded as the benchmark reaction for the rhodium catalyzed conjugate addition chemistry.[17] Since this first report, the process has been constantly refined with a variety of rhodium sources, ligands (*e.g.*, diene,[18] NHC[19]), and base additives to improve the catalytic activity and selectivity.

The reaction mechanism of 1,4-arylation of cyclohexenone was reported to be the three-step catalytic cycle as shown in Scheme 4.2.[20] The first step involves the formation of the active Rh hydroxyl species and a transmetalation with an arylboronic acid. The next step contains adsorption and subsequent insertion of cyclohexenone to the aryl-rhodium intermediate. The enantioselectivity of the product is determined by the facial selectivity of the chiral ligand in this step. In the final step, hydrolysis of the rhodium-enolate occurs to produce the product and to regenerate the active Rh hydroxyl species.

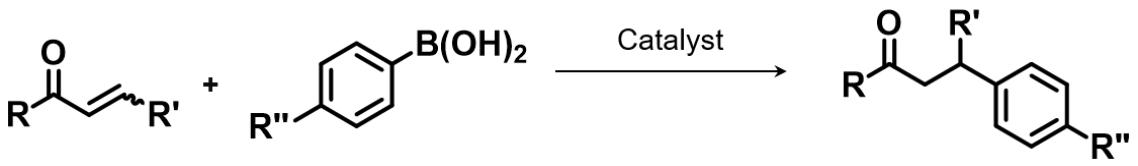

Scheme 4.1. 1,4-Arylation of α,β-unsaturated ketones with arylboronic acids.

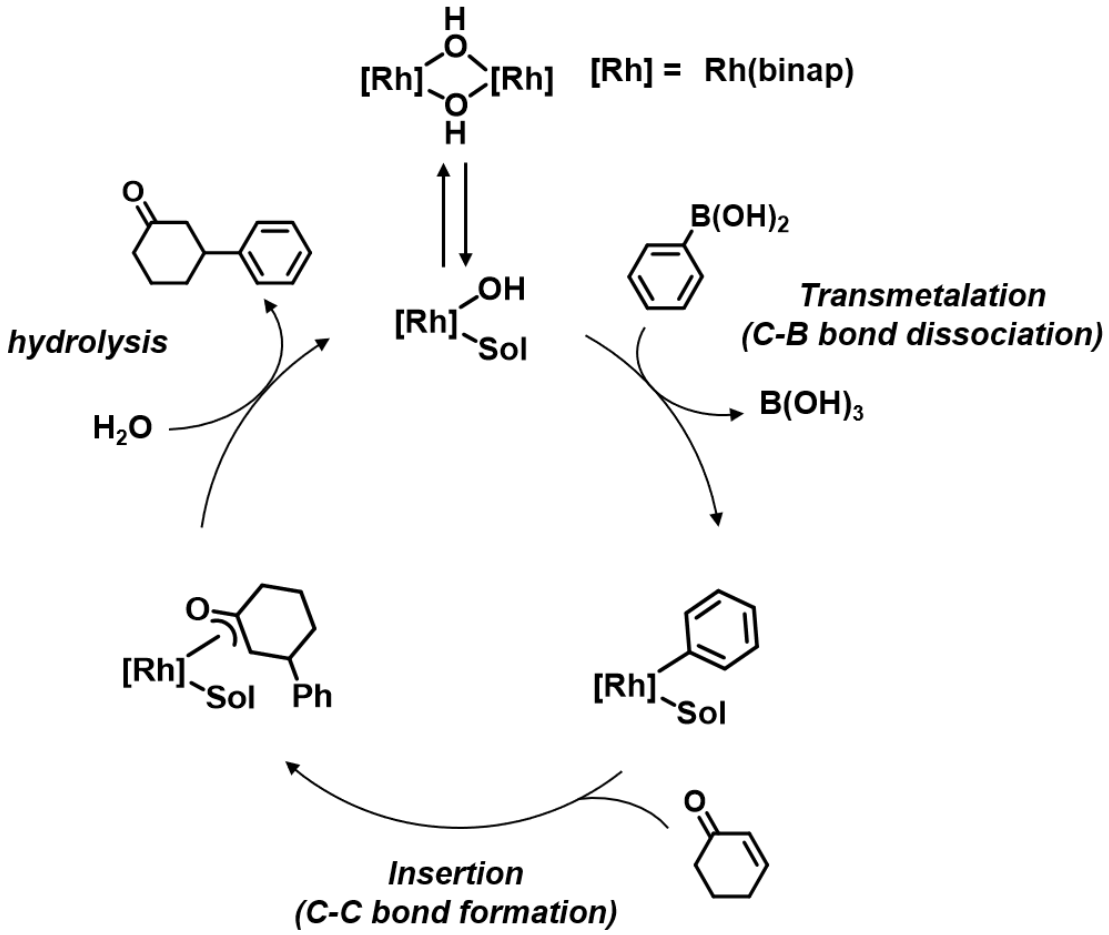

Scheme 4.2. The proposed reaction mechanism of 1,4-arylation of cyclohexenone with phenylboronic acids on a Rh-BINAP catalyst.[20]

4.1.3. The aim of this research

In this chapter, I focused on the surface functionalization of Rh nanoclusters with NHC ligands and their catalytic induction.[21] The ceria catalyst that incorporates Cr and Rh ($Cr_{0.19}Rh_{0.06}CeO_z$) is a unique material that forms small Rh nanoclusters and $Cr(OH)_3$ species on its surface via a simple hydrogen reduction as discussed in Section 2.3.2. H_2-reduced $Cr_{0.19}Rh_{0.06}CeO_z$ (denoted as *r*-$Cr_{0.19}Rh_{0.06}CeO_z$) is a good candidate for investigating the effect of direct modification with NHC on Rh nanoclusters and $Cr(OH)_3$ on the surface structures and catalytic performance. I prepared ICy-decorated *r*-$Cr_{0.19}Rh_{0.06}CeO_z$ (ICy-*r*-$Cr_{0.19}Rh_{0.06}CeO_z$) by the direct decoration method and revealed that ICy-*r*-$Cr_{0.19}Rh_{0.06}CeO_z$ exhibited the substantial catalytic activity for the 1,4-arylation reaction of cyclohexenone with phenylboronic acid, whereas *r*-$Cr_{0.19}Rh_{0.06}CeO_z$ without ICy modification was inactive. The coordination structure of NHC ligands on the catalyst surface was characterized by Rh *K*-edge XAFS, FT-IR, XPS, and photoluminescence (PL) spectroscopy, and it was found that the ICy carbene-coordinated Rh nanoclusters were key active species. DFT calculations proposed the coordination of the ICy carbene to the Rh nanocluster induced an activity trigger for 1,4-arylation activity of *r*-$Cr_{0.19}Rh_{0.06}CeO_z$ by controlling adsorption sites.

4.2. Experimental section

4.2.1. Materials and instruments

N-heterocyclic carbene (NHC) precursor salts and their carbenes were abbreviated as listed in Table 4.1. NHC salts (ICy·HBF_4 (98.0%), I*t*Bu·HBF_4 (98.0%), and IMe·HCl (98.0%)), potassium *tert*-butoxide (KO*t*Bu, 97%), 2-cyclohexenone (96%), 4-methylphenylboronic acid (97.0%), and cyclohexylboronic acid (97.0%), tetrahydrothiophene (99.0%) were purchased form Tokyo Chemical Industry. Phenylboronic acid ($PhB(OH)_2$, 95.0%), 2-cyclopentenone (97.0%), benzylideneacetone (97.0%), 4-methoxyphenylboronic acid (96%), 4-chlorophenylboronic acid (95%), 4-trifluoromethylphenylboronic acid (96%), benzyl mercaptan (96%), triphenylphosphine (97.0%), dodecane (internal standard for GC, 99.0%), adamantane (internal standard for ^1H NMR, 99.0%) and super dehydrated solvents (toluene (99.5%), dichloromethane (99.5%), cyclohexane (99.5%), ethanol (EtOH, 99.5%), and tetrahydrofuran (THF, stabilizer free, 99.5%)) were purchased from Wako Chemicals. 4-Hexen-3-one (98%) was purchased from BLDpharm. 3-Phenylcyclohexanone (97%) was purchased from Chem-Impex International. IMe·HBF_4 was prepared by anion exchange of IMe·HCl according to the literature.[22] IBn·HBF_4 and IMes·HBF_4 were prepared according to the literature.[23] Rh(ICy)(cod)(OH) (cod: 1,5-cyclooctadiene) was prepared from $[Rh(cod)Cl]_2$ (Strem Chemicals, 98%) according to the literature.[19b] Toluene-d_8 was purchased from Wako Chemicals, and it was distilled with calcium dihydride (CaH_2, Wako Chemicals) under N_2 atmosphere, and was stored under an argon (Ar) atmosphere before use. Chloroform-*d* ($CDCl_3$) was purchased from Cambridge Isotope Laboratories. The purchased chemicals were used without further purification unless noted. Chemicals for the preparation of $Cr_{0.19}Rh_{0.06}CeO_z$, $Rh_{0.04}CeO_z$, $Cr_{0.17}CeO_z$, and CeO_2 were purchased from Sigma-Aldrich and Wako Chemicals. H_2 gas of G1 grade (99.99995%) was used for reducing the oxides. CO (G1 grade, 99.95%) and CO_2 (G1 grade, 99.995%) gases were used for estimating Rh dispersion.

A high-vacuum glass line with dry N_2 and a glove box with dry Ar were used for experiments under inert conditions. ^1H and ^{13}C NMR spectra were measured by JNM-ECA600 (JEOL) to determine the purity of the products.

Table 4.1. Abbreviations of NHC Precursors

Abbreviation	Name
ICy·HBF_4	1,3-Dicyclohexylimidazolium tetrafluoroborate
IMe·HBF_4	1,3-Dimethylimidazolium tetrafluoroborate
IMe·HCl	1,3-Dimethylimidazolium chloride
I*t*Bu·HBF_4	1,3-Di-*tert*-butylimidazolium tetrafluoroborate
IBn·HBF_4	1,3-Dibenzylimidazolium tetrafluoroborate
IMes·HBF_4	1,3-Bis(2,4,6-trimethylphenyl)imidazolium tetrafluoroborate
ICy	1,3-Dicyclohexylimidazol-2-ylidene
IMe	1,3-Dimethylimidazol-2-ylidene
I*t*Bu	1,3-Di-*tert*-butylimidazol-2-ylidene
IBn	1,3-Dibenzylimidazol-2-ylidene
IMes	1,3-Bis(2,4,6-trimethylphenyl)imidazol-2-ylidene

4.2.2. Preparation of NHC-decorated ceria catalysts incorporating Cr and Rh

Preparation of free NHCs

All procedures for NHC decoration were performed under a N_2 or an Ar atmosphere, and all glass equipment was preheated and dried with a heat gun in vacuo before use. NHC·HBF_4, KO*t*Bu (1.2 equiv.), and dry toluene were added to a Schlenk tube (Table 4.2), and then the mixture was stirred for 4 h at room temperature. The solution was filtered with a dry Celite column to obtain a 13 mM NHC-toluene solution.

An ICy-toluene solution prepared by the above procedure was evaporated to obtain free solid ICy carbene for $^1H/^{13}C$ NMR, FT-IR, and XPS measurements.

The quantitative formation of ICy carbene was checked by ^1H NMR in toluene-d_8. ICy·HBF_4 (3 mg, 0.01 mmol), KO*t*Bu (2 mg, 0.02 mmol), and toluene-d_8 (1.0 mL, 0.005 mmol) with adamantane (0.5 mM) was added to an NMR tube and sealed with a Teflon cap under an Ar atmosphere. The mixture was sonicated for 4 h at room temperature, and ^1H NMR was measured.

Table 4.2. Preparation Conditions for the 13 mM NHC-Toluene Solution

NHC·HBF_4	Amount of NHC·HBF_4 /mg (mmol)	Amount of KO*t*Bu /mg (mmol)	Volume of toluene /mL
ICy·HBF_4	82 (0.26)	35 (0.31)	20.0
IMe·HBF_4	47 (0.26)	35 (0.31)	20.0
I*t*Bu·HBF_4	68 (0.25)	34 (0.31)	20.0
IBn·HBF_4	21 (0.062)	8.5 (0.076)	5.0
IMes·HBF_4	25 (0.064)	8.8 (0.078)	5.0

Preparation of the reduced $Cr_{0.19}Rh_{0.06}CeO_z$ and control oxides and the estimation of Rh dispersion

The preparation procedure of $Cr_{0.19}Rh_{0.06}CeO_z$, $Rh_{0.04}CeO_z$, $Cr_{0.17}CeO_z$, and CeO_2 was described in Section 2.2.2.

The oxides were reduced with H_2 (40 kPa) at 573 K for 1 h (ramp rate: 5 K min^{-1}), and kept under an Ar atmosphere before NHC decoration (Scheme 4.3). The reduced oxides are denoted as *r*-$Cr_{0.19}Rh_{0.06}CeO_z$, *r*-$Rh_{0.04}CeO_z$, *r*-$Cr_{0.17}CeO_z$, and *r*-CeO_z, respectively.

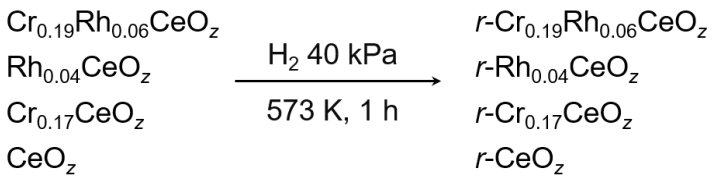

Scheme 4.3. Preparation scheme of *r*-$Cr_{0.19}Rh_{0.06}CeO_z$, *r*-$Rh_{0.04}CeO_z$, *r*-$Cr_{0.17}CeO_z$, and *r*-CeO_z.

The number of Rh atoms exposed at the outermost surface (Table 4.3) was estimated by CO adsorption.[24] The as-prepared oxide (500 mg) was added in a glass cell, and the cell was connected to a closed glass equipment. The system was first evacuated and charged with H_2 (27 kPa), and the cell was heated to 573 K (ramp rate: 5 K min^{-1}). After heating for 1 h, gases were evacuated and the cell was cooled down to room temperature. Then, CO_2 (21 kPa) was introduced and the remained gas was evacuated. After that, CO (21 kPa) was introduced and the amount of adsorbed CO was monitored by a difference in a pressure gauge.

Table 4.3. Amounts of Surface Rh Species and its Dispersity of *r*-$Cr_{0.19}Rh_{0.06}CeO_z$ and *r*-$Rh_{0.04}CeO_z$ Estimated from CO Adsorption

Sample	Outermost surface Rh amount[a] /$mmol_{Rh}$ g^{-1}	Rh dispersion %[b]
r-$Cr_{0.19}Rh_{0.06}CeO_z$	0.102 ± 0.006	33.7 ± 2.0
r-$Rh_{0.04}CeO_z$	0.008 ± 0.001	2.5 ± 0.4

[a] Outermost surface Rh = adsorbed CO/2.

[b] Rh dispersion % = outermost surface Rh / contained Rh amount in sample×100%

NHC decoration on the reduced $Cr_{0.19}Rh_{0.06}CeO_z$ and control oxides

A typical NHC decoration procedure on ICy-decorated *r*-$Cr_{0.19}Rh_{0.06}CeO_z$ was as follows (Scheme 4.4). All procedures were performed under a N_2 or an Ar atmosphere. The 13 mM ICy-toluene solution (3.0 mL) was added to *r*-$Cr_{0.19}Rh_{0.06}CeO_z$ (960 mg) in a Schlenk tube. After stirring for 1 h, the mixture was allowed to stand to collect the precipitate, and the upper solution was removed. The remaining solid was dried under vacuum. The prepared catalyst is denoted as ICy-*r*-$Cr_{0.19}Rh_{0.06}CeO_z$ (ICy loading: 0.8 wt%). The other NHC-decorated oxides were prepared in a similar way by adjusting the amount of the 13 mM NHC-toluene solution using different reduced oxides (Table 4.4).

ICy·HBF_4-decorated *r*-$Cr_{0.19}Rh_{0.06}CeO_z$ was also prepared by a similar method mentioned above using a 13 mM ICy·HBF_4-dichloromethane solution. The prepared catalyst is denoted as ICy·HBF_4-*r*-$Cr_{0.19}Rh_{0.06}CeO_z$ (ICy·HBF_4 loading: 1.0 wt%).

The loading amounts of NHC ligands were measured by thermogravimetric analysis (TGA; TGA550, TA Instruments). A sample (5-15 mg) was loaded into a Pt pan and changes in the weights of the samples were recorded during heating from 303 to 773 K (10 K min^{-1}) in an air flow. The NHC loading amounts were determined by the weight decreases from 403 to 623 K.

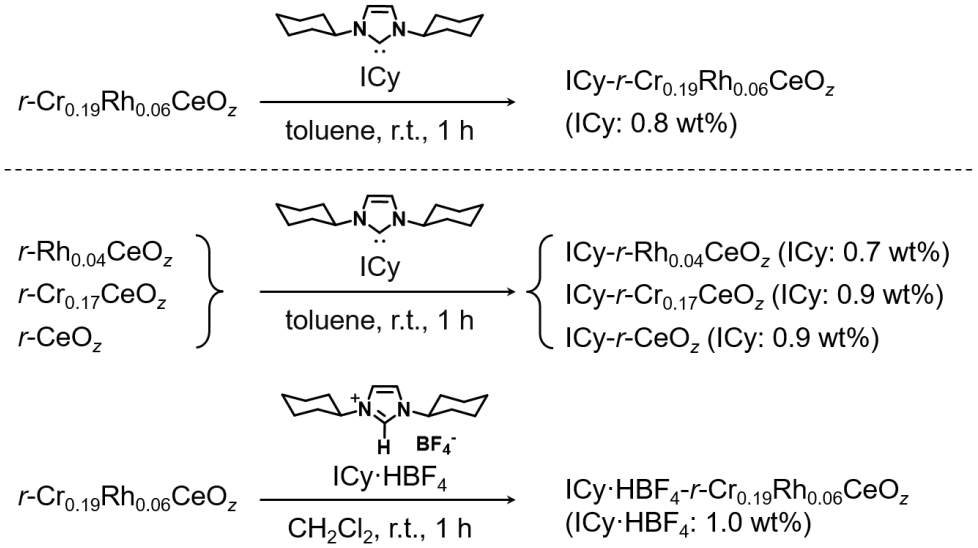

Scheme 4.4. Preparation scheme of ICy-*r*-$Cr_{0.19}Rh_{0.06}CeO_z$ and reference catalysts.

Table 4.4. Preparation Conditions for the NHC-Decorated Oxides

Prepared catalyst (NHC ligands wt%[a], Rh wt%)	Volume of the NHC solution /mL	Amount of reduced oxide /mg
ICy-*r*-$Cr_{0.19}Rh_{0.06}CeO_z$ (0.8 wt%, 3.3 wt%,)	3.0	960
ICy-*r*-$Rh_{0.04}CeO_z$ (0.7 wt%, 2.2 wt%)	3.0	960
ICy-*r*-$Cr_{0.17}CeO_z$ (0.9 wt%)	3.0	960
ICy-*r*-CeO_z (0.9 wt%)	3.0	960
ICy-*r*-$Cr_{0.19}Rh_{0.06}CeO_z$ (0.3 wt%, 3.3 wt%)	0.35	448
ICy-*r*-$Cr_{0.19}Rh_{0.06}CeO_z$ (0.4 wt%, 3.3 wt%)	0.50	320
ICy-*r*-$Cr_{0.19}Rh_{0.06}CeO_z$ (1.6 wt%, 3.3 wt%)	10.0	400
IMe-*r*-$Cr_{0.19}Rh_{0.06}CeO_z$ (0.5 wt%, 3.3 wt%)	1.0	320
I*t*Bu-*r*-$Cr_{0.19}Rh_{0.06}CeO_z$ (0.8 wt%, 3.3 wt%)	1.0	320
IBn-*r*-$Cr_{0.19}Rh_{0.06}CeO_z$ (1.1 wt%, 3.3 wt%)	0.63	200
IMes-*r*-$Cr_{0.19}Rh_{0.06}CeO_z$ (1.5 wt%, 3.3 wt%)	0.63	200
ICy·HBF_4-*r*-$Cr_{0.19}Rh_{0.06}CeO_z$ (1.0 wt%[b], 3.3 wt%)	1.0	320

[a] The amounts of NHC ligands were determined by TGA.

[b] The values were calculated as ICy·HBF_4.

4.2.3. Structural characterizations of ICy-*r*-$Cr_{0.19}Rh_{0.06}CeO_z$

FT-IR

FT-IR spectra were measured by an FT-IR spectrometer (FT/IR-4200, JASCO). Prepared catalysts (20 mg) were loaded on a copper mount in a cell with a CaF_2 window under an Ar atmosphere, and the FT-IR spectra were measured in diffuse reflectance mode at a resolution of 4 cm^{-1} with 512 scans. Free ICy carbene and ICy·HBF_4 were sandwiched with KBr plates under an Ar atmosphere and an air atmosphere, respectively, and the FT-IR spectra were measured in transmission mode at a resolution of 4 cm^{-1} with 128 scans.

XAFS

XAFS spectra at the Rh *K*-edge were measured in transmission mode at room temperature at the NW10A station of the Photon Factory (PF) at KEK-IMSS (Tsukuba, Japan) and at the BL11S2 station of the Aichi Synchrotron Radiation Center (Aichi SR, Seto, Japan). The energy and current of the electrons in the storage ring were 6.5 GeV and 60 mA at the PF, and 1.2 GeV and 300 mA at the Aichi SR, respectively. X-rays from the storage ring were monochromatized with a Si(311) double-crystal monochromator. At the NW10A station of the Photon Factory, two ionization chambers filled with pure Ar and krypton (Kr) gases were used to monitor the incident and transmitted X-rays, respectively. At the BL11S2 station of the Aichi SR, two ionization chambers filled with pure Ar and a mixture of Ar and Kr gases (8.5/1.5, v/v) were used to monitor the incident and transmitted X-rays, respectively. Rh foil and Rh_2O_3 (diluted with boron nitride) were used as references. Samples were grounded and packed into a cell (4 mmϕ, 32 mg), and the cell was sealed with Kapton films under an Ar atmosphere.

XAFS spectra were analyzed using ATHENA and ARTEMIS with IFEFFIT (version 1.2.11).[25] The threshold energy was tentatively set at the inflection point for the Rh *K*-edge (Rh foil: 23219.8 eV).[26] Background subtraction was performed using the Autobk method and the spline smoothing algorithm in ATHENA.[27] The k^3-weighted extended XAFS (EXAFS) oscillations were Fourier transformed into *R*-space. Curve-fitting analysis was carried out in the *R*-space. Fitting parameters for each shell were coordination number (CN), interatomic distance (*R*), Debye–Waller factor (σ^2; mean-square displacement), and correction-of-edge energy (ΔE_0). For the Rh *K*-edge, S_0^2 was 1 based on the fitting of Rh foil, and S_0^2 for Rh_2O_3 was fitted to be 0.92, which was rounded to 1. Phase shifts and backscattering amplitudes for Rh–O and Rh–Rh were calculated with FEFF 8 code[28] using structural parameters obtained from the crystal structures of Rh[29] and Rh_2O_3[30].

XPS

XPS was performed using an X-ray photoelectron spectrometer (Scienta Omicron R4000, base pressure: 4×10^{-8} Pa) with the monochromatized Al K_α X-ray source (Scienta Omicron MX650, photon energy: 1486.7 eV, power: 180 W). Catalyst samples were grounded and pressed into pellet disks (10 mmϕ, 20 mg, pressed at 20 MPa), which were attached to the cell holder with a carbon tape under an Ar atmosphere. Free ICy carbene, ICy·HBF_4, and Rh(ICy)(cod)(OH) were directly pasted on a carbon tape on the cell holder under an Ar atmosphere. These samples were directly transferred to the XPS measurement chamber without exposure to air. Spectra were measured with a pass energy of 200 eV and a step size of 0.1 eV. Binding energies were referenced to the Au $4f_{7/2}$ peak of metallic Au foil (83.96 eV).[31] The Shirley background was subtracted, and each peak was fitted by the Voigt function.[32]

Photoluminescence spectroscopy

Photoluminescence spectra were measured by a spectrofluorometer (PF-6600, JASCO) with an excitation wavelength of 240 nm for solid state measurements and 268 nm for solution state measurements. For solid-state photoluminescence analysis, a solid sample (100 mg) was diluted with polytetrafluoroethylene (PTFE) powder (400 mg) treated at 523 K for 24 h under vacuum and sealed in a quartz cell under an Ar atmosphere (Figure 4.5). For solution-state photoluminescence analysis, a Rh complex was diluted to 1.0×10^{-3} M in THF.

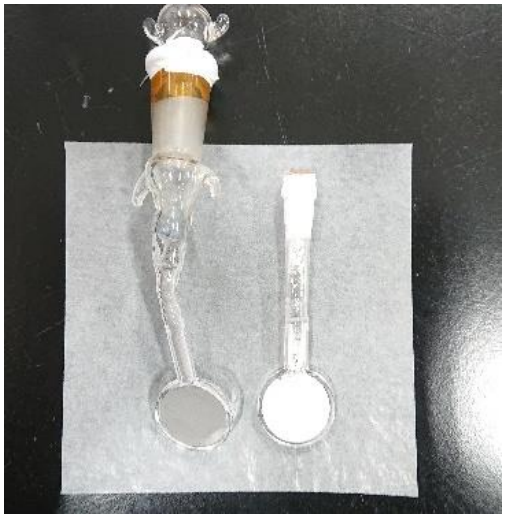

Figure 4.5. Quartz cells for solid-state photoluminescence measurements.

4.2.4. 1,4-Arylation reaction of α,β-unsaturated ketones with arylboronic acids

General procedure

All procedures were performed under a N_2 or an Ar atmosphere. The catalyst (32 mg) and phenylboronic acid (36 mg, 0.30 mmol) were added to a 20 mL Schlenk tube. A stock solution of 2-cyclohexenone (19 μL, 0.20 mmol), dodecane (23 μL, 0.10 mmol), cyclohexane (2.0 mL), and ethanol (0.2 mL) was added to the reactor. The reactor was tightly capped, and then it was heated to 343 K for 12 h. As for time-course experiments, the reactor was equipped with a balloon containing N_2, and then it was heated to 343 K. The reaction solutions were sampled at appropriate intervals. Products were quantified by gas chromatography (GC-2014 Shimadzu; InertCap 5 column, 0.25 μm × 0.25 mm × 30 m) equipped with hydrogen flame ionization detector (FID) from standard curves as shown in Figure 4.6.

The amount of phenyboronic acid was changed from 0.30 mmol to 0.20 mmol and 0.10 mmol, respectively, to obtain the dependency of the reaction rate for the product yield on the concentration of phenylboronic acid. The reaction temperature was changed from 343 K to 338 K, 333 K, and 328 K, respectively, to obtain the Arrhenius plot.

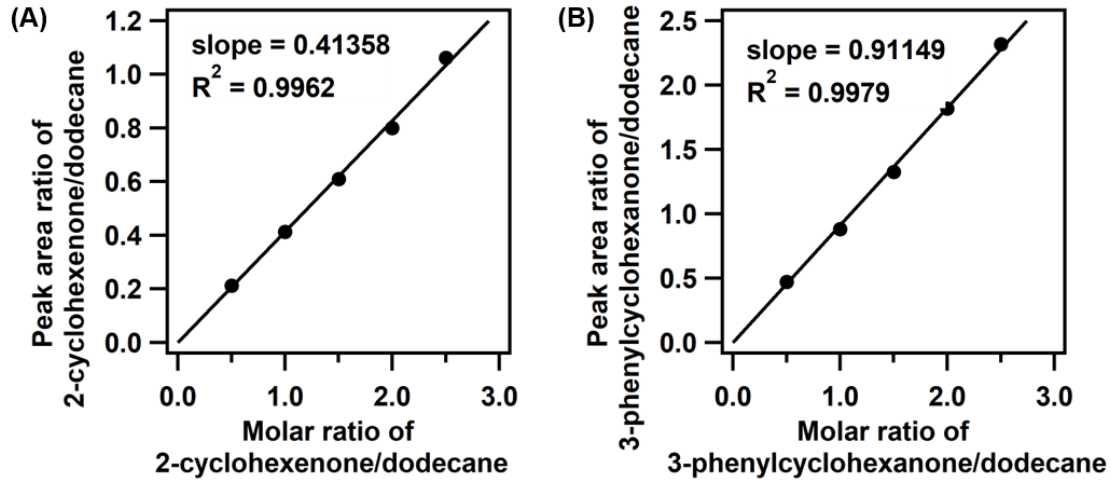

Figure 4.6. Standard curves of (A) 2-cyclohexenone and (B) 3-phenylcyclohenxanone.

Examination of substrate scope

All procedures were performed under a N_2 or an Ar atmosphere. The catalyst (32 mg) and the corresponding arylboronic acid (0.30 mmol) were added to a 20 mL Schlenk tube under Ar. The corresponding α,β-unsaturated ketone (0.20 mmol), cyclohexane (2.0 mL), and ethanol (0.2 mL) was added to the reactor under N_2. The reactor was tightly capped, and then it was heated to 343 K for 12 h.

After the reaction mixture was cooled to room temperature, the reaction mixture was filtered and washed with cyclohexane (3×2.0 mL), and the solvents were evaporated. The volatile products were quantified by ^{1}H NMR (600 MHz, $CDCl_3$) with ethyl acetate (20 μL, 0.20 mmol) as an internal standard. As for the other products, the residues were purified by flash column chromatography with medium pressure liquid chromatograph (YFLC AI-580, Yamazen Corporation, Silica: HI-FLASH column) with 5-20% ethyl acetate in *n*-hexane to afford the products. The ^{1}H/^{13}C NMR charts of the isolated products are listed in Section 4.6.

4.2.5. Heterogeneity tests for 1,4-arylation reaction of cyclohexenone with phenylboronic acid on ICy-*r*-$Cr_{0.19}Rh_{0.06}CeO_z$

Hot-filtration test[33]

All procedures were performed under a N_2 or an Ar atmosphere. The 1,4-arylation reaction was initiated according to the general procedure. The catalyst was separated by hot filtration with a syringe filter 3 h after starting the reaction. The filtrate was kept at 343 K in another 20 mL Schlenk tube to restart the reaction. Products were quantified by FID-GC (GC-2014, Shimadzu; InertCap 5 column, 0.25 μm × 0.25 mm × 30 m).

Mass spectrometry detection[33a]

All procedures were performed under a N_2 or an Ar atmosphere. The 1,4-arylation reaction was initiated according to the general procedure, and the reaction solution was hot-filtered after the reaction times of 3 h and 12 h at 343 K. After diluting the solution with a solvent (cyclohexane/ethanol = 10/1 (v/v)), the solution was analyzed by mass spectrometry (ESI-MS, compact, Bruker).

Mercury drop test[33]

All procedures were performed under a N_2 or an Ar atmosphere. The 1,4-arylation reaction was initiated according to the general procedure. A 10 μL droplet of Hg (68 equivs with respect to Rh) was added to the reaction mixture 3 h after starting the reaction. The reaction solutions were sampled at appropriate intervals. Products were quantified by FID-GC (GC-2014, Shimadzu; InertCap 5 column, 0.25 μm × 0.25 mm × 30 m).

Stoichiometric poisoning test[33]

All procedures were performed under a N_2 or an Ar atmosphere. The catalyst (32 mg) and phenyl boronic acid (36 mg, 0.30 mmol) were added to a 20 mL Schlenk tube. A stock solution of 2-cyclohexenone (19 μL, 0.20 mmol), dodecane (23 μL, 0.10 mmol), poison (benzyl mercaptan (1.2 μL, 0.010 mmol or 0.35 μL, 0.003 mmol), tetrahydrothiophene (0.88 μL, 0.010 mmol or 0.26 μL, 0.003 mmol), or triphenylphosphine (2.6 mg, 0.010 mmol or 0.81 mg, 0.003 mmol)), cyclohexane (2.0 mL), and ethanol (0.2 mL) was added to the reactor, and the reactor was tightly capped. After stirring for 2.5 h at room temperature, it was heated to 343 K for 12 h. Products were quantified by FID-GC (GC-2014, Shimadzu; InertCap 5 column, 0.25 μm × 0.25 mm × 30 m).

Leaching test[33]

All procedures were performed under a N_2 or an Ar atmosphere. The 1,4-arylation reaction was initiated according to the general procedure, and the reaction solution was hot-filtered after the reaction at 343 K for 24 h. The filtrate was evaporated and dissolved with fuming nitric acid at 353 K. Leached metals in the filtrate were quantified by ICP-OES (Vista-PRO, Varian Inc.). The measurement wavelengths were as follows; Cr: 267.716 nm, Rh: 343.448 nm, Ce: 418.659 nm.

4.2.6. Theoretical calculations

Computational methods for simulating FT-IR spectra

Vibrational frequencies of ICy and $ICyH^+$ were calculated by density functional theory (DFT) with the Gaussian16 (Rev. C. 01) suite of programs.[34] The electron exchange–correlation was treated by Becke's three–parameter hybrid exchange functional and the Perdew and Wang correlation functional (B3PW91).[35] The 6–31+G(d,p) basis sets were employed for all atoms.[36] The molecular structures were fisty fully optimized, and after the energies were confirmed to be minimum by showing that no imaginary frequency was appeared, vibrational frequencies were calculated. The calculated frequencies were multiplied by the scale factor (0.9602 for B3PW91/6–31+G(d,p)) to correct anharmonicity effects.[37]

Computational methods for calculating the modelled structure of ICy-*r*-$Cr_{0.19}Rh_{0.06}CeO_z$ and reaction profiles

Spin-polarized DFT calculations were performed with Vienna ab initio simulation package (VASP) version 5.4.4.[38] The projector augmented wave (PAW) method described the interactions between ion cores and electrons.[39] The electron exchange–correlation was treated with the Perdew–Burke–Ernzerhof functional of the generalized gradient approximation with a Hubbard-like parameter (PBE-GGA+U) to represent the nature of the 4d electrons of Rh and 4f electrons of Ce.[40] The U_{eff} values were set to 3.3 and 6.3 eV for the Rh 4d and Ce 4f states, respectively.[41] The DFT-D3 dispersion scheme using Becke–Johnson damping was adopted.[42] The calculations were carried out using plane wave basis sets with a cutoff energy of 600 eV. Because of the relatively large unit cell size described below, the sampling of the Brillouin zone was restricted to the Γ point only. The convergence threshold for the self-consistent field iteration was set to 1.0×10^{-5} eV. The convergence of the structural optimization was determined when the maximum forces on unconstrained atoms were less than 0.05 eV $Å^{-1}$. The atomic charge was calculated by the Bader analysis algorithm.[43]

To obtain the transition-state structure for each step in the catalytic process, we used the climbing image-nudged elastic band (CI-NEB) method,[44] as implemented in VASP through the VTST Tools. The spring constant between adjacent NEB images was set to 5.0 eV/Å. The other calculation conditions were the same as those used for the geometry optimization calculation mentioned above.

Structural modelling of ICy-*r*-$Cr_{0.19}Rh_{0.06}CeO_z$ (ICy-Rh_4/CeO_2(111))

CeO_2 supports were modelled as a periodic slab model of the (4 × 4) stoichiometric CeO_2(111) surface without oxygen defects. The slab model consisted of two CeO_2 trilayers (O–Ce–O) with 96 atoms. A unit cell size of 15.50 × 15.50 × 21.33 Å with a vacuum space of 15 Å was used to minimize the interactions between the periodically repeated crystal faces. To focus on the interaction between Rh species and ICy ligands of ICy-*r*-$Cr_{0.19}Rh_{0.06}CeO_z$, a rhodium cluster consisting of four Rh atoms (Rh_4) with a pyramidal structure was placed on a hollow site of the CeO_2(111) surface, except for Cr species (denoted as Rh_4/CeO_2). According to previous theoretical studies,[45] the pyramidal Rh_4 cluster was more stable than the planar Rh_4 cluster on the CeO_2(111) surface. This structure corresponded to the CNs of the Rh–O bonds and Rh–Rh bonds from Rh *K*-edge EXAFS curve-fitting analysis of *r*-$Cr_{0.19}Rh_{0.06}CeO_z$ with and without ICy. The most stable adsorption site of the ICy ligand was evaluated by comparing Rh_4/CeO_2 with the ICy ligand adsorbed on a bridge site, hollow site, and top site of the Rh_4 cluster. The most stable Rh_4/CeO_2 with the ICy ligand adsorbed on a bridge site (denoted as ICy-Rh_4/CeO_2) was used for Bader charge analysis and reaction profile calculations. During calculations, only the molecules, the Rh_4 cluster, and the topmost CeO_2 trilayer of the slab surface were allowed to relax fully, while the bottom CeO_2 trilayer of the slab was kept fixed in its bulk position.

4.3. Results and discussions

4.3.1. Coordination structure of NHC on *r*-$Cr_{0.19}Rh_{0.06}CeO_z$

ICy-*r*-$Cr_{0.19}Rh_{0.06}CeO_z$ and reference catalysts were prepared by a simple decoration method with *in situ* generated NHC solutions. Loading amounts of NHC in NHC-*r*-$Cr_{0.19}Rh_{0.06}CeO_z$ was evaluated by TGA as shown in Figure 4.7. The weight loss of NHC-*r*-$Cr_{0.19}Rh_{0.06}CeO_z$ increased with the increasing in the loading amount of NHC, which includes the removal of NHC. The NHC loading amounts were estimated from the weight decreases from 403 to 623 K minus those of corresponding oxides undecorated with NHC ligands as listed in Table 4.5.

The addition of Cr species was key to produce novel small Rh nanoclusters on the surface of $Cr_{0.19}Rh_{0.06}CeO_z$ together with the formation of $Cr(OH)_3$ species by the reduction with H_2 below 423 K as described in Section 2.3.2. Rh *K*-edge EXAFS of *r*-$Cr_{0.19}Rh_{0.06}CeO_z$ indicated the formation of the similar Rh nanoclusters with the coordination number (CN) of 2.8 ± 0.4 for Rh−Rh bonds despite the treatment with H_2 at higher temperature of 573 K as shown in Figure 4.8 (A-b, B-b) and Table 4.6. After the ICy decoration, the CN of Rh−Rh bonds for ICy-*r*-$Cr_{0.19}Rh_{0.06}CeO_z$ was curve-fitted to be 2.8 ± 0.3 from Rh *K*-edge EXAFS (Figure 4.8 (A-a, B-a), Table 4.6). This CN value was similar to that of *r*-$Cr_{0.19}Rh_{0.06}CeO_z$ without ICy, indicating that the structure of the Rh nanocluster remained unchanged after the ICy decoration. After the decoration of a ICy·HBF_4 salt, the structure of the Rh nanocluster also remained unchanged (Figure 4.8 (A-c, B-c), Table 4.6). Without Cr, the size of Rh nanoclusters was large (Figure 4.8 (A-d, B-d), Table 4.6).

FT-IR spectra were measured to determine whether the attached ICy ligands existed as carbenes. The obtained FT-IR spectra are shown in Figure 4.9, and their peak assignments are listed in Table 4.7. Although the spectrum of *r*-$Cr_{0.19}Rh_{0.06}CeO_z$ without ICy showed no peak between 1100 and 1300 cm^{-1} (Figure 4.9 (a)), a broad FT-IR peak at 1194 cm^{-1} appeared in the spectrum of ICy-*r*-$Cr_{0.19}Rh_{0.06}CeO_z$ (Figure 4.9 (b)), the position of which was larger in wavenumber than that of ICy·HBF_4-*r*-$Cr_{0.19}Rh_{0.06}CeO_z$ at 1152 cm^{-1} (Figure 4.9 (c)). In comparison of the FT-IR spectra of ICy and ICy·HBF_4 and the DFT calculations of the modelled molecules, the characteristic peak at 1194 cm^{-1} was assigned to the asymmetric in-plane rocking vibration mode at the N-heterocycle of the ICy carbene species, indicating that the decorated ICy was present as the carbene species to the surface of ICy-*r*-$Cr_{0.19}Rh_{0.06}CeO_z$.

N 1s XPS spectra and their curve-fitting analyses unveiled the presence of ICy carbene interacting with the Rh nanoclusters of ICy-*r*-$Cr_{0.19}Rh_{0.06}CeO_z$ as shown in Figure

4.10 and Table 4.8. The N 1s XPS spectrum of ICy-*r*-$Cr_{0.19}Rh_{0.06}CeO_z$ contained a large peak at 400.6 eV (peak β) and two smaller peaks at 398.9 eV (peak α) and 402.3 eV (peak γ) (Figure 4.10 (b)). Peak α was attributed to the adsorbed NH_3 species by comparing with the N 1s peaks of *r*-$Cr_{0.19}Rh_{0.06}CeO_z$ (Figure 4.10 (a)).[46] The intensity of peak β (400.6 eV) of ICy-*r*-$Cr_{0.19}Rh_{0.06}CeO_z$ was much larger than that of *r*-$Cr_{0.19}Rh_{0.06}CeO_z$ (400.4 eV, NH_4^+ derived from the reduction of nitrate salts[46]) (Figure 4.11). The peak β was in the region for the NHCs interacting with reduced metallic species (400.2–401.2 eV)[4j,k,m,5j,o,47,48], the increased intensity of which suggested the presence of ICy carbene species interacting with Rh nanoclusters. The N 1s binding energy of 400.4 eV for Rh(ICy)(cod)(OH) supported the assignment of peak β (Figure 4.10 (h)). The peak γ was at higher binding energies of 402.3 eV, and it was attributed to an ICy carbene coordinating to a cationic metal species (*e.g.*, Cr^{3+} of $Cr(OH)_3$ and Ce^{3+}).[49] ICy·HBF_4-*r*-$Cr_{0.19}Rh_{0.06}CeO_z$ without the carbene formation treatment showed another peak δ at 401.9 eV (Figure 4.10 (c)), and the binding energy of peak δ was comparable to that of ICy·HBF_4 (Figure 4.10 (f)), indicating the peak δ was attributed to $ICyH^+$.[5j] ICy-*r*-$Cr_{0.17}CeO_z$ without the Rh nanoclusters showed an increase in the intensity of peak α at 398.8 eV instead of peak β (Figure 4.10 (d, e)). The N 1s XPS peak of ICy carbene was observed at 399.3 eV (Figure 4.10 (g)), and the increase in the intensity of peak α in ICy-*r*-$Cr_{0.17}CeO_z$ was attributed to the free ICy carbene adsorbed on the surface (Figure 4.11). The absence of the increase in peak β in ICy-*r*-$Cr_{0.17}CeO_z$ strongly corroborated that the increase in peak β in ICy-*r*-$Cr_{0.19}Rh_{0.06}CeO_z$ was assigned to the ICy carbene coordinating to Rh species.

Characteristic emissions at 320 nm were observed in the photoluminescence (PL) spectra of ICy-*r*-$Cr_{0.19}Rh_{0.06}CeO_z$ and ICy-*r*-$Rh_{0.04}CeO_z$ (Figure 4.12), whereas no emission was observed at 320 nm for the spectrum of *r*-$Cr_{0.19}Rh_{0.06}CeO_z$ without ICy decoration. Considering that the Rh(ICy)(cod)(OH) complex showed a PL signal at 314 nm (Figure 4.13), the PL signals at 320 nm also supported the interaction of the ICy carbene with the Rh nanoclusters on the surface.

A schematic of the surface coordination structure of ICy-*r*-$Cr_{0.19}Rh_{0.06}CeO_z$ based on the above surface characterizations is shown in Figure 4.14. Cr species assisted the production of the small Rh nanoclusters with the coordination sites for ICy, which can cause coordination-induced effects in efficient catalysis (See Section 4.3.2).

Coordination structures of other NHC ligands (IMe, I*t*Bu, IBn, and IMes) were also investigated by XAFS, FT-IR, and XPS. Rh *K*-edge EXAFS spectra and their curve-fitting analyses showed that the CN of Rh-Rh bonds were between 2.5 and 2.8 (Figure 4.15,

Table 4.9), indicating the decoration of the NHC ligands, independent of their structures, did almost not change the structure of the Rh nanocluster. FT-IR spectra of NHC-*r*-$Cr_{0.19}Rh_{0.06}CeO_z$ decorated with IMe, I*t*Bu, IBn, and IMes showed broad peaks at 1195, 1196, 1196, and 1203 cm^{-1} as shown in Figure 4.16, respectively, the positions of which were similar to that of the ICy carbene. Thus, the grafted NHC ligands were present as carbene forms. The structures of NHC ligands were similar in NHC-*r*-$Cr_{0.19}Rh_{0.06}CeO_z$; however, interaction of NHC ligands with the catalyst surface were different from ICy and the others, which were revealed from N 1s XPS as shown in Figure 4.17. The N 1s XPS spectra of NHC-*r*-$Cr_{0.19}Rh_{0.06}CeO_z$ of IMe, I*t*Bu, IBn, and IMes showed two peaks α, β in addition to a small or negligible peak γ, and the peak β was smaller than that of the peak α. The XPS peak of NHC-*r*-$Cr_{0.19}Rh_{0.06}CeO_z$ and their increases compared with *r*-$Cr_{0.19}Rh_{0.06}CeO_z$ were summarized in Figure 4.18, and the intensities of peak α distinctly increased, which was not observed in ICy-*r*-$Cr_{0.19}Rh_{0.06}CeO_z$. The largest increase in the peak β area of ICy-*r*-$Cr_{0.19}Rh_{0.06}CeO_z$ suggested the ICy carbene efficiently coordinated to the Rh nanoclusters.

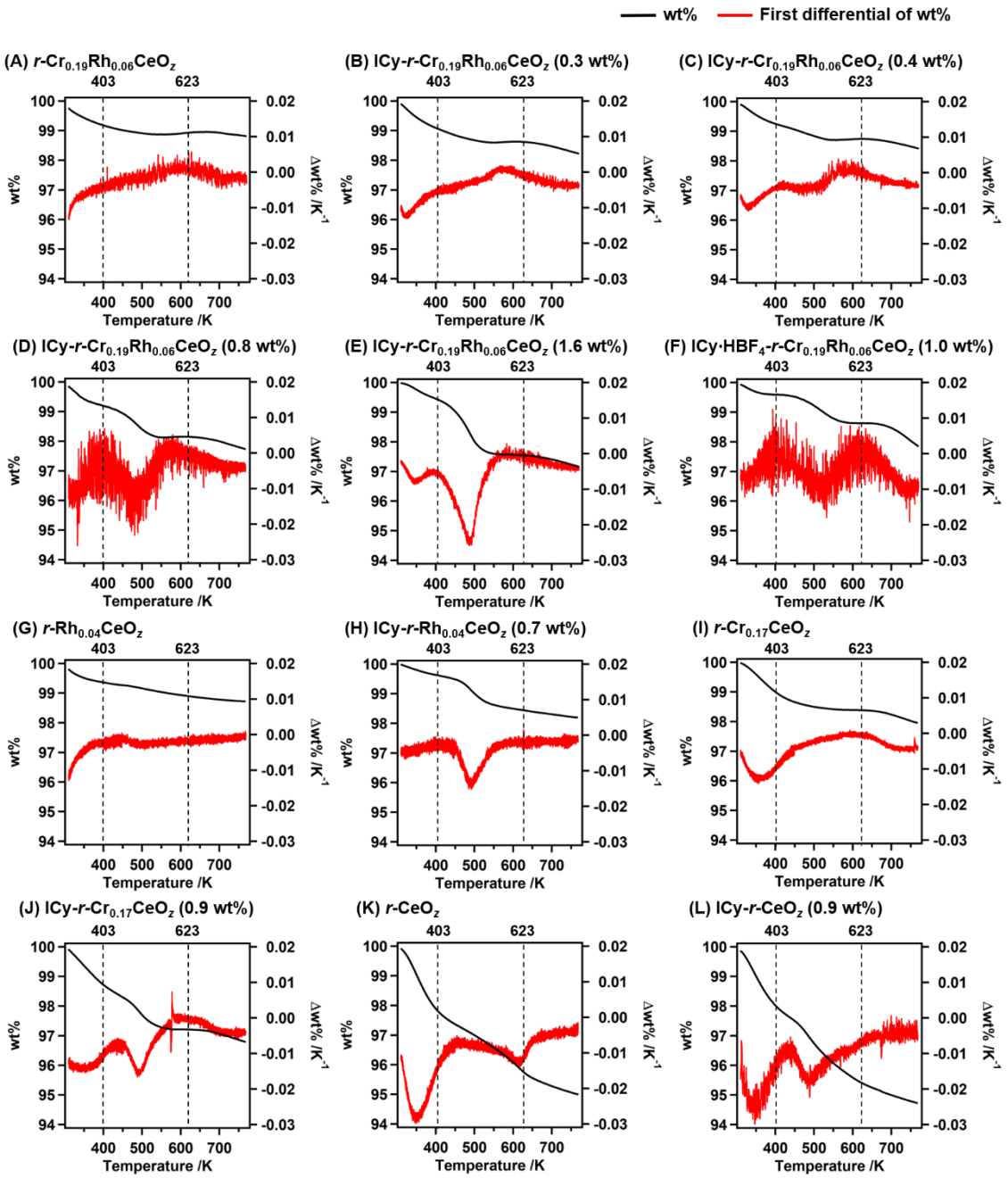

Figure 4.7. TGA curves (black) and their 1st differential plots (red) of (A) *r*-$Cr_{0.19}Rh_{0.06}CeO_z$, (B) ICy-*r*-$Cr_{0.19}Rh_{0.06}CeO_z$ (ICy: 0.3 wt%), (C) ICy-*r*-$Cr_{0.19}Rh_{0.06}CeO_z$ (ICy: 0.4 wt%), (D) ICy-*r*-$Cr_{0.19}Rh_{0.06}CeO_z$ (ICy: 0.8 wt%), (E) ICy-*r*-$Cr_{0.19}Rh_{0.06}CeO_z$ (ICy: 1.6 wt%), (F) ICy·HBF_4-ICy-*r*-$Cr_{0.19}Rh_{0.06}CeO_z$ (ICy·HBF_4: 1.0 wt%), (G) *r*-$Rh_{0.04}CeO_z$, (H) ICy-*r*-$Rh_{0.04}CeO_z$ (ICy: 0.7 wt%), (I) *r*-$Cr_{0.17}CeO_z$, (J) ICy-*r*-$Cr_{0.17}CeO_z$ (ICy: 0.9 wt%), (K) *r*-CeO_z, (L) ICy-*r*-CeO_z (ICy: 0.9 wt%).[21]

Table 4.5. Preparation Conditions and Characterization Data for the NHC-Decorated Oxides

Prepared catalyst (NHC ligands wt%, Rh wt%)	The amount of Rh /mmol g^{-1}	The estimated amount of NHC /mmol g^{-1}	NHC/surface Rh ratio
ICy-*r*-$Cr_{0.19}Rh_{0.06}CeO_z$ (0.8 wt%, 3.3 wt%,)	0.31	0.036	0.35
ICy-*r*-$Rh_{0.04}CeO_z$ (0.7 wt%, 2.2 wt%)	0.21	0.031	3.86
ICy-*r*-$Cr_{0.17}CeO_z$ (0.9 wt%)	–	0.038	–
ICy-*r*-CeO_z (0.9 wt%)	–	0.039	–
ICy-*r*-$Cr_{0.19}Rh_{0.06}CeO_z$ (0.3 wt%, 3.3 wt%)	0.31	0.011	0.11
ICy-*r*-$Cr_{0.19}Rh_{0.06}CeO_z$ (0.4 wt%, 3.3 wt%)	0.31	0.017	0.17
ICy-*r*-$Cr_{0.19}Rh_{0.06}CeO_z$ (1.6 wt%, 3.3 wt%)	0.31	0.071	0.70
IMe-*r*-$Cr_{0.19}Rh_{0.06}CeO_z$ (0.5 wt%, 3.3 wt%)	0.31	0.042	0.41
I*t*Bu-*r*-$Cr_{0.19}Rh_{0.06}CeO_z$ (0.8 wt%, 3.3 wt%)	0.31	0.043	0.42
IBn-*r*-$Cr_{0.19}Rh_{0.06}CeO_z$ (1.1 wt%, 3.3 wt%)	0.31	0.046	0.45
IMes-*r*-$Cr_{0.19}Rh_{0.06}CeO_z$ (1.5 wt%, 3.3 wt%)	0.31	0.050	0.49
ICy·HBF_4-*r*-$Cr_{0.19}Rh_{0.06}CeO_z$ (1.0 wt%[c], 3.3 wt%)	0.31	0.031[c]	0.31[c]

[a] The amounts of NHC ligands were determined by TGA. [b] NHC/Rh ratio = NHC loading ($mmol_{NHC}$ g^{-1}) / (Outermost surface Rh amount ($mmol_{Rh}$ g^{-1}). [c] The values were calculated as ICy·HBF_4.

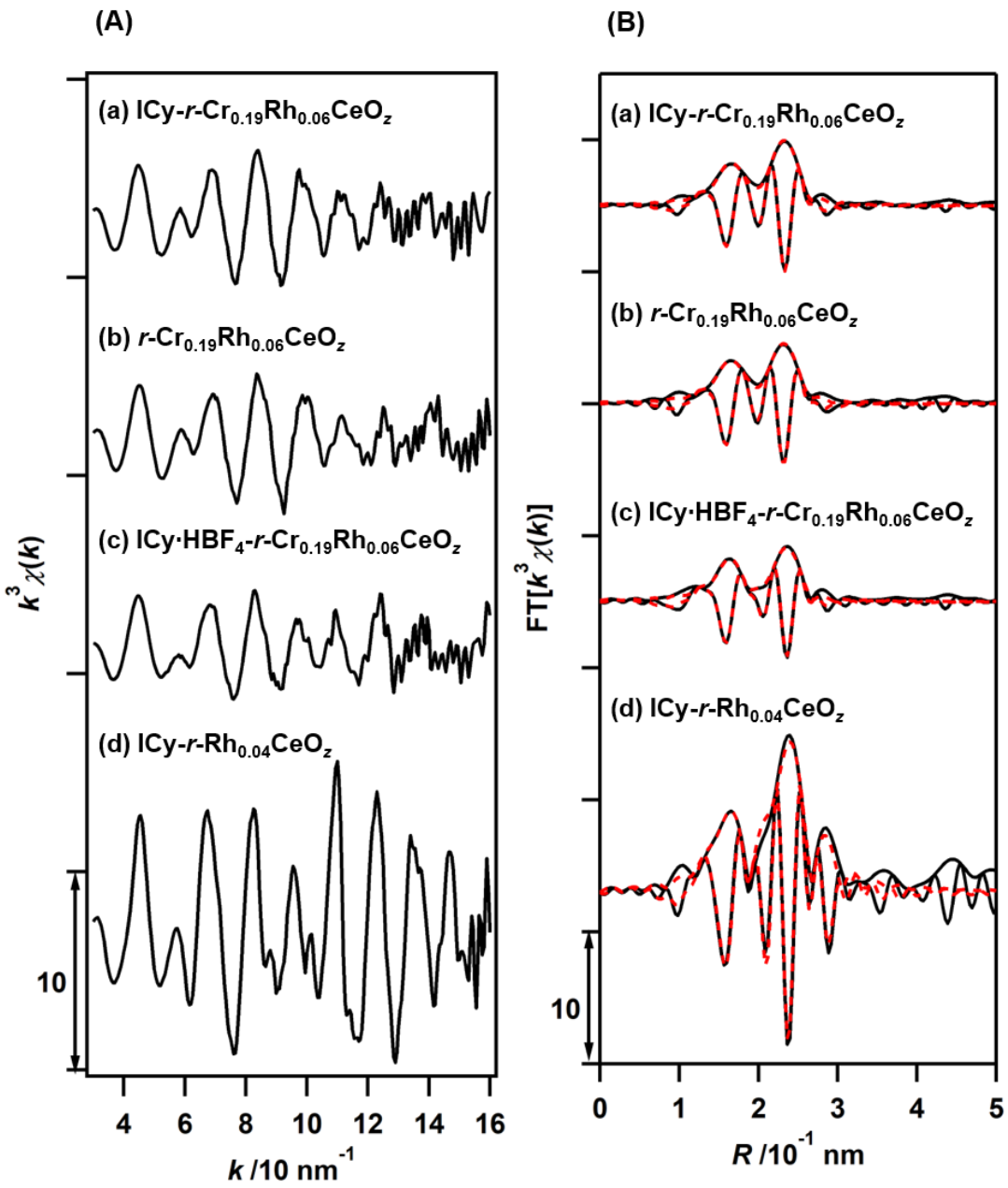

Figure 4.8. (A) k^3-Weighted Rh *K*-edge EXAFS oscillations and (B) their Fourier transforms (k = 30-140 nm^{-1}) of (a) ICy-*r*-$Cr_{0.19}Rh_{0.06}CeO_z$, (b) *r*-$Cr_{0.19}Rh_{0.06}CeO_z$, (c) ICy·HBF_4-*r*-$Cr_{0.19}Rh_{0.06}CeO_z$, and (d) ICy-*r*-$Rh_{0.04}CeO_z$.[21] (B) Black solid lines show observed data and red dashed lines show fitted data.

Table 4.6. Structural Parameters Determined by the Curve-fitting Analysis of Rh *K*-edge EXAFS Fourier Transforms of ICy-*r*-$Cr_{0.19}Rh_{0.06}CeO_z$, *r*-$Cr_{0.19}Rh_{0.06}CeO_z$, and ICy·HBF_4-*r*-$Cr_{0.19}Rh_{0.06}CeO_z$, and ICy-*r*-$Rh_{0.04}CeO_z$

Sample	Shell	CN	*R* /nm	ΔE /eV	σ^2 /10^{-5} nm^2	R_f /%
ICy-	Rh–O	1.3 ± 0.2	0.207 ± 0.001	10 ± 2	5 ± 1	0.2
r-$Cr_{0.19}Rh_{0.06}CeO_z$ [a]	Rh–Rh	2.8 ± 0.3	0.262 ± 0.001	-2 ± 1	10 ± 1	
r-$Cr_{0.19}Rh_{0.06}CeO_z$ [a]	Rh–O	1.3 ± 0.2	0.207 ± 0.001	9 ± 2	5 ± 1	0.4
	Rh–Rh	2.8 ± 0.4	0.261 ± 0.001	-2 ± 1	10 ± 1	
ICy·HBF_4-	Rh–O	1.2 ± 0.2	0.205 ± 0.001	10 ± 2	4 ± 1	0.4
r-$Cr_{0.19}Rh_{0.06}CeO_z$ [a]	Rh–Rh	2.7 ± 0.3	0.265 ± 0.001	-2 ± 1	8 ± 1	
ICy-*r*-$Rh_{0.04}CeO_z$ [b]	Rh–O	2.4 ± 1.3	0.202 ± 0.004	6 ± 8	4 ± 3	1.8
	Rh–Rh	6.0 ± 2.5	0.272 ± 0.001	9 ± 2	6 ± 2	
	Rh···Rh	3.9 ± 2.3	0.288 ± 0.002	9 ± 2	6 ± 2	

S_0^2 was fixed as 1. k = 30-140 nm^{-1}. [a] R = 0.12-0.27 nm. [b] R = 0.12-0.31 nm.

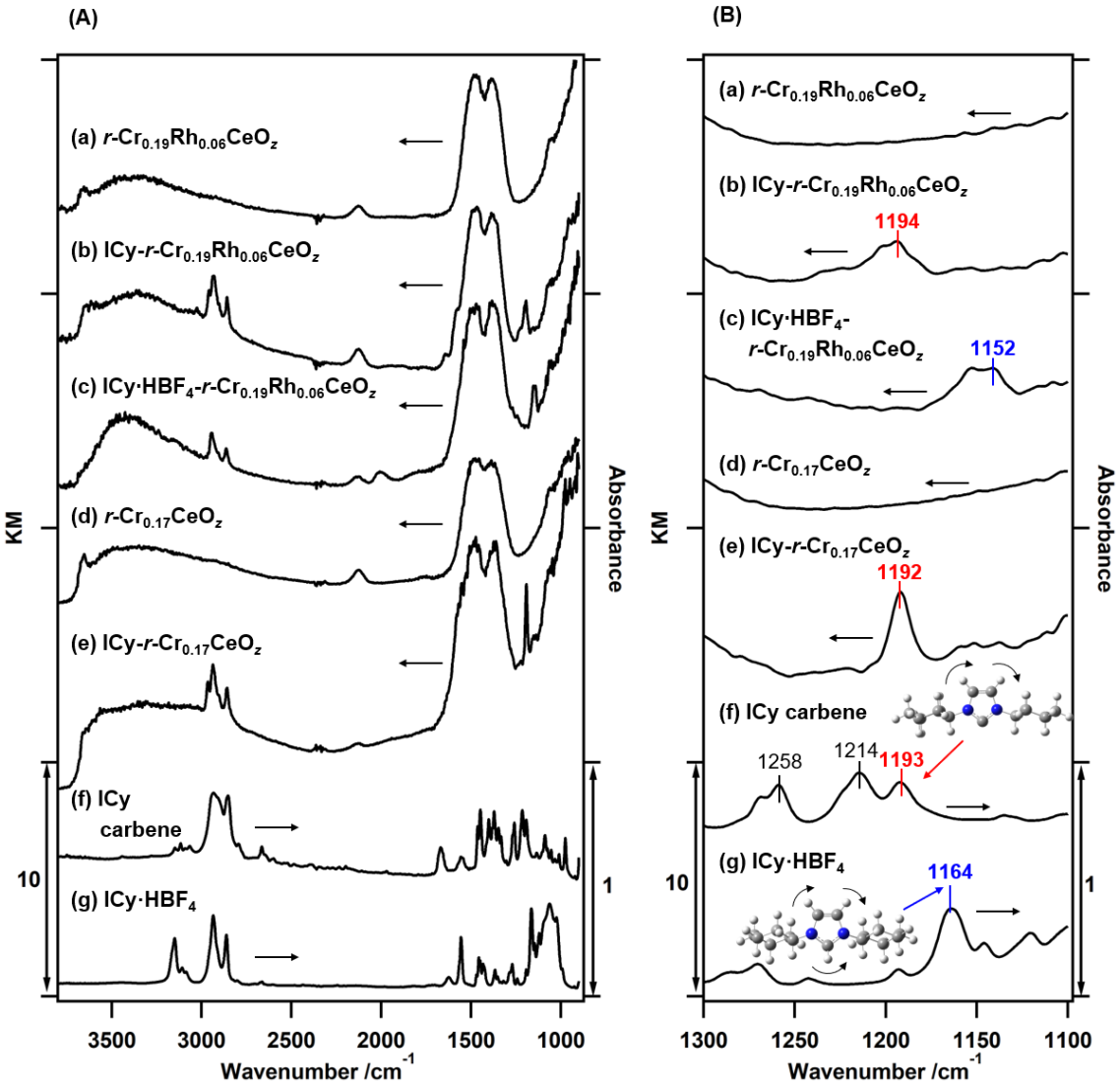

Figure 4.9. Diffuse reflectance FT-IR spectra of (a) *r*-$Cr_{0.19}Rh_{0.06}CeO_z$, (b) ICy-*r*-$Cr_{0.19}Rh_{0.06}CeO_z$, (c) ICy·HBF_4-*r*-$Cr_{0.19}Rh_{0.06}CeO_z$, (d) *r*-$Cr_{0.17}CeO_z$, and (e) ICy-*r*-$Cr_{0.17}CeO_z$, and transmission FT-IR spectra of (f) ICy carbene and (g) ICy·HBF_4 salt.[21] (A) 900-3800 cm^{-1}, (B) 1100-1300 cm^{-1}. Inset: An optimized structures of ICy and $ICyH^+$ by the DFT calculations, and schematic illustrations of asymmetric in-plane rocking vibration modes.

Table 4.7. FT-IR Peak Assignments and Their Peak Positions of *r*-$Cr_{0.19}Rh_{0.06}CeO_z$, ICy-*r*-$Cr_{0.19}Rh_{0.06}CeO_z$, ICy·HBF_4-*r*-$Cr_{0.19}Rh_{0.06}CeO_z$, ICy carbene, and ICy·HBF_4

Species	*r*-$Cr_{0.19}Rh_{0.06}CeO_z$	ICy-*r*-$Cr_{0.19}Rh_{0.06}CeO_z$	ICy·HBF_4-*r*-$Cr_{0.19}Rh_{0.06}CeO_z$	ICy carbene	ICy·HBF_4
n (Bridged OH)[a]	3655	3649	–	–	–
n (Hydrogen bonded OH)[a]	~3400	~3400	~3400	–	–
n (Aromatic N-heterocycle)[b]	–	_[e]	_[e]	3148 3116	3149 3108
n (C-H of cyclohexyl)[b]	–	2958 2931 2858	2945 2862	2933 2852	2935 2862
Defects of Ce^{3+} or oxygen vacancies[a,c]	2128	2125	2126	–	–
n (Carbonates)[a]	1485 1388 <1100	1467 1387 <1100	1471 1383 <1100	–	–
d (C-H of cyclohexyl)[b]	–	_[f]	_[f]	1258 1214	1366 1270
d (Aromatic N-heterocycle)[b,d]	–	1194	1152	1193 (1170)[g]	1164 (1138)[g]

[a] The peaks were assigned from the previous paper.[50] [b] The peaks were assigned from the DFT calculations. [c] The peak can be attributed to an electronic transition from donor levels located near the conduction band of Ce^{3+} or oxygen vacancies or the forbidden $^2F_{5/2}$ -> $^2F_{7/2}$ electronic transition of Ce^{3+}. [d] Asymmetric in-plane rocking vibration mode. [e] The peaks might be overlapped with the peaks of surface OH. [f] Not apparently observed. [g] Values obtained from the DFT calculations.

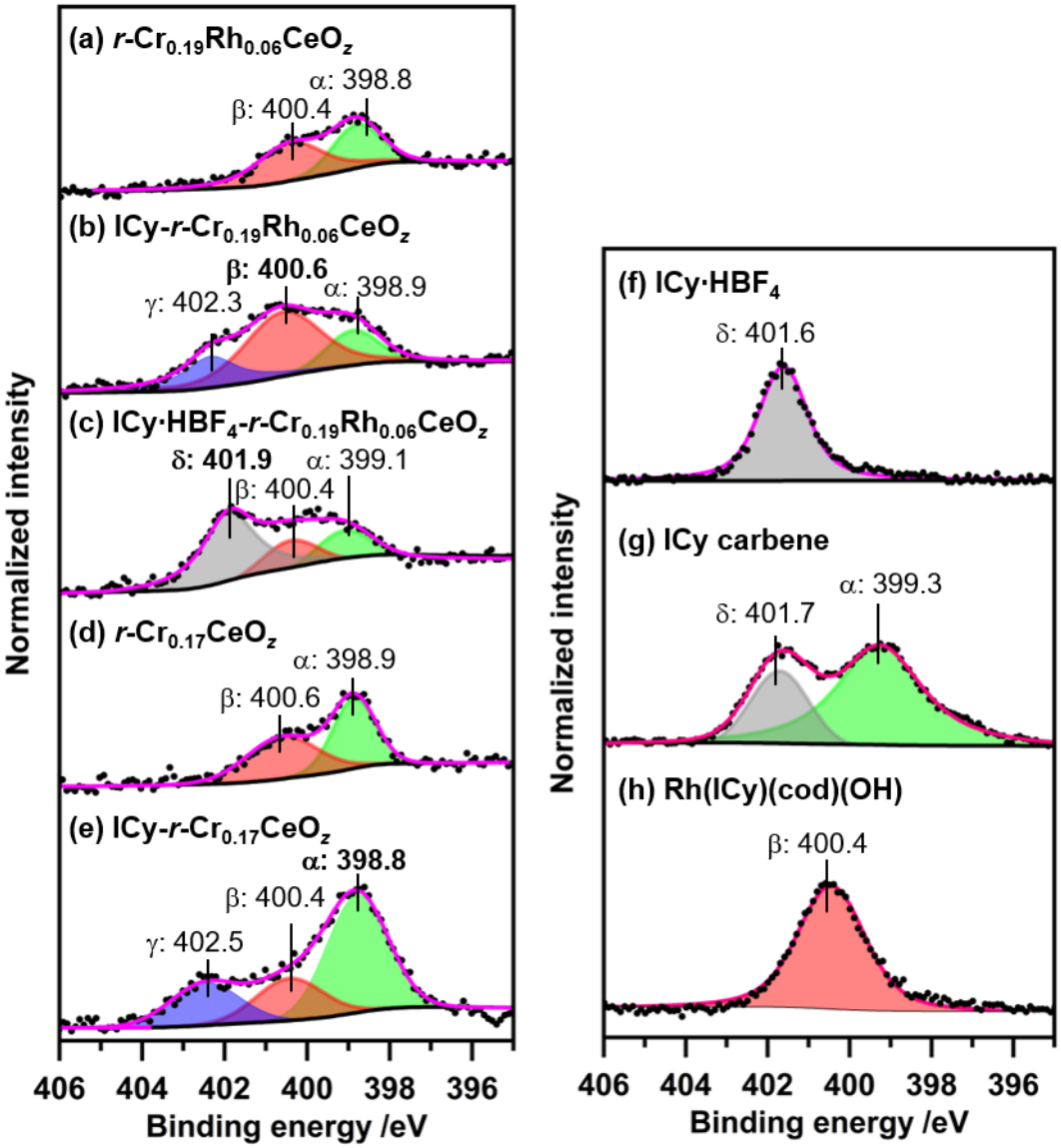

Figure 4.10. N 1s XPS spectra of (a) *r*-$Cr_{0.19}Rh_{0.06}CeO_z$, (b) ICy-*r*-$Cr_{0.19}Rh_{0.06}CeO_z$, (c) ICy·HBF_4-*r*-$Cr_{0.19}Rh_{0.06}CeO_z$, (d) *r*-$Cr_{0.17}CeO_z$, (e) ICy-*r*-$Cr_{0.17}CeO_z$, (f) ICy·HBF_4, (g) ICy carbene, and (h) Rh(ICy)(cod)(OH).[21] Black dots: raw data; green (α): adsorbed NH_3 or free ICy; red (β): adsorbed NH_4^+ or ICy carbene interacting with Rh; blue (γ): ICy carbene coordinating to metal cation species, gray (d): $ICyH^+$ (imidazolium); pink: total fitted data; black line: Shirley background. Note that the peak d observed at 401.7 eV of (g) was emerged during the XPS measurement, due to the re-protonation.[5j]

Table 4.8. N 1s XPS Binding Energies and Counts per Scan (CPS) Normalized with CPS of O 1s XPS Peak (CeO_2) of *r*-$Cr_{0.19}Rh_{0.06}CeO_z$, ICy-*r*-$Cr_{0.19}Rh_{0.06}CeO_z$, ICy·HBF_4-*r*-$Cr_{0.19}Rh_{0.06}CeO_z$, *r*-$Cr_{0.17}CeO_z$, and ICy-*r*-$Cr_{0.17}CeO_z$

Sample	N 1s BE /eV and CPS ratio of N 1s/O 1s (CeO_2) ×100							
	Peak α (adsorbed NH_3 or free ICy carbene)		Peak β (adsorbed NH_4^+ or ICy carbene interacting with Rh)		Peak γ (ICy carbene coordinating to metal cation species)		Peak δ ($ICyH^+$ imidazolium)	
	BE /eV	CPS ratio	BE /eV	CPS ratio	BE /eV	CPS ratio	BE /eV	CPS ratio
r-$Cr_{0.19}Rh_{0.06}CeO_z$	398.8	0.322	400.4	0.482	–	–	–	–
ICy-*r*-$Cr_{0.19}Rh_{0.06}CeO_z$	398.8	0.274	400.6	0.864	402.3	0.394	–	–
ICy·HBF_4-*r*-$Cr_{0.19}Rh_{0.06}CeO_z$	399.1	0.261	400.4	0.260	–	–	401.9	0.919
r-$Cr_{0.17}CeO_z$	398.9	0.469	400.6	0.463	–	–	–	–
ICy-*r*-$Cr_{0.17}CeO_z$	398.8	1.103	400.4	0.431	402.5	0.457	–	–

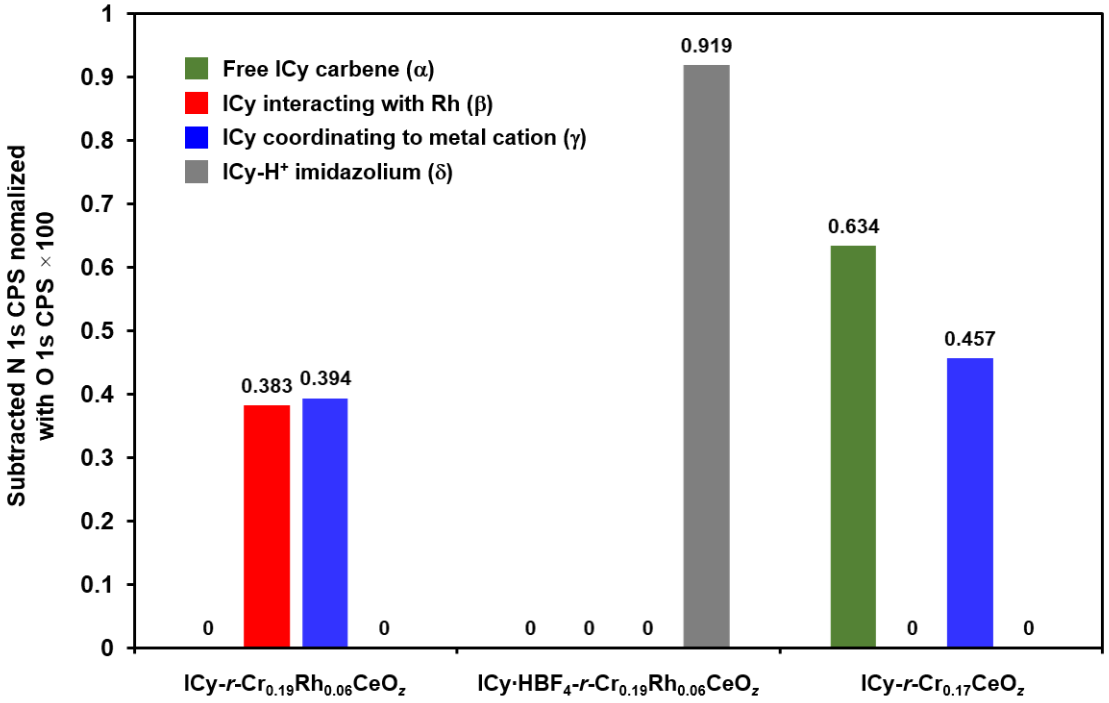

Figure 4.11. Counts per scan (CPS) of N 1s XPS peaks (normalized by CPS of O 1s XPS peak (CeO_2)) of ICy-*r*-$Cr_{0.19}Rh_{0.06}CeO_z$, ICy·HBF_4-*r*-$Cr_{0.19}Rh_{0.06}CeO_z$, and ICy-*r*-$Cr_{0.17}CeO_z$. subtracted by the CPS of corresponding oxides.[21] These values represent the net amounts of the adsorbed ICy species. Note that the value was round to zero when the subtracted value was below 0.

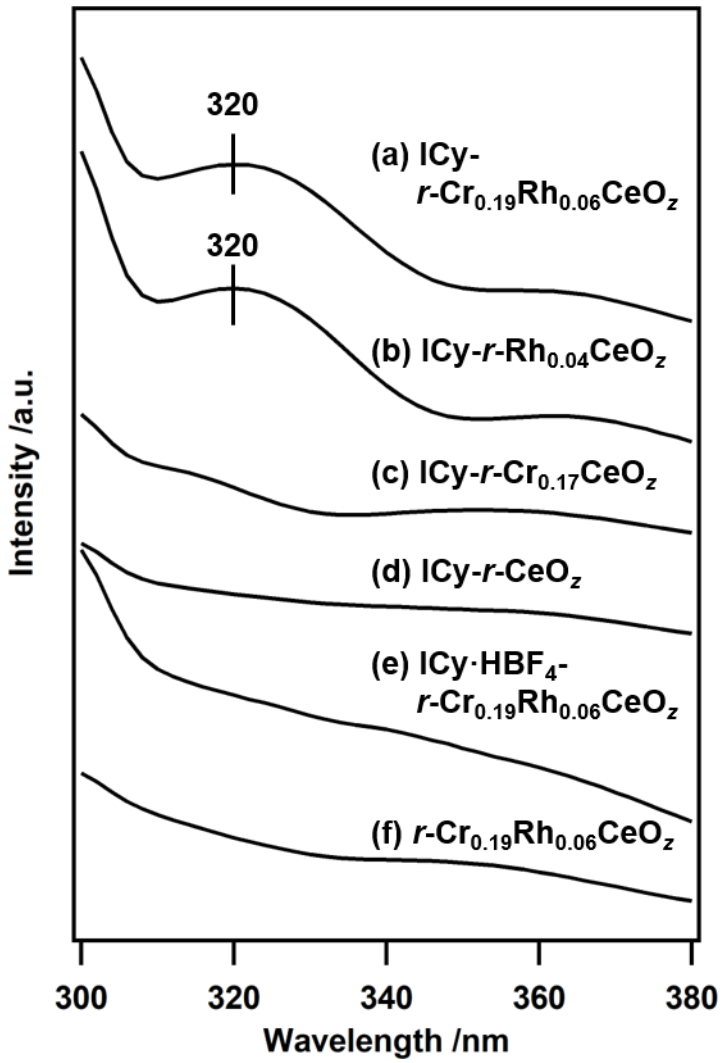

Figure 4.12. Solid-state photoluminescence spectra of (a) ICy-*r*-$Cr_{0.19}Rh_{0.06}CeO_z$, (b) ICy-*r*-$Rh_{0.04}CeO_z$, (c) ICy-*r*-$Cr_{0.17}CeO_z$, (d) ICy-*r*-CeO_z, (e) ICy·HBF_4-*r*-$Cr_{0.19}Rh_{0.06}CeO_z$, and (f) *r*-$Cr_{0.19}Rh_{0.06}CeO_z$.[21] The samples were diluted with 4-times of PTFE powder. Excitation wavelength: 240 nm.

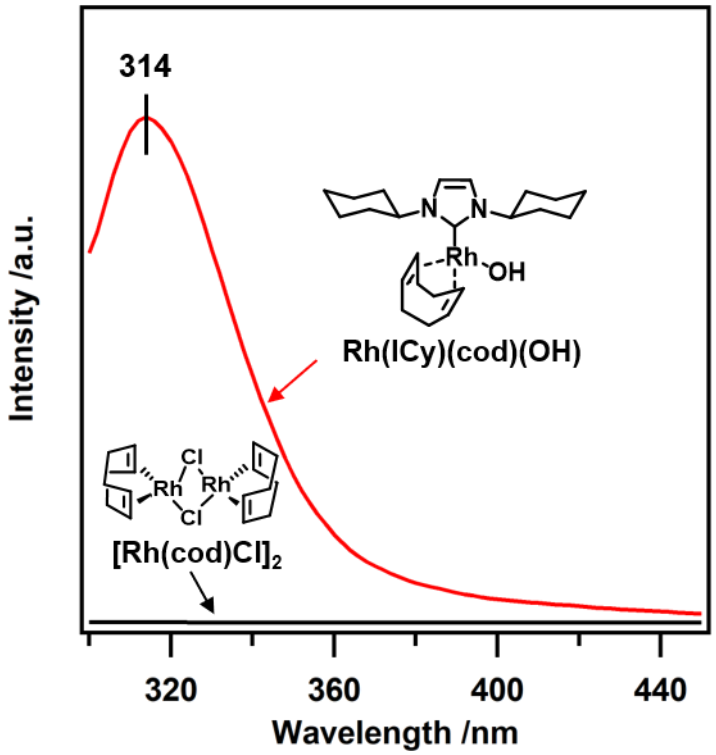

Figure 4.13. Photoluminescence spectra of the solutions of Rh(ICy)(cod)(OH) (red) and $[Rh(cod)Cl]_2$ (black) (1.0×10^{-3} M in THF).[21] Excitation wavelength: 268 nm.

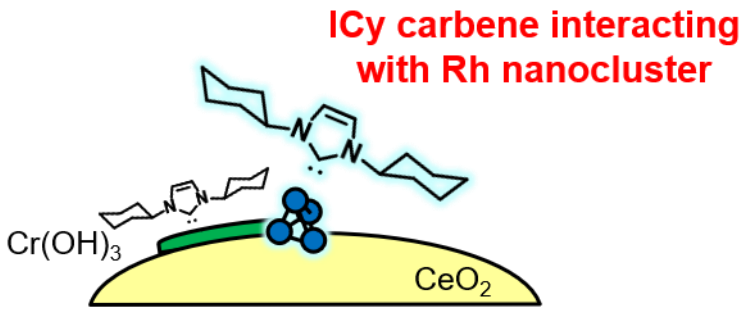

Figure 4.14. Schematic of the surface structure of ICy-*r*-$Cr_{0.19}Rh_{0.06}CeO_z$.[21]

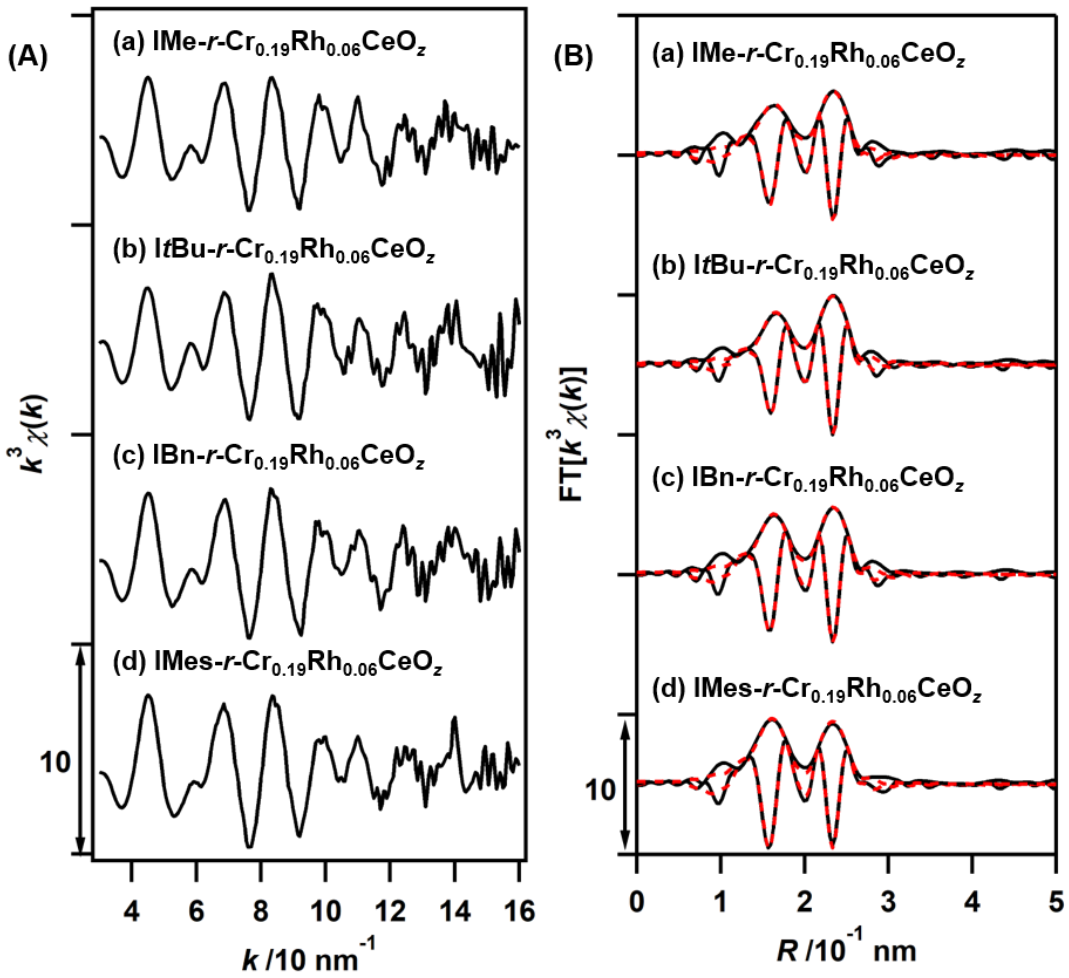

Figure 4.15. (A) k^3-Weighted Rh *K*-edge EXAFS oscillations and (B) their Fourier transforms (k = 30-140 nm^{-1}) of (a) IMe-*r*-$Cr_{0.19}Rh_{0.06}CeO_z$, (b) I*t*Bu-*r*-$Cr_{0.19}Rh_{0.06}CeO_z$, (c) IBn-*r*-$Cr_{0.19}Rh_{0.06}CeO_z$, and (d) IMes-*r*-$Cr_{0.19}Rh_{0.06}CeO_z$. (B) Black solid lines show observed data and red dashed lines show fitted data.

Table 4.9. Structural Parameters Determined by the Curve-fitting Analysis of Rh *K*-edge EXAFS Fourier Transforms of IMe-*r*-$Cr_{0.19}Rh_{0.06}CeO_z$, I*t*Bu-*r*-$Cr_{0.19}Rh_{0.06}CeO_z$, IBn-*r*-$Cr_{0.19}Rh_{0.06}CeO_z$, and IMes-*r*-$Cr_{0.19}Rh_{0.06}CeO_z$

Sample	Shell	CN	*R* /nm	ΔE /eV	σ^2 /10^{-5} nm^2	R_f /%
IMe-	Rh–O	1.6 ± 0.3	0.205 ± 0.001	9 ± 3	5 ± 2	0.7
r-$Cr_{0.19}Rh_{0.06}CeO_z$	Rh–Rh	2.5 ± 0.5	0.263 ± 0.001	-2 ± 2	10 ± 1	
I*t*Bu-	Rh–O	1.3 ± 0.1	0.207 ± 0.001	10 ± 2	3 ± 1	0.2
r-$Cr_{0.19}Rh_{0.06}CeO_z$	Rh–Rh	2.8 ± 0.3	0.263 ± 0.001	-2 ± 1	10 ± 1	
IBn-	Rh–O	1.7 ± 0.2	0.205 ± 0.001	9 ± 2	4 ± 1	0.3
r-$Cr_{0.19}Rh_{0.06}CeO_z$	Rh–Rh	2.7 ± 0.4	0.263 ± 0.001	-1 ± 1	10 ± 1	
IMes-	Rh–O	2.1 ± 0.4	0.204 ± 0.001	8 ± 2	5 ± 1	0.7
r-$Cr_{0.19}Rh_{0.06}CeO_z$	Rh–Rh	2.7 ± 0.6	0.263 ± 0.001	-1 ± 2	10 ± 1	

S_0^2 was fixed as 1. k = 30-140 nm^{-1}. R = 0.12-0.27 nm.

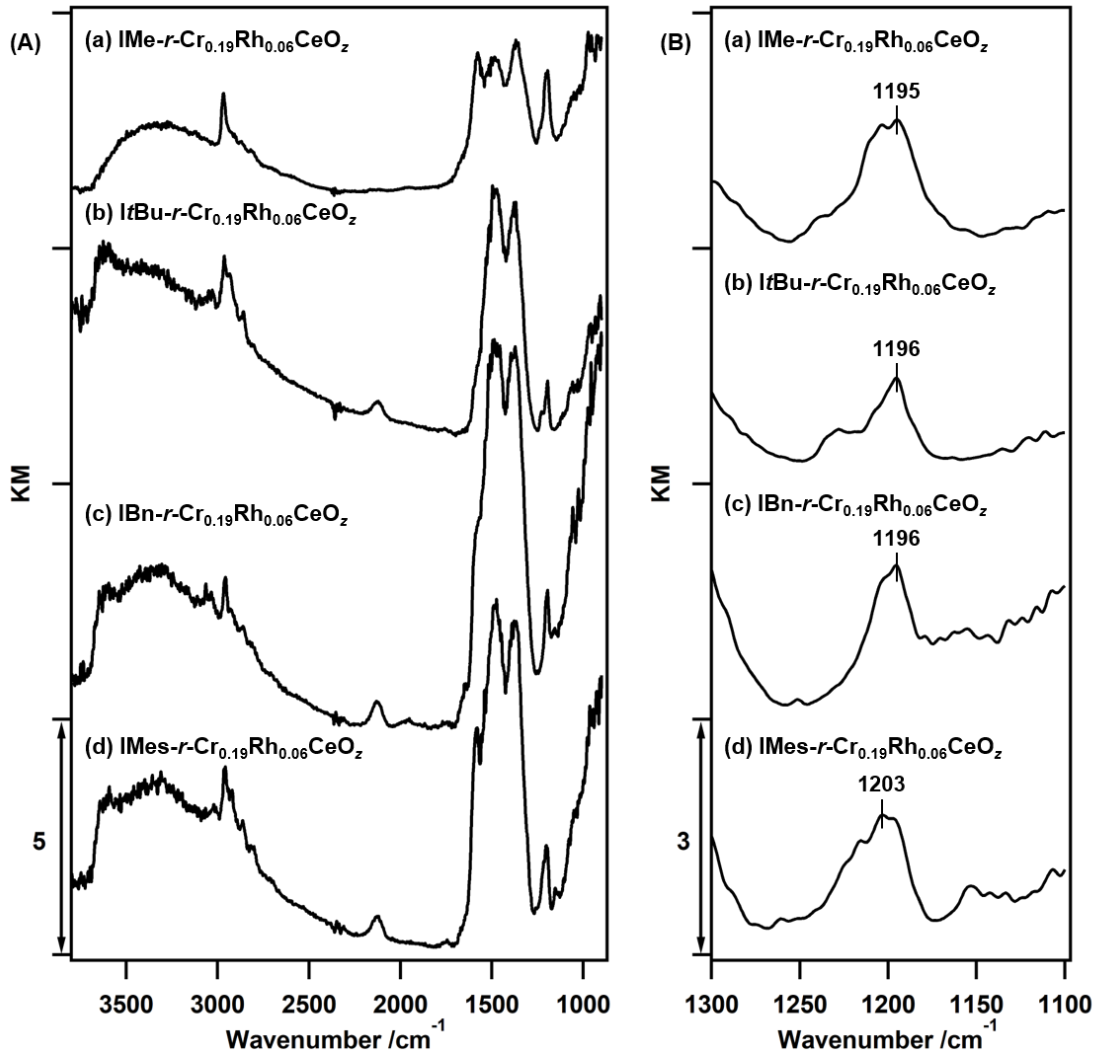

Figure 4.16. Diffuse reflectance FT-IR spectra of (a) IMe-*r*-$Cr_{0.19}Rh_{0.06}CeO_z$, (b) I*t*Bu-*r*-$Cr_{0.19}Rh_{0.06}CeO_z$, (c) IBn-*r*-$Cr_{0.19}Rh_{0.06}CeO_z$, and (d) IMes-*r*-$Cr_{0.19}Rh_{0.06}CeO_z$. (A) 900-3800 cm^{-1}, (B) 1100-1300 cm^{-1}.

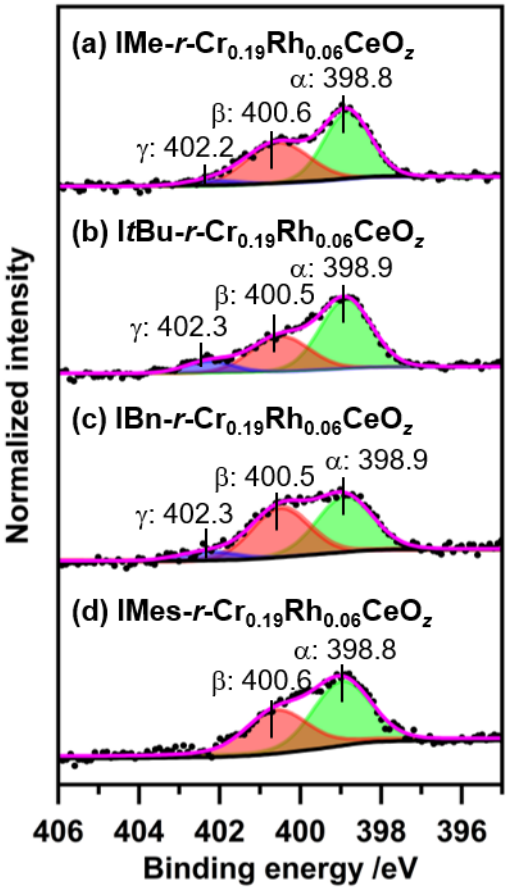

Figure 4.17. N 1s XPS spectra of (a) IMe-*r*-$Cr_{0.19}Rh_{0.06}CeO_z$, (b) I*t*Bu-*r*-$Cr_{0.19}Rh_{0.06}CeO_z$, (c) IBn-*r*-$Cr_{0.19}Rh_{0.06}CeO_z$, and (d) IMes-*r*-$Cr_{0.19}Rh_{0.06}CeO_z$. Black dots: raw data; green (α): adsorbed NH_3 or free ICy carbene; red (β): adsorbed NH_4^+ or ICy carbene coordinating with Rh; blue (γ): ICy carbene coordinating with metal cation species; pink: total fitted data; black line: Shirley background.

Table 4.10. N 1s XPS Binding Energies and Counts per Scan (CPS) Normalized with CPS of O 1s XPS Peak (CeO_2) of IMe-*r*-$Cr_{0.19}Rh_{0.06}CeO_z$, I*t*Bu-*r*-$Cr_{0.19}Rh_{0.06}CeO_z$, IBn-*r*-$Cr_{0.19}Rh_{0.06}CeO_z$, and IMes-*r*-$Cr_{0.19}Rh_{0.06}CeO_z$

Sample	N 1s BE /eV and CPS ratio of N 1s/O 1s (CeO_2) ×100					
	Peak α (adsorbed NH_3 or free ICy carbene)		Peak β (adsorbed NH_4^+ or ICy carbene interacting with Rh)		Peak γ (ICy carbene coordinating to metal cation species)	
	BE /eV	CPS ratio	BE /eV	CPS ratio	BE /eV	CPS ratio
IMe-*r*-$Cr_{0.19}Rh_{0.06}CeO_z$	398.8	0.767	400.6	0.616	402.2	0.075
I*t*Bu-*r*-$Cr_{0.19}Rh_{0.06}CeO_z$	398.9	0.856	400.5	0.489	402.3	0.134
IBn-*r*-$Cr_{0.19}Rh_{0.06}CeO_z$	398.9	0.769	400.5	0.678	402.3	0.121
IMes-*r*-$Cr_{0.19}Rh_{0.06}CeO_z$	399.0	0.833	400.6	0.651	–	–

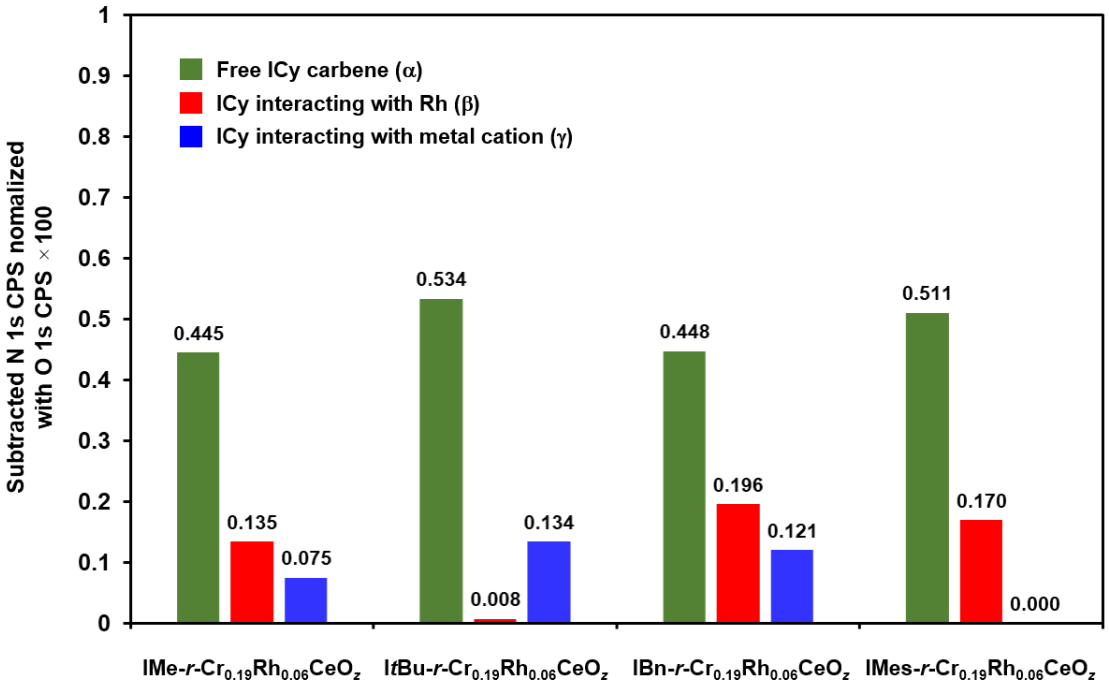

Figure 4.18. Counts per scan (CPS) of N 1s XPS peaks (normalized by CPS of O 1s XPS peak (CeO_2)) of IMe-*r*-$Cr_{0.19}Rh_{0.06}CeO_z$, I*t*Bu-*r*-$Cr_{0.19}Rh_{0.06}CeO_z$, IBn-*r*-$Cr_{0.19}Rh_{0.06}CeO_z$, and IMes-*r*-$Cr_{0.19}Rh_{0.06}CeO_z$. subtracted by the CPS of corresponding oxides. These values represent the net amounts of the adsorbed ICy species. Note that the value was round to zero when the subtracted value was below 0.

4.3.2. Catalytic activity induction in 1,4-arylation of cyclohexenone with phenylboronic acid on prepared catalysts

To investigate the catalytic activities of ICy-*r*-$Cr_{0.19}Rh_{0.06}CeO_z$, and the 1,4-arylation of cyclohexenone with phenylboronic acid was performed as a benchmark reaction (Table 4.11), since it is one of the crucial C−C bond formation reactions.[14] ICy-*r*-$Cr_{0.19}Rh_{0.06}CeO_z$ (ICy: 0.8 wt%) exhibited a remarkable catalytic activity with over 99% yield of the product (Entry 1), whereas *r*-$Cr_{0.19}Rh_{0.06}CeO_z$ showed no catalytic activity (Entry 2). Hence, the decoration with the ICy ligands induced the catalytic activity for 1,4-arylation on *r*-$Cr_{0.19}Rh_{0.06}CeO_z$. ICy-*r*-$Rh_{0.04}CeO_z$ showed low catalytic activity (10% yield, Entry 3), and ICy-*r*-$Cr_{0.17}CeO_z$ and ICy-*r*-CeO_z without the Rh species provided no products (Entries 4, 5). ICy·HBF_4-*r*-$Cr_{0.19}Rh_{0.06}CeO_z$ also showed no catalytic activity (Entry 6). Therefore, the interaction of the ICy carbene with the Rh nanoclusters was key in the induction of the catalytic 1,4-arylation activity.

Reaction condition was optimized by changing solvents, additives, kinds of NHC ligands, and loading amounts of ICy. Cyclohexane as a solvent and ethanol as an additive with the ratio of 10/1 provided better yields compared to other solvents and additives (Table 4.12), and 0.8 wt% of ICy was found to be the best loading amounts (Figure 4.19). Several heterogeneity tests were executed, which included a hot filtration test, a leaching test, a mercury drop test, a stoichiometric poisoning test.[9c, 33] The hot filtration of the heterogeneous catalyst in the middle progress of the reaction led to inhibit the reaction (Figure 4.20), and Rh cluster species were undetectable in the hot-filtered solution by ESI-MS. Addition of Hg droplet (62.5 equiv. to Rh) or stoichiometric catalytic poisons (0.3 or 1.0 equiv. to Rh) such as benzyl mercaptan, tetrahydrothiophene, and triphenylphosphine strongly suppressed the reaction (Figure 4.21 and Table 4.13), suggesting heterogeneous noble metal species (*i.e.*, Rh nanoclusters) could be the catalytically active species. These heterogeneity tests indicated that the catalytic reaction proceeded heterogeneously. The fact that excess loading of ICy ligands decreased the reaction rates (Figure 4.19) also supported heterogeneous reaction because higher amounts of NHC ligands caused blocking of the active sites.

The ICy carbene induced superior catalytic activity compared to the other NHC ligands (Entries 7–10, Scheme 4.5). The N 1s XPS spectra of NHC-*r*-$Cr_{0.19}Rh_{0.06}CeO_z$ showed that ICy-*r*-$Cr_{0.19}Rh_{0.06}CeO_z$ had the largest amounts of NHC carbenes interacting with Rh nanoclusters (Figure 4.17 in Section 3.3.1), suggesting that ICy ligands efficiently generated the catalytically active coordination structure of the Rh nanoclusters.

Scope of several substrates on ICy-*r*-$Cr_{0.19}Rh_{0.06}CeO_z$ was also investigated as

summarized in Table 4.14. The catalyst was active not only cyclic α,β-unsaturated ketones (Entries 1 and 2) but also linear α,β -unsaturated ketones (Entries 3 and 4). The reaction was also proceeded with phenylboronic acids substituted at 4-position (Entries 5-8); however, the non-substituted phenylboronic acid was the most active (Entry 1). 4-Methoxyphenylboronic acid was the most active among the substituted phenylboronic acids (Entry 5). The activity of 4-chlorophenylboronic acid (Entry 7) was comparable to that of 4-methylphenylboronic acid (Entry 6), and the activity of 4-trifluoromethyl-phenylboronic was the lowest (Entry 8). These results suggested that the catalytic activity on ICy-*r*-$Cr_{0.19}Rh_{0.06}CeO_z$ might be influenced by both inducive effect and resonance effect of the substituent groups. The reaction did not proceed when aliphatic boronic acid (cyclohexylboronic acid) was used (Entry 9).

Table 4.11. 1,4-Arylation of Cyclohexenone with Phenylboronic Acid on the Prepared Catalysts

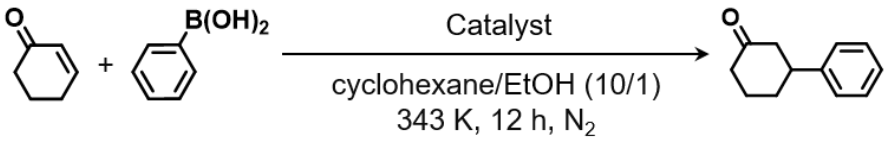

Entry	Catalyst	Yield %
1	ICy-*r*-$Cr_{0.19}Rh_{0.06}CeO_z$ (ICy: 0.8 wt%)	>99
2	*r*-$Cr_{0.19}Rh_{0.06}CeO_z$ (without ICy)	0
3	ICy-*r*-$Rh_{0.04}CeO_z$ (ICy: 0.7 wt%)	10
4	ICy-*r*-$Cr_{0.17}CeO_z$ (ICy: 0.9 wt%)	0
5	ICy-*r*-CeO_z (ICy: 0.9 wt%)	0
6	ICy·HBF_4-*r*-$Cr_{0.19}Rh_{0.06}CeO_z$ (ICy·HBF_4: 1.0 wt%)	0
7	IMe-*r*-$Cr_{0.19}Rh_{0.06}CeO_z$ (IMe: 0.5 wt%)	41
8	I*t*Bu-*r*-$Cr_{0.19}Rh_{0.06}CeO_z$ (I*t*Bu: 0.8 wt%)	4
9	IBn-*r*-$Cr_{0.19}Rh_{0.06}CeO_z$ (IBn: 1.1 wt%)	25
10	IMes-*r*-$Cr_{0.19}Rh_{0.06}CeO_z$ (IMes: 1.5 wt%)	3
11	(Blank)	0

Reaction conditions: catalyst (32 mg; Rh: 5 mol %), cyclohexenone (0.20 mmol), $PhB(OH)_2$ (0.30 mmol), dodecane (internal standard; 0.10 mmol), cyclohexane (2.0 mL), EtOH (0.2 mL), 343 K, 12 h, under N_2. Note that the molar loading of NHC per catalyst weight was unified to be 0.03–0.05 mmol g_{cat}^{-1}.

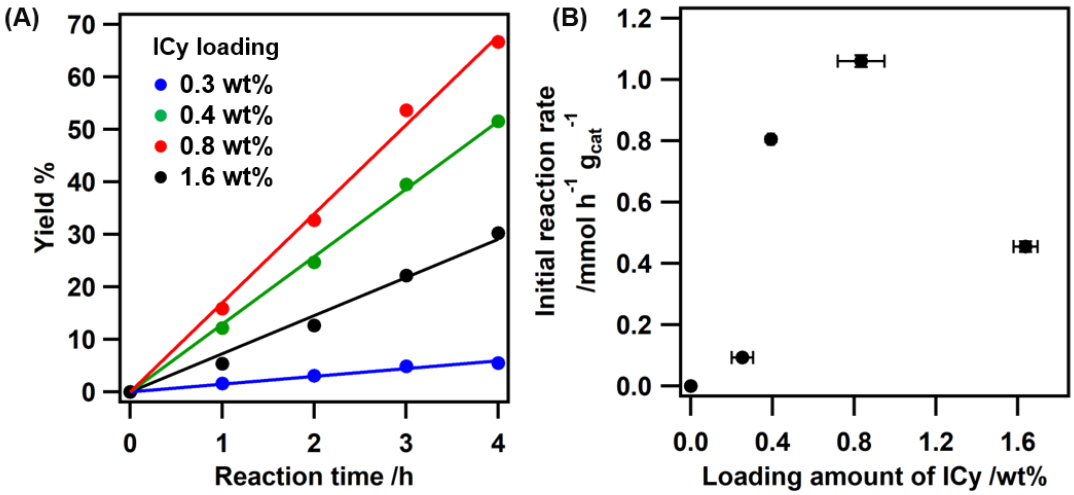

Figure 4.19. (A) Time-yield plots for the 1,4-arylation of cyclohexanone with phenylboronic acid on the ICy-*r*-$Cr_{0.19}Rh_{0.06}CeO_z$ catalysts with the ICy loading range of 0.3-1.6 wt%.[21] (B) Relationship between loading amounts of ICy and initial reaction rates for 1,4-arylation of cyclohexenone on ICy-*r*-$Cr_{0.19}Rh_{0.06}CeO_z$.[21]

Reaction Conditions: ICy-*r*-$Cr_{0.19}Rh_{0.06}CeO_z$ (32 mg; Rh: 5 mol %), cyclohexenone (0.20 mmol), $PhB(OH)_2$ (0.30 mmol), dodecane (internal standard; 0.10 mmol), cyclohexane (2.0 mL), EtOH (0.2 mL), 343 K, under N_2.

Table 4.12. 1,4-Arylation of Cyclohexenone with Phenylboronic Acid on ICy-*r*-$Cr_{0.19}Rh_{0.06}CeO_z$

Entry	Solvent	Yield %
1	cyclohexane/EtOH (10/1)	91
2	cyclohexane/EtOH (20/1)	55
3	cyclohexane/EtOH (4/1)	51
4	cyclohexane/EtOH (2/1)	53
5	cyclohexane/H_2O (10/1)	5
6	cyclohexane/MeOH (10/1)	24
7	cyclohexane/*i*-PrOH (10/1)	35
8	cyclohexane/*n*-BuOH (10/1)	94
9	cyclohexane/CyOH (10/1)	39
10	*n*-nonane/H_2O (10/1)	10
11	*n*-nonane/MeOH (10/1)	54
12	*n*-nonane/EtOH (10/1)	85
13	*n*-nonane/*i*-PrOH (10/1)	37
14	*n*-nonane/*n*-BuOH (10/1)	81
15	*n*-nonane/CyOH (10/1)	0
16	*t*-BuOH/EtOH (10/1)	8
17	*t*-BuOH /MeOH (10/1)	18
18	MeOH/H_2O (10/1)	7
19	MeOH	4
20	EtOH	69

Reaction conditions: ICy-*r*-$Cr_{0.19}Rh_{0.06}CeO_z$ (ICy: 1.6 wt%) 32 mg (Rh: 5 mol%), cyclohexenone 0.2 mmol, $PhB(OH)_2$ 0.3 mmol, dodecane (internal standard) 0.10 mmol, cyclohexane 2.0 mL, EtOH 0.2 mL, 343 K, 24 h, under N_2.

Scheme 4.5. 1,4-Arylation of Cyclohexenone with Phenylboronic Acid on NHC-*r*-$Cr_{0.19}Rh_{0.06}CeO_z$ (*r*-$Cr_{0.19}Rh_{0.06}CeO_z$ Decorated by NHC Ligands with Different *N*-Substituents)[21]

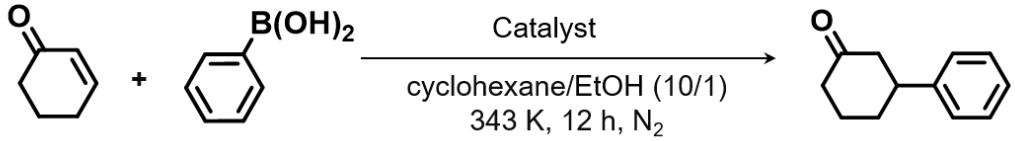

ICy (0.8 wt%)
>99% yield

IMe (0.5 wt%)
41% yield

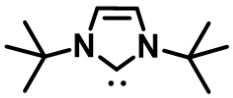

I*t*Bu (0.8 wt%)
4% yield

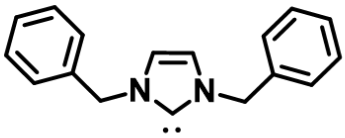

IBn (1.1 wt%)
25% yield

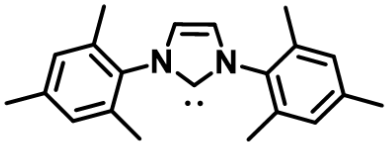

IMes (1.5 wt%)
3% yield

Reaction conditions: catalyst (32 mg; Rh: 5 mol %), cyclohexenone (0.20 mmol), $PhB(OH)_2$ (0.30 mmol), dodecane (internal standard; 0.10 mmol), cyclohexane (2.0 mL), EtOH (0.2 mL), 343 K, 12 h, under N_2. Note that the molar loading per catalyst weight was unified to be 0.03–0.05 mmol/g_{cat}.

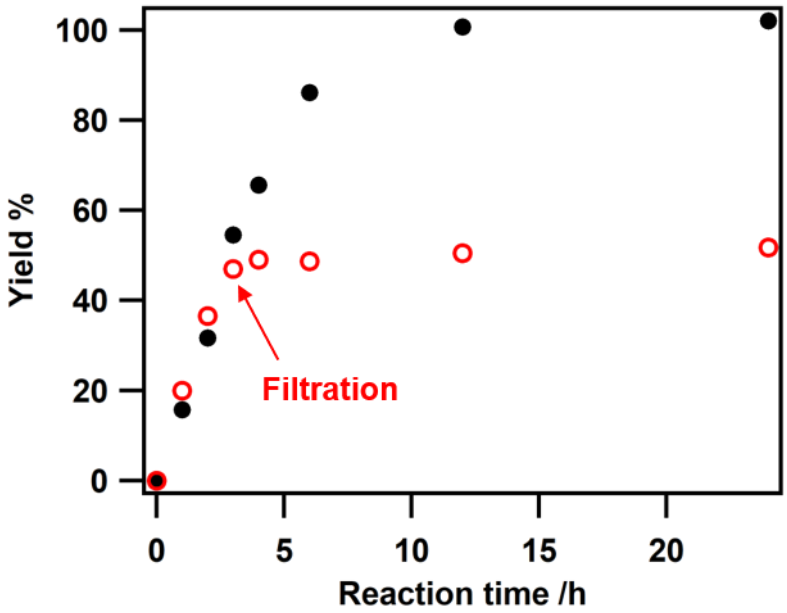

Figure 4.20. Hot filtration test for 1,4-arylation of cyclohexenone with phenylboronic acid on ICy-*r*-$Cr_{0.19}Rh_{0.06}CeO_z$.[21]

Reaction conditions: ICy-*r*-$Cr_{0.19}Rh_{0.06}CeO_z$ (32 mg; Rh: 5 mol %; ICy: 0.8 wt%), cyclohexenone (0.20 mmol), $PhB(OH)_2$ (0.30 mmol), dodecane (internal standard; 0.10 mmol), cyclohexane (2.0 mL), EtOH (0.2 mL), 343 K, under N_2. Black: heterogeneous conditions; red: hot-filtration of the catalyst 3 h after starting the reaction.

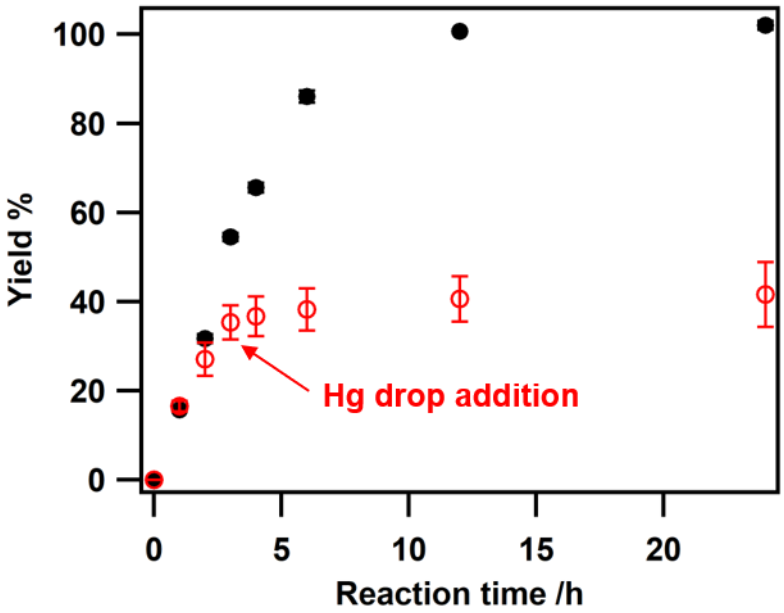

Figure 4.21. Mercury drop test for the 1,4-arylation of cyclohexenone with phenylboronic acid on ICy-*r*-$Cr_{0.19}Rh_{0.06}CeO_z$.[21]

Reaction conditions: ICy-*r*-$Cr_{0.19}Rh_{0.06}CeO_z$ (32 mg; ICy: 0.8 wt%; Rh: 5 mol %), cyclohexenone (0.20 mmol), $PhB(OH)_2$ (0.30 mmol), dodecane (internal standard; 0.10 mmol), cyclohexane (2.0 mL), EtOH (0.2 mL), 343 K, under N_2. Black: standard conditions. Red: an Hg droplet (10 µL, 68 equivs with respect to Rh) was added to the reaction mixture 3 h after starting the reaction.

Table 4.13. Results of Stoichiometric Poisoning Test for the 1,4-Arylation of Cyclohexenone with Phenylboronic Acid on ICy-*r*-$Cr_{0.19}Rh_{0.06}CeO_z$

Entry	Poison	Yield %
1	Benzyl mercaptan (1.0 equiv. to Rh)	0
2	Benzyl mercaptan (0.3 equiv. to Rh)	0
3	Tetrahydrothiophene (1.0 equiv. to Rh)	0
4	Tetrahydrothiophene (0.3 equiv. to Rh)	0
5	Triphenylphosphine (1.0 equiv. to Rh)	0
6	Triphenylphosphine (0.3 equiv. to Rh)	1

Reaction Conditions: ICy-*r*-$Cr_{0.19}Rh_{0.06}CeO_z$ (32 mg; ICy: 0.8 wt%; Rh: 5 mol %), cyclohexenone (0.20 mmol), $PhB(OH)_2$ (0.30 mmol), dodecane (internal standard; 0.10 mmol), cyclohexane (2.0 mL), EtOH (0.2 mL), poison (0.003 or 0.010 mmol), 343 K, 12 h, under N_2.

Table 4.14. Scope of Several Substrates for the 1,4-Arylation of *α,β*-Unsaturated Ketones with Arylboronic Acids on ICy-*r*-$Cr_{0.19}Rh_{0.06}CeO_z$

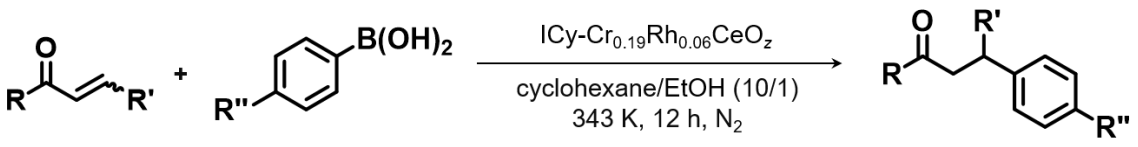

Entry	*α,β*-Unsaturated ketone	Arylboronic acid	Product	Yield %
1		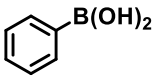	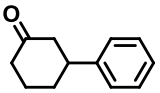	92[a]
2		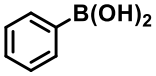	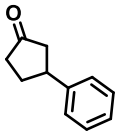	38[b]
3	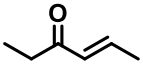	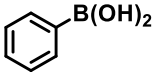	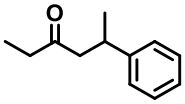	67[a]
4	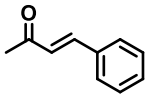	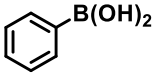	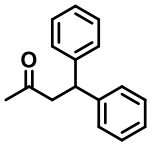	68[a]
5		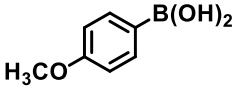	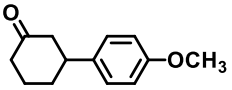	61[a]
6		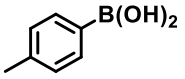	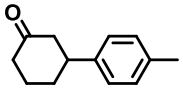	36[b]
7		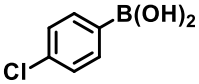	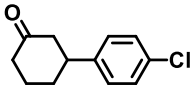	43[b]
8		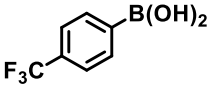	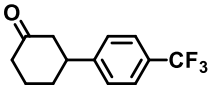	7[b]
9		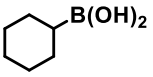	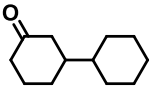	0

Reaction Conditions: ICy-*r*-$Cr_{0.19}Rh_{0.06}CeO_z$ (32 mg; ICy: 0.8 wt%; Rh: 5 mol %), a,b-unsaturated ketone (0.20 mmol), arylboronic acid (0.30 mmol), cyclohexane (2.0 mL), EtOH (0.2 mL), 343 K, 12 h, under N_2.

[a] Isolated yield. [b] ^1H NMR product yield using ethyl acetate (0.20 mmol) as an internal standard.

4.3.3. Coordination-induced trigger by decoration of NHC ligands

The effects of ICy on the Rh nanoclusters were studied in order to elucidate the catalytic activity generation further. First, the electron donation effect of ICy to the Rh nanocluster was investigated by XANES and XPS spectroscopies. Rh *K*-edge XANES (Figure 4.22) and Rh 3d XPS (Figure 4.23) spectra of ICy-*r*-$Cr_{0.19}Rh_{0.06}CeO_z$ displayed similar structures to those of *r*-$Cr_{0.19}Rh_{0.06}CeO_z$, indicating that ICy had a negligible effect on the electronic state of Rh nanoclusters, which was different from previous reports of Pd nanoparticles and Rh complexes coordinated with NHC ligands.[9c,51] Therefore, ICy induced the catalytic activity in a different manner from the electron donation.

The ICy interaction on the Rh nanoclusters was investigated by DFT calculations. The catalyst structure of *r*-$Cr_{0.19}Rh_{0.06}CeO_z$ was modelled as Rh_4/CeO_2 (Figure 4.24 (A)) from the CN of Rh-Rh bonds to focus on the reaction on the Rh active species.[52] The Rh-Rh CN of *r*-$Cr_{0.19}Rh_{0.06}CeO_z$ (CN = 2.8 ± 0.3) was much smaller than the CN for bulk Rh (CN = 12), and the average Rh-Rh CN of 3 suggested the formation of Rh nanoclusters of small nuclearity. For instances, the CN of tetrahedral $Rh_4(CO)_{12}$ cluster is three, and the average CN of Rh/Al_2O_3 catalyst prepared from the grafting of $Rh_4(CO)_{12}$ on Al_2O_3 was reported to be three.[53] Although it is not possible to determine the exact number of nuclei of Rh nanoclusters on the catalyst surface, tetrahedral Rh_4 cluster is one of the plausible structures for the active Rh nanoclusters on *r*-$Cr_{0.19}Rh_{0.06}CeO_z$. The modelled structure of ICy-*r*-$Cr_{0.19}Rh_{0.06}CeO_z$ (ICy-Rh_4/CeO_2) was structurally optimized, and the ICy ligand was favorably coordinated at a bridge site between Rh atoms compared with a top site and a hollow site of the Rh cluster (Figures 4.24 (B), 4.25).[54,55] Bader charge analysis of Rh_4/CeO_2 and ICy-Rh_4/CeO_2 showed similar charge distributions of Rh atoms (Figure 4.26), supporting the experimental results of Rh *K*-edge XANES and Rh 3d XPS analyses.

Based on the suggested reaction mechanism for Rh complex catalysts, [18b,19,20] the reaction profiles of 1,4-arylation in each reaction step were calculated as shown in Figures 4.27-28: step 1, the transmetalation of phenylboronic acid to form the phenyl group on the Rh nanocluster (C–B bond dissociation); step 2, the adsorption and insertion of cyclohexenone into the phenyl group (C–C bond formation); and step 3, the protonation of the product by EtOH (hydrolysis). The full reaction pathway on Rh_4/CeO_2 with several cascades was suggested, and there were three activation barriers from the C−B bond dissociation to the hydrolysis (Figure 4.29). On the contrary, it is to be noted that the C−C bond formation step on ICy-Rh_4/CeO_2 did not have significant activation barrier (Figure 4.27). Kinetic analyses indicated the 1st order to the concentration of phenyl boronic acid

(Figure 4.29) and 54.5 kJ mol^{-1} of the apparent activation energy (Figure 4.30) in the reaction. The decrease in the reaction cascades in the full reaction pathway on ICy-Rh_4/CeO_2 was proposed to be one of the reasons for the induction of the catalytic activity.

Examining the initial structures in the C–C bond formation steps revealed that the coordination of ICy changed the adsorption site of the phenyl group on the Rh cluster. The phenyl group endergonically formed from phenylboronic acid was located on the top of the Rh cluster of ICy-Rh_4/CeO_2, and the distance between the phenyl group and the adsorbed cyclohexenone was 0.267 nm (Figure 4.28, INI2). In contrast, the bridged phenyl group was exergonically formed on Rh_4/CeO_2, and the distance between the bridged phenyl group and the adsorbed cyclohexenone was large (0.400 nm) (Figure 4.27, INI2). These differences in the coordination structures suggested that the ICy ligand controlled the adsorption sites of the phenyl group closer to cyclohexenone (ICy might also block favorable adsorption sites for the phenyl group and prevent the formation of stable intermediate.) and promoted the C–C bond formation, resulting in the increase in the 1,4-arylation activity.

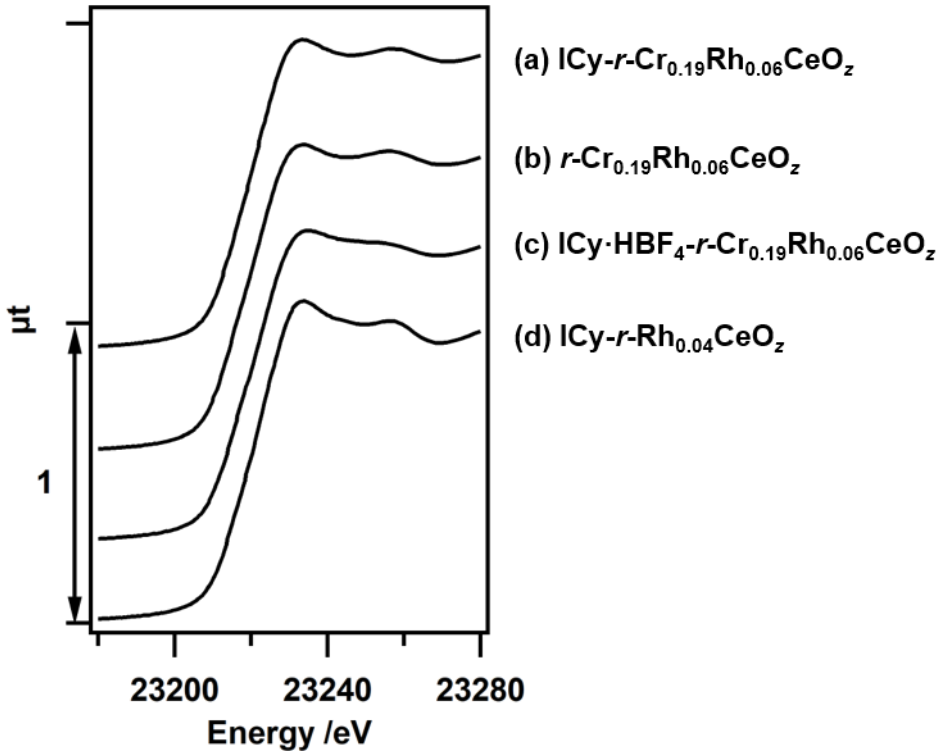

Figure 4.22. Rh *K*-edge XANES spectra of (a) ICy-*r*-$Cr_{0.19}Rh_{0.06}CeO_z$, (b) *r*-$Cr_{0.19}Rh_{0.06}CeO_z$, (c) ICy·HBF_4-*r*-$Cr_{0.19}Rh_{0.06}CeO_z$, and (d) ICy-*r*-$Rh_{0.04}CeO_z$.[21]

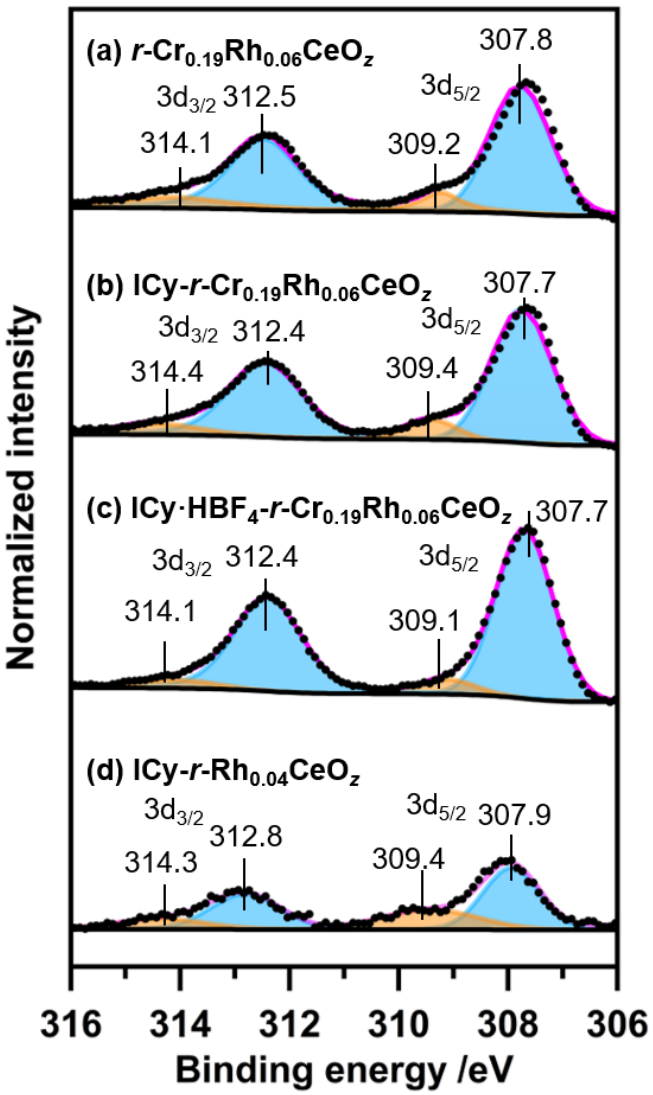

Figure 4.23. Rh 3d XPS spectra of (a) *r*-$Cr_{0.19}Rh_{0.06}CeO_z$, (b) ICy-*r*-$Cr_{0.19}Rh_{0.06}CeO_z$, (c) ICy·HBF_4-*r*-$Cr_{0.19}Rh_{0.06}CeO_z$, and (d) ICy-*r*-$Rh_{0.04}CeO_z$.[21] Black dots: raw data; light blue: reduced Rh nanocluster on CeO_2[56]; orange: Rh^{3+} interacting with CeO_2[56,57]; pink: total fitted data; black line: Shirley background.

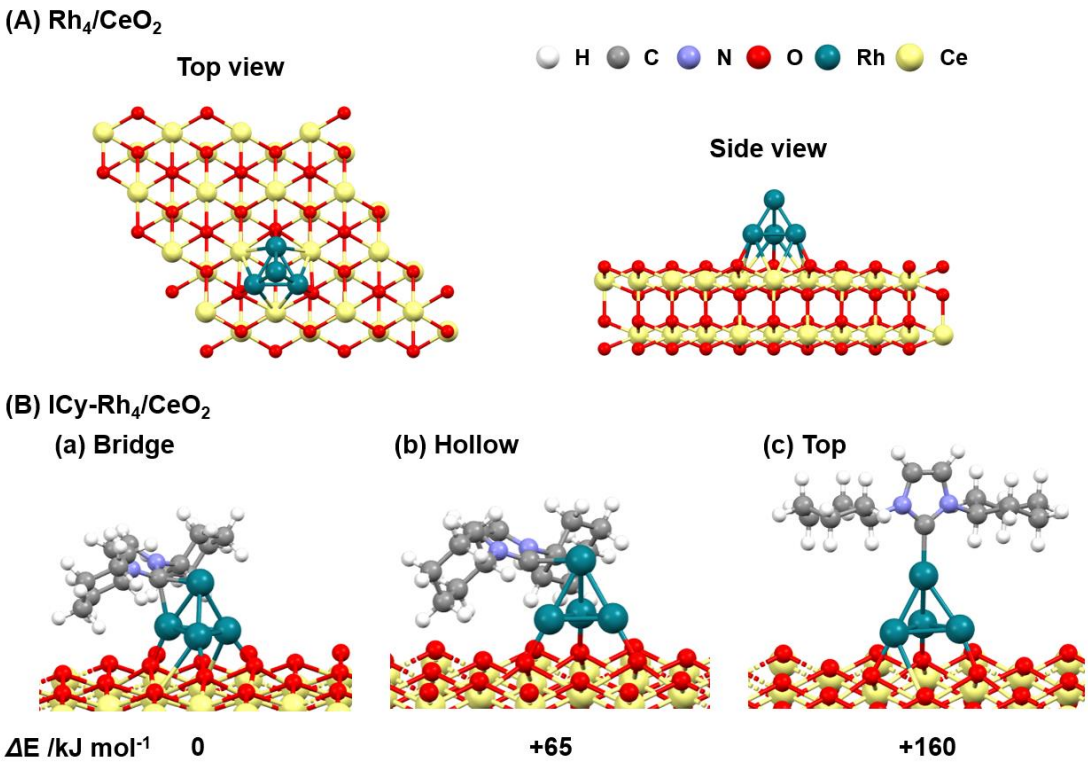

Figure 4.24. Optimized structures and their relative energies of (A) Rh_4/CeO_2 without ICy and (B) Rh_4/CeO_2 adsorbed with ICy at a (a) bridge site, (b) hollow site, and (c) top site calculated by DFT.[21]

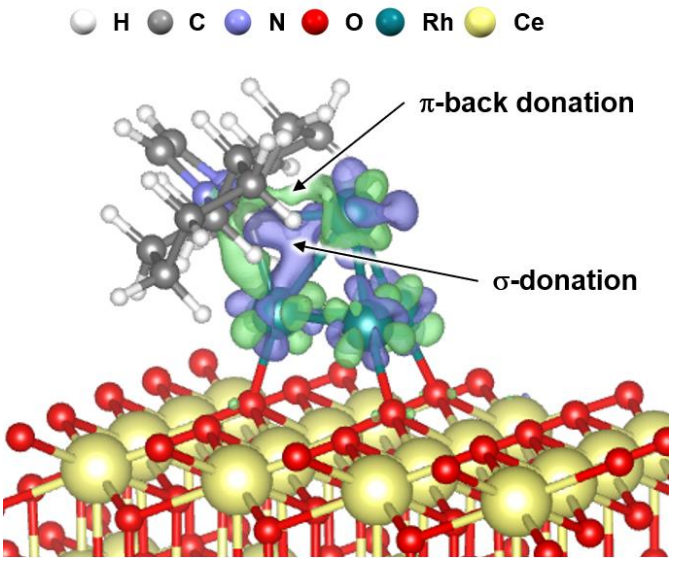

Figure 4.25. Charge density difference upon the adsorption of ICy on the Rh nanocluster in ICy-Rh_4/CeO_2.[21] Green and purple indicate charge accumulation and depletion, respectively. Isovalue = 0.007 e $bohr^{-3}$. White ball: H, gray ball: C, blue ball: N, red ball: O, blue-green ball: Rh, yellow ball: Ce.

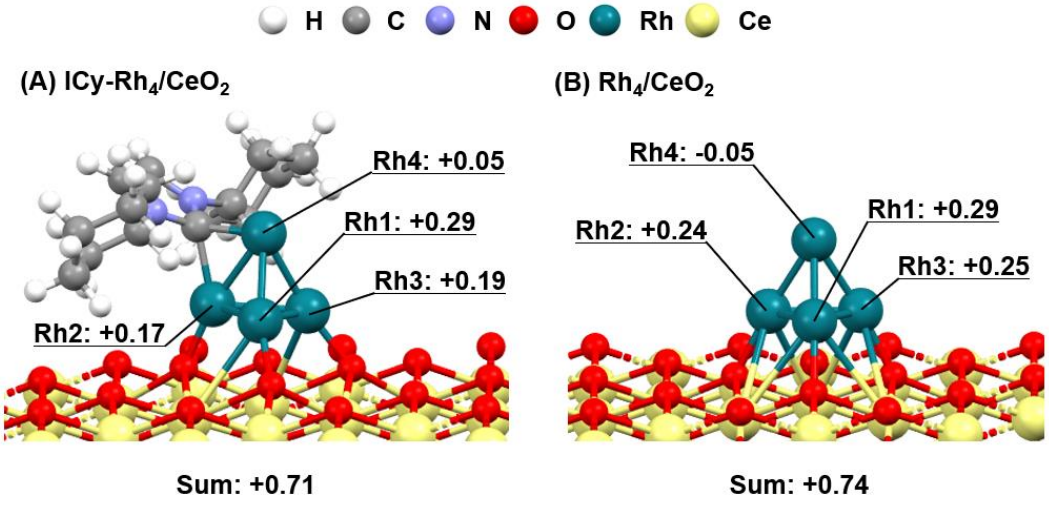

Figure 4.26. Bader charge analyses of (A) ICy- Rh_4/CeO_2 and (B) Rh_4/CeO_2.[21]

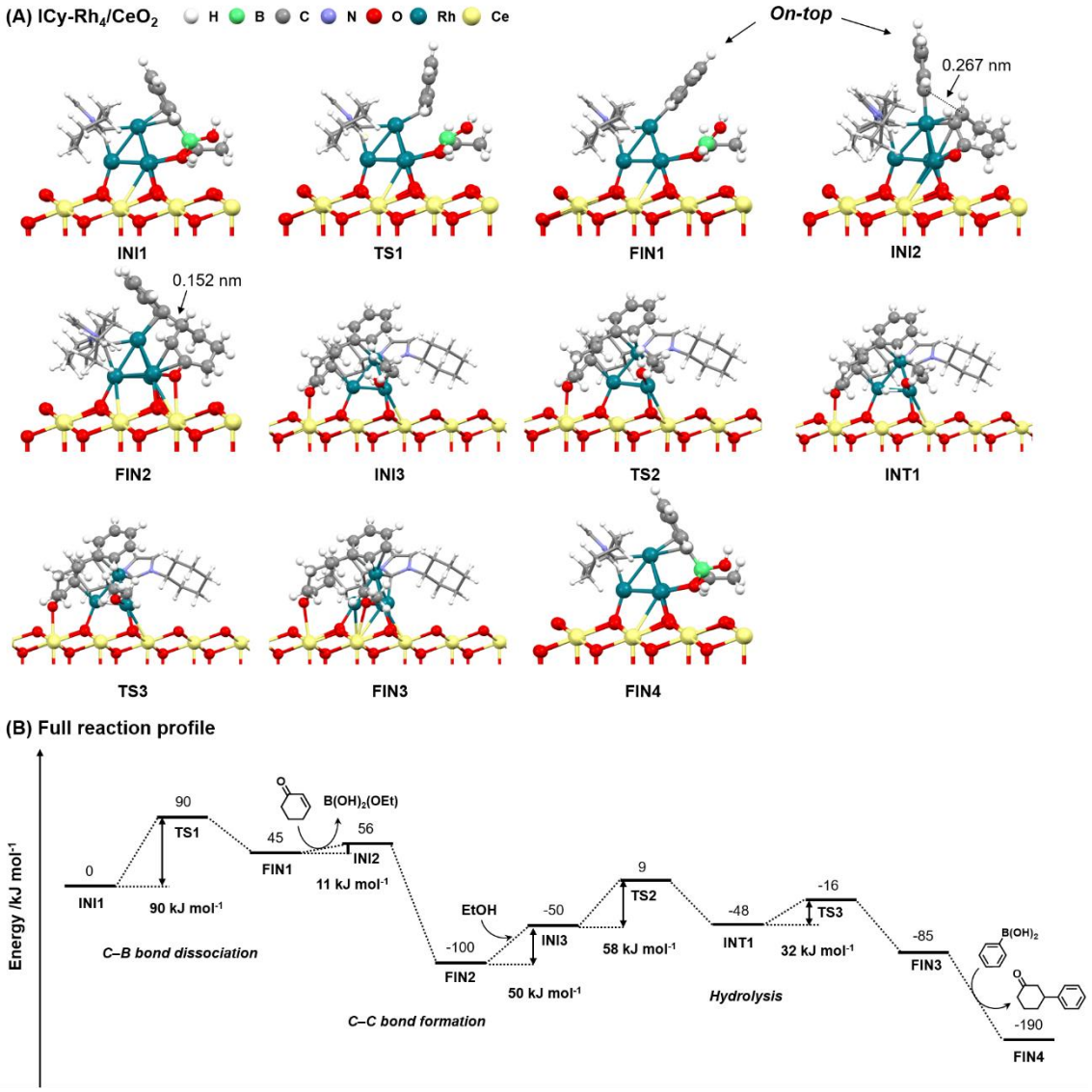

Figure 4.27. (A) Optimized structures of ICy-Rh_4/CeO_2 during the full reaction profiles in the 1,4-arylation reaction of cyclohexenone with phenylboronic acid calculated by DFT.[21] (B) Energy diagrams for the full reaction profiles of ICy-Rh_4/CeO_2.[58] ICy was displayed with atoms of half radius.

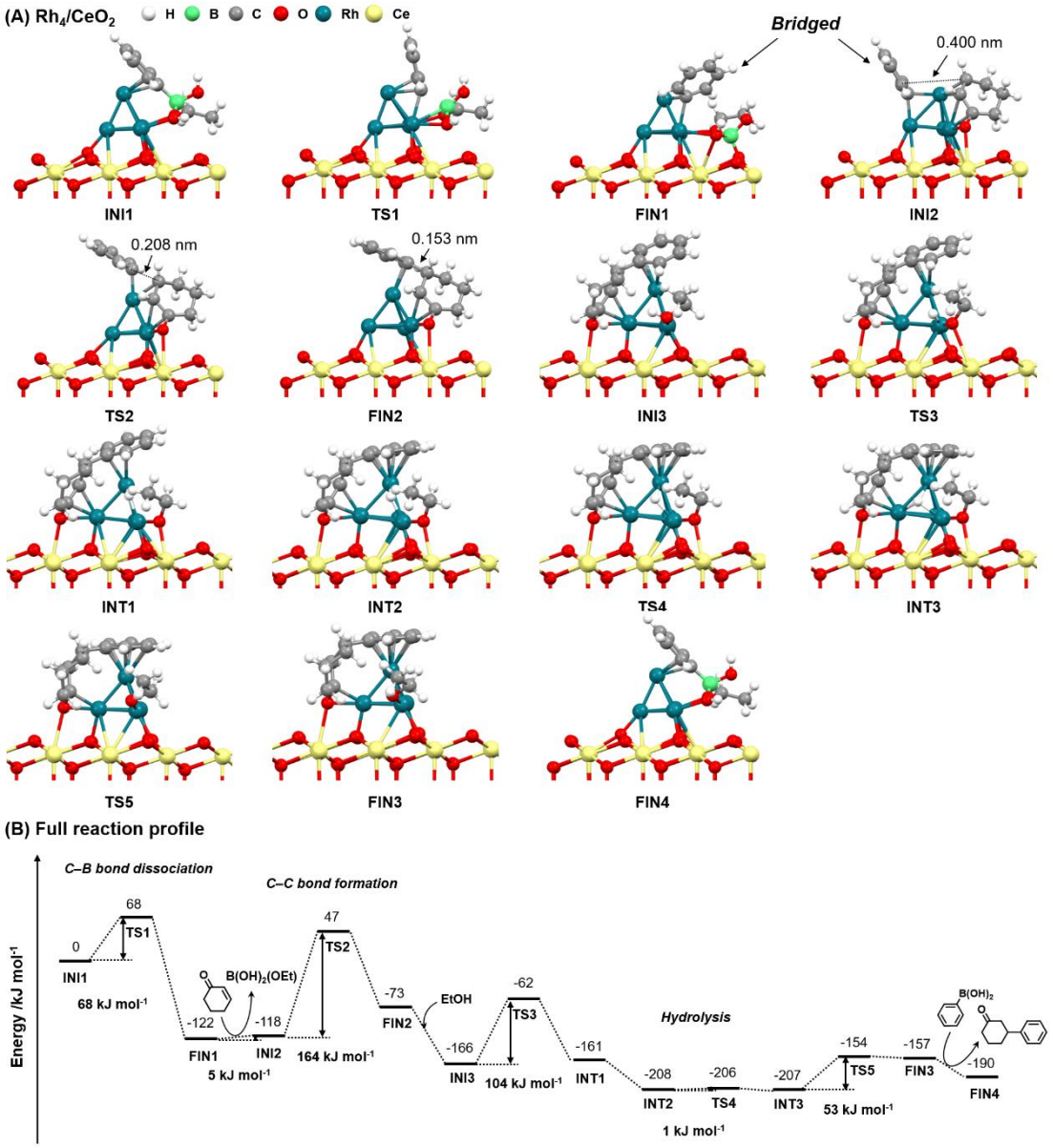

Figure 4.28. (A) Optimized structures of Rh_4/CeO_2 during the full reaction profiles in the 1,4-arylation reaction of cyclohexenone with phenylboronic acid calculated by DFT.[21] (B) Energy diagrams for the full reaction profiles of Rh_4/CeO_2.[58]

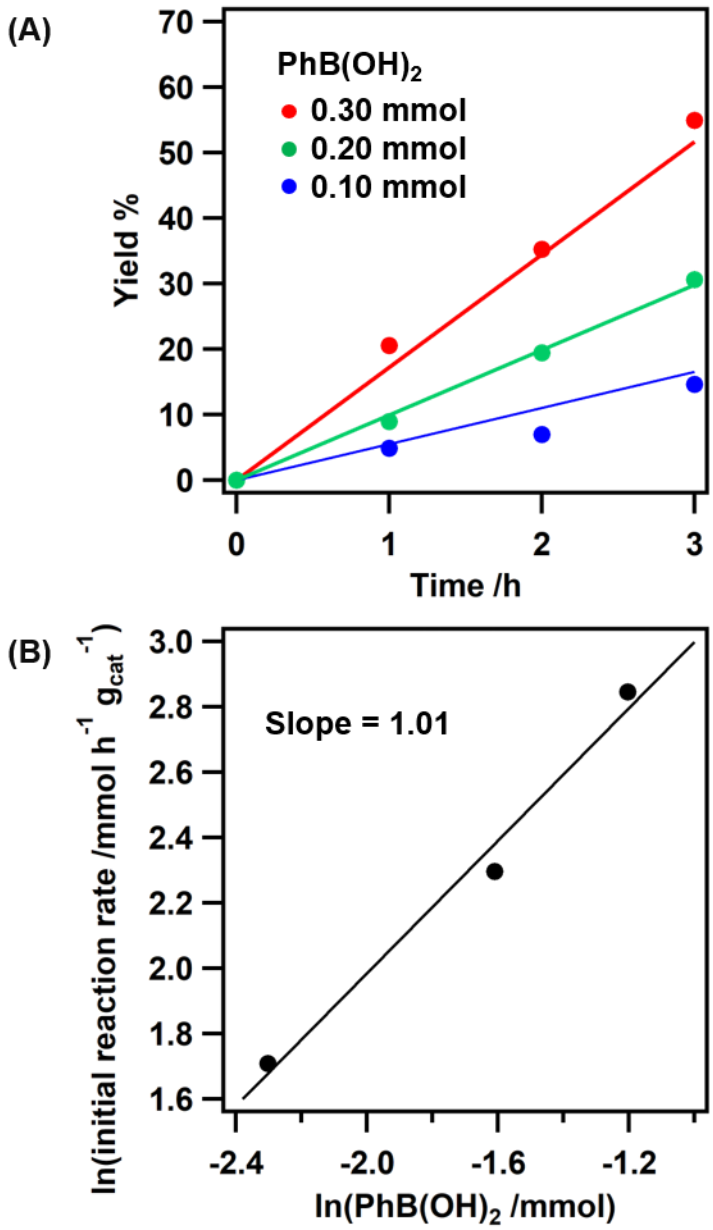

Figure 4.29. (A) Time-yield plots in the 1,4-addition of cyclohexanone with phenylboronic acid on ICy-*r*-$Cr_{0.19}Rh_{0.06}CeO_z$ with different amount of phenylboronic acid.[21] (B) Dependency of the reaction rates for the product yield on the concentration of phenylboronic acid in the 1,4-addition of cyclohexanone with phenylboronic acid on ICy-*r*-$Cr_{0.19}Rh_{0.06}CeO_z$.[21]

Reaction Conditions: ICy-*r*-$Cr_{0.19}Rh_{0.06}CeO_z$ (32 mg; ICy: 0.8 wt%; Rh: 5 mol %), cyclohexenone (0.20 mmol), $PhB(OH)_2$ (0.10, 0.20, or 0.30 mmol), dodecane (internal standard; 0.10 mmol), cyclohexane (2.0 mL), EtOH (0.2 mL), 343 K, under N_2.

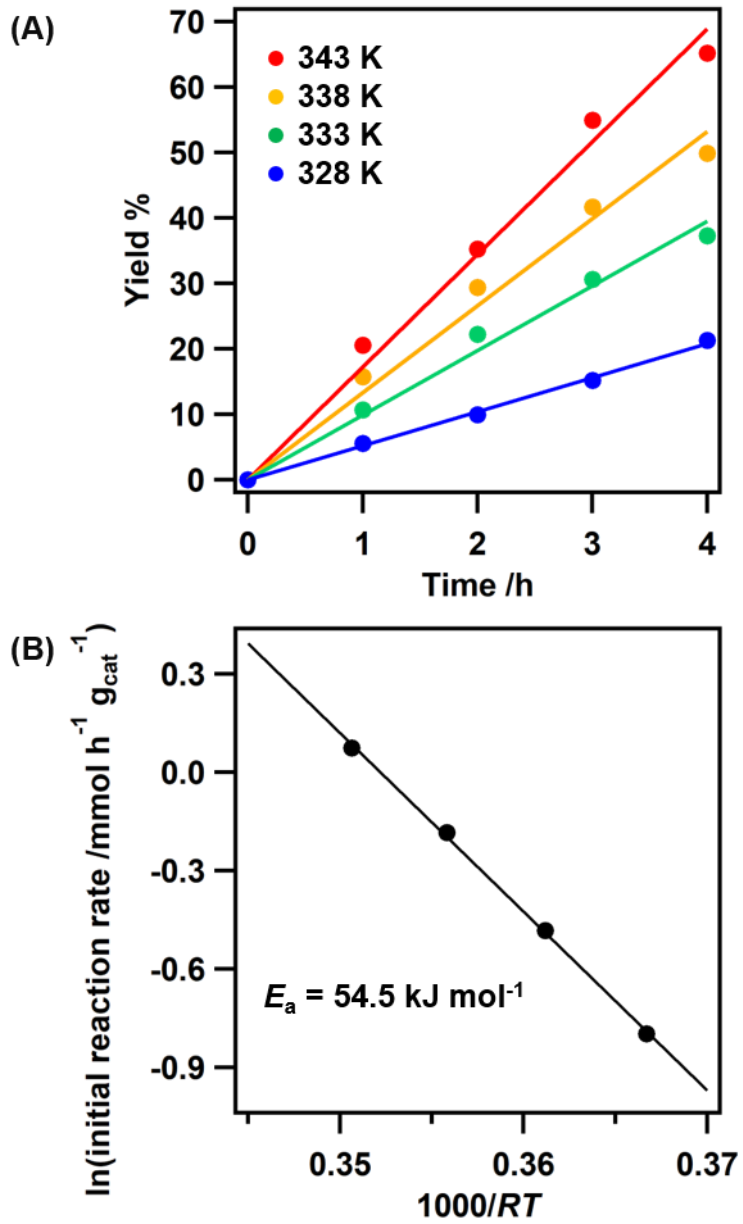

Figure 4.30. (A) Time-yield plots for the 1,4-arylation of cyclohexenone with phenylboronic acid on ICy-*r*-$Cr_{0.19}Rh_{0.06}CeO_z$ at 343, 338, 333, and 328 K.[21] (B) Arrhenius plot for the 1,4-arylation of cyclohexenone with phenylboronic acid on ICy-*r*-$Cr_{0.19}Rh_{0.06}CeO_z$.[21] E_a: activation energy.

Reaction Conditions: ICy-*r*-$Cr_{0.19}Rh_{0.06}CeO_z$ (32 mg; ICy: 0.8 wt%; Rh: 5 mol %), cyclohexenone (0.20 mmol), $PhB(OH)_2$ (0.30 mmol), dodecane (internal standard; 0.10 mmol), cyclohexane (2.0 mL), EtOH (0.2 mL), 343, 338, 333, or 328 K, under N_2.

4.4. Conclusions

The coordination-induced trigger for catalytic activity on the ICy carbene-decorated *r*-$Cr_{0.19}Rh_{0.06}CeO_z$ for 1,4-arylation was proposed for the first time. The ICy ligand was attached as a carbene and mainly interacted with Rh nanoclusters of *r*-$Cr_{0.19}Rh_{0.06}CeO_z$, which was clarified by XAFS, FT-IR, XPS, and PL measurements. The formation of Rh coordination structure with ICy assisted by the Cr species, triggered the induction of the catalytic activity. Several heterogeneity tests indicated that the catalytic reaction proceeded heterogeneously. ICy ligands significantly enhanced catalytic activity for 1,4-arylation compared the other NHC ligands by the efficient coordination to the active Rh nanoclusters. The electronic donation effect of ICy to Rh nanoclusters was negligible, and ICy offered closer adsorption sites of the phenyl group and cyclohexenone on the Rh cluster and facilitated the C−C bond formation of the two moieties, resulting in the changes in the cascade reaction mechanism for the C−C bond formation step, which was proposed by DFT calculations. The current findings will advance the field of catalyst activation by the coordination-induced trigger with NHCs on more complicated heterogeneous catalyst systems.

4.5. Advanced interdisciplinary research in this study

In this study, it is the significant challenges to clarify the interaction of NHC ligands with active surface metal species and its influence to catalytic activity. To address these challenges, I conducted advanced interdisciplinary research collaborated with the fields of surface chemistry, computational chemistry, and organic chemistry.

Since ICy-*r*-$Cr_{0.19}Rh_{0.06}CeO_z$ had a trace amount of ICy ligands (0.8 wt%), surface-sensitive structural characterization such as XPS was necessary to determine the surface coordination structure of the NHC ligands. XPS surface analysis of ICy-*r*-$Cr_{0.19}Rh_{0.06}CeO_z$ was strong and indispensable evidence of the direct interaction of the ICy ligands with the Rh nanoclusters by comparison with reference samples. XPS also revealed not only the chemical state of the surface NHC ligands but also the electronic state of the Rh nanoclusters, indicating that electron donation from the ICy ligand to the Rh nanoclusters is negligible.

In general, heterogeneous catalysts have complicated surface structures, and it is difficult to rigorously determine the active structure on the surface. Multi structural analysis can estimate the average active surface structure. DFT calculations of experimentally estimated model structures are greatly powerful tools to reveal local coordination structures and electronic states of the catalysts. ICy-Rh_4/CeO_2 model structure of ICy-*r*-$Cr_{0.19}Rh_{0.06}CeO_z$ was optimized by DFT and it was revealed that ICy coordinated to a bridge site of the Rh nanocluster. Bader charge analysis supported the experimental results of the negligible electron donation from the ICy carbene to the Rh nanocluster. Furthermore, advanced reaction pathway calculations allowed to estimate the active structures of reaction intermediates that could not be revealed experimentally because XPS is not applicable to liquid-phase reactions.

Suggestions from an organic chemistry perspective made this study more rewarding. The heterogeneity tests provided fundamental evidence that the catalytic reaction heterogeneously proceeded on the catalyst surface. In addition, examination of substrate scope justified the utility on the heterogeneous catalysis. Furthermore, the reciprocal provision of some NHC ligands from Professor Glorius' laboratory and heterogeneous Rh catalysts form our laboratory stimulated and advanced each other's research.

Through the above advanced interdisciplinary research, I was able to propose a new concept of coordination-induced trigger for activity, which could not be uncovered only in my own research field.

4.6. NMR charts

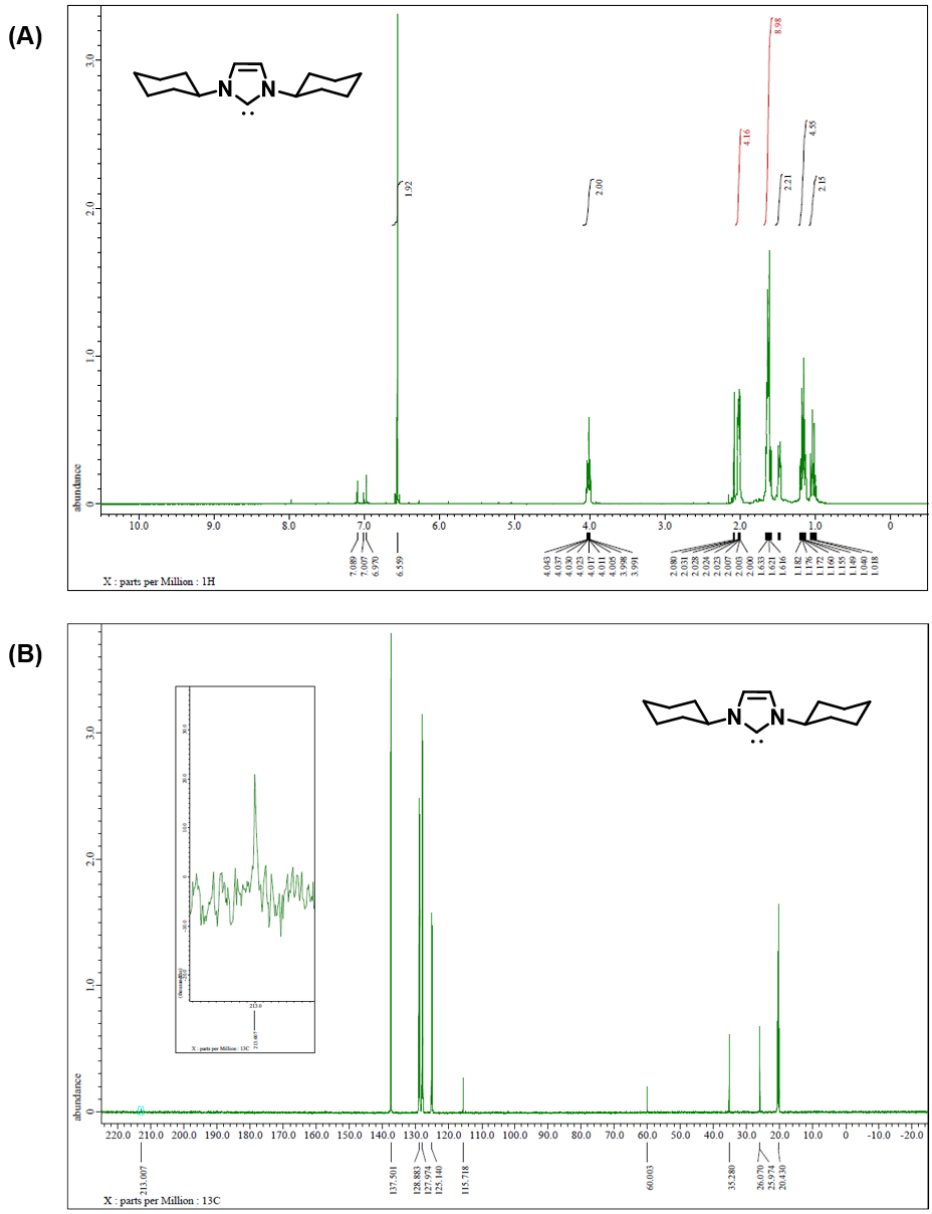

Figure 4.30. (A) ^{1}H NMR of isolated ICy carbene (600 MHz, toluene-d_8). d = 6.56 (s, 2H, NC*H*C*H*N), 4.02 (tt, 2H, J = 11.7, 3.0 Hz, NC*H*), 2.03-2.00 (m, 2H, CH_2), 1.66-1.59 (m, 4H, CH_2), 1.49-1.47 (m, 2H, CH_2), 1.20-1.13 (m, 4H, CH_2), 1.07-0.99 (m, 2H, CH_2). (B) ^{13}C NMR of isolated ICy carbene (150 MHz, toluene-d_8). d = 213.0 (N*C*N), 115.7 (NCHCHN), 60.0 (NCH), 35.3 (*C*H$_2$), 26.1 (*C*H$_2$), 26.0 (*C*H$_2$). (C) ^{1}H NMR (600 MHz) of ICy carbene *in situ* generated in toluene-d_8. Reaction conditions: ICy·HBF$_4$ (0.01 mmol), KO*t*Bu (0.02 mmol), 0.5 mM adamantane solution in toluene-d_8 (1.0 mL), under Ar. Signals of adamantane: d = 1.83 (m, 4H, C*H*), 1.73 (t, 12H, CH_2).

(C)

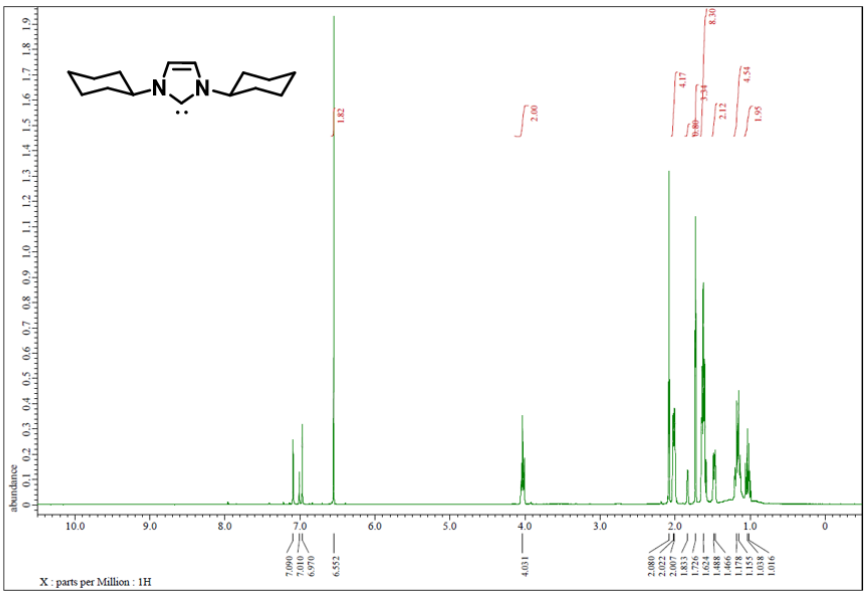

Figure 4.30. [Continued] (A) ^{1}H NMR of isolated ICy carbene (600 MHz, toluene-d_8). d = 6.56 (s, 2H, NC*H*C*H*N), 4.02 (tt, 2H, J = 11.7, 3.0 Hz, NC*H*), 2.03-2.00 (m, 2H, CH_2), 1.66-1.59 (m, 4H, CH_2), 1.49-1.47 (m, 2H, CH_2), 1.20-1.13 (m, 4H, CH_2), 1.07-0.99 (m, 2H, CH_2). (B) ^{13}C NMR of isolated ICy carbene (150 MHz, toluene-d_8). d = 213.0 (N*C*N), 115.7 (N*C*HC*H*N), 60.0 (N*C*H), 35.3 (*C*H$_2$), 26.1 (*C*H$_2$), 26.0 (*C*H$_2$). (C) ^{1}H NMR (600 MHz) of ICy carbene *in situ* generated in toluene-d_8. Reaction conditions: ICy·HBF$_4$ (0.01 mmol), KO*t*Bu (0.02 mmol), 0.5 mM adamantane solution in toluene-d_8 (1.0 mL), under Ar. Signals of adamantane: d = 1.83 (m, 4H, C*H*), 1.73 (t, 12H, CH_2).

Isolated products in 1,4-arylation reaction

3-Phenylcyclohexanone

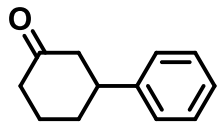

^{1}H NMR (600 MHz, $CDCl_3$): *d* = 7.33 (t, 2H, *J* = 7.5 Hz), 7.26-7.22 (m, 3H), 3.01 (tt, 1H, *J* = 12.0, 3.6 Hz), 2.61-2.35 (m, 4H), 2.17-2.08 (m, 2H), 1.89-1.77 (m, 2H).

^{13}C NMR (150 MHz, $CDCl_3$): *d* = 211.0, 144.4, 128.7, 126.7, 126.6, 49.0, 44.8, 41.2, 32.8, 25.6.

Eluent: 6% ethyl acetate in *n*-hexane

5-Phenylhexan-3-one

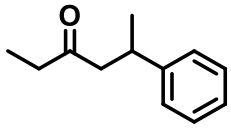

^{1}H NMR (600 MHz, $CDCl_3$): *d* = 7.29 (t, 2H, *J* = 7.8 Hz), 7.21-7.19 (m, 3H), 3.34-3.30 (m, 1H), 2.74-2.61 (m, 2H), 2.37-2.27 (m, 2H), 1.26 (d, 3H, *J* = 6.6 Hz), 0.98 (t, 3H, *J* = 7.2 Hz).

^{13}C NMR (150 MHz, $CDCl_3$): *d* = 210.5, 146.3, 128.5, 126.8, 126.3, 50.8, 36.7, 35.5, 22.0, 7.6.

Eluent: 5% ethyl acetate in *n*-hexane

4,4-Diphenylbutan-2-one

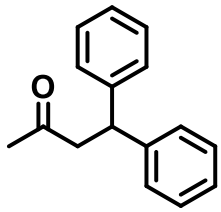

^{1}H NMR (600 MHz, $CDCl_3$): *d* = 7.28-7.25 (m, 4H), 7.22-7.21 (m, 4H), 7.18-7.16 (m, 2H), 4.58 (t, 1H, *J* = 7.5 Hz), 3.18 (d, 2H, *J* = 7.2 Hz), 2.07 (s, 1H).

^{13}C NMR (150 MHz, $CDCl_3$): *d* = 206.9, 143.8, 128.6, 127.7, 126.5, 49.7, 46.1, 30.6.

Eluent: 6% ethyl acetate in *n*-hexane

3-(4-Methoxyphenyl)cyclohexanone

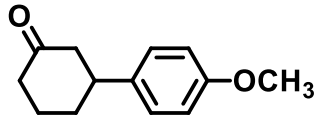

^{1}H NMR (600 MHz, $CDCl_3$): *d* = 7.14 (d, 2H, *J* = 8.4 Hz), 6.87 (d, 2H, 9.0 Hz), 3.80 (s, 3H), 2.97 (tt, 1H, 11.7, 3.6 Hz), 2.59-2.34 (m, 4H), 2.16-2.05 (m, 2H), 1.85-1.74 (m, 2H).

^{13}C NMR (150 MHz, $CDCl_3$): *d* = 211.2, 158.3, 136.6, 127.5, 114.0, 55.3, 49.3, 44.0, 41.2, 33.0. 25.5.

Eluent: 13% ethyl acetate in *n*-hexane

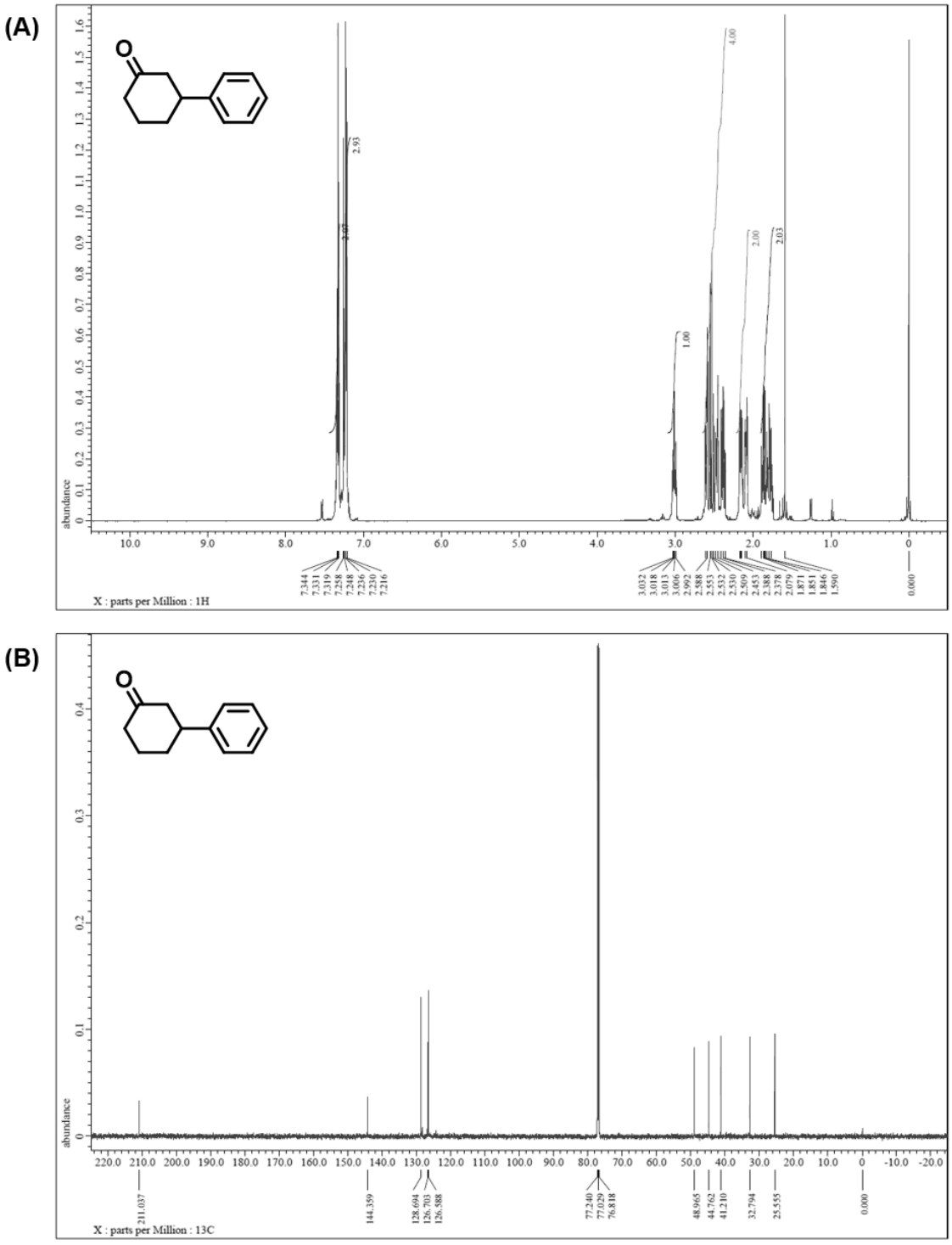

Figure 4.31. (A) ^{1}H NMR (600 MHz, $CDCl_3$) and (B) ^{13}C NMR (150 MHz, $CDCl_3$) of 3-phenylcyclohexanone.

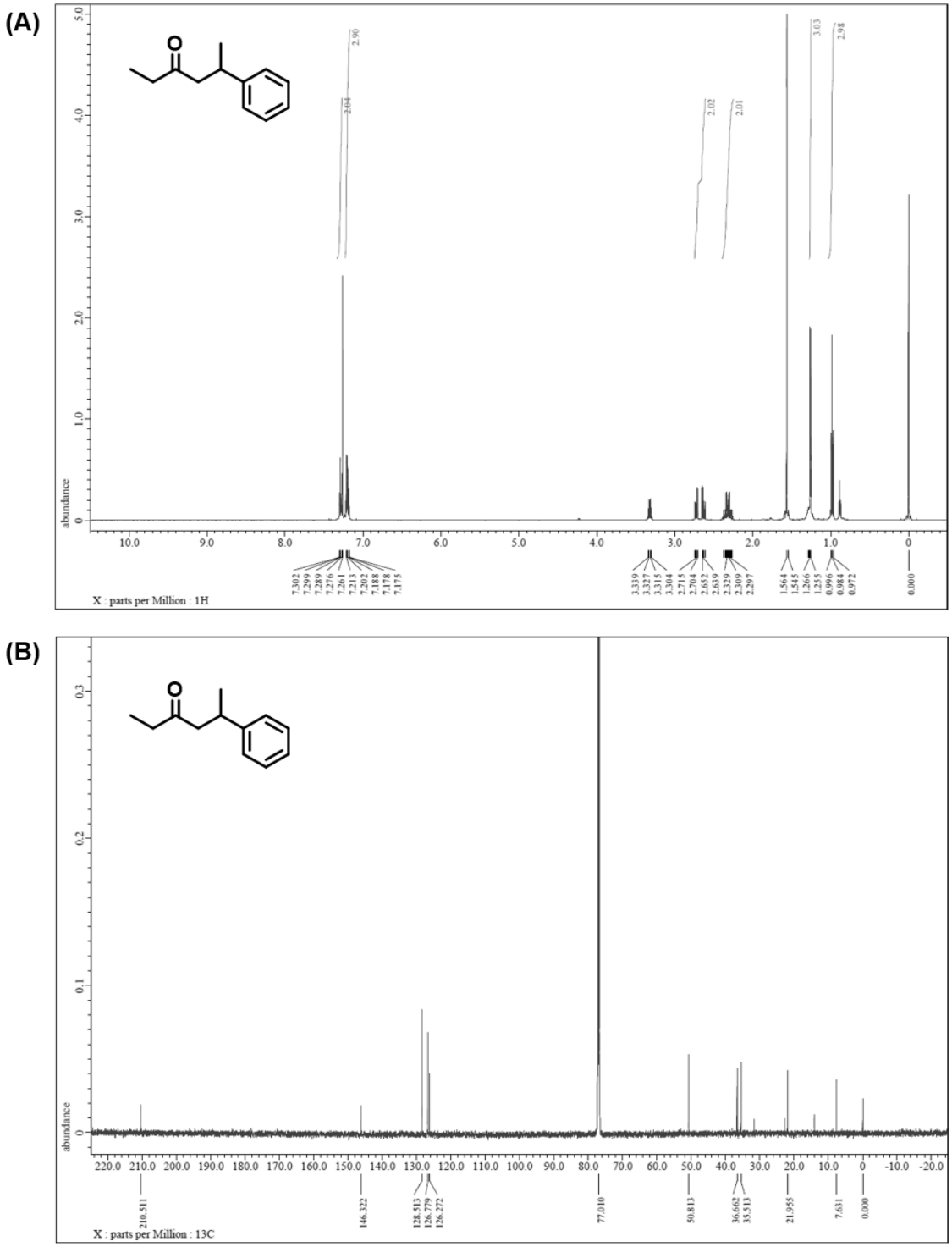

Figure 4.32. (A) ^{1}H NMR (600 MHz, $CDCl_3$) and (B) ^{13}C NMR (150 MHz, $CDCl_3$) of 5-phenylhexan-3-one.

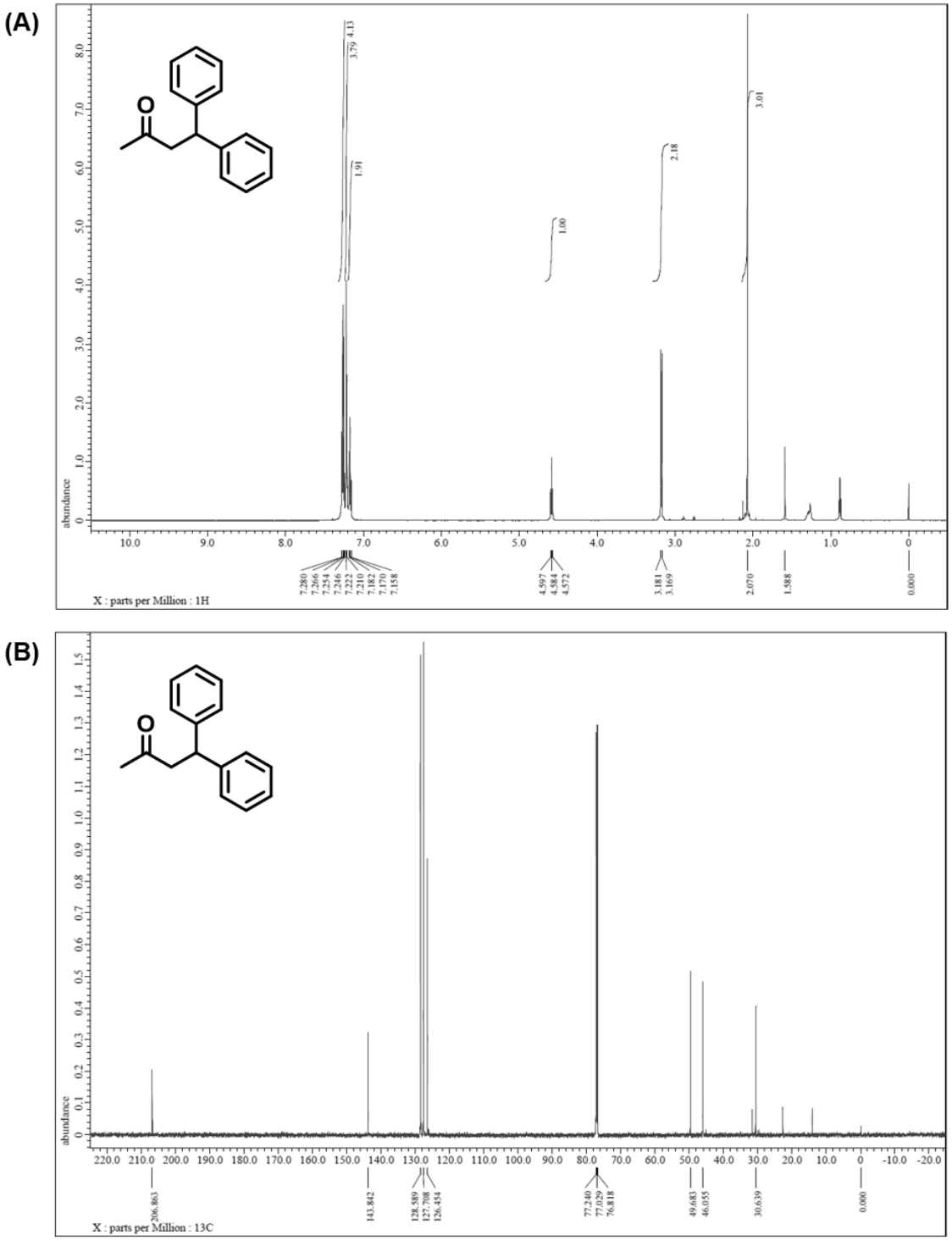

Figure 4.33. (A) ^{1}H NMR (600 MHz, $CDCl_3$) and (B) ^{13}C NMR (150 MHz, $CDCl_3$) of 4,4-diphenylbutan-2-one.

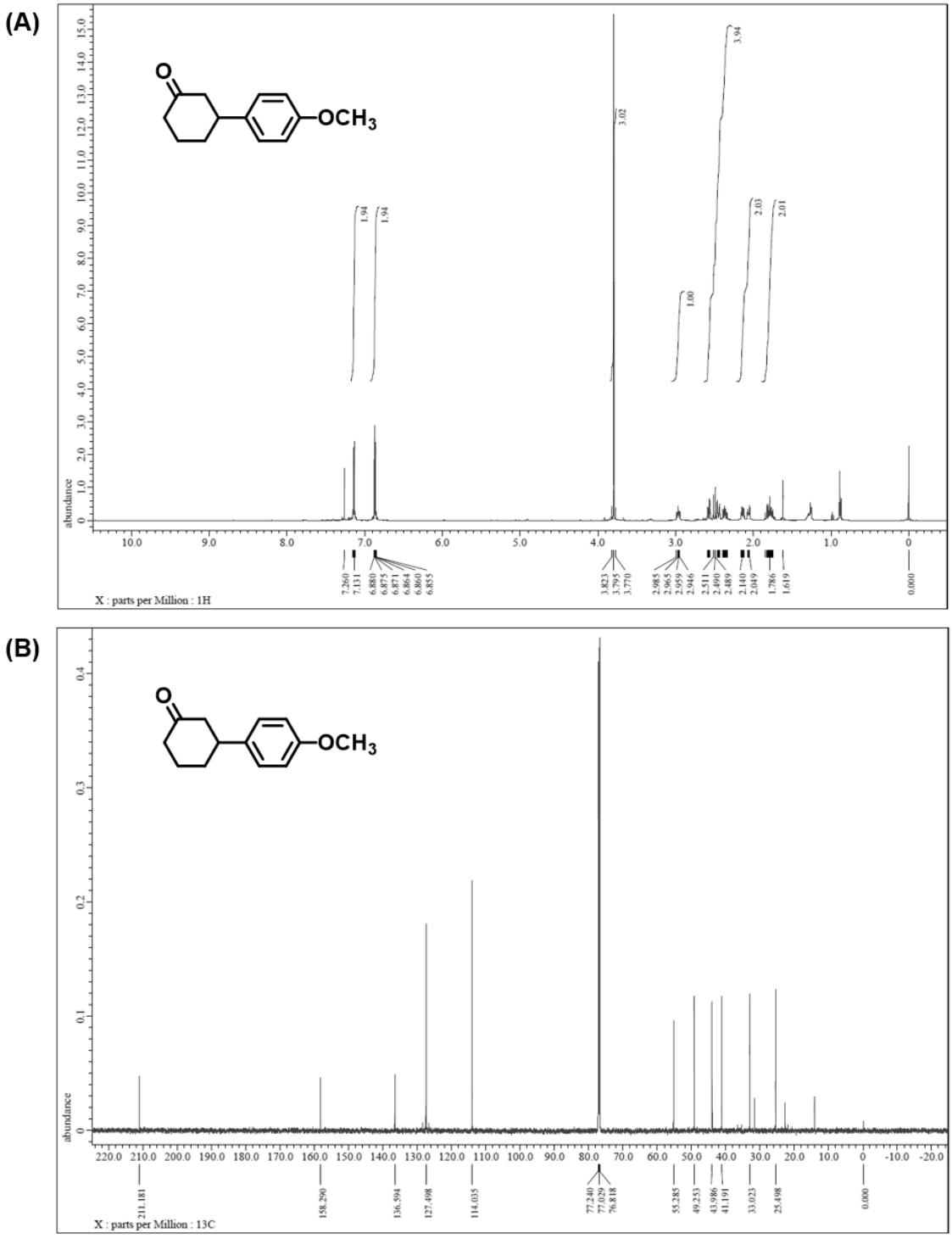

Figure 4.34. (A) ^{1}H NMR (600 MHz, $CDCl_3$) and (B) ^{13}C NMR (150 MHz, $CDCl_3$) of 3-(4-methoxyphenyl)-cyclohexanone.

4.7. References

(1) (a) Arduengo, A. J.; Harlow, R. L.; Kline, M. A Stable Crystalline Carbene. *J. Am. Chem. Soc.* **1991**, *113*, 361−363. (b) Crudden, C. M.; Allen, D. P. Stability and Reactivity of N-Heterocyclic Carbene Complexes. *Coord. Chem. Rev.* **2004**, *248*, 2247−2273. (c) Kantchev, E. A. B.; O'Brien, C. J.; Organ, M. G. Palladium Complexes of N-Heterocyclic Carbenes as Catalysts for Cross-Coupling Reactions−A Synthetic Chemist's Perspective. *Angew. Chem., Int. Ed.* **2007**, *46*, 2768−2813.

(2) (a) *N-Heterocyclic Carbenes in Transition Metal Catalysis*; Glorius, F. Ed.; Springer: Berlin, Heidelberg, 2007. (b) *N-Heterocyclic Carbenes: From Laboratory Curiosities to Efficient Synthetic Tools*: Edition 2; Díez-González, S. Ed.; RSC Publishing: Cambridge, 2017. (c) *N-Heterocyclic Carbenes in Organocatalysis*; Biju, A. T. Ed.; Wiley-VCH: Weinheim, 2019. (d) Hopkinson, M. N.; Richter, C.; Schedler, M.; Glorius, F. An Overview of N-Heterocyclic Carbenes. *Nature* **2014**, *510*, 485–496. (e) Bellotti, P.; Koy, M.; Hopkinson, M. N.; Glorius, F. Recent Advances in the Chemistry and Applications of N-Heterocyclic Carbenes. *Nat. Rev. Chem.* **2021**, *5*, 711–725.

(3) (a) Zhukhovitskiy, A. V.; MacLeod, M. J.; Johnson, J. A. Carbene Ligands in Surface Chemistry: From Stabilization of Discrete Elemental Allotropes to Modification of Nanoscale and Bulk Substrates. *Chem. Rev.* **2015**, *115*, 11503–11532. (b) Engel, S.; Fritz, E.-C.; Ravoo, B. J. New Trends in the Functionalization of Metallic Gold: From Organosulfer Ligands to N-Heterocyclic Carbenes. *Chem. Soc. Rev.* **2017**, *46*, 2057–2075. (c) An, Y.-Y.; Yu, J.-G.; Han, Y.-F. Recent Advances in the Chemistry of N-Heterocyclic-Carbene-Functionalized Metal-Nanoparticles and Their Applications. *Chin. J. Chem.***2019**, *37*, 76–87. (d) Smith, C. A.; Narouz, M. R.; Lummis, P. A.; Singh, I.; Nazemi, A.; Li, C.-H.; Crudden, C. M. N-Heterocyclic Carbenes in Materials Chemistry. *Chem. Rev.* **2019**, *119*, 4986–5056. (e) Koy, M.; Bellotti, P.; Das, M.; Glorius, F. N-Heterocyclic Carbenes as Tunable Ligands for Catalytic Metal Surfaces. *Nat. Catal.* **2021**, *4*, 352–363. (f) Shen, H.; Tian, G.; Xu, Z.; Wang, L.; Wu, Q.; Zhang, Y.; Teo, B. K.; Zheng, N. N-Heterocyclic Carbene Coordinated Metal Nanoparticles and Nanoclusters. *Coord. Chem. Rev.* **2022**, *458*, 214425.

(4) (a) Narouz, M. R.; Osten, K. M.; Unsworth, P. J.; Man, R. W. Y.; Salorinne, K.; Takano, S.; Tomihara, R.; Kaappa, S.; Malola, S.; Dinh, C.-T.; Padmos, J. D.; Ayoo, K.; Garrett, P. J.; Nambo, M.; Horton, J. H.; Sargent, E. H.; Häkkinen, H.; Tsukada, T.; Crudden, C. M. N-Heterocyclic Carbene-Functionalized Magic-Number Gold

Nanoclusters. *Nat. Chem.* **2019**, *11*, 419–425. (b) Narouz, M. R.; Takano, S.; Lummis, P. A.; Levchenko, T. I.; Nazemi, A.; Kaappa, S.; Malola, S.; Yousefalizadeh, G.; Calhoun, L. A.; Stamplecoskie, K. G.; Häkkinen, H.; Tsukuda, T.; Crudden, C. M. Robust, Highly Luminescent Au_{13} Superatoms Protected by N-Heterocyclic Carbenes. *J. Am. Chem. Soc.* **2019**, *141*, 14997–15002. (c) Salorinne, K.; Man, R. W. Y.; Lummis, P. A.; Hazer, M. S. A.; Malola, S.; Yim, J. C.-H.; Veinot, A. J.; Zhou, W.; Häkkinen, H.; Nambo, M.; Crudden, C. M. Synthesis and Properties of an Au_6 Cluster Supported by a Mixed N-Heterocyclic Carbene-Thiolate Ligand. *Chem. Commun.* **2020**, *56,* 6102–6105. (d) Yi, H.; Osten, K. M.; Levchenko, T. I.; Veinot, A. J.; Aramaki, Y.; Ooi, T.; Nambo, M.; Crudden, C. M. Synthesis and Enantioseparation of Chiral Au_{13} Nanoclusters Protected by Bis-N-Heterocyclic Carbene Ligands. *Chem. Sci.* **2021**, *12*, 10436–10440. (e) Man, R. W. Y.; Yi, H.; Malola, S.; Takano, S.; Tsukuda, T.; Häkkinen, H.; Nambo, M.; Crudden, C. M. Synthesis and Characterization of Enantiopure Chiral Bis NHC-Stabilized Edge-Shared Au_{10} Nanocluster with Unique Prolate Shape. *J. Am. Chem. Soc.* **2022**, *144*, 2056–2061. (f) Kulkarni, V. K.; Khiarak, B. N.; Takano, S.; Malola, S.; Albright, E. L.; Levchenko, T. I.; Aloisio, M. D.; Dinh, C.-T.; Tsukuda, T.; Häkkinen, H.; Crudden, C. M. N-Heterocyclic Carbene-Stabilized Hydrido Au_{24} Nanoclusters: Synthesis, Structure, and Electrocatalytic Reduction of CO_2. *J. Am. Chem. Soc*. **2022**, *144*, 9000–9006. (g) Lara, P. Rivada-Wheelaghan, O.; Conejero, S.; Poteau, R.; Philippot, K.; Chaudret, B. Ruthenium Nanoparticles Stabilized by N-Heterocyclic Carbenes: Ligand Location and Influence on Reactivity. *Angew. Chem. Int. Ed.* **2011**, *50*, 12080–12084. (h) Asensio, J. M.; Tricard, S.; Coppel, Y.; Andrés, R.; Chaudret, B.; de Jesús, E. Synthesis of Water-Soluble Palladium Nanoparticles Stabilized by Sulfonated N-Heterocyclic Carbenes. *Chem. Eur. J.* **2017**, *23*, 13435–13444. (i) Salorinne, K.; Man, R. W. Y.; Li, C.-H.; Taki, M.; Nambo, M.; Crudden, C. M. Water-Soluble N-Heterocyclic Carbene-Protected Gold Nanoparticles: Size-Controlled Synthesis, Stability, and Optical Properties. *Angew. Chem. Int. Ed.* **2017**, *56*, 6198–6202. (j) Man, R. W. Y.; Li, C.-H.; MacLean, M. W. A.; Zenkina, O. V.; Zamora, M. T.; Saunders, L. N.; Rousina-Webb, A.; Nambo, M.; Crudden, C. M. Ultrastable Gold Nanoparticles Modified by Bidentate N-Heterocyclic Carbene Ligands. *J. Am. Chem. Soc.* **2018**, *140*, 1576–1579. (k) Bridonneau, N.; Hippolyte, L.; Mercier, D.; Portehault, D.; Desage-El Murr, M.; Marcus, P.; Fensterbank, L.; Chanéac, C.; Ribot, F. N-Heterocyclic Carbene-Stabilized Gold Nanoparticles with Tunable Sizes. *Dalton Trans.* **2018**, *47*, 6850–6859. (l) MacLeod, M. J.; Goodman, A. J.; Ye, H.-Z.;

Nguyen, H. V.-T.; Van Voorhis, T.; Johnson, J. A. Robust Gold Nanorods Stabilized by Bidentate N-Heterocyclic-Carbene-Thiolate Ligands. *Nat. Chem.* **2019**, *11*, 57–63. (m) Crudden, C. M.; Horton, J. H.; Ebralidze, I. I.; Zenkina, O. V.; McLean, A. B.; Drevniok, B.; She, Z.; Kraatz, H.-B.; Mosey, N. J.; Seki, T.; Keske, E. C.; Leake, J. D.; Rousina-Webb, A.; Wu, G. Ultra Stable Self-Assembled Monolayers of N-Heterocyclic Carbenes on Gold. *Nat. Chem.* **2014**, *6*, 409–414. (n) Berg, I.; Amit, E.; Hale, L.; Toste, F. D.; Gross, E. N-Heterocyclic Carbene Based Nanolayer for Copper Film Oxidation Mitigation. *Angew. Chem. Int. Ed.* **2022**, *61*, e202201093.

(5) (a) Soulé, J.-F.; Miyamura, H.; Kobayashi, S. Copolymer-Incarcerated Nickel Nanoparticles with N-Heterocyclic Carbene Precursors as Active Cross-Linking Agents for Corriu-Kumada-Tamao Reaction. *J. Am. Chem. Soc.* **2013**, *135*, 10602–10605. (b) Min, H.; Miyamura, H.; Kobayashi, S. N-Heterocyclic Carbene Coordinated Heterogeneous Pd Nanoparticles as Catalysts for Suzuki-Miyaura Coupling. *Chem. Lett.* **2016**, *45*, 837–839. (c) Zhou, Z.; Li, M.; Liu, G.; Xu, G.; Xue, J. Ultra-Small Sugar-Substituted N-Heterocyclic Carbene-Protected Palladium Nanoparticles and Catalytic Activity. *Appl. Organometal. Chem.* **2019**, *33*, e4942. (d) Yue, C.; Xing, Q.; Sun, P.; Zhao, Z.; Lv, H.; Li, F. Enhancing Stability by Trapping Palladium inside N-Heterocyclic Carbene-Functionalized Hypercrosslinked Polymers for Heterogeneous C–C Bond Formations. *Nat. Commun.* **2021**, *12*, 1875. (e) Gonzalez-Galvez, D.; Lara, P.; Rivada-Wheelaghan, O.; Conejero, S.; Chaudret, B.; Philippot, K.; van Leeuwen, P. W. N. M. NHC-Stabilized Ruthenium Nanoparticles as New Catalysts for the Hydrogenation of Aromatics. *Catal. Sci. Technol.* **2013**, *3*, 99–105. (f) Richter, C.; Schaepe, K.; Glorius, F.; Ravoo, B. J. Tailor-made N-Heterocyclic Carbenes for Nanoparticle Stabilization. *Chem. Commun.* **2014**, *50*, 3204–3207. (g) Ferry, A.; Schaepe, K.; Tegeder, P.; Richter, C.; Chepiga, K. M.; Ravoo, B. J.; Glorius, F. Negatively Charged N-Heterocyclic Carbene-Stabilized Pd and Au Nanoparticles and Efficient Catalysis in Water. *ACS Catal.* **2015**, *5*, 5414–5420. (h) Martínez-Prieto, L. M.; Ferry, A.; Lara, P.; Richter, C.; Philippot, K.; Glorius, F.; Chaudret, B. New Route to Stabilize Ruthenium Nanoparticles with Non-Isolable Chiral N-Heterocyclic Carbenes. *Chem. Eur. J.* **2015**, *21*, 17495–17502. (i) Martínez-Prieto, L. M.; Ferry, A.; Rakers, L.; Richter, C.; Lecante, P.; Philippot, K.; Chaudret, B.; Glorius, F. Long-Chain NHC-Stabilized RuNPs as Versatile Catalysts for One-Pot Oxidation/Hydrogenation Reactions. *Chem. Commun.* **2016**, *52*, 4768–4771. (j) Rühling, A.; Schaepe, K.; Rakers, L.; Vonhören, B.; Tegeder, P.; Ravoo, B. J.; Glorius, F. Modular Bidentate Hybrid NHC-Thioether

Ligands for the Stabilization of Palladium Nanoparticles in Various Solvents. *Angew. Chem. Int. Ed.* **2016**, *55*, 5856–5860. (k) Martinez-Espinar, F.; Blondeau, P.; Nolis, P.; Chaudret, B.; Claver, C.; Castillón, S.; Godard, C. NHC-Stabilised Rh Nanoparticles: Surface Study and Application in the Catalytic Hydrogenation of Aromatic Substrates. *J. Catal.* **2017**, *354*, 113–127. (l) Tegeder, P.; Marelli, M.; Freitag, M.; Polito, L.; Lamping, S.; Psaro, R.; Glorius, F.; Ravoo, B. J.; Evangelisti, C. Metal Vapor Synthesis of Ultrasmall Pd Nanoparticles Functionalized with N-Heterocyclic Carbenes. *Dalton Trans.* **2018**, *47*, 12647–12651. (m) Rakers, L.; Martínez-Prieto, L. M.; López-Vinasco, A. M.; Philippot, K.; van Leeuwen, P. W. N. M.; Chaudret, B.; Glorius, F. Ruthenium Nanoparticles Ligated by Cholesterol-Derived NHCs and Their Application in the Hydrogenation of Arenes. *Chem. Commun.* **2018**, *54*, 7070–7073. (n) Tegeder, P.; Freitag, M.; Chepiga, K. M.; Muratsugu, S.; Möller, N.; Lamping, S.; Tada, M.; Glorius, F.; Ravoo, B. J. N-Heterocyclic Carbene-Modified Au-Pd Alloy Nanoparticles and Their Application as Biomimetic and Heterogeneous Catalysts. *Chem. Eur. J.* **2018**, *24*, 18682–18688. (o) Martínez-Prieto, L. M.; Rakers, L.; López-Vinasco, A. M.; Cano, I.; Coppel, Y.; Philippot, K.; Glorius, F.; Chaudret, B.; van Leeuwen, P. W. N. M. Soluble Platinum Nanoparticles Ligated by Long-Chain N-Heterocyclic Carbenes as Catalysts. *Chem. Eur. J.* **2017**, *23*, 12779–12786. (p) Ye, R.; Zhukhovitskiy, A. V.; Kazantsev, R. V.; Fakra, S. C.; Wickemeyer, B. B.; Toste, F. D.; Somorjai, G. A. Supported Au Nanoparticles with N-Heterocyclic Carbene Ligands as Active and Stable Heterogeneous Catalysts for Lactonization. *J. Am. Chem. Soc.* **2018**, *140*, 4144–4149. (q) Bouzouita, D.; Lippens, G.; Baquero, E. A.; Fazzini, P. F.; Pieters, G.; Coppel, Y.; Lecante, P.; Tricard, S.; Martínez-Prieto, L. M.; Chaudret, B. Tuning the Catalytic Activity and Selectivity of Water-Soluble Bimetallic RuPt Nanoparticles by Modifying Their Surface Metal Distribution. *Nanoscale* **2019**, *11*, 16544–16552. (r) Valero, M.; Bouzouita, D.; Palazzolo, A.; Atzrodt, J.; Dugave, C.; Tricard, S.; Feuillastre, S.; Pieters, G.; Chaudret, B.; Derdau, V. NHC-Stabilized Iridium Nanoparticles as Catalysts in Hydrogen Isotope Exchange Reactions of Anilines. *Angew. Chem. Int. Ed.* **2020**, *59*, 3517–3522.

(6) (a) Crudden, C. M.; Horton, J. H.; Narouz, M. R.; Li, Z.; Smith, C. A.; Munro, K.; Baddeley, C. J.; Larrea, C. R.; Drevniok, B.; Thanabalasingam, B.; McLean, A. B.; Zenkina, O. V.; Ebralidze, I. I.; She, Z.; Kraatz, H.-B.; Mosey, N. J.; Saunders, L. N.; Yagi, A. Simple Direct Formation of Self-Assembled N-Heterocyclic Carbene Monolayers on Gold and Their Application in Biosensing. *Nat. Commun.* **2016**, *7*,

12654. (b) Li, Z.; Narouz, M. R.; Munro, K.; Hao, B, Crudden, C. M.; Horton, J. H.; Hao, H. Carboxymethylated Dextran-Modified N-Heterocyclic Carbene Self-Assembled Monolayers on Gold for Use in Surface Plasmon Resonance Biosensing. *ACS Appl. Mater. Interfaces* **2017**, *9*, 39223–39234. (c) Li, Z.; Munro, K.; Narouz, M. R.; Lau, A.; Hao, H.; Crudden, C. M.; Horton, J. H. Self-Assembled N-Heterocyclic Carbene-Based Carboxymethylated Dextran Monolayers on Gold as a Tunable Platform for Designing Affinity-Capture Biosensor Surfaces. *ACS Appl. Mater. Interfaces* **2018**, *10*, 17560–17570. (d) Singh, I.; Lee, D. S.; Huang, S.; Bhattacharjee, H.; Xu, W.; MacLead, J. F.; Crudden, C. M.; She, Z. N-Heterocyclic Carbenes Meet Toll-like Receptors. *Chem. Commun*. **2021**, *57*, 8421–8424.

(7) (a) Levratovsky, Y.; Gross, E. High Spatial Resolution Mapping of Chemically-Active Self-Assembled N-Heterocyclic Carbenes on Pt Nanoparticles. *Faraday Discuss.* **2016**, *188*, 345–353. (b) Wu, C.-Y.; Wolf, W. J.; Levartovsky, Y.; Bechtel, H. A.; Martin, M. C.; Toste, F. D.; Gross, E. High-Spatial-Resolution Mapping of Catalytic Reactions on Single Particles. *Nature* **2017**, *541*, 511–515. (c) Dery, S.; Kim, S.; Haddad, D.; Cossaro, A.; Verdini, A.; Floreano, L.; Toste, F. D.; Gross, E. Identifying Site-Dependent Reactivity in Oxidation Reactions on Single Pt Particles. *Chem. Sci.* **2018**, *9*, 6523–6531. (d) Dery, S.; Amit, E.; Gross, E. Identifying Catalytic Reactions on Single Nanoparticles. *Top. Catal.* **2018**, *61*, 923–939. (e) Dery, S.; Kim, S; Tomaschun, G.; Berg, I.; Feferman, D.; Cossaro, A.; Verdini, A.; Floreano, L.; Klüner, T.; Toste, F. D.; Gross, E. Elucidating the Influence of Anchoring Geometry on the Reactivity of NO_2-Functionalized N-Heterocyclic Carbene Monolayers. *J. Phys. Chem. Lett.* **2019**, *10*, 5099–5104. (f) Dery, S.; Kim, S; Tomaschun, G.; Haddad, D.; Cossaro, A.; Verdini, A.; Floreano, L.; Klüner, T.; Toste, F. D.; Gross, E. Flexible NO_2-Functionalized N-Heterocyclic Carbene Monolayers on Au (111) Surface. *Chem. Eur. J.* **2019**, *25*, 15067–15072. (g) Dery, S.; Berg, I.; Kim, S.; Cossaro, A.; Verdini, A.; Floreano, L.; Toste, F. D.; Gross, E. Strong Metal-Adsorbate Interactions Increase the Reactivity and Decrease the Orientational Order of OH-Functionalized N-Heterocyclic Carbene Monolayers. *Langmuir* **2020**, *36*, 697–703. (h) Dery, S.; Kim, S.; Feferman, D.; Mehlman, H.; Toste, F. D.; Gross, E. Site-Dependent Selectivity in Oxidation Reactions on Single Pt Nanoparticles. *Phys. Chem. Chem. Phys.* **2020**, *22*, 18765–18769. (i) Dery, S.; Mehlman, H.; Hale, L.; Carmiel-Kostan, M.; Yemini, R.; Ben-Tzvi, T.; Noked, M.; Toste, F. D.; Gross, E. Site-Independent Hydrogenation Reactions on Oxide-Supported Au Nanoparticles Facilitated by Intraparticle Hydrogen Atom Diffusion. *ACS Catal.* **2021**, *11*, 9875–9884. (j) Dery,

S.; Bellotti, P.; Ben-Tzvi, T.; Freitag, M.; Shahar, T.; Cossaro, A.; Verdini, A.; Floreano, L.; Glorius, F.; Gross, E. Influence of N-Substituents on the Adsorption Geometry of OH-Functionalized Chiral N-Heterocyclic Carbenes. *Langmuir* **2021**, *37*, 10029–10035.

(8) (a) Lv, A.; Freitag, M.; Chepiga, K. M.; Schäfer, A. H.; Glorius, F.; Chi, L. N-Heterocyclic-Carbene-Treated Gold Surfaces in Pentacene Organic Field-Effect Transistors: Improved Stability and Contact at the Interface. *Angew. Chem. Int. Ed.* **2018**, *57*, 4792–4796. (b) Nguyen, D. T.; Freitag, M.; Körsgen, M.; Lamping, S.; Rühling, A.; Schäfer, A. H.; Siekman, M. H.; Arlinghaus, H. F.; van der Wiel, W. G.; Glorius, F.; Ravoo, B. J. Versatile Micropatterns of N-Heterocyclic Carbenes on Gold Surfaces: Increased Thermal and Pattern Stability with Enhanced Conductivity. *Angew. Chem. Int. Ed.* **2018**, *57*, 11465–11469. (c) Nguyen, D. T.; Freitag, M.; Gutheil, C.; Sotthewes, K.; Tyler, B. J.; Böckmann, M.; Das, M.; Schlüter, F.; Doltsinis, N. L.; Arlinghaus, H. F.; Ravoo, B. J.; Glorius, F. An Arylazopyrazole-Based N-Heterocyclic Carbene as a Photoswitch on Gold Surfaces: Light-Switchable Wettability, Work Function, and Conductance. *Angew. Chem. Int. Ed.* **2020**, *59*, 13651–13656. (d) Wang, Z.; Das, M.; Gutheil, C.; Osthues, H.; Strieth-Kalthoff, F.; Timmer, A.; Doltsinis, N. L.; Wang, W.; Chi, L.; Glorius, F. Surface Modification with a Fluorinated N-Heterocyclic Carbene on Au: Effect on Contact Resistance in Organic Field-Effect Transistors. *J. Mater. Chem. C* **2022**, *10*, 8589–8595.

(9) (a) Ranganath, K. V. S.; Kloesges, J.; Schäfer, A. H.; Glorius, F. Asymmetric Nanocatalysis: N-Heterocyclic Carbenes as Chiral Modifiers of Fe_3O_4/Pd Nanoparticles. *Angew. Chem. Int. Ed.* **2010**, *49*, 7786–7789. (b) Ernst, J. B.; Muratsugu, S.; Wang, F.; Tada, M.; Glorius, F. Tunable Heterogeneous Catalysis: N-Heterocyclic Carbenes as Ligands for Supported Heterogeneous Ru/K-Al_2O_3 Catalysts to Tune Reactivity and Selectivity. *J. Am. Chem. Soc.* **2016**, *138*, 10718–10721. (c) Ernst, J. B.; Schwermann, C.; Yokota, G.; Tada, M.; Muratsugu, S.; Doltsinis, N. L.; Glorius, F. Molecular Adsorbates Switch on Heterogeneous Catalysis: Induction of Reactivity by N-Heterocyclic Carbenes. *J. Am. Chem. Soc.* **2017**, *139*, 9144–9147. (d) Lewis, R. J.; Koy, M.; Macino, M.; Das, M.; Carter, J. H.; Morgan, D. J.; Davies, T. E.; Ernst, J. B.; Freakley; S. J.; Glorius, F.; Hutchings, G. J. N-Heterocyclic Carbene Modified Palladium Catalysts for the Direct Synthesis of Hydrogen Peroxide. *J. Am. Chem. Soc.* **2022**, *144*, 15431–15436.

(10) (a) Kaeffer, N.; Liu, H.-J.; Lo, H.-K.; Fedorov, A.; Copéret, C. An N-Heterocyclic Carbene Ligand Promotes Highly Selective Alkyne Semihydrogenation with Copper

Nanoparticles Supported on Passivated Silica. *Chem. Sci.* **2018**, *9*, 5366–5371. (b) Kaeffer, N.; Mance, D.; Copéret, C. N-Heterocyclic Carbene Coordination to Surface Copper Sites in Selective Semihydrogenation Catalysts from Solid-State NMR Spectroscopy. *Angew. Chem. Int. Ed.* **2020**, *59*, 19999–20007.

(11) Palazzolo, A.; Naret, T.; Daniel-Bertrand, M.; Buisson, D.-A.; Tricard, S.; Lesot, P.; Coppel, Y.; Chaudret, B.; Feuillastre, S.; Pieters, G. Tuning the Reactivity of a Heterogeneous Catalyst using N-Heterocyclic Carbene Ligands for C–H Activation Reactions. *Angew. Chem. Int. Ed.* **2020**, *59*, 20879–20884.

(12) Lewis, R. J.; Koy, M.; Macino, M.; Das, M.; Carter, J. H.; Morgan, D. J.; Davies, T. E.; Ernst, J. B.; Freakley, S. J.; Glorius, F.; Hutchings, G. J. N-Heterocyclic Carbene Modified Palladium Catalysts for the Direct Synthesis of Hydrogen Peroxide. *J. Am. Chem. Soc.* **2022**, *144*, 15431–15436.

(13) (a) Hayashi, T. Rhodium-Catalyzed Asymmetric Addition of Organo-Boron and -Titanium Reagents to Electron-Deficient Olefins. *Bull. Chem. Soc. Jpn.* **2004**, *77*, 13–21. (b) Christoffers, J.; Koripelly, G.; Rosiak, A.; Rössle, M. Recent Advances in Metal-Catalyzed Asymmetric Conjugate Additions. *Synthesis*, **2007**, *9*, 1279–1300. (c) Alexakis, A.; Bäckvall, J. E.; Krause, M.; Pàmies, O.; Diéguez, M. Enantioselective Copper-Catalyzed Conjugate Addition and Allylic Substitution Reactions. *Chem. Rev.* **2008**, *108*, 2796–2823. (d) Jerphagnon, T.; Pizzuti, M. G.; Minnaard, A. J.; Feringa, B. L. Recent Advances in Enantioselective Copper-Catalyzed 1,4-Addition. *Chem. Soc. Rev.* **2009**, *38*, 1039–1075.

(14) (a) Hayashi, T.; Yamasaki, K. Rhodium-Catalyzed Asymmetric 1,4-Addition and Its Related Asymmetric Reactions. *Chem. Rev.* **2003**, *103*, 2829–2844. (b) Guo, H.-C.; Ma, J.-A. Catalytic Asymmetric Tandem Transformations Triggered by Conjugate Additions. *Angew. Chem. Int. Ed.* **2006**, *45*, 354–366. (c) Hargrave, J. D.; Allen, J. C.; Frost, C. G. Alternatives to Organoboron Reagents in Rhodium-Catalyzed Conjugate Additions. *Chem.–Asian J.* **2010**, *5*, 386–396.

(15) Sakai, M.; Hayashi H.; Miyaura, N. Rhodium-Catalyzed Conjugate Addition of Aryl- or 1-Alkenylboronic Acids to Enones. *Organometallics* **1997**, *16*, 4229–4231.

(16) Takaya, Y.; Ogasawara, M.; Hayashi, T.; Sakai, M.; Miyaura, N. Rhodium-Catalyzed Asymmetric 1,4-Addition of Aryl- and Alkenylboronic Acids to Enones. *J. Am. Chem. Soc.* **1998**, *120*, 5579–5580.

(17) Edwards, H. J.; Hargrave, J. D.; Penrose, S. D.; Frost, C. G. Synthetic Applications of Rhodium Catalysed Conjugate Addition. *Chem. Soc. Rev.* **2010**, *39*, 2093–2105.

(18) (a) Hayashi, T.; Ueyama, K.; Tokunaga, N.; Yoshida, K. A Chiral Chelating Diene as a New Type of Chiral Ligand for Transition Metal Catalysts: Its Preparation and Use for the Rhodium-Catalyzed Asymmetric 1,4-Addition. *J. Am. Chem. Soc.* **2003**, *125*, 11508–11509. (b) Kina, A.; Yasuhara, Y.; Nishimura, T.; Iwamura, H.; Hayashi, T. Kinetic Studies Prove High Catalytic Activity of a Diene-Rhodium Complex in 1,4-Addition of Phenylboronic Acid to α, β-Unsaturated Ketones. *Chem. Asian J.* **2006**, *1*, 707–711. (c) Defieber, C.; Grützmacher, H.; Carreira, E. M. Chiral Olefins as Steering Ligands in Asymmetric Catalysis. *Angew. Chem. Int. Ed.* **2008**, *47*, 4482–4502.

(19) (a) Ma, Y.; Song, C.; Ma, C.; Sun, Z.; Chai, Q.; Andrus, M. B. Asymmetric Addition of Aryl Boron Reagents to Enones with Rhodium Dicyclophane Imidazolium Carbene Catalysis. *Angew. Chem. Int. Ed.* **2003**, *42*, 5871–5874. (b) Truscott, B. J.; Fortman, G. C.; Slawin, A. M. Z.; Nolan, S. P. Well-Defined [Rh(NHC)(OH)] Complexes Enabling the Conjugate Addition of Arylboronic Acids to α,β-Unsaturated Ketones. *Org. Biomol. Chem.* **2011**, *9*, 7038–7041.

(20) Hayashi, T.; Takahashi, M.; Takaya, Y.; Ogasawara, M. Catalytic Cycle of Rhodium-Catalyzed Asymmetric 1,4-Addition of Organoboronic Acids. Arylrhodium, Oxa-π-allylrhodium, and Hydroxorhodium Intermediates. *J. Am. Chem. Soc.* **2002**, *124*, 5052–5058.

(21) Ikemoto, S.; Muratsugu, S.; Koitaya, T.; Tsuji, Y.; Das, M.; Yoshizawa, K.; Glorius, F.; Tada, M. Coordination Induced Trigger for Activity: N-Heterocyclic Carbene-Decorated Ceria Catalysts Incorporating Cr and Rh with Activity Induction by Surface Adsorption Site Control. *J. Am. Chem. Soc.* **2023**, *145*, 1497–1504.

(22) Bakulina, O. D.; Ivanov, M. Y.; Prikhod'ko, S. A; Pylaeva, S.; Zaytseva, I. V.; Surovtsev, N. V.; Adonin, N. Y.; Fedin, M. V. Nanocage Formation and Structural Anomalies in Imidazolium Ionic Liquid Glasses Governed by Alkyl Chains of Cations. *Nanoscale* **2020**, *12*, 19982–19991.

(23) (a) Van Ausdall, B. R.; Glass, J. L.; Wiggins, K. M.; Aarif, A. M.; Louie J. A Systematic Investigation of Factors Influencing the Decarboxylation of Imidazolium Carboxylates. *J. Org. Chem.* **2009**, *74*, 7935–7942. (b) Hans, M.; Lorkowski, J.; Demonceau, A.; Delaude, L. Efficient Synthetic Protocols for the Preparation of Common N-Heterocyclic Carbene Precursors. *Beilstein J. Org. Chem.* **2015**, *11*, 2318–2325.

(24) (a) Jeong, H.; Lee, G.; Kim, B.-S.; Bae, J.; Han, J. W.; Lee, H. Fully Dispersed Rh Ensemble Catalyst to Enhance Low Temperature Activity. *J. Am. Chem. Soc.* **2018**,

140, 9558–9565. (b) Takeguchi, T.; Manabe, S.; Kikuchi, R.; Eguchi, K.; Kanazawa, T.; Matsumoto, S.; Ueda, W. Determination of Dispersion of Precious Metals on CeO_2-Containing Supports. *Appl. Catal. A* **2005**, *293*, 91–96.

(25) (a) Ravel, B.; Newville, M. ATHENA, ARTEMIS, HEPHAESTUS: Data Analysis for X-ray Absorption Spectroscopy Using IFEFFIT. *J. Synchrotron Rad.* **2005**, *12*, 537–541. (b) Newville, M.; Ravel, B.; Haskel, D.; Rehr, J. J.; Stern, E. A.; Yacoby, Y. Analysis of Multiple-Scattering XAFS Data Using Theoretical Standards. *Physica B* **1995**, *208–209*, 154–156.

(26) Bearden, J. A.; Burr, A. F. Reevaluation of X-Ray Atomic Energy Levels. *Rev. Mod. Phys.* **1967**, *39*, 125–142.

(27) (a) Newville, M. IFEFFIT: Interactive XAFS Analysis and FEFF Fitting. *J. Synchrotron Rad.* **2001**, *8*, 322–324. (b) Newville, M.; Līviņš, P.; Yacoby, Y.; Rehr, J. J.; Stern, E. A. Near-Edge X-Ray-Absorption Fine Structure of Pb: A Comparison of Theory and Experiment. *Phys. Rev. B: Condens. Matter Mater. Phys.* **1993**, *47*, 14126–14131.

(28) Ankudinov, A. L.; Ravel, B.; Rehr, J. J.; Conradson, S. D. Real-Space Multiple-Scattering Calculation and Interpretation of X-Ray-Absorption Near-Edge Structure. *Phys. Rev. B: Condens. Matter Mater. Phys.* **1998**, *58*, 7565–7576.

(29) Swanson, H. E.; Gilfrich, N. T.; Ugrinic, G. M. Standard X-ray Diffraction Powder Pattern. *National Bureau of Standards Circular (U. S.)* **1954**, *539*, 1–75.

(30) Coey, J. M. D. The Crystal Structure of Rh_2O_3. *Acta Crystallogr. B* **1970**, *26*, 1876–1877.

(31) Seah, M. P.; Glimore, I. S.; Beamson, G. XPS: Binding Energy Calibration of Electron Spectrometers 5 – Re-evaluation of the Reference Energies. *Surf. Interface Anal.* **1998**, *26*, 642–649.

(32) Repoux, M. Comparison of Background Removal Methods for XPS *Surf. Interface Anal.* **1992**, *18*, 567–570.

(33) (a) Widegren, J. A.; Finke, R. G. A Review of the Problem of Distinguishing True Homogeneous Catalysis from Soluble or Other Metal-Particle Heterogenous Catalysis under Reducing Conditions. *J. Mol. Catal.* **2003**, *198*, 317–341. (b) Crabtree, R. H. Resolving Heterogeneity Problems and Impurity Artifacts in Operationally Homogeneous Transition Metal Catalysts. *Chem. Rev.* **2012**, *112*, 1536–1554. (c) Ernst, J. B.; Schwermann, C.; Yokota, G.; Tada, M.; Muratsugu, S.; Doltsinis, N. L.; Glorius, F. Molecular Adsorbates Switch on Heterogeneous Catalysis: Induction of Reactivity by N-Heterocyclic Carbenes. *J. Am. Chem. Soc.*

2017, *139*, 9144–9147. (d) Moock, D.; Wiesenfeldt, M. P.; Freitag, M.; Muratsugu, S.; Ikemoto, S.; Knitsch, R.; Schneidewind, J.; Baumann, W.; Schäfer, A. H.; Timmer, A.; Tada, M.; Hansen, M. R.; Glorius, F. Mechanistic Understanding of the Heterogeneous, Rhodium-Cyclic(Alkyl)(Amino)Carbene-Catalyzed (Fluoro-)Arene Hydrogenation, *ACS Catal.* **2020**, *10*, 6309–6317.

(34) Frisch, M. J.; Trucks, G. W.; Schlegel, H. B.; Scuseria, G. E.; Robb, M. A.; Cheeseman, J. R.; Scalmani, G.; Barone, V.; Petersson, G. A.; Nakatsuji, H.; Li, X.; Caricato, M.; Marenich, A. V.; Bloino, J.; Janesko, B. G.; Gomperts, R.; Mennucci, B.; Hratchian, H. P.; Ortiz, J. V.; Izmaylov, A. F.; Sonnenberg, J. L.; Williams-Young, D.; Ding, F.; Lipparini, F.; Egidi, F.; Goings, J.; Peng, B.; Petrone, A.; Henderson, T.; Ranasinghe, D.; Zakrzewski, V. G.; Gao, J.; Rega, N.; Zheng, G.; Liang, W.; Hada, M.; Ehara, M.; Toyota, K.; Fukuda, R.; Hasegawa, J.; Ishida, M.; Nakajima, T.; Honda, Y.; Kitao, O.; Nakai, H.; Vreven, T.; Throssell, K.; Montgomery, J. A., Jr.; Peralta, J. E.; Ogliaro, F.; Bearpark, M. J.; Heyd, J. J.; Brothers, E. N.; Kudin, K. N.; Staroverov, V. N.; Keith, T. A.; Kobayashi, R.; Normand, J.; Raghavachari, K.; Rendell, A. P.; Burant, J. C.; Iyengar, S. S.; Tomasi, J.; Cossi, M.; Millam, J. M.; Klene, M.; Adamo, C.; Cammi, R.; Ochterski, J. W.; Martin, R. L.; Morokuma, K.; Farkas, O.; Foresman, J. B.; Fox, D. J. *Gaussian 16, Revision C.01*, Gaussian, Inc., Wallingford CT, 2019.

(35) (a) Becke, A. D. Density-Functional Exchange-Energy Approximation with Correct Asymptotic Behavior. *Phys. Rev. A: At., Mol., Opt. Phys.* **1988**, *38*, 3098–3100. (b) Becke, A. D. Density-Functional Thermochemistry. III. The Role of Exact Exchange. *J. Chem. Phys.* **1993**, *98*, 5648–5652. (c) Perdew, J. P.; Chevary, J. A.; Vosko, S. H.; Jackson, K. A.; Pederson, M. R.; Singh, D. J.; Fiolhais, C. Atoms, Molecules, Solids, and Surfaces: Applications of the Generalized Gradient Approximation for Exchange and Correlation. *Phys. Rev. B: Condens. Matter Mater. Phys.* **1992**, *46*, 6671–6687. (d) Perdew, J. P.; Burke, K.; Wang, Y. Generalized Gradient Approximation for the Exchange-Correlation Hole of a Many-Electron System. *Phys. Rev. B: Condens. Matter Mater. Phys.* **1996**, *54*, 16533–16539. (e) Burke, K.; Perdew, J. P.; Wang, Y. Derivation of a Generalized Gradient Approximation: The PW91 Density Functional. In *Electronic Density Functional Theory: Recent Progress and New Directions*; Dobson, J. F.; Vignale, G.; Das, M. P. Eds.; Springer, 1998; pp 81–111.

(36) (a) Ditchfield, R.; Hehre, W. J.; Pople, J. A. Self-Consistent Molecular-Orbital Methods. IX. An Extended Gaussian-Type Basis for Molecular-Orbital Studies of Organic Molecules. *J. Chem. Phys.* **1971**, *54*, 724–728. (b) Hehre, W. J.; Ditchfield,

R.; Pople, J. A. Self-Consistent Molecular Orbital Methods. XII. Further Extensions of Gaussian-Type Basis Sets for Use in Molecular Orbital Studies of Organic Molecules. *J. Chem. Phys.* **1972**, *56*, 2257–2261. (c) Hariharan, P. C.; Pople, J. A. Accuracy of AH_n Equilibrium Geometries by Single Determinant Molecular Orbital Theory. *Mol. Phys.* **1974**, *27*, 209–214. (d) Hariharan, P. C.; Pople, J. A. The Influence of Polarization Functions on Molecular Orbital Hydrogenation Energies. *Theoret. Chim. Acta* **1973**, *28*, 213–222. (e) Clark, T.; Chandrasekhar, J.; Spitznagel, G. W.; Schleyer, P. v. R. Efficient Diffuse Function- Augmented Basis Sets for Anion Calculations. III. The 3-21+G Basis Set for First-Row Elements, Li–F. *J. Comp. Chem.* **1983**, *4*, 294–301.

(37) Merrick, J. P.; Moran, D.; Radom, L. An Evaluation of Harmonic Vibrational Frequency Scale Factors. *J. Phys. Chem. A* **2007**, *111*, 11683–11700.

(38) (a) Kresse, G.; Furthmüller, J. Efficiency of Ab-initio Total Energy Calculations for Metals and Semiconductors Using a Plane-Wave Basis Set. *Comput. Mater. Sci.* **1996**, 6, 15–50. (b) Kresse, G.; Furthmüller, J. Efficient Iterative Schemes for Ab Initio Total-Energy Calculations Using a Plane-Wave Basis Set. *Phys. Rev. B: Condens. Matter Mater. Phys.* **1996**, *54*, 11169–11186.

(39) Kresse, G.; Joubert, D. From Ultrasoft Pseudopotentials to the Projector Augmented-Wave Method. *Phys. Rev. B: Condens. Matter Mater. Phys.* **1999**, *59*, 1758–1775.

(40) Perdew, J. P.; Burke, K.; Ernzerhof, M. Generalized Gradient Approximation Made Simple. *Phys. Rev. Lett.* **1996**, *77*, 3865–3868.

(41) Calderon, C. E.; Plata, J. J.; Toher, C.; Oses, C.; Levy, O.; Fornari, M.; Natan, A.; Mehl, M. J.; Hart, G.; Buongiorno Nardelli, M.; Curtarolo, S. The AFLOW Standard for High-Throughput Materials Science Calculations. *Comput. Mater. Sci.* **2015**, *108*, 233–238.

(42) (a) Grimme, S.; Antony, J.; Ehrlich, S.; Krieg, H. A Consistent and Accurate Ab Initio Parametrization of Density Functional Dispersion Correction (DFT-D) for the 94 Elements H-Pu. *J. Chem. Phys.* **2010**, *132*, 154104. (b) Grimme, S.; Ehrlich, S.; Goerigk, L. Effect of the Damping Function in Dispersion Corrected Density Functional Theory. *J. Comput. Chem.* **2011**, *32*, 1456–1465.

(43) (a) Henkelman, G.; Arnaldsson, A.; Jónsson, H. A Fast and Robust Algorithm for Bader Decomposition of Charge Density. *Comput. Mater. Sci.* **2006**, *36*, 354–360. (b) Sanville, E.; Kenny, S. D.; Smith, R.; Henkelman, G. Improved Grid-Based Algorithm for Bader Charge Allocation. *J. Comput. Chem.* **2007**, *28*, 899–908.

(44) Henkelman, G.; Uberuaga, B. P.; Jónsson, H. A Climbing Image Nudged Elastic Band

Method for Finding Saddle Points and Minimum Energy Paths. *J. Chem. Phys.* **2000**, *113*, 9901–9904.

(45) (a) Song, W.; Popa, C.; Jansen, A. P. J.; Hensen, E. J. M. Formation of a Rhodium Surface Oxide Film in $Rh_n/CeO_2(111)$ Relevant for Catalytic CO Oxidation: A Computational Study. *J. Phys. Chem. C* **2012**, *116*, 22904–22915. (b) Lu, Z.; Yang, Z. Interfacial Properties of $NM/CeO_2(111)$ (NM = Nobel Metal Atoms or Clusters of Pd, Pt and Rh): A First Principles Study. *J. Phys.: Condens. Matter* **2010**, *22*, 475003.

(46) Chuang, F.-Y.; Yang, S.-M. Cerium Dioxide/Polyaniline Core-Shell Nanocomposites. *J. Colloid Interface Sci.* **2008**, *320*, 194–201.

(47) Hara, K.; Iwahashi, K.; Takakusagi, S.; Uosaki, K.; Sawamura, M. Construction of Self-Assembled Monolayer Terminated with N-Heterocyclic Carbene-Rhodium(I) Complex Moiety. *Surf. Sci.* **2007**, *601*, 5127–5132.

(48) Jiang, L.; Zhang, B.; Médard, G.; Seitsonen, A. P.; Haag, F.; Allegretti, F.; Reichert, J.; Kuster, B.; Barth, J. V.; Papageorgiou, A. C. N-Heterocyclic Carbenes on Close-Packed Coinage Metal Surfaces: Bis-carbene Metal Adatom Bonding Scheme of Monolayer Films on Au, Ag and Cu. *Chem. Sci.* **2017**, *8*, 8301–8308.

(49) Möller, N.; Rühling, A.; Lamping, S.; Hellwig, T.; Fallnich, C.; Ravoo, B. J.; Glorius, F. Stabilization of High Oxidation State Upconversion Nanoparticles by N-Heterocyclic Carbenes. *Angew. Chem. Int. Ed.* **2017**, *56*, 4356–4360.

(50) Binet, C.; Daturi, M.; Lavalley, J.-C. IR Study of Polycrystalline Ceria Properties in Oxidised and Reduced States. *Catal. Today* **1999**, *50*, 207–225.

(51) Türkmen, H.; Çetinkaya, B. N-Heterocyclic Carbene Complexes of Rh(I) and Electronic Effects on Catalysts for 1,2-Addition of Phenylboronic Acid to Aldehydes. *Appl. Organometal. Chem.* **2011**, *25*, 226–232.

(52) (a) Song, W.; Popa, C.; Jansen, A. P. J.; Hensen, E. J. M. Formation of a Rhodium Surface Oxide Film in $Rh_n/CeO_2(111)$ Relevant for Catalytic CO Oxidation: A Computational Study. *J. Phys. Chem. C* **2012**, *116*, 22904–22915. (b) Lu, Z.; Yang, Z. Interfacial Properties of $NM/CeO_2(111)$ (NM = Nobel Metal Atoms or Clusters of Pd, Pt and Rh): A First Principles Study. *J. Phys.: Condens. Matter* **2010**, *22*, 475003.

(53) Grunwaldt, J. D.; Basini, L.; Clausen, B. S. *In Situ* EXAFS Study of Rh/Al_2O_3 Catalysts for Catalytic Partial Oxidation of Methane. *J. Catal.* **2001**, *200*, 321–329.

(54) Several examples of the multi-metallic complexes with bridging NHCs were reported. In these cases, coordinative ligands are included in the side chain of NHCs. (a) Catalano, V. J.; Malwitz, M. A. Short Metal-Metal Separations in a Highly Luminescent Trimetallic Ag(I) Complex Stabilized by Bridging NHC Ligands. *Inorg.*

Chem. **2003**, *42*, 5483–5485. (b) Catalano, V. J.; Munro, L. B.; Strasser, C. E.; Samin, A. F. Modulation of Metal-Metal Separations in a Series of Ag(I) and Intensely Blue Photoluminescent Cu(I) NHC-Bridged Triangular Clusters. *Inorg. Chem.* **2011**, *50*, 8465–8476. (c) Thoi, V. S.; Chang, C. J. Nickel *N*-Heterocyclic Carbene–Pyridine Complexes that Exhibit Selectivity for Electrocatalytic Reduction of Carbon Dioxide over Water. *Chem. Commun.* **2011**, *47*, 6578–6580. (d) Liu, B.; Chen, C.; Zhang, Y.; Liu, X.; Chen, W. Dinuclear Copper(I) Complexes of Phenanthrolinyl-Functionalized NHC Ligands. *Organometallics* **2013**, *32*, 5451–5460. (e) Evans, K. J.; Campbell, C. L.; Haddow, M. F.; Luz, C.; Morton, P. A. Mansell, S. M. Lithium Complexes with Bridging and Terminal NHC Ligands: The Decisive Influence of an Anionic Tether. *Eur. J. Inorg. Chem.* **2019**, 4894–4901.

(55) The bridging NHC was also predicted/calculated by DFT on the multi-metallic complexes. (a) Tsipis, A. C.; Tsipis, C. A. Ligand-Stabilized Aromatic Three-Membered Gold Rings and Their Sandwichlike Complexes. *J. Am. Chem. Soc.* **2005**, *127*, 10623–10638. (b) Francisco, M. A. S.; Fantuzzi, F.; Cardozo, T. M.; Esteves, P. M.; Engels, B.; Oliveira, R. R. Taming the Antiferromagnetic Beast: Computational Design of Ultrashort Mn-Mn Bonds Stabilized by N-Heterocyclic Carbenes. *Chem. Eur. J.* **2021**, *27*, 12126–12136.

(56) (a) Ševčíková, K.; Nehasil, V.; Vorokhta, M.; Haviar, S.; Matolín, V.; Matolínová, I.; Mašek, K.; Píš, I.; Kobayashi, K.; Kobata, M.; Nagata, T.; Matsushita, Y.; Yoshikawa, H. Altering Properties of Cerium Oxide Thin Films by Rh doping. *Mater. Res. Bull.* **2015**, *67*, 5–13. (b) Kibis, L. S.; Kardash, T. Y.; Derevyannikova, E. A.; Stonkus, O. A.; Slavinskaya, E. M.; Svetlichnyi, V. A.; Boronin, A. I. Redox and Catalytic Properties of $Rh_xCe_{1-x}O_{2-d}$ Solid Solution. *J. Phys. Chem, C* **2017**, *121*, 26925–26938. (c) Kibis, L. S.; Svintsitskiy, D. A.; Derevyannikova, E. A.; Kardash, T. Y.; Slavinskaya, E. M.; Stonkus, O. A.; Svetlichnyi, V. A.; Boronin, A. I. From Highly Dispersed Rh^{3+} to Nanoclusters and Nanoparticles: Probing the Low-Temperature NO+CO Activity of Rh-Doped CeO_2 Catalysts. *Appl. Surf. Sci.* **2019**, *493*, 1055–1066.

(57) Kurnatowska, M.; Schuster, M.; Mista, W.; Kepinski, L. Self-Regenerative Property of Nanocrystalline $Ce_{0.89}M_{0.11}O_{2-y}$ (M=Pd, Rh) Mixed Oxides. *ChemCatChem* **2014**, *6*, 3125–3131.

(58) (a) The changes in the total electronic energy were calculated at $T = 0$ K with the current DFT method; therefore, they cannot directly be compared with the energy obtained in experiment. This is because the zero-point energy (coming from zero-

point oscillations) and temperature dependent vibrational energy are not included. Also, the choice of density functional may make a difference in the calculated energy values. (b) Velikokhatnyi, O. I.; Kumta, P. N. Energetics of the Lithium-Magnesium Imide–Magnesium Amide and Lithium Hydride Reaction for Hydrogen Storage: An Ab Initio Study. *Mater. Sci. Eng. B* **2007**, *140*, 114–122. (c) Tsuji, Y.; Kurino, K.; Yoshizawa, K. Mixed Anion Control of the Partial Oxidation of Methane to Methanol on the β-PtO_2 Surface. *ACS Omega* **2021**, *6*, 13858–13869.

Chapter 5

Concluding remarks

I have designed ceria-based catalysts by modulating Rh species with Cr oxides and by decorating with NHC ligands and demonstrated that the fine modification of active surface structures can bring about the enhancement of catalytic activity. Incorporated multiple transition metal species of Cr and Rh produced not only concertedly active redox properties of CeO_2 but also highly dispersed cooperative active sites, resulting in enhanced the catalytic performances with oxygen transfer. NHC ligands coordinated to Rh nanoclusters formed by the assist of Cr oxides and the concerted coordination structure triggered catalytic activity for C-C bond formation reaction.

In chapter 2, a ceria-based catalyst incorporated with Cr and a trace amount of Rh ($Cr_{0.19}Rh_{0.06}CeO_z$) was prepared by a hydrothermal method. The $Cr_{0.19}Rh_{0.06}CeO_z$ oxide had the structure that $Cr^{6-\gamma}O_{3-x}$ nanodomains and $Rh^{3+\delta}$ species were dispersed on the surface of fluorite CeO_2, which were characterized by HAADF-STEM-EDS/EELS, XAFS, and XPS. It was found that $Cr_{0.19}Rh_{0.06}CeO_z$ exhibited the remarkable and reversible low-temperature redox properties at < 373 K. *In situ* XAFS and *in situ* AP-XPS characterizations during the redox processes clarified that not only Cr and Rh but also Ce cooperatively involved in the low-temperature redox processes of the $Cr_{0.19}Rh_{0.06}CeO_z$. The dispersed $Rh^{3+\delta}$ species was transformed to Rh nanoclusters under the H_2 reduction, and the formation of the Rh nanoclusters promoted the dual reductions of the Cr and Ce oxides.

In chapter 3, the reversible low-temperature redox activity of $Cr_{0.19}Rh_{0.06}CeO_z$ was found to lead to the efficient catalysis for the complete reduction of NO with high N_2 selectivity at 473 K. The $Cr_{0.19}Rh_{0.06}CeO_z$ catalyst exhibited higher NO conversion and N_2 selectivity below 473 K than those of $Rh_{0.04}CeO_z$ and $Cr_{0.17}CeO_z$, indicating cooperative catalytic enhancement by Cr and Rh species. $Cr_{0.19}Rh_{0.06}CeO_z$ also showed the remarkable durability for the NO reduction at 473 K for up to 216 h without large agglomeration of the dispersed Cr and Rh species. *In situ* FT-IR and *in situ* XAFS characterizations provided mechanistic insights for understanding the roles of Cr and Rh in the NO reduction with CO. The Cr oxides played a key role not only to generate the highly dispersed Rh species, responsible for the co-activation of CO and NO, but also to transfer the oxygen species from the cleaved NO to CO on the CeO_2 surface, resulting in the promotion of the efficient NO reduction with CO at the low temperature.

In chapter 4, the coordination-induced trigger for catalytic activity by the decoration of heterogeneous structure with NHC ligands was found. ICy-decorated $Cr_{0.19}Rh_{0.06}CeO_z$ reduced with H_2 (ICy-*r*-$Cr_{0.19}Rh_{0.06}CeO_z$) was prepared by a direct decoration method with *in situ* generated ICy carbene. ICy ligand was grafted keeping a carbene structure,

and mainly interacted with Rh nanoclusters of *r*-$Cr_{0.19}Rh_{0.06}CeO_z$, which was revealed by XAFS, FT-IR, XPS, and PL spectroscopy. ICy-*r*-$Cr_{0.19}Rh_{0.06}CeO_z$ exhibited catalytic activities for the 1,4-arylation of cyclohexenone with phenylboronic acid, which was not catalyzed by *r*-$Cr_{0.19}Rh_{0.06}CeO_z$ without ICy decoration and ICy·HBF_4-*r*-$Cr_{0.19}Rh_{0.06}CeO_z$ without ICy carbene formation. ICy-*r*-$Rh_{0.04}CeO_z$ showed low catalytic activity, and ICy-*r*-$Cr_{0.17}CeO_z$ and ICy-*r*-CeO_z without the Rh species provided no products. The catalytic performances thus suggested that the interaction of the ICy carbene with the Rh nanoclusters was essential for the induction of the catalytic activity. ICy ligands more efficiently enhanced the catalytic activity compared with the other NHC ligands (IMe, I*t*Bu, IBn, and IMes). The induction of the catalytic activity could not be attributed to the electronic donation effect of ICy to Rh nanoclusters, which was characterized by Rh *K*-edge XANES and Rh 3d XPS. DFT calculations of the modelled ICy-decorated surface Rh nanocluster suggested that the ICy carbene manipulated adsorption sites of the phenyl group close to cyclohexenone on the Rh cluster, and prompted the C−C bond formation of the phenyl group and cyclohexenone.

Briefly, in the present thesis, I have demonstrated that the modification with multiple metal species and organic ligands creates novel active structures on the catalyst surface and brings about the remarkable catalytic activities. The current findings will cultivate heterogeneous mixed metal oxide catalysis and advance the strategies of catalyst activation in more complicated heterogeneous catalyst systems by the addition of third or fourth redox active metal ions and by the coordination-induced trigger with other types of NHC ligands.

List of publications

Publications related to this thesis

(1) Ikemoto, S.; Huang, X.; Muratsugu, S.; Nagase, S.; Koitaya, T.; Matsui, H.; Yokota, G.; Sudoh, T.; Hashimoto, A.; Tan, Y.; Yamamoto, S.; Tang, J.; Matsuda, I.; Yoshinobu, J.; Yokoyama, T.; Kusaka, S.; Matsuda, R.; Tada, M. Reversible Low-Temperature Redox Activity and Selective Oxidation Catalysis Derived from the Concerted Activation of Multiple Metal Species on Cr and Rh-Incorporated Ceria Catalysts. *Phys. Chem. Chem. Phys.* **2019**, *21*, 20868–20877. DOI: 10.1039/C9CP04625A.

(2) Ikemoto, S.; Muratsugu, S.; Koitaya, T.; Tada, M. Chromium Oxides as Structural Modulators of Rhodium Dispersion on Ceria to Generate Active Sites for NO Reduction. *ACS Catal.* **2022**, *12*, 431–441. DOI: 10.1021/acscatal.1c03807.

(3) Ikemoto, S.; Muratsugu, S.; Koitaya, T.; Tsuji, Y.; Das, M.; Yoshizawa, K.; Glorius, F.; Tada, M. Coordination Induced Trigger for Activity: N-Heterocyclic Carbene-Decorated Ceria Catalysts Incorporating Cr and Rh with Activity Induction by Surface Adsorption Site Control. *J. Am. Chem. Soc.* **2023**, *145*, 1497–1504. DOI: 10.1021/jacs.2c07290.

Other publications

(1) Muratsugu, S.; Baba, H.; Tanimoto, T.; Sawaguchi, K.; Ikemoto, S.; Tasaki, M.; Terao, Y.; Tada M. Chemoselective Epoxidation of Cholesterol Derivatives on a Surface-Designed Molecularly Imprinted Ru-Porphyrin Catalyst. *Chem. Commun.* **2018**, *54*, 5114–5117. DOI: 10.1039/C8CC00896E.

(2) Morisako, S.; Watanabe, S.; Ikemoto, S.; Muratsugu, S.; Tada, M.; Yamashita, M. Synthesis of A Pincer-Ir(V) Complex with A Base-Free Alumanyl Ligand and Its Application toward Dehydrogenation of Alkanes. *Angew. Chem. Int. Ed.* **2019**, *58*, 15031–15035. DOI: 10.1002/anie.201909009.

(3) Akiyama, S.; Ikemoto, S.; Muratsugu, S.; Tada, M.; Yamashita, M. Copper Complexes Bearing a Dianionic Diborane(4) Ligand: Synthesis and Evaluation of the Donor Property. *Organometallics* **2020**, *39*, 500–504. DOI: 10.1021/acs.organomet.0c00027.

(4) Moock, D.; Wiesenhfeldt, M. P.; Freitag, M.; Muratsugu, S.; Ikemoto, S.; Knitsch, R.; Schneidewind, J.; Bauman, W.; Shafer, A. H.; Timmer, A.; Tada, M.; Hansen, M. R.; Glorius, F. Mechanistic Understanding of the Heterogeneous, Rhodium-Cyclic(Alkyl)(Amino)Carbene-Catalyzed (Fluoro-)Arene Hydrogenation. *ACS Catal.* **2020**, *10*, 6309–6317. DOI: 10.1021/acscatal.0c01074

(5) Iwano, T.; Shitamatsu, K.; Ogiwara, N.; Okuno, M.; Kikukawa, Y.; Ikemoto, S.; Shirai, S.; Muratsugu, S.; Waddell, P. G.; Errington, R. J.; Sadakane, M.; Uchida, S. Ultrahigh Proton Conduction via Extended Hydrogen-Bonding Network in a Preyssler-Type Polyoxometalate-Based Framework Functionalized with a Lanthanide Ion. *ACS Appl. Mater. Interfaces* **2021**, *13*, 19138–19147. DOI: 10.1021/acsami.1c01752.

Acknowledgements

This research was carried out under the supervision of Professor Dr. Mizuki Tada (Nagoya University). I would like to present my sincere gratitude to for giving me not only an opportunity of this attractive and challenging research but also her profitable discussion, valuable suggestion, and continuous encouragement. I would like to express my faithful gratitude to Associate Professor Dr. Satoshi Muratsugu (Nagoya University), my direct supervisor, for his numerous invaluable suggestions, meaningful discussions, and enthusiastic encouragement. He has also guided me in research planning, experimental operation, and presentations.

The current interdisciplinary research was promoted by many co-researchers in various research fields. I would like to express my deep gratitude to Associate Professor Dr. Takanori Koitaya (Kyoto University) for supporting XPS and *in situ* AP-XPS measurements and giving me his many suggestions on surface characterization. I would like to express my appreciation to Professor Dr. Frank Glorius (Westfälische Wilhelms-Universität Münster) and Dr. Mowpriya Das (Westfälische Wilhelms-Universität Münster) for their constructive discussions and suggestions on organic chemistry and providing NHC precursors. I would like to appreciate to Professor Dr. Kazunari Yoshizawa (Kyushu University) and Associate Professor Dr. Yuta Tsuji (Kyushu University) for the DFT calculations and their worthful suggestions in the computational chemistry.

The professors in our laboratory gave me a lot of helpful suggestions. I am deeply grateful to Associate Professor/Lecturer Dr. Hirosuke Matsui (Nagoya University) for his valuable suggestions, discussions, and kind supports. I would like to express my deep gratitude to Professor Dr. Gabor Samjeske (Nagoya University), Professor Dr. Yasuhiro Ohki (Kyoto University), Associate Professor Dr. Hirotoshi Sakamoto (Kyoto University), Assistant Professor Dr. Caterina Suzanna Wondergem (Nagoya University) for giving me a lot of suggestions.

The characterization in this research was supported by many co-researchers and technical staffs. I would like to deeply acknowledge Professor Dr. Ryotaro Matsuda (Nagoya University) and Assistant Professor Dr. Shinpei Kusaka (Nagoya University) for their help with low-temperature TPO measurements. I would like to thank Mr. Kimitaka Higuchi (Nagoya University) for HAADF-STEM measurements. I would like to thank Dr. Ayako Hashimoto (National Institute for Materials Science) for her useful suggestions on HAADF-STEM-EELS analysis. I am particularly grateful to a former technical staff of our laboratory Ms. Ayu Kodaira (Nagoya University) for her help with HAADF-

STEM-EELS/EDS measurements and preparation of oxide catalysts. I would like to thank Dr. Kin-ichi Oyama (Nagoya University) for kind suggestions on ESI-MS measurement. I am deeply grateful to the beamline staff at KFK-PF and the Aichi Synchrotron Radiation Center for their many suggestions on XAFS and *in situ* experiments.

I would like to thank all the members of our laboratory for having a nice daily life in the lab together.

I would like to acknowledge a JSPS fellowship and GTR program for financial supports of this work.

Finally, I would like to greatly thank my family for supporting my research life.